

INITIAL DATA FOR BLACK HOLE EVOLUTIONS

A Dissertation

Presented to the Faculty of the Graduate School
of Cornell University

in Partial Fulfillment of the Requirements for the Degree of
Doctor of Philosophy

by

Harald Paul Pfeiffer

August 2003

arXiv:gr-qc/0510016v1 4 Oct 2005

© 2003 Harald Paul Pfeiffer
ALL RIGHTS RESERVED

INITIAL DATA FOR BLACK HOLE EVOLUTIONS

Harald Paul Pfeiffer, Ph.D.

Cornell University 2003

We discuss the initial value problem of general relativity in its recently unified Lagrangian and Hamiltonian pictures and present a multi-domain pseudo-spectral collocation method to solve the resulting coupled nonlinear partial differential equations. Using this code, we explore several approaches to construct initial data sets containing one or two black holes: We compute quasi-circular orbits for spinning equal mass black holes and unequal mass (nonspinning) black holes using the effective potential method with Bowen-York extrinsic curvature. We compare initial data sets resulting from different decompositions, and from different choices of the conformal metric with each other. Furthermore, we use the quasi-equilibrium method to construct initial data for single black holes and for binary black holes in quasi-circular orbits. We investigate these binary black hole data sets and examine the limits of large mass-ratio and wide separation. Finally, we propose a new method for constructing spacetimes with superposed gravitational waves of possibly very large amplitude.

BIOGRAPHICAL SKETCH

Harald Pfeiffer was born on January 29 1974, and spent his childhood in Rüdendhausen, Germany. Having done elementary school, high-school and civil service just two miles away from home, he decided to increase distance from home to study physics at the university of Bayreuth, a sleepy town mostly known for the composer Wagner. Being adventurous, and somewhat bored with the pace the usual courses proceeded, he ended up in a lecture, and subsequently in a seminar, about general relativity, a topic which has had captured him in the form of popular books since much earlier days.

Asking a few professors for opportunities to spend *one* year abroad, one of them, Werner Pesch, simply answered “Go to Cornell,” an idea that caught his fancy immediately. He applied for grad school in the US and, as he wasn’t sure he wanted to go so far away for such a long time, he also applied to the University of Cambridge, UK. When he learned that he could defer admission to Cornell for a year, he decided to take both and went to Cambridge in October 1997 to “attend diligently a Course in Advanced Study in Mathematics” (so says the Cambridge diploma), or, as it is known to the world, to do Part III.

Besides classes, Cambridge was great for punting, Backgammon and enjoying good food at various formal dinners. However, socially, Cambridge turned out to differ only slightly from Germany; important foods like Croissants were readily available, and there were just too many Germans to hang out with. Harald needed to go further away into real alien territory and started graduate school at Cornell in 1998. Ithaca has been a really nice place, and Cornell a great school to learn physics, do physics, and meet a large variety of amazing people.

One year before he went to England, Sylke entered his life. But she left immediately to study in Ireland and when she returned, Harald was getting ready for England. It was finally in Ithaca that they could spent an extended period of time together. Sylke and Harald got married in 2000, and a precious son was born to them in Spring 2003.

Harald has accepted a postdoctoral position at Caltech, the very school that didn’t receive any of his letters of recommendation when he applied to its PhD program six years earlier.

ACKNOWLEDGEMENTS

It is a pleasure to express my gratitude to all those people who have helped me toward this point in my life. First of all, I would like to thank Saul Teukolsky, my thesis adviser, for his guidance and support throughout my time at Cornell. Saul was available for advice whenever I needed it, but also gave me considerable freedom to pursue my own ideas. I continue to be amazed by his ability to answer very concisely whatever question I put before him as well as his talent to ask relevant questions. I am very much indebted to Greg Cook with whom I have worked on several projects over the years, and who taught me a lot about the initial value problem. The idea of developing a spectral elliptic solver is his. It is a pleasure to thank James York for many discussions and a joint paper, which have refined my understanding of general relativity and the initial value problem tremendously. I am also grateful to Jimmy for serving as a proxy on my B-exam. On a day to day basis, I worked with Larry Kidder, Mark Scheel and, later, Deirdre Shoemaker. I thank Mark and Larry for sharing their code with me, and all three for putting up with my sometimes too short patience and too high temper. I enjoyed working with them and look forward to continue to do so. I am also indebted to Dong Lai for guiding me through a completely different research project. Thanks go to Éanna Flanagan and Eberhard Bodenschatz who served on my special committee, and to Werner Pesch and Helmut Brand for significant advice since my time at Bayreuth.

The development of my code depended crucially on an existing code base for spectral methods written by Larry and Mark, on modern iterative methods for linear systems made available by the PETSc-team, and on visualization software developed by the Cornell undergraduates Adam Bartnik, Hiro Oyaizu and Yor Limkummer; I thank all these people. I also acknowledge the Department of Physics, Wake Forest University, for access to their IBM SP2, on which most of the computations in this thesis were performed.

I am very grateful for the many people who made life in Ithaca and in Space Sciences so comfortable and fun: The sixth floor crowd, among them Steve Drasco, Étienne Racienne, Marc Favata, Wolfgang Tichy, John Karcz, Akiko Shirakawa, Wynn Ho, and in particular Jeandrew Brink with her love for ice cream and deep and/or crazy ideas. Furthermore Gil Toombes, Eileen Tan (thanks for the car at several occasions), Wulf Hofbauer, Horace & Ileana Stoica and Shaffique Adam. St. Luke Lutheran church has always been a warm, welcoming and supportive

place. Maybe even more important are friends back home, among them Stephan Wildner, Uli Schwarz, Günter Auernhammer, Elke Götz, Katharina Eisen, Uli Schwantag and Dirk Haderlein.

I wish to thank my parents Betty and Wilhelm Pfeiffer for teaching me the truly important things in life and for supporting me throughout my studies. They provided the roots and the foundation that enabled me to reach for things they never imagined to exist. Finally, I wish to thank my wife, although words cannot capture her impact on me: Thank you for accompanying me through this amazing life.

TABLE OF CONTENTS

1	Introduction	1
2	The initial value problem of general relativity	5
2.1	Preliminaries	7
2.2	Conformal thin sandwich formalism	8
2.2.1	Fixing \tilde{N} via \tilde{K}	11
2.2.2	Invariance to conformal transformations of the free data	12
2.2.3	Gauge degrees of freedom	13
2.2.4	Implications for an evolution of the initial data	14
2.3	Extrinsic curvature decomposition	16
2.3.1	Remarks on the extrinsic curvature decomposition	18
2.3.2	Identification of σ with the lapse N	19
2.3.3	Stationary spacetimes have $A_{TT}^{ij} = 0$	20
2.3.4	Earlier decompositions of the extrinsic curvature	21
2.4	Black hole initial data	21
3	A multidomain spectral method for solving elliptic equations	25
3.1	Introduction	25
3.2	Spectral Methods	27
3.2.1	Chebyshev polynomials	29
3.2.2	Basis functions in higher dimensions	30
3.2.3	Domain Decomposition	30
3.3	Implementation	32
3.3.1	One-dimensional Mappings	32
3.3.2	Basis functions and Mappings in higher Dimensions	34
3.3.3	The operator \mathcal{S}	36
3.3.4	Solving $\mathcal{S}u = 0$	39
3.3.5	\mathcal{S} in higher dimensions	42
3.3.6	Extension of \mathcal{S} to Spherical Shells	43
3.3.7	Implementation Details	44
3.4	Examples	45
3.4.1	$\nabla^2 u = 0$ in 2-D	45
3.4.2	Quasilinear Laplace equation with two excised spheres	48
3.4.3	Coupled PDEs in nonflat geometry with excised spheres	57
3.5	Improvements	59
3.6	Conclusion	60
3.7	Appendix A: Preconditioning of inverse mappings	61
3.8	Appendix B: Preconditioning the nonflat Laplacian	61

4	Quasi-circular orbits for spinning binary black holes	64
4.1	Introduction	64
4.2	Implementation	66
4.3	Results	70
4.3.1	Behavior at large separations	71
4.3.2	Behavior at small separations – ISCO	76
4.3.3	Common apparent horizons	81
4.4	Discussion	83
4.5	Conclusion	87
4.6	Appendix: Common apparent horizons	88
5	Quasi-circular orbits in the test-mass limit	92
5.1	Introduction	92
5.2	Implementation & Results	93
5.3	Discussion	99
5.4	Appendix: L depends quadratically on β close to ISCO	101
6	Comparing initial-data sets for binary black holes	102
6.1	Introduction	102
6.2	Decompositions of Einstein’s equations and the constraint equations	105
6.2.1	3+1 Decomposition	105
6.2.2	Decomposition of the constraint equations	106
6.3	Choices for the freely specifiable data	112
6.3.1	Kerr-Schild coordinates	112
6.3.2	Freely specifiable pieces	114
6.4	Numerical Implementation	116
6.4.1	Testing the conformal TT and physical TT decompositions	117
6.4.2	Testing conformal thin sandwich equations	121
6.4.3	Convergence of binary black hole solutions	124
6.5	Results	125
6.5.1	Binary black hole at rest	125
6.5.2	Configurations with angular momentum	130
6.5.3	Reconciling conformal TT and thin sandwich	132
6.5.4	Dependence on the size of the excised spheres	134
6.6	Discussion	138
6.7	Conclusion	140
7	Quasi-equilibrium initial data	143
7.1	Stationary spacetimes	144
7.2	Quasi-equilibrium boundary conditions	145
7.3	Implementation details	150
7.4	Single black hole solutions	151
7.4.1	Eddington-Finkelstein coordinates	152
7.4.2	Solving for spherically symmetric spacetimes	153

7.4.3	The lapse boundary condition	158
7.5	Binary black hole solutions	161
7.5.1	Choices for the remaining free data	161
7.5.2	Eddington-Finkelstein slicings	163
7.5.3	Maximal slices	164
7.5.4	Toward the test mass limit	168
7.5.5	Toward the post-Newtonian limit	174
7.6	Discussion	178
7.7	Appendix A: Detailed quasi-equilibrium calculations	180
7.8	Appendix B: Code Tests	181
7.9	Appendix C: Extrapolation into the interior of the excised spheres .	183
8	Initial data with superposed gravitational waves	186
8.1	Introduction	186
8.2	Method	188
8.3	Quadrupole waves	191
8.4	Results	191
8.4.1	Flat space with ingoing pulse	191
8.4.2	Black hole with gravitational wave	195
8.5	Discussion	196
	Bibliography	199

LIST OF TABLES

3.1	Runtime and scaling efficiency of the spectral code.	56
4.1	Orbital parameters of the innermost stable circular orbit for equal-mass spinning holes	
4.2	Summary of common apparent horizon searches	81
5.1	ISCO parameters for different mass-ratios obtained with the effective potential method.	
6.1	Solutions of different decompositions for two black holes at rest . .	127
6.2	Initial-data sets generated by different decompositions for binary black holes with orbit.	
6.3	Solutions of ConfTT for different radii of the excised spheres, r_{exc} .	136
6.4	Solutions of CTS as a function of radius of excised spheres, r_{exc} . Different choices of the	
7.1	Spherically symmetric single black hole solutions	156
7.2	Parameters for equal mass binary black hole solutions constructed with the quasi-equili	

LIST OF FIGURES

2.1	Setup for conformal thin sandwich equations	9
3.1	Illustration of matching with three subdomains in one dimension	37
3.2	Domain decomposition for Laplace equation in a square	45
3.3	Convergence of solution of Laplace equation in a square	46
3.4	Iteration count of the linear solver for different types of preconditioning	47
3.5	Domain decomposition for the domain \mathbb{R}^3 with two excised spheres	49
3.6	Convergence of solution of Eqs. (3.52)-(3.55) for equal-sized holes	50
3.7	Convergence of solution of Eqs. (3.52)-(3.55) for widely separated, unequal sized holes	51
3.8	Comparison of runtime vs. achieved accuracy for the new spectral solver and the Cadéz solver	52
3.9	Convergence of solution to coupled PDEs (3.58) and (3.59)	58
4.1	Sequences of quasi-circular orbits for different spin configurations: binding energy E_b/μ	60
4.2	Sequences of quasi-circular orbits for different spin configurations: binding energy E_b/μ	61
4.3	Sequences of quasi-circular orbits for different spin configurations: angular momentum $J/\mu m$	62
4.4	Difference in binding energy $\Delta E_b/\mu$ between $+-$ sequences and non-rotating sequence as a function of separation ℓ/m	63
4.5	Constant $J/\mu m$ contours of the effective potential E_b/μ as a function of separation ℓ/m	64
4.6	Enlargement of the $++0.17$ sequence of Fig. 4.5	79
4.7	Values of several physical parameters at the ISCO of the $++$ and $--$ sequences.	80
4.8	Shapes of the common apparent horizons for different spin configurations	82
4.9	Illustration of the effects of a systematic underestimation of E_b/μ	85
4.10	Residual of the minimization in the apparent horizon finder as a function of expansion parameter α	86
5.1	Sequences of quasi-circular orbits for different mass-ratios obtained with inversion symmetric Bowen-York initial conditions	87
5.2	Sequences of quasi-circular orbits for different mass-ratios obtained with inversion symmetric Bowen-York initial conditions	88
5.3	Sequences of quasi-circular orbits for different mass-ratios obtained with inversion symmetric Bowen-York initial conditions	89
5.4	ISCO's for different mass-ratios obtained with inversion symmetric Bowen-York initial conditions	90
6.1	Domain decomposition for binary black hole	116
6.2	Plot of the functions Ψ and W^i from Eqs. (6.61) and (6.62)	119
6.3	Testing the solver for the conformal TT decomposition	119
6.4	Testing the solver for the physical TT decomposition with domain decomposition	120
6.5	Testing thin sandwich decomposition with apparent horizon searches	123
6.6	Convergence of binary black hole solution with conformal TT decomposition	124
6.7	The conformal factor ψ along the axis connecting the holes for several decompositions	125
6.8	Black holes at rest: Contour plots of the conformal factor ψ for ConfTT and CTS-add1	126
6.9	Plots of ψ and V^x along the positive x -axis for ConfTT for different radii $r_{exc} = 2M, M$	127
6.10	Apparent horizons for ConfTT with different radii of excised spheres	135
6.11	Cuts through ψ and β^x for CTS-mult for different radii r_{exc}	138
6.12	Apparent horizons for CTS with $\tilde{\alpha} = N_A N_B$ and inner boundary condition $d\psi/dr = 0$	139
7.1	Inner boundary for quasi-equilibrium boundary conditions	146
7.2	Solving the quasi-equilibrium equations (7.28) on an Eddington-Finkelstein slice	154

7.3	Minimum of N as a function of the coefficient Ξ in the modified lapse boundary condition.	161
7.4	Quasi-equilibrium binary black hole initial data sets on Eddington-Finkelstein slices: dependence on Ω .	165
7.5	Quasi-equilibrium binary black hole initial data set on an Eddington-Finkelstein slice	165
7.6	Quasi-equilibrium binary black hole initial data sets on maximal slices: Dependence on Ω .	166
7.7	Quasi-equilibrium binary black hole initial data set on an maximal slice	167
7.8	Quasi-equilibrium method in the test-mass limit: Various quantities as a function of the mass-ratio.	171
7.9	$\partial_t \ln \psi$ and shift β^i for initial data sets with mass-ratio 16.	171
7.10	$\partial_t \ln \psi$ and shift β^i for a single boosted black hole.	173
7.11	Testing the quasi-equilibrium equations and the lapse quasi-equilibrium condition on an Eddington-Finkelstein slice.	177
7.12	Convergence of selected terms of the lapse boundary condition. . .	183
8.1	Domain decomposition used for elliptic solves in full R^3	192
8.2	Constraint violation of linear gravitational wave in flat background.	193
8.3	ADM energy of an ingoing Gaussian pulse in flat space.	193
8.4	Cuts through the equatorial plane of the $A=0.3$ data set of Fig. 8.3.	194
8.5	Black hole with superposed gravitational wave: ADM-energy and apparent horizon mass	195
8.6	Apparent horizon mass during an evolution of a perturbed black hole spacetime.	196

Chapter 1

Introduction

General relativity is entering a very exciting phase with the commissioning of several gravitational wave detectors. The detection of gravitational waves serves two main purposes. It allows fundamental tests of the theory of general relativity in the genuinely nonlinear regime, and it advances astrophysics by opening a new observational window which can be used for detailed studies of individual sources and for source statistics.

One prime target for gravitational wave detectors is binary systems of compact objects, black holes or neutron stars. Such a binary system emits energy and angular momentum through gravitational radiation, so that the orbital separation slowly decreases. The best-known example is the “Hulse-Taylor” pulsar. Gravitational radiation tends to circularize orbits, leading to almost circular orbits during late inspiral. For binary black holes, the orbits become unstable at some small separation, the so-called *innermost stable circular orbit*, where the slow adiabatic inspiral changes to a dynamical plunge. The two black holes merge and form a single distorted black hole, which subsequently settles down to a stationary black hole by emission of further gravitational radiation during the ring-down phase.

Early inspiral can be treated with post-Newtonian expansion, and the late ring-down phase is accessible to perturbation theory. It is generally believed, however, that the late inspiral and the dynamical merger can only be treated with a full numerical evolution of Einstein’s equations, which is therefore essential to obtain the complete waveform of a binary black hole coalescence. The knowledge of the wave-form is essential for finding the gravitational wave signal amidst the detector noise in the first place (cross-correlation with known waveform templates greatly enhances the sensitivity of the detectors), and to extract as much information as possible about identified events. One needs to know the prediction of general relativity, especially in the nonlinear regime, to compare it to the observations.

Besides the importance of numerical relativity for the experiments, it also encompasses the intellectual challenge of solving the two-body problem. While the Newtonian two-body problem is treated completely in freshman mechanics, the general relativistic analogue, the binary black hole, is still unsolved.

Any evolution must start with *initial data*. For an evolution of Einstein’s equations, setting initial data is difficult for several reasons:

First, the initial data must satisfy constraints, analogous to the divergence equations of electrodynamics,

$$\begin{aligned}\nabla \cdot \vec{E} &= 4\pi\rho, \\ \nabla \cdot \vec{B} &= 0.\end{aligned}\tag{1.1}$$

Any initial data \vec{E} and \vec{B} for an evolution of Maxwell’s equations must satisfy Eqs. (1.1). Similarly, initial data for Einstein’s equations must satisfy constraint equations, which are, however, much more complicated than Eqs.(1.1). Thus, one is faced with the *mathematical* task of finding a well-defined method to construct solutions to the constraint equations of general relativity. This problem has been an active research area for almost sixty years.

Second, formalisms to solve the constraint equations usually lead to sets of coupled nonlinear elliptic partial differential equations in three dimensions, often on a computational domain which has excised regions. Solving such a set of equations is a formidable *numerical* task.

Third, the mathematical formalisms to construct initial data sets leave an enormous amount of freedom. Some ten functions of space can be freely specified. These functions are generally called the “free data.” Hence, even with an elliptic solver in hand, one is faced with the *physical* question of which initial data sets from the infinite parameter space are astrophysically relevant. Initial data representing a binary black hole, for example, must contain two black holes which, if evolved, actually move on almost circular orbits. Furthermore, the initial data should not contain unphysical gravitational radiation; ideally, however, it should contain the outgoing gravitational radiation emitted during the preceding inspiral.

This thesis attempts to contribute to each of these three aspects.

In chapter 2 we present the latest formalisms to decompose the constraint equations. We outline the main ideas of the two relevant papers by York [1] and Pfeiffer & York [2]. We also comment on various issues which are important in general, and/or will arise in later chapters of the thesis.

Chapter 3 develops a new code to solve elliptic partial differential equations, a pseudospectral collocation method with domain decomposition. The exponential convergence of spectral methods for smooth functions allows very accurate solutions. The domain decomposition makes it possible to handle complex topologies, e.g. with excised spheres, and to distribute grid-points to improve accuracy. Last, but not least, the code is designed to be modular and very flexible, making it easy

to explore different partial differential equations or different boundary conditions. All three of these characteristics have proved to be essential for the present work.

The remaining chapters of the thesis explore initial data sets with a variety of approaches.

Chapters 4 and 5 compute binary black holes in circular orbits for spinning black holes (chapter 4) and unequal mass black holes (chapter 5). We employ the effective potential method based on conformally flat inversion-symmetric Bowen-York initial data. The most important result from these two chapters is, perhaps, that this method is not optimal. In the test-mass limit one can assess the quality of many of the approximations used, and one can compare the numerical method against an analytical result. This makes it possible to pin-point the problem of the numerical method with some confidence. We argue that the choice of the so-called extrinsic curvature, namely the Bowen-York extrinsic curvature is problematic. In the calculation for spinning equal-mass black holes, the symptoms of failure are easily seen (disappearance of the ISCO for corotating holes with moderate spin, and an unphysical (spin)⁴-effect); however, the causes are less clear due to the large number of assumptions made.

As there is widespread belief that the approximation of conformal flatness limits the physical relevance of initial data sets (for example, binary compact objects are not conformally flat at second post-Newtonian order), we relax this approximation in chapter 6. We compute data sets that are not conformally flat using different mathematical formalisms and different choices for the free data. We then compare these data sets with each other. For the data sets considered, we do not find evidence that the non-conformally flat initial data sets are superior. We find, however, a sensitive dependence on the extrinsic curvature. Two different choices for the extrinsic curvature (“ConfTT” and “mConfTT” in the language of chapter 6), which are equally well motivated, result in drastically different initial data sets. While the approximation of conformal flatness will have to be addressed eventually, especially for rotating black holes, I believe that it is currently not the limiting factor.

One formalism to solve the constraints, the conformal thin sandwich method, does not require specification of an extrinsic curvature. It thus might well avoid ambiguities like the one we just mentioned. A special case of this method was recently used in another approach to compute quasi-circular orbits of binary black holes, the *helical Killing vector approximation*, which has been generalized by Cook

to the *quasi-equilibrium method*. Chapter 7 describes this method and examines the resulting set of partial differential equations and boundary conditions. We compute single black hole spacetimes, and binary black holes in circular orbits with two different choices of the remaining free data. We further examine the test-mass limit as well as the limit of widely separated black holes. In both limits, we show that the current choices for the remaining free data are unsatisfactory. We also discuss a proposal for a lapse boundary condition put forth by Cook, and explain how to perform a certain extrapolation required to use these data sets as initial data for evolutions.

Chapter 8, finally, changes gear again and describes a new and general way to construct spacetimes with superposed gravitational radiation. The attractive feature of this method is that it admits a simple physical interpretation of the wave, and one can specify directly the radial shape and angular dependence of the wave, as well as the direction of propagation. As examples, I construct spacetimes without a black hole containing ingoing spherical pulses of varying amplitude, as well as spacetimes containing one black hole surrounded by a similar pulse. The amplitude of these pulses can be very large; in extreme cases most of the energy contained in the spacetime is *outside* the black hole. In this chapter, we solve the conformal thin sandwich equations on very general, nonflat conformal manifolds; the fact that this is easily possible highlights the robustness of the conformal thin sandwich formalism and of the spectral elliptic solver.

During the work described in this thesis, I have also improved an apparent horizon finder that was developed at Cornell a few years ago. Details can be found in sections 4.6 and 6.4.2.

The primary goal of this thesis is to construct initial data *for evolutions*. Indeed, data sets from chapters 6, 7 and 8 are used in evolutions by the numerical relativity group at Cornell. As the results from evolutions are preliminary so far, I restrict discussion here to the initial data sets.

Chapter 2

The initial value problem of general relativity

Numerical relativity attempts to construct a spacetime with metric ${}^{(4)}\mathbf{g}_{\mu\nu}$ ($\mu, \nu, \dots = 0, 1, 2, 3$) which satisfies Einstein's equations,

$$G_{\mu\nu} = 8\pi GT_{\mu\nu}. \quad (2.1)$$

Within the standard 3+1 decomposition [3, 4] of Einstein's equations, the first step is to single out a time coordinate “ t ” by foliating the spacetime with spacelike $t=\text{const.}$ hypersurfaces. Each such hypersurface surface has a future pointing unit-normal n^μ , induced metric $g_{\mu\nu} = {}^{(4)}\mathbf{g}_{\mu\nu} + n_\mu n_\nu$ and extrinsic curvature $K_{\mu\nu} = -\frac{1}{2}\mathcal{L}_n g_{\mu\nu}$. We use the label t of the hypersurfaces as one coordinate and choose 3-dimensional coordinates x^i within each hypersurface ($i, j, \dots = 1, 2, 3$). The three dimensional metric $g_{\mu\nu}$ and $K_{\mu\nu}$ are purely spatial tensors; we denote their spatial components by g_{ij} and K_{ij} . The spacetime metric can be written as

$$ds^2 = -N^2 dt + g_{ij} (dx^i + \beta^i dt) (dx^j + \beta^j dt), \quad (2.2)$$

where N and β^i denote the lapse function and shift vector, respectively. N measures the proper separation between neighboring hypersurfaces along the surface normals and β^i determines how the coordinate labels move between hypersurfaces: Points along the integral curves of the “time”-vector $t^\mu = Nn^\mu + \beta^\mu$ (where $\beta^\mu = [0, \beta^i]$), have the same spatial coordinates x^i .

Einstein's equations (2.1) decompose into evolution equations and constraint equations for the quantities g_{ij} and K_{ij} .

The *evolution equations* determine how g_{ij} and K_{ij} are related between neighboring hypersurfaces,

$$\partial_t g_{ij} = -2NK_{ij} + \nabla_i \beta_j + \nabla_j \beta_i \quad (2.3)$$

$$\begin{aligned} \partial_t K_{ij} = & N (R_{ij} - 2K_{ik}K_j^k + KK_{ij} - 8\pi GS_{ij} + 4\pi Gg_{ij}(S - \rho)) \\ & - \nabla_i \nabla_j N + \beta^k \nabla_k K_{ij} + K_{ik} \nabla_j \beta^k + K_{kj} \nabla_i \beta^k. \end{aligned} \quad (2.4)$$

Here, ∇_i and R are the covariant derivative and the scalar curvature (trace of the Ricci tensor) of g_{ij} , respectively, $K = K_{ij}g^{ij}$ is the trace of K^{ij} , the so-called

mean curvature, ρ and S_{ij} are matter density and stress tensor¹, respectively, and $S = S_{ij}g^{ij}$ denotes the trace of S_{ij} .

The *constraint equations* are conditions within each hypersurface alone, ensuring that the three-dimensional surface can be embedded into the four-dimensional spacetime:

$$R + K^2 - K_{ij}K^{ij} = 16\pi G\rho, \quad (2.5)$$

$$\nabla_j (K^{ij} - g^{ij}K) = 8\pi Gj^i, \quad (2.6)$$

with j^i denoting the matter momentum density. Equation (2.5) is called the *Hamiltonian constraint*, and Eq. (2.6) is the *momentum constraint*.

Cauchy initial data for Einstein's equations consists of (g_{ij}, K^{ij}) on one hypersurface satisfying the constraint equations (2.5) and (2.6). After choosing lapse and shift (which are arbitrary — they merely choose a specific coordinate system), Eqs. (2.3) and (2.4) determine (g_{ij}, K^{ij}) at later times. Analytically, the constraints equations are preserved under the evolution. (In practice during numerical evolution of Eqs. (2.3) and (2.4), or any other formulation of Einstein's equations, many problems arise. However, we will focus on the initial value problem here.)

The constraints (2.5) and (2.6) restrict four of the twelve degrees of freedom of (g_{ij}, K^{ij}) . As these equations are not of any standard mathematical form, it is not obvious which four degrees of freedom are restricted. Hence, finding any solutions is not trivial, and it is even harder to construct specific solutions that represent certain astrophysically relevant situations like a binary black hole.

Work on solving the constraint equation dates back almost sixty years to Lichnerowicz [5], but today's picture emerged only very recently in work due to York [1, 2]. I will describe two general approaches to solving the constraint equations. The first one is based on the metric and its *time-derivative* on a hypersurface, whereas the second one rests on the metric and the *extrinsic curvature*. Since the extrinsic curvature is essentially the canonical momentum of the metric (e.g. [6]), the latter approach belongs to the Hamiltonian picture of mechanics whereas the former one is in the spirit of Lagrangian mechanics.

¹In later chapters of this thesis, we deal exclusively with vacuum spacetimes for which all matter terms vanish; we include them in this chapter for completeness.

2.1 Preliminaries

Both pictures make use of a conformal transformation on the metric,

$$g_{ij} = \psi^4 \tilde{g}_{ij} \quad (2.7)$$

with strictly positive *conformal factor* ψ . \tilde{g}_{ij} is referred to as the *conformal metric*. From (2.7) it follows that the Christoffel symbols of the physical and conformal metrics are related by

$$\Gamma_{jk}^i = \tilde{\Gamma}_{jk}^i + 2\psi^{-1} (\delta_j^i \partial_k \psi + \delta_k^i \partial_j \psi - \tilde{g}_{jk} \tilde{g}^{il} \partial_l \psi). \quad (2.8)$$

Equation (2.8) implies that the scalar curvatures of g_{ij} and \tilde{g}_{ij} are related by

$$R = \psi^{-4} \tilde{R} - 8\psi^{-5} \tilde{\nabla}^2 \psi. \quad (2.9)$$

Equations (2.7)–(2.9) were already known to Eisenhart [7]. Furthermore, for any symmetric tracefree tensor \tilde{S}^{ij} ,

$$\nabla_j (\psi^{-10} \tilde{S}^{ij}) = \psi^{-10} \tilde{\nabla}_j \tilde{S}^{ij}, \quad (2.10)$$

where $\tilde{\nabla}$ is the covariant derivative of \tilde{g}_{ij} . Lichnerowicz [5] used Eqs. (2.7) to (2.10) to treat the initial value problem on maximal slices, $K = 0$. For non-maximal slices, we split the extrinsic curvature into trace and tracefree parts,

$$K^{ij} = A^{ij} + \frac{1}{3} g^{ij} K. \quad (2.11)$$

With (2.9) and (2.11), the Hamiltonian constraint (2.5) becomes

$$\tilde{\nabla}^2 \psi - \frac{1}{8} \psi \tilde{R} - \frac{1}{12} \psi^5 K^2 + \frac{1}{8} \psi^5 A_{ij} A^{ij} + 2\pi G \psi^5 \rho = 0, \quad (2.12)$$

a quasi-linear Laplace equation for ψ . Local uniqueness proofs of equations like (2.12) usually linearize around an (assumed) solution, and then use the maximum principle to conclude that “zero” is the only solution of the linearized equation. However, the signs of the last two terms of (2.12) are such that the maximum principle cannot be applied. Consequently, it is not immediately guaranteed that Eq. (2.12) has unique (or even locally unique) solutions². The term proportional

²As a physical illustration of possible problems, consider the matter term $2\pi G \psi^5 \rho$, a source which pushes ψ to larger values. The physical volume element, $dV = \sqrt{g} d^3x = \psi^6 \sqrt{\tilde{g}} d^3x$, expands as ψ becomes larger. With *physical* matter energy density ρ given, the total matter content will grow like ψ^6 and will therefore become *stronger*, pushing ψ to even larger values. Beyond some critical value of ρ , a “run-away” might set in pushing ψ to infinity. Indeed I observed this behavior while solving the constraint equations coupled to a scalar field.

to $A_{ij}A^{ij}$ will be dealt with later; for the matter terms we follow York [4] and introduce conformally scaled source terms:

$$j^i = \psi^{-10} \tilde{j}^i, \quad (2.13)$$

$$\rho = \psi^{-8} \tilde{\rho}. \quad (2.14)$$

The scaling for j^i makes the momentum constraint below somewhat nicer; the scalings of ρ and j^i are tied together such that the dominant energy condition preserves sign:

$$\rho^2 - g_{ij}j^i j^j = \psi^{-16} (\tilde{\rho}^2 - \tilde{g}_{ij}\tilde{j}^i \tilde{j}^j) \geq 0. \quad (2.15)$$

The scaling of ρ , Eq. (2.14) modifies the matter term in (2.12) to $2\pi G\psi^{-3}\tilde{\rho}$ with negative semi-definite linearization for $\tilde{\rho} \geq 0$.

The decomposition of K_{ij} into trace and tracefree part, Eq. (2.11), turns the momentum constraint (2.6) into

$$\nabla_j A^{ij} - \frac{2}{3} \nabla^i K = 8\pi G j^i. \quad (2.16)$$

For time-symmetric vacuum spacetimes (where $A^{ij} = K = j^i = 0$ solve the momentum constraint (2.16) trivially), only the first two terms of (2.12) remain. This simplified equation was used in beautiful early work on vacuum spacetimes, for example a positivity of energy proof by Brill [8] and construction of multi black hole spacetimes by Misner [9] and Brill & Lindquist [10].

The conformal transformation (2.7) implies one additional, very simple, conformal scaling relation. The longitudinal operator [11, 12, 13]

$$(\mathbb{L}V)^{ij} \equiv \nabla^i V^j + \nabla^j V^i - \frac{2}{3} g^{ij} \nabla_k V^k, \quad (2.17)$$

satisfies [12]

$$(\mathbb{L}V)^{ij} = \psi^{-4} (\tilde{\mathbb{L}}V)^{ij}. \quad (2.18)$$

Here $(\tilde{\mathbb{L}}V)^{ij}$ is given by the same formula (2.17) but with quantities associated with the conformal metric \tilde{g}_{ij} . (In fluid dynamics $(\mathbb{L}V)^{ij}$ is twice the shear of the velocity field V^i). In d dimensions, the factor $2/3$ in Eq. (2.17) is replaced by $2/d$; Eq. (2.18) holds for all d .

2.2 Conformal thin sandwich formalism

We now derive a formalism to solve the constraint equations [1] which deals with the conformal metric and its *time derivative*. This formalism thus represents the

Lagrangian viewpoint. Figure 2.1 illustrates the basic setup; we deal with *two* hypersurfaces separated by the infinitesimal δt (thus the name “thin sandwich”), and connected by the lapse N and the shift β^i . The mean curvature of each hypersurface is K and $K + \dot{K}\delta t$, respectively. The metric is split into conformal factor and conformal metric; on the first hypersurface, this is simply Eq. (2.7). On the second hypersurface, the conformal factor and the conformal metric will both be different from their values on the first hypersurface. The split into conformal factor and conformal metric is not unique and is synchronized between the two surfaces by requiring that the conformal metrics on both hypersurfaces have the same determinant to first order in δt . The variation of the determinant of \tilde{g}_{ij} is given by

$$\delta\tilde{g} = \tilde{g}\tilde{g}^{ij}\delta\tilde{g}_{ij} = \tilde{g}\tilde{g}^{ij}\tilde{u}_{ij}\delta t \quad (2.19)$$

(the first identity holds for any square matrix), so that $\tilde{u}_{ij} = \partial_t\tilde{g}_{ij}$ must be traceless. On the first hypersurface the Hamiltonian constraint will eventually determine ψ .

Besides the relationships indicated in Figure 2.1, the conformal thin sandwich formalism rests on the nontrivial scaling behavior of the lapse function:

$$N = \psi^6\tilde{N}. \quad (2.20)$$

The scaling (2.20) appears in a bewildering variety of contexts (see references in [1, 2]). For example, studies of *hyperbolic* evolution systems for Einsteins equations (e.g. [14, 15]) find that hyperbolicity requires that the lapse anti-density (“densitized lapse”) $\alpha \equiv g^{-1/2}N$ is freely specifiable, not N directly (recall $\sqrt{g} = \psi^6\sqrt{\tilde{g}}$, so that α is essentially equivalent to \tilde{N}). The scaling (2.20) is crucial in the present context as well, cf. Eq. (2.26) below.

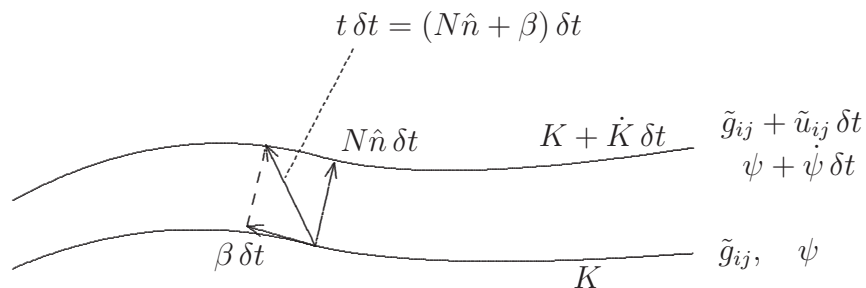


Figure 2.1: Setup for conformal thin sandwich equations

Substitution of Eq. (2.7) into the evolution equation for the metric, Eq. (2.3), yields

$$4\psi^4(\partial_t \ln \psi)\tilde{g}_{ij} + \psi^4\partial_t\tilde{g}_{ij} = -2NK_{ij} + \nabla_i\beta_j + \nabla_j\beta_i. \quad (2.21)$$

Since $\partial_t\tilde{g}_{ij} = \tilde{u}_{ij}$ is traceless, the left hand side of Eq. (2.21) is already split into trace and tracefree parts. Splitting the right hand side, too, gives

$$\psi^4\tilde{u}_{ij} = -2NA_{ij} + (\mathbb{L}\beta)_{ij} \quad (2.22)$$

and

$$\partial_t \ln \psi = -\frac{1}{6}NK + \frac{1}{6}\nabla_k\beta^k. \quad (2.23)$$

(The factor ψ^4 in (2.23) cancels because the trace is performed with the physical inverse metric $g^{ij} = \psi^{-4}\tilde{g}^{ij}$). Equation (2.22) is the tracefree piece of $\partial_t g_{ij}$, thus for $u_{ij} \equiv \psi^4\tilde{u}_{ij}$,

$$u_{ij} = \partial_t g_{ij} - \frac{1}{3}g_{ij}g^{kl}\partial_t g_{kl}. \quad (2.24)$$

Now solve Eq. (2.22) for A^{ij} ,

$$A^{ij} = \frac{1}{2N}((\mathbb{L}\beta)^{ij} - u^{ij}), \quad (2.25)$$

and rewrite with conformal quantities [using (2.20), (2.18) and $u^{ij} = \psi^{-4}\tilde{u}^{ij}$]:

$$A^{ij} = \frac{1}{2\psi^6\tilde{N}}(\psi^{-4}(\tilde{\mathbb{L}}\beta)^{ij} - \psi^{-4}\tilde{u}^{ij}) = \psi^{-10}\frac{1}{2\tilde{N}}((\tilde{\mathbb{L}}\beta)^{ij} - \tilde{u}^{ij}) \equiv \psi^{-10}\tilde{A}^{ij} \quad (2.26)$$

with the conformal tracefree extrinsic curvature

$$\tilde{A}^{ij} = \frac{1}{2\tilde{N}}((\tilde{\mathbb{L}}\beta)^{ij} - \tilde{u}^{ij}). \quad (2.27)$$

Equation (2.26) shows that the formula for A^{ij} is form invariant under conformal transformations; this hinges on the scaling of N in Eq. (2.20). Substitution of Eq. (2.26) into the momentum constraint (2.16) and application of Eq. (2.10) yields

$$\tilde{\nabla}_j \left(\frac{1}{2\tilde{N}}(\tilde{\mathbb{L}}\beta)^{ij} \right) - \tilde{\nabla}_j \left(\frac{1}{2\tilde{N}}\tilde{u}^{ij} \right) - \frac{2}{3}\psi^6\tilde{\nabla}^i K = 8\pi G\tilde{j}^i, \quad (2.28)$$

whereas Eq. (2.26) modifies the Hamiltonian constraint (2.12) to³

$$\tilde{\nabla}^2\psi - \frac{1}{8}\psi\tilde{R} - \frac{1}{12}\psi^5 K^2 + \frac{1}{8}\psi^{-7}\tilde{A}_{ij}\tilde{A}^{ij} = -2\pi G\psi^{-3}\tilde{\rho}. \quad (2.29)$$

³Indices on conformal quantities are raised and lowered with the conformal metric, for example

$$A_{ij} = g_{ik}g_{jl}A^{kl} = \psi^4\tilde{g}_{ik}\psi^4\tilde{g}_{jl}\psi^{-10}\tilde{A}^{kl} = \psi^{-2}\tilde{A}_{ij}.$$

Equations (2.28) and (2.29) constitute elliptic equations for β^i and ψ . We thus find the following procedure to compute a valid initial data set:

A. Choose the free data

$$(\tilde{g}_{ij}, \tilde{u}_{ij}, K, \tilde{N}) \quad (2.30)$$

(and matter terms if applicable).

B. Solve Eqs. (2.28) and (2.29) for β^i and ψ .

C. Assemble $g_{ij} = \psi^4 \tilde{g}_{ij}$ and $K^{ij} = \psi^{-10} \tilde{A}^{ij} + \frac{1}{3} g^{ij} K$.

The conformal thin sandwich formalism does not involve transverse-traceless decompositions, and is therefore somewhat more convenient than the extrinsic curvature decomposition discussed in section 2.3. We now comment on several issues related to the conformal thin sandwich formalism.

2.2.1 Fixing \tilde{N} via \dot{K}

The free data so far is given by (2.30). Whereas \tilde{g}_{ij} and $\tilde{u}_{ij} = \partial_t \tilde{g}_{ij}$ constitute a “variable & velocity pair” (q, \dot{q}) in the spirit of Lagrangian mechanics, the remaining free data does not.

As we show starting with Eq. (2.32) below, specification of $\partial_t K = \dot{K}$ fixes \tilde{N} through an elliptic equation. If we take \dot{K} as the “free” quantity instead of \tilde{N} , then the free data for the conformal thin sandwich formalism becomes

$$(\tilde{g}_{ij}, \tilde{u}_{ij}, K, \dot{K}) \quad (2.31)$$

plus matter terms if applicable. These free data consists completely of (q, \dot{q}) pairs as appropriate for a Lagrangian viewpoint. The free data (2.31) is also useful practically for computations of quasi-equilibrium initial data sets in chapter 7. In quasi-equilibrium, $\dot{K} = 0$ is a natural and simple choice, whereas it is not obvious at all which conformal lapse \tilde{N} one should use. In particular, \tilde{N} will depend on the slicing of the spacetime.

We now derive the elliptic equation for \tilde{N} (see, e.g., [16]). The trace of the evolution equation for K_{ij} , Eq. (2.4), gives after some calculations

$$\partial_t K - \beta^k \partial_k K = N (R + K^2 + 4\pi G(S - 3\rho)) - \nabla^2 N. \quad (2.32)$$

Elimination of R with the Hamiltonian constraint (2.5) yields

$$\nabla^2 N - N (K_{ij} K^{ij} + 4\pi G(S + \rho)) = -\partial_t K + \beta^k \partial_k K. \quad (2.33)$$

Rewriting the Laplace operator with conformal derivatives,

$$\begin{aligned} \nabla^2 N &= \frac{1}{\sqrt{g}} \partial_i (\sqrt{g} g^{ij} \partial_j N) \\ &= \frac{\psi^{-6}}{\sqrt{\tilde{g}}} \partial_i (\psi^2 \sqrt{\tilde{g}} \tilde{g}^{ij} \partial_j N) \\ &= \psi^{-4} \tilde{\nabla}^2 N + 2\psi^{-4} \tilde{\nabla}_i \ln \psi \tilde{\nabla}^i N, \end{aligned}$$

together with Eqs. (2.20) and (2.29) gives

$$\begin{aligned} \tilde{\nabla}^2 \tilde{N} + 14 \tilde{\nabla}^i \ln \psi \tilde{\nabla}_i \tilde{N} + \tilde{N} \left[\frac{3}{4} \tilde{R} + \frac{1}{6} \psi^4 K^2 - \frac{7}{4} \psi^{-8} \tilde{A}_{ij} \tilde{A}^{ij} \right. \\ \left. + 42 \tilde{\nabla}_i \ln \psi \tilde{\nabla}^i \ln \psi - 4\pi G \psi^4 (S + 4\rho) \right] = -\psi^{-2} (\partial_t K - \beta^k \partial_k K), \end{aligned} \quad (2.34)$$

which can also be rewritten as

$$\begin{aligned} \tilde{\nabla}^2 (\tilde{N} \psi^7) - (\tilde{N} \psi^7) \left[\frac{1}{8} \tilde{R} + \frac{5}{12} \psi^4 K^2 + \frac{7}{8} \psi^{-8} \tilde{A}_{ij} \tilde{A}^{ij} + 2\pi G \psi^4 (\rho + 2S) \right] \\ = -\psi^5 (\partial_t K - \beta^k \partial_k K). \end{aligned} \quad (2.35)$$

Equation (2.34) determines the freely specifiable \tilde{N} directly, whereas Eq. (2.35) is shorter and therefore computationally somewhat more convenient.

We now have a system of *five* coupled partial differential equations, (2.28), (2.29) and (2.34) [or (2.35)] with freely specifiable data (2.31).

2.2.2 Invariance to conformal transformations of the free data

Assume we specify free data (2.30), solve the conformal thin sandwich equations for conformal factor ψ and shift β^i , and assemble the physical initial data (g_{ij}, K^{ij}) . We now pick a function $\Psi > 0$, and perform a conformal transformation on the free data (2.30) by setting

$$\tilde{g}'_{ij} = \Psi^{-4} \tilde{g}_{ij}, \quad \tilde{u}'^{ij} = \Psi^4 \tilde{u}^{ij}, \quad K' = K, \quad \tilde{N}' = \Psi^{-6} \tilde{N}, \quad (2.36)$$

plus the scalings $\tilde{\rho}' = \Psi^8 \tilde{\rho}$, $\tilde{j}'^i = \Psi^{10} \tilde{j}^i$ for matter terms if applicable. These free data, together with conformal factor $\psi' = \Psi \psi$ and the shift $\beta'^i = \beta^i$ (where ψ and

β^i are the solutions to the conformal thin sandwich equations using the *original* free data) lead to the *same* physical initial data (g_{ij}, K^{ij}) :

$$g'_{ij} = \psi'^4 \tilde{g}'_{ij} = \psi^4 \tilde{g}_{ij} = g_{ij}, \quad (2.37)$$

$$\begin{aligned} A'^{ij} &= \psi'^{-10} \frac{1}{2\tilde{N}'} \left((\tilde{\mathbb{L}}' \beta')^{ij} - \tilde{u}'^{ij} \right) \\ &= (\Psi\psi)^{-10} \frac{1}{2\Psi^{-6}\tilde{N}} \left(\Psi^4 (\tilde{\mathbb{L}} \beta)^{ij} - \Psi^4 \tilde{u}^{ij} \right) = A^{ij}. \end{aligned} \quad (2.38)$$

Here, we used Eqs. (2.7), (2.18) and (2.26). Adding the trace of the extrinsic curvature to (2.38) is trivial.

We thus find that only the *conformal equivalence class* of \tilde{g}_{ij} is relevant for the physical solution. This is a very desirable property; we introduced \tilde{g}_{ij} as a *conformal* metric, so its overall scaling should not matter. Fixing \tilde{N} by specification of \tilde{K} preserves this invariance, as the \tilde{K} -equation, (2.34), is derived from *physical* quantities in the first place.

The extrinsic curvature decomposition introduced in the next section is also invariant under conformal transformations of the free data. We note that invariance under conformal transformations of the free data is not trivial; earlier variants of the constraint decompositions did not possess it, giving rise to ambiguities in the free data [17].

2.2.3 Gauge degrees of freedom

The physical initial data (g_{ij}, K^{ij}) has twelve degrees of freedom⁴. It is constrained by four constraint equations, so there should be eight degrees of freedom in the freely specifiable data. However, taking into account that only the conformal equivalence class of \tilde{g}_{ij} is relevant and that \tilde{u}_{ij} is traceless, one sees that the free data (2.30) or (2.31) consists of *twelve* quantities, not eight. To examine this further, we consider the substitutions

$$\begin{aligned} \tilde{u}^{ij} &\rightarrow \tilde{u}^{ij} + (\tilde{\mathbb{L}}W)^{ij}, \\ \beta^i &\rightarrow \beta^i + W^i. \end{aligned} \quad (2.39)$$

The vector W^i disappears from Eqs. (2.27)–(2.29), therefore the substitution (2.39) will not change the physical initial data set (g_{ij}, K^{ij}) ; it merely tilts the time-axis

⁴Matter just adds four additional degrees of freedom in $\tilde{\rho}$ and \tilde{j}^i which determine the four physical matter variables ρ and j^i . It therefore does not influence the counting of degrees of freedom of the geometrical objects g_{ij} and K^{ij} .

and changes the coordinate labels on the second hypersurface. Thus, \tilde{u}_{ij} contains three gauge degrees of freedom associated with the shift. (W^i enters into Eq. (2.34) as an advection term, though, because $\partial_t K$ is the derivative *along* the time-vector, which of course must be sensitive to the direction *of* the time-vector).

The fourth “missing” degree of freedom is hidden in the lapse function \tilde{N} : One can construct every possible initial data set (g_{ij}, K^{ij}) with *any* (non-pathologic) choice of \tilde{N} . This is easiest seen by going backward from the physical initial data (g_{ij}, K^{ij}) (satisfying the constraints) to the free data. Given (g_{ij}, K^{ij}) and any \tilde{N} and β^i , there exists free data such that solving the conformal thin sandwich equations gives back the original physical initial data set (g_{ij}, K^{ij}) . These free data are:

$$\tilde{g}_{ij} = g_{ij}, \quad \tilde{u}^{ij} = (\mathbb{L}\beta)^{ij} - 2\tilde{N}A^{ij}, \quad K = K^{ij}g_{ij} \quad (2.40)$$

plus the given \tilde{N} (whatever it may be). With these choices for the free data, $\psi \equiv 1$ and the given β^i will reconstruct the physical spacetime (g_{ij}, K^{ij}) as can be seen from Eqs. (2.7) and (2.26). Therefore, $\psi \equiv 1$ and the given β^i will solve the conformal thin sandwich equations (2.28) and (2.29).

The fact that we were free to choose β^i reflects again the gauge-symmetry illustrated in Eq. (2.39), but in addition, we showed that the choice of \tilde{N} does not restrict the set of “achievable” initial data sets.

Note that the physical initial data contain further gauge freedom: Covariance under spatial transformations implies that g_{ij} (and \tilde{g}_{ij}) contain three gauge degrees of freedom associated with the choice of coordinates. Furthermore, K can be interpreted as *time* [18], fixing the temporal gauge. Thus, an initial data set has only four physical degrees of freedom—in perturbed flat space they are simply the two polarizations of gravitational waves.

2.2.4 Implications for an evolution of the initial data

During the solution of the conformal thin sandwich equations, one finds a shift β^i and a lapse N . If one uses this lapse and shift in a subsequent evolution of the initial data (g_{ij}, K^{ij}) —recall that any lapse and shift can be used—then Eq. (2.24) implies that *initially*,

$$\partial_t g_{ij} - \frac{1}{3}g_{ij}g^{kl}\partial_t g_{kl} = \psi^A \tilde{u}_{ij}. \quad (2.41)$$

The freely specifiable piece \tilde{u}_{ij} thus directly controls the tracefree part of the time-derivative of the metric. If we specified \dot{K} as part of the free data, then, of course,

the evolution will initially have $\partial_t K = \dot{K}$, too. Finally, from (2.23), we find

$$\begin{aligned}\partial_t \ln \psi &= \frac{1}{6} (\nabla_k \beta^k - NK) \\ &= \frac{1}{6} \tilde{\nabla}_k \beta^k + \beta^k \partial_k \ln \psi - \frac{1}{6} \psi^6 \tilde{N} K.\end{aligned}\quad (2.42)$$

This is essentially the trace of $\partial_t g_{ij}$.

Since we have been very successful so far with specification of time-derivatives ($\partial_t \tilde{g}_{ij}$ and $\partial_t K$), one might be tempted to turn (2.42) around and use it as the *definition* of K in terms of $\partial_t \ln \psi$. This idea certainly comes to mind when looking for quasi-equilibrium solutions, for which as many time-derivatives as possible should vanish. From (2.42) we find

$$K = \frac{1}{\psi^6 \tilde{N}} \left(\tilde{\nabla}_k \beta^k - 6 (\partial_t - \beta^k \partial_k) \ln \psi \right). \quad (2.43)$$

We see that K contains first derivatives of the shift. The gradient of K enters the momentum constraint (2.28), therefore (2.43) will modify the second derivatives of the elliptic operator in (2.28). The terms containing second derivatives of β^i in Eq. (2.28) become

$$\tilde{\nabla}_j \left(\frac{1}{2\tilde{N}} (\tilde{\mathbb{L}}\beta)^{ij} \right) - \frac{2}{3} \psi^6 \tilde{\nabla}^i \left(\frac{1}{\psi^6 \tilde{N}} \tilde{\nabla}_k \beta^k \right). \quad (2.44)$$

Using the product rule, discarding first derivatives of β^i , and using the definition of $\tilde{\mathbb{L}}$, Eq. (2.17), we find

$$\frac{1}{2\tilde{N}} \left(\tilde{\nabla}_j \tilde{\nabla}^j \beta^i + \tilde{\nabla}_j \tilde{\nabla}^i \beta^j - 2\tilde{\nabla}^i \tilde{\nabla}_k \beta^k \right). \quad (2.45)$$

Commuting the derivatives in the second term yields a term proportional to the Riemann tensor, which is discarded as it contains no derivatives of β^i at all. After multiplication by \tilde{N} , the highest-order derivatives of β^i in the momentum constraint become

$$\partial_j \partial^j \beta^i - \partial^i \partial_k \beta^k. \quad (2.46)$$

This operator is non-invertible; for example it maps the functions

$$f^j(x^l) = k^j \exp(i k^l x_l) \quad (2.47)$$

to zero for any choice of the wave-vector k^i . Thus, the attempt to fix K via (2.43) makes the momentum constraint non-invertible.

In practice I encountered a consequence of this fact when constructing quasi-equilibrium slices of spherically symmetric spacetimes. For that case, we show in section 7.4.2 that the conformal thin sandwich equations with $\tilde{u}_{ij} = 0$ and $\dot{K} = 0$ (and appropriate boundary conditions) are so successful in picking out the time-like Killing vector that for *any* choice of K , the solution satisfies $\partial_t \ln \psi = 0$. If $\partial_t \ln \psi = 0$ for any choice of K , then $\partial_t \ln \psi = 0$ obviously cannot determine a unique K .

In contrast to the trace-free part (2.41) we can *not* easily control $\partial_t \ln \psi$ by choices of the free data. We can only evaluate (2.42) *after* solving the conformal thin sandwich equations.

2.3 Extrinsic curvature decomposition

The second method to construct solutions of the constraint equations is based on a decomposition of the extrinsic curvature. Early variants of this approach [19, 4] have been available for almost thirty years, but the final version was developed only very recently [2]. We will make use of the equations and results from section 2.1, in particular, we use a conformal metric, $g_{ij} = \psi^4 \tilde{g}_{ij}$, and split the extrinsic curvature into trace and trace-free parts, $K^{ij} = A^{ij} + 1/3 g^{ij} K$, cf. Eqs. (2.7) and (2.11).

We start with a *weighted transverse traceless* decomposition of A^{ij} ,

$$A^{ij} = A_{TT}^{ij} + \frac{1}{\sigma} (\mathbb{L}V)^{ij}. \quad (2.48)$$

Here, A_{TT}^{ij} is transverse, $\nabla_j A_{TT}^{ij} = 0$, and traceless, $g_{ij} A_{TT}^{ij} = 0$, and σ is a strictly positive and bounded function. Appearance of the weight function σ is a key point in the extrinsic curvature formulation; its inclusion is the major improvement of [2] over the older variants.

Given a symmetric tracefree tensor like A^{ij} , the decomposition (2.48) can be obtained by taking the divergence of Eq. (2.48),

$$\nabla_j A^{ij} = \nabla_j [\sigma^{-1} (\mathbb{L}V)^{ij}]. \quad (2.49)$$

The right hand side, $\nabla_j [\sigma^{-1} (\mathbb{L}V)^{ij}]$, is a well-behaved elliptic operator in divergence form, so no problem should arise when solving (2.49) for V^i . Substitution of the solution V^i back into (2.48) yields the transverse traceless part A_{TT}^{ij} . In the

presence of boundaries, Eq. (2.49) requires boundary conditions which will influence the solution V^i and the decomposition (2.48). For closed manifolds, existence and uniqueness of the decomposition (2.48) for the case $\sigma \equiv 1$ was shown in [13].

We now conformally scale the quantities on the right hand side of (2.48) with the goal of rewriting the momentum constraint in conformal space.

First, we set

$$A_{TT}^{ij} \equiv \psi^{-10} \tilde{A}_{TT}^{ij}. \quad (2.50)$$

Equation (2.10) ensures that \tilde{A}_{TT}^{ij} is transverse with respect to \tilde{g}_{ij} if and only if A_{TT}^{ij} is transverse with respect to the physical metric g_{ij} .

Because of Eq. (2.18), and because \mathbb{L} is the conformal Killing operator, we will not scale the vector V^i .

The conformal scaling of the weight function is given by

$$\sigma = \psi^6 \tilde{\sigma}. \quad (2.51)$$

The most immediate reason for this scaling is that it allows Eq. (2.52) below; several more reasons will be mentioned in the sequel.

Using the scaling relations (2.18), (2.50) and (2.51), we can now rewrite Eq. (2.48) as

$$A^{ij} = \psi^{-10} \left(\tilde{A}_{TT}^{ij} + \frac{1}{\tilde{\sigma}} (\tilde{\mathbb{L}}V)^{ij} \right) \equiv \psi^{-10} \tilde{A}^{ij}, \quad (2.52)$$

where

$$\tilde{A}^{ij} = \tilde{A}_{TT}^{ij} + \tilde{\sigma}^{-1} (\tilde{\mathbb{L}}V)^{ij} \quad (2.53)$$

is a weighted transverse traceless decomposition in the conformal space. By virtue of the scaling of the weight function σ , Eq. (2.51), the weighted transverse traceless decomposition thus commutes with the conformal transformation.

Equations (2.10) and (2.52) allow us to rewrite the momentum constraint (2.16) as

$$\tilde{\nabla}_j \left(\frac{1}{\tilde{\sigma}} (\tilde{\mathbb{L}}V)^{ij} \right) - \frac{2}{3} \psi^6 \tilde{\nabla}^i K = 8\pi G \tilde{j}^i, \quad (2.54)$$

an elliptic equation for V^i . The Hamiltonian constraint Eq. (2.12) reads

$$\tilde{\nabla}^2 \psi - \frac{1}{8} \tilde{R} \psi - \frac{1}{12} \psi^5 K^2 + \frac{1}{8} \psi^{-7} \tilde{A}_{ij} \tilde{A}^{ij} = -2\pi G \psi^{-3} \tilde{\rho}, \quad (2.55)$$

with \tilde{A}^{ij} given by (2.53). Equation (2.55) is identical to Eq. (2.29) since in both formulations $A^{ij} = \psi^{-10} \tilde{A}^{ij}$, however, the definitions of \tilde{A}^{ij} differ.

Starting from the *physical* initial data (g_{ij}, K^{ij}) , we have now rewritten the constraints (2.5) and (2.6) as elliptic equations (2.54) and (2.55). In order to construct a valid initial data set (g_{ij}, K^{ij}) , one performs this program backward:

A. Choose the free data

$$\left(\tilde{g}_{ij}, K, \tilde{A}_{TT}^{ij}, \tilde{\sigma} \right) \quad (2.56)$$

and matter terms if applicable.

B. Solve Eqs. (2.54) and (2.55) for V^i and ψ .

C. Assemble the physical solution by Eqs. (2.7), (2.11), and (2.52):

$$g_{ij} = \psi^4 \tilde{g}_{ij}, \quad (2.57)$$

$$K^{ij} = \psi^{-10} \left(\tilde{A}_{TT}^{ij} + \tilde{\sigma}^{-1} (\tilde{\mathbb{L}}V)^{ij} \right) + \frac{1}{3} g^{ij} K. \quad (2.58)$$

The next subsection contains a few brief remarks, whereas later subsections comment on specific issues in more detail.

2.3.1 Remarks on the extrinsic curvature decomposition

Invariance to conformal transformations of the free data

Similar to section 2.2.2, one can show that the physical initial data (g_{ij}, K^{ij}) is *invariant* to a conformal transformation of the free data. For $\Psi > 0$, the relevant transformations are [cf. Eq. (2.36)]:

$$\tilde{g}'_{ij} = \Psi^{-4} \tilde{g}_{ij}, \quad \tilde{A}'_{TT}{}^{ij} = \Psi^{10} \tilde{A}_{TT}^{ij}, \quad K' = K, \quad \tilde{\sigma}' = \Psi^{-6} \tilde{\sigma}, \quad (2.59)$$

plus the scalings $\tilde{\rho}' = \Psi^8 \tilde{\rho}$, $\tilde{j}'^i = \Psi^{10} \tilde{j}^i$ for matter terms if applicable. The calculation is straightforward, the key-point being that the scaling of the weight-function (2.51) synchronizes the conformal scaling of the transverse-traceless and longitudinal parts of the weighted transverse traceless decomposition.

Gauge degrees of freedom

Because of the invariance to conformal scalings of the free data, \tilde{g}_{ij} supplies only five degrees of freedom, so that the free data Eq. (2.56) contains nine degrees of freedom. The weight σ (or $\tilde{\sigma}$) merely parametrizes the transverse traceless decomposition (2.48). For any choice of σ , the decomposition (2.48) can be performed, therefore with any choice of $\tilde{\sigma}$, all initial data sets can be generated for appropriate choices of the free data.

Construction of \tilde{A}_{TT}^{ij}

To construct a transverse traceless tensor \tilde{A}_{TT}^{ij} compatible with the metric \tilde{g}_{ij} , one decomposes a general symmetric tracefree tensor \tilde{M}^{ij} . Write

$$\tilde{M}^{ij} = \tilde{A}_{TT}^{ij} + \frac{1}{\tilde{\sigma}}(\tilde{\mathbb{L}}W)^{ij}. \quad (2.60)$$

The divergence of this equation,

$$\tilde{\nabla}_j \tilde{M}^{ij} = \tilde{\nabla}_j \left[\tilde{\sigma}^{-1}(\tilde{\mathbb{L}}W)^{ij} \right], \quad (2.61)$$

represents an elliptic equation for W^i . Solving this equation, and substituting W^i back into (2.60) yields

$$\tilde{A}_{TT}^{ij} = \tilde{M}^{ij} - \frac{1}{\tilde{\sigma}}(\tilde{\mathbb{L}}W)^{ij}. \quad (2.62)$$

The formula for \tilde{A}^{ij} , Eq. (2.53), now reads

$$\tilde{A}^{ij} = \tilde{M}^{ij} + \frac{1}{\tilde{\sigma}}[\tilde{\mathbb{L}}(V - W)]^{ij}, \quad (2.63)$$

which depends only on the *difference* $V^i - W^i$. On the other hand, subtraction of (2.61) from the momentum constraint (2.54) yields

$$\tilde{\nabla}_j \left(\frac{1}{\tilde{\sigma}}[\tilde{\mathbb{L}}(V - W)]^{ij} \right) + \tilde{\nabla}_j \tilde{M}^{ij} - \frac{2}{3}\psi^6 \tilde{\nabla}^i K = 8\pi G \tilde{j}^i, \quad (2.64)$$

which is an equation for the *difference* $V^i - W^i$. Thus one can combine the construction of \tilde{A}_{TT}^{ij} from \tilde{M}^{ij} with the solution of the momentum constraint. Instead of solving (2.61) for W^i and then (2.54) for V^i , one can directly solve (2.64) for $V^i - W^i$.

In the presence of boundaries, solutions of elliptic equations like (2.64) or (2.61) will depend on *boundary conditions*. In chapter 6 of this thesis, for example, we encounter the situation that we know boundary conditions for the combined solve for $V^i - W^i$, but we do not know boundary conditions for the individual solves for W^i and V^i (see section 6.5.3).

2.3.2 Identification of σ with the lapse N

The extrinsic curvature formulation of the initial value problem as presented so far is perfectly adequate for the mathematical task of rewriting the constraints as

well-defined equations. However, it is very natural to further identify the weight-function σ with the lapse function N ,

$$\sigma = 2N, \quad \tilde{\sigma} = 2\tilde{N}. \quad (2.65)$$

One reason for this identification is that σ and N have the same conformal scaling behavior, cf. Eqs. (2.20) and (2.51). A second reason is that with this identification, the conformal thin sandwich equations become equivalent to the extrinsic curvature formulation. To see this, note that by virtue of (2.65), Eqs. (2.63) and (2.64) become

$$\tilde{A}^{ij} = \tilde{M}^{ij} + \frac{1}{2\tilde{N}} \left[\tilde{\mathbb{L}}(V - W) \right]^{ij}, \quad (2.66)$$

and

$$\tilde{\nabla}_j \left(\frac{1}{2\tilde{N}} \left[\tilde{\mathbb{L}}(V - W) \right]^{ij} \right) + \tilde{\nabla}_j \tilde{M}^{ij} - \frac{2}{3} \psi^6 \tilde{\nabla}^i K = 8\pi G \tilde{j}^i. \quad (2.67)$$

With the identifications

$$\tilde{M}^{ij} \leftrightarrow -\frac{1}{2\tilde{N}} \tilde{u}^{ij}, \quad V^i - W^i \leftrightarrow \beta^i, \quad (2.68)$$

Eqs. (2.66) and (2.67) are *identical* to Eqs. (2.27) and (2.28) of the conformal thin sandwich formalism. The Lagrangian picture agrees completely with the Hamiltonian picture. A third reason for (2.65) is given in the immediately following section.

2.3.3 Stationary spacetimes have $A_{TT}^{ij} = 0$

Consider a stationary solution of Einstein's equations with timelike Killing vector l . Given a spacelike hypersurface Σ , there is a preferred gauge so that the time-vector of an evolution coincides with l , namely $N = -n \cdot l$, $\beta = \perp l$, where n is the unit normal to Σ , and \perp is the projection operator into Σ . With this choice of lapse and shift, g_{ij} and K^{ij} will be time-independent. Using $\partial_t g_{ij} = 0$ in Eq. (2.3) yields

$$K_{ij} = \frac{1}{2N} (\nabla_i \beta_j + \nabla_j \beta_i). \quad (2.69)$$

The tracefree part of this equation is

$$A^{ij} = \frac{1}{2N} (\mathbb{L}\beta)^{ij}, \quad (2.70)$$

which is a weighted transverse traceless decomposition with $A_{TT}^{ij} \equiv 0$. Thus, with the appropriate weight factor $\sigma = 2N$, the extrinsic curvature has *no transverse traceless piece* for any spacelike slice in any spacetime with timelike Killing vector (A similar argument is applicable in the ergosphere of a Kerr black hole; however, one must be more careful with the choice of Σ relative to l).

This is a great result! One generally identifies the transverse traceless piece of the extrinsic curvature with *radiative degrees of freedom*. For stationary spacetimes which do not radiate, A_{TT}^{ij} should therefore vanish.

A transverse-traceless decomposition of A^{ij} without the weight-factor, however, will in general lead to a nonzero transverse traceless piece. Thus, such a decomposition is incompatible with the identification of A_{TT}^{ij} with “gravitational radiation.”

These considerations provide another argument for the introduction of the weight-function in Eq. (2.48), and the identification of σ with the lapse-function in Eq. (2.65).

2.3.4 Earlier decompositions of the extrinsic curvature

The scaling $\sigma = \psi^6 \tilde{\sigma}$ in Eq. (2.51) *synchronizes* the conformal scalings of the transverse traceless and longitudinal parts of A^{ij} . Consequently, a transverse-traceless decomposition *without* the weight-function does *not* commute with the conformal transformation giving rise to two inequivalent extrinsic curvature decompositions [12, 4, 20]. They differ in whether one performs first the transverse traceless decomposition or the conformal scalings. Both these variants are inequivalent to the Lagrangian viewpoint, the conformal thin sandwich formalism.

Nonetheless these earlier decompositions, especially the “Conformal transverse traceless decomposition” [4], have been used very successfully in a wide variety of contexts. Indeed, since part of this thesis was done before the modern decompositions were developed, we use them as well in chapters 4 to 6.

2.4 Black hole initial data

So far we were concerned with describing mathematically well-defined procedures for constructing initial data (g_{ij}, K^{ij}) . Both the conformal thin sandwich equations and the the extrinsic curvature decomposition can generate every possible initial

data set, and in chapter 3 of this thesis we will present a numerical code to solve these equations.

Having these mathematical and numerical tools, we now face the *physical* question *how* to choose the free data such that the final physical initial data sets have certain properties. Moreover, the presence of black holes often leads to *excised* regions from the computational domain, which require *boundary conditions*. For elliptic equations, boundary conditions influence the solution everywhere, so one must choose them with great care.

Both questions –how to choose the free data and how to choose boundary conditions at the excised regions⁵– are difficult, because we do not know exactly how these choices influence the physical solution, neither do we know what the physical solution “should” be for certain astrophysically relevant situations, for example an inspiraling binary black hole.

The approach taken in this thesis is to compute initial data sets with both formalisms and with several different choices of free data. Then we look for consistency among these initial data sets. Particularly helpful are *sequences* of initial data sets. For example, we compute initial data representing binary black holes in quasi-circular orbits as a function of the separation between the black holes. Analysis of such a sequence, and verification that certain properties along the sequence seem physically “reasonable,” can increase or decrease the confidence one has in the relevance of the particular approach used to construct the sequences.

In the rest of this section, we briefly review the choices made in each of the subsequent chapters to put them into context. From now on, we focus exclusively on vacuum spacetimes with vanishing matter terms, $\rho = j^i = S_{ij} = 0$, containing one or two black holes.

The project presented in chapter 4 was begun before the modern constraint decompositions were discovered. Therefore it uses one of the older methods, the “Conformal transverse traceless decomposition” [4, 20]. It is a special case of the extrinsic curvature decomposition outlined in section 2.3 which is obtained by setting $\tilde{\sigma} \equiv 1$. It further assumes the simplest possible free data: conformal flatness, $\tilde{g}_{ij} = \text{flat}$, maximal slicing, $K = 0$, and $\tilde{A}_{TT}^{ij} = 0$. The momentum constraint (2.54) decouples from the Hamiltonian constraint (2.55), and simplifies to

$$\tilde{\nabla}_j(\tilde{\mathbb{L}}V)^{ij} = 0, \quad (2.71)$$

⁵Boundary conditions at *infinity* are easily derived from asymptotic flatness.

where in Cartesian coordinates, the derivatives are simple partial derivatives. Bowen and York [21, 22] found *analytic* solutions, V_{BY}^i , to (2.71) describing one or multiple black holes carrying linear and angular momenta.

The initial value problem is thus reduced to solving the Hamiltonian constraint (2.55), which becomes

$$\Delta\psi + \frac{1}{8}\psi^{-7}(\tilde{\mathbb{L}}V_{BY})_{ij}(\tilde{\mathbb{L}}V_{BY})^{ij} = 0, \quad (2.72)$$

a quasi-linear flat space Laplace equation.

The boundary conditions at the black holes are derived by requiring *inversion symmetry* with respect to the throat of each black hole. This leads to a two-sheeted topology, where each black hole connects “our” universe through an Einstein-Rosen bridge to the same “mirror” universe [9]. To satisfy inversion symmetry, $\tilde{A}_{BY}^{ij} = (\tilde{\mathbb{L}}V_{BY})^{ij}$ must be modified by an ingenious imaging process [23]⁶. This method is described in detail by Cook [26, 27, 28]. Cook also developed an elliptic solver for this problem [28], which I use in chapter 4.

Chapter 5 is a variation on chapter 4, exploring quasi-circular orbits for unequal mass black holes (as opposed to spinning black holes). It uses the inversion symmetric Bowen-York data to construct sequences of quasi-circular orbits extending toward the test-mass limit. This limit is known analytically, so one can compare directly the computations against the correct results.

The “Bowen-York initial data” is relatively easy to construct (one flat space Laplace equation instead of four or five coupled equations; moreover, the puncture method [24] does not even require internal boundaries). However, it makes very special assumptions about the free data, $\tilde{g}_{ij} = \text{flat}$, $K = 0$, $\tilde{A}_{TT}^{ij} = 0$, $\tilde{\sigma} = 1$. Only a small subset of all initial data sets can be reached with these restrictive assumptions. As it is not clear that realistic binary black hole data belongs into this class, one needs to go beyond this approach.

In chapter 6, we compare different constraint decompositions, namely the two previous variants of the extrinsic curvature decomposition, as well as the conformal thin sandwich equations with free data (2.30) (specification of \tilde{N} , not \tilde{K}). We also

⁶The *puncture method* [24] makes the same assumptions on the free data, but uses a three-sheeted topology instead, with each black hole connecting to “its own” universe (cf. [10]). This approach does not require excised regions in the computational domain. A very recent paper [25] indicates that the puncture method cannot be easily extended to the conformal thin sandwich equations.

explore different choices for some of the free data by choosing \tilde{g}_{ij} and K (and \tilde{N} for conformal thin sandwich) based on superposed Kerr-Schild data.

Chapter 7 employs the conformal thin sandwich formalism with specification of \dot{K} , i.e. we solve the five coupled partial differential equations (2.28), (2.29), (2.35). We also explore different boundary conditions at the horizons of the black holes.

Chapter 8, finally, explores spacetimes without black holes, or with just one. We use the conformal thin sandwich equations with \dot{K} -equation to construct initial data for a spacetime with superposed gravitational radiation. In this chapter, we solve the conformal thin sandwich equations on very general, nonflat conformal manifolds \tilde{g}_{ij} .

Chapter 3

A multidomain spectral method for solving elliptic equations*

3.1 Introduction

Elliptic partial differential equations (PDE) are a basic and important aspect of almost all areas of natural science. Numerical solutions of PDEs in three or more dimensions pose a formidable problem, requiring a significant amount of memory and CPU time. Off-the-shelf solvers are available; however, it can be difficult to adapt such a solver to a particular problem at hand, especially when the computational domain of the PDE is nontrivial, or when one deals with a set of coupled PDEs.

There are three basic approaches to solving PDEs: Finite differences, finite elements and spectral methods. Finite differences are easiest to code. However, they converge only algebraically and therefore need a large number of grid points and have correspondingly large memory requirements. Finite elements and spectral methods both expand the solution in basis functions. Finite elements use many subdomains and expand to low order in each subdomain, whereas spectral methods use comparatively few subdomains with high expansion orders. Finite elements are particularly well suited to irregular geometries appearing in many engineering applications. For sufficiently regular domains, however, spectral methods are generally faster and/or more accurate.

Multidomain spectral methods date back at least to the work of Orszag[29]. In a multidomain spectral method, one has to match the solution across different subdomains. Often this is accomplished by a combination of solves on individual subdomains together with a global scheme to find the function values at the internal subdomain boundaries. Examples of such global schemes are relaxational iteration[30], an influence matrix[31, 32], or the spectral projection decomposition method[33]. For simple PDEs like the Helmholtz equation, fast solvers for the subdomain solves are available. For more complicated PDEs, or for coupled PDEs, the subdomain solves will typically use an iterative solver. One drawback of these

*H. P. Pfeiffer, L. E. Kidder, M. A. Scheel and S. A. Teukolsky, *Comput. Phys. Commun.* **152**, 253 (2003).

schemes is that information from the iterative subdomain solves is not used in the global matching procedure until the subdomain solves have completely converged. The question arises whether efficiency can be improved by avoiding this delay in communication with the matching procedure.

In this paper we present a spectral method for coupled nonlinear PDEs based on pseudospectral collocation with domain decomposition. This method does not split subdomain solves and matching into two distinct elements. Instead it combines satisfying the PDE on each subdomain, matching between subdomains, and satisfying the boundary conditions into one set of equations. This system of equations is then solved with an iterative solver, typically GMRES[34]. At each iteration, this solver thus has up-to-date information about residuals on the individual subdomains and about matching and thus can make optimal use of all information.

The individual subdomains implemented are rectangular blocks *and* spherical shells. Whereas either rectangular blocks (see e.g. [35, 36, 37]) or spherical shells[38] have been employed before, we are not aware of work using both. The code supports an arbitrary number of blocks and shells that can touch each other and/or overlap.

Moreover, the operator \mathcal{S} at the core of the method (see section 3.3.3) turns out to be modular, i.e. the code fragments used to evaluate the PDE, the boundary conditions, and the matching conditions are independent of each other. Thus the structure of the resulting code allows for great flexibility, which is further enhanced by a novel point of view of the mappings that are used to map collocation coordinates to the physical coordinates. This flexibility is highlighted in the following aspects:

- The user code for the particular PDE at hand is completely independent from the code dealing with the spectral method and domain decomposition. For a new PDE, the user has to supply only the code that computes the residual and its linearization.
- *Mappings* are employed to control how collocation points and thus resolution are distributed within each subdomain. New mappings can be easily added which are then available for *all* PDEs that have been coded.
- The solver uses standard software packages for the Newton-Raphson step, the iterative linear solvers, and the preconditioning. Thus one can experi-

ment with many different linear solvers and different preconditioners to find an efficient combination. The code will also automatically benefit from improvements to these software packages.

- The code is dimension independent (up to three dimensions).
- Many properties of a particular solve can be chosen at runtime, for example the domain decomposition, the mappings used in each subdomain, as well as the choice of the iterative solver. The user can also choose among differential operators and boundary conditions previously coded at runtime.

In the next section we recall some basics of the pseudo-spectral collocation method. In section 3.3 we describe our approach of combining matching with solving of the PDE. For ease of exposition, we interweave the new method with more practical issues like mappings and code modularity. The central piece of our method, the operator \mathcal{S} , is introduced in section 3.3.3 for a one-dimensional problem and then extended to higher dimensions and spherical shells. In section 3.4 we solve three example problems. Many practical issues like preconditioning and parallelization are discussed in this section, and we also include a detailed comparison to a finite difference code.

3.2 Spectral Methods

Spectral methods have been widely used for many years, and several good books are available (e.g.[39, 40, 32]). Therefore we present here only the most important ideas relevant to our problem. We deal with a second order nonlinear elliptic partial differential equation or system of equations,

$$(\mathcal{N}u)(x) = 0, \quad x \in \mathcal{D}, \quad (3.1)$$

in some domain $\mathcal{D} \subset \mathbb{R}^d$ with boundary conditions

$$g(u)(x) = 0, \quad x \in \partial\mathcal{D}. \quad (3.2)$$

The function u can be a single variable giving rise to a single PDE, or it can be vector-valued giving rise to a coupled set of PDEs. Throughout this paper we assume that the problem has a unique solution. We also absorb a possible right-hand side into the elliptic operator \mathcal{N} .

The fundamental idea of spectral methods is to approximate functions, like the solution to the PDE (3.1), as a truncated series in some basis functions $\Phi_k(x)$:

$$u(x) \approx u^{(N)}(x) \equiv \sum_{k=0}^N \tilde{u}_k \Phi_k(x). \quad (3.3)$$

The coefficients \tilde{u}_k are called the *spectral coefficients*. The choice of basis functions depends on the boundary conditions; for periodic problems, a Fourier series or an expansion in spherical harmonics are suitable, for nonperiodic problems, eigenfunctions of singular Sturm-Liouville operators are used. With the appropriate Φ_k , the series (3.3) converges exponentially in N , provided $u(x)$ is smooth.

Derivatives of $u^{(N)}$ are computed via

$$\frac{du^{(N)}(x)}{dx} = \sum_{k=0}^N \tilde{u}_k \frac{d\Phi_k(x)}{dx}, \quad (3.4)$$

and similarly for higher derivatives. As $d\Phi_k/dx$ are known analytically, Eq. (3.4) can be used to evaluate derivatives exactly (i.e. to numerical roundoff) at any point x^1 . No special treatment of boundary points is necessary. Thus $(\mathcal{N}\Pi^{(\mathcal{N})})(\xi)$ can be evaluated exactly at any x , too. The resulting function $(\mathcal{N}\Pi^{(\mathcal{N})})(\xi)$, however, can in general *not* be represented exactly as a truncated series (3.3). Nonlinearities in \mathcal{N} will introduce higher frequency modes, and expressing $(\mathcal{N}u^{(N)})(x)$ by the series (3.3) will fold these modes back into the retained $N + 1$ modes. This is called *aliasing*; the errors are exponentially small, however, with sufficient resolution.

In order to compute the spectral coefficients \tilde{u}_k we use *pseudo-spectral collocation* where one requires

$$(\mathcal{N}u^{(N)})(x_i) = 0, \quad i = 0, \dots, N. \quad (3.5)$$

The points x_i are called *collocation points*, and are chosen as the abscissas of the Gaussian quadrature associated with the basis set Φ_k . Eq. (3.5) is essentially equivalent to approximating the residual $(\mathcal{N}u^{(N)})(x)$ as a truncated series (3.3), and requiring that this approximation vanishes.

Although we concentrate on elliptic problems, we note that spectral methods are also widely used for hyperbolic and parabolic PDEs. The spectral coefficients

¹In practice, derivatives, Eq. (3.4), are computed via a truncated series in Φ_k . In this case, derivatives will be exact only if $d\Phi_k/dx$ can be represented by a truncated series (3.3).

become functions of time, $\tilde{u}_k(t)$, and one rewrites the hyperbolic or parabolic PDE as a system of ordinary differential equations for $\tilde{u}_k(t)$, which can be solved by various time stepping methods (e.g. Runge-Kutta). For details, see e.g. [39, 40, 32].

3.2.1 Chebyshev polynomials

Chebyshev polynomials are widely used as basis functions for spectral methods. They satisfy the convenient analytical properties of “classical” orthogonal polynomials. Their defining differential equation is a *singular* Sturm-Liouville problem, and so Chebyshev expansions converge exponentially for smooth functions u *independent* of the boundary conditions satisfied by u [39, 32].

Chebyshev polynomials are defined by

$$T_k(X) = \cos(k \arccos X), \quad X \in [-1, 1]. \quad (3.6)$$

They are defined on the interval $X \in [-1, 1]$ only; usually one needs to map the *collocation coordinate* $X \in [-1, 1]$ to the physical coordinate of the problem, $x \in [a, b]$. We use the convention that the variable X varies over the interval $[-1, 1]$, whereas x is defined over arbitrary intervals. We will describe our approach to mappings below in the implementation section.

For an expansion up to order N (i.e. having a total of $N + 1$ basis functions) the associated collocation points are

$$X_i = \cos\left(\frac{i\pi}{N}\right), \quad i = 0, \dots, N. \quad (3.7)$$

Define the real space values

$$u_i \equiv u^{(N)}(X_i) = \sum_{k=0}^N \tilde{u}_k T_k(X_i). \quad (3.8)$$

Using the discrete orthogonality relation

$$\delta_{jk} = \frac{2}{N\bar{c}_k} \sum_{i=0}^N \frac{1}{\bar{c}_i} T_j(X_i) T_k(X_i) \quad (3.9)$$

with

$$\bar{c}_i = \begin{cases} 2 & k = 0 \text{ or } k = N \\ 1 & k = 1, \dots, N - 1, \end{cases} \quad (3.10)$$

we can invert (3.8) and find

$$\tilde{u}_j = \frac{2}{N\bar{c}_j} \sum_{i=0}^N \frac{u_i}{\bar{c}_i} T_j(X_i). \quad (3.11)$$

Both matrix multiplications (3.8) and (3.11) can be performed with a fast cosine transform in $\mathcal{O}(N \ln N)$ operations, another reason for the popularity of Chebyshev basis functions.

There are the same number of real space values u_i and spectral coefficients \tilde{u}_k , and there is a one-to-one mapping between $\{u_i\}$ and $\{\tilde{u}_k\}$. Hence one can represent the function $u^{(N)}$ by either $\{u_i\}$ or $\{\tilde{u}_k\}$.

The spectral coefficients of the derivative,

$$\frac{du^{(N)}}{dX}(X) = \sum_{k=0}^N \tilde{u}'_k T_k(X), \quad (3.12)$$

are given by the recurrence relation

$$\begin{aligned} \tilde{u}'_i &= \tilde{u}'_{i+2} + 2(i+1)\tilde{u}_{i+1}, & i = 1, \dots, N-1, \\ \tilde{u}'_0 &= \frac{1}{2}\tilde{u}'_2 + \tilde{u}_1, \end{aligned} \quad (3.13)$$

with $\tilde{u}_{N+1} = \tilde{u}_N = 0$. The coefficients of the second derivative,

$$\frac{d^2u^{(N)}}{dX^2}(X) = \sum_{k=0}^{N-1} \tilde{u}''_k T_k(X), \quad (3.14)$$

are obtained by a similar recurrence relation, or by applying (3.13) twice.

3.2.2 Basis functions in higher dimensions

In higher dimensions one can choose tensor grids of lower dimensional basis functions. For example, a d -dimensional cube $[-1, 1]^d$ can be described by Chebyshev polynomials along each coordinate axis. For a three-dimensional sphere or spherical shell, tensor products of spherical harmonics for the angles and a Chebyshev series for the radial coordinate[38] are used. It is also possible to expand the angular piece in a double Fourier-series[41].

3.2.3 Domain Decomposition

If the computational domain \mathcal{D} has a different topology than the basis functions, then an expansion in the basis functions cannot cover \mathcal{D} completely. Moreover, the

particular problem at hand might require different resolution in different regions of the computational domain which will render a single overall expansion inefficient.

One circumvents these problems with domain decomposition. The computational domain \mathcal{D} is covered by $N_{\mathcal{D}}$ subdomains

$$\mathcal{D} = \bigcup_{\mu=1}^{N_{\mathcal{D}}} \mathcal{D}_{\mu}, \quad (3.15)$$

each having its own set of basis functions and expansion coefficients:

$$u^{(\mu)}(x) = \sum_{k=0}^{N_{\mu}} \tilde{u}_k^{(\mu)} \Phi_k^{(\mu)}(x), \quad x \in \mathcal{D}_{\mu}, \quad \mu = 1, \dots, N_{\mathcal{D}}. \quad (3.16)$$

Here $u^{(\mu)}$ denotes the approximation in the μ -th domain, and we have dropped the additional label N denoting the expansion order of $u^{(\mu)}$. The individual subdomains \mathcal{D}_{μ} can touch each other or overlap each other. To ensure that the functions $u^{(\mu)}$ —each defined on a single subdomain \mathcal{D}_{μ} only—actually fit together and form a smooth solution of the PDE (3.1) on the full domain \mathcal{D} , they have to satisfy matching conditions. In the limit of *infinite* resolution, we must have that

- for touching subdomains \mathcal{D}_{μ} and \mathcal{D}_{ν} the function and its normal derivative must be smooth on the surface where the subdomains touch:

$$\begin{aligned} u^{(\mu)}(x) &= u^{(\nu)}(x) \\ \frac{\partial u^{(\mu)}}{\partial n}(x) &= -\frac{\partial u^{(\nu)}}{\partial n}(x) \end{aligned} \quad x \in \partial\mathcal{D}_{\mu} \cap \partial\mathcal{D}_{\nu} \quad (3.17)$$

(The minus sign in the second equation of (3.17) occurs because we use the outward-pointing normal in each subdomain.)

- for overlapping subdomains \mathcal{D}_{μ} and \mathcal{D}_{ν} the functions $u^{(\mu)}$ and $u^{(\nu)}$ must be identical in $\mathcal{D}_{\mu} \cap \mathcal{D}_{\nu}$. By uniqueness of the solution of the PDE, it suffices to require that the functions are identical on the boundary of the overlapping domain:

$$u^{(\mu)}(x) = u^{(\nu)}(x), \quad x \in \partial(\mathcal{D}_{\mu} \cap \mathcal{D}_{\nu}). \quad (3.18)$$

For *finite* resolution, Eqs. (3.17) and (3.18) will in general not hold for all x , but only at a discrete set of points. Between these points, these equations will be violated by an exponentially small amount. We will see in the next section how these conditions are actually implemented in the code.

3.3 Implementation

In this section we describe our specific approaches to several aspects of multi-dimensional pseudo-spectral collocation with domain decomposition.

3.3.1 One-dimensional Mappings

Chebyshev polynomials are defined for $X \in [-1, 1]$. Differential equations in general will be defined on a different interval $x \in [a, b]$. In order to use Chebyshev polynomials, one introduces a mapping

$$X : [a, b] \rightarrow [-1, 1], \quad x \rightarrow X = X(x) \quad (3.19)$$

that maps the *physical coordinate* x onto the *collocation coordinate* X .

One could explicitly substitute this mapping into the PDE under consideration. Derivatives would be multiplied by a Jacobian, and we would obtain the PDE on the interval $[-1, 1]$. For example, the differential equation in the variable x

$$\frac{\partial^2 u}{\partial x^2} + u = 0, \quad x \in [a, b], \quad (3.20)$$

becomes the following differential equation in the variable X :

$$X'^2 \frac{\partial^2 u}{\partial X^2} + X'' \frac{\partial u}{\partial X} + u = 0, \quad X \in [-1, 1], \quad (3.21)$$

where $X' = \partial X / \partial x$ and $X'' = \partial^2 X / \partial x^2$. Now one could expand $u(X)$ in Chebyshev polynomials, compute derivatives $\partial / \partial X$ via the recurrence relation (3.13) and code Eq. (3.21) in terms of $\partial u / \partial X$. This approach is common in the literature [32, 42]. However, it has several disadvantages: As one can already see from this simple example, the equations become longer and one has to code and debug more terms. Second, and more important, it is inflexible, since for each different map one has to derive and code a mapped equation (3.21). *A priori* one might not know the appropriate map for a differential equation, and in order to try several maps, one has to code the mapped equation several times. Also, for domain decomposition, a different map is needed for each subdomain.

We propose a different approach. We still expand in terms of Chebyshev polynomials on $X \in [-1, 1]$ and obtain the physical solution via a mapping $X(x)$,

$$u(x) = \sum_{k=0}^N \tilde{u}_k T_k(X(x)), \quad (3.22)$$

and we still compute $\partial u(X)/\partial X$ and $\partial^2 u(X)/\partial X^2$ via the recurrence relation (3.13). However, now we do *not* substitute $\partial u(X)/\partial X$ and $\partial^2 u(X)/\partial X^2$ into the mapped differential equation, Eq. (3.21). Instead we compute first numerically

$$\frac{\partial u(x)}{\partial x} = X' \frac{\partial u(X)}{\partial X} \quad (3.23)$$

$$\frac{\partial^2 u(x)}{\partial x^2} = X'^2 \frac{\partial^2 u(X)}{\partial X^2} + X'' \frac{\partial u(X)}{\partial X} \quad (3.24)$$

and substitute these values into the original physical differential equation (3.20). The collocation points are thus mapped to the physical coordinates

$$x_i = X^{-1}(X_i). \quad (3.25)$$

This approach separates the code into three distinct parts:

1. Code dealing with the basis functions: transforms between collocation space X and spectral space, evaluation of derivatives $\partial/\partial X$ via recurrence relations. This code depends only on the collocation coordinates $X \in [-1, 1]$ (and on the angular coordinates θ, ϕ for spherical shells).
2. Mappings that map between collocation coordinate X and physical coordinates x .
3. The “user code” implementing the physical PDE [in our example Eq. (3.20)] that deals only with the physical coordinate x .

These three elements are independent of each other:

- A user who wants to code another differential equation has only to write the code that evaluates the differential operator \mathcal{N} in the physical space with physical derivatives. Then immediately all previously coded mappings are available for this new differential equation, as well as all basis functions.
- In order to introduce a new mapping, one has to code only four functions, namely $X(x)$, its inverse $x(X)$, as well as the derivatives $X'(x)$ and $X''(x)$. This new map can then be used for any differential equation already coded or to be coded later.
- In order to switch to a different set of basis functions, one has only to code the transforms and the recurrence relations for the derivatives.

In practice we use three different mappings

$$\begin{aligned}
\text{linear: } & X(x) = Ax + B \\
\text{log: } & X(x) = A \log(Bx + C) \\
\text{inverse: } & X(x) = \frac{A}{x} + B
\end{aligned} \tag{3.26}$$

In each case the constants A, B are chosen such that $[a, b]$ is mapped to $[-1, 1]$. The log mapping has one additional parameter which is used to fine-tune the relative density of collocation points at both ends of the interval $[a, b]$. We show the effects of different mappings in our first example in section 3.4.1.

3.3.2 Basis functions and Mappings in higher Dimensions

Rectangular Blocks

In order to expand in a d -dimensional rectangular block,

$$\mathcal{D} = [a_1, b_1] \times [a_2, b_2] \times \dots \times [a_d, b_d], \tag{3.27}$$

we use a tensor product of Chebyshev polynomials with a 1- d mapping along each coordinate axis:

$$u(x_1, \dots, x_d) = \sum_{k_1=0}^{N_1} \sum_{k_2=0}^{N_2} \dots \sum_{k_d=0}^{N_d} \tilde{u}_{k_1 \dots k_d} T_{k_1}(X^{(1)}(x_1)) \dots T_{k_d}(X^{(d)}(x_d)). \tag{3.28}$$

We use d mappings

$$X^{(l)} : [a_l, b_l] \rightarrow [-1, 1], \quad l = 1, \dots, d, \tag{3.29}$$

and the collocation points in physical space are the mapped collocation points along each dimension,

$$x_{i_1 \dots i_d} = \left(x_{i_1}^{(1)}, \dots, x_{i_d}^{(d)} \right), \tag{3.30}$$

where the coordinate along the l -th dimension $x_{i_l}^{(l)}$ is given by Eq. (3.25) using $X^{(l)}$.

Note that such a d -dimensional rectangle has as many spectral coefficients $\tilde{u}_{k_1 \dots k_d}$ as grid point values $u_{i_1 \dots i_d} = u(x_{i_1}, \dots, x_{i_d})$. Therefore we can equivalently solve for the spectral coefficients or the real space values. We will solve for the real space values $u_{i_1 \dots i_d}$.

Spherical Shell

In a spherical shell with inner and outer radii $0 < R_1 < R_2$ we use a mapping for the radial coordinate. A function $u(r, \theta, \phi)$ is thus expanded as

$$u(r, \theta, \phi) = \sum_{k=0}^{N_r} \sum_{l=0}^L \sum_{m=-l}^l \tilde{u}_{klm} T_k(X(r)) Y_{lm}(\theta, \phi), \quad (3.31)$$

where real-valued spherical harmonics are used:

$$Y_{lm}(\theta, \phi) \equiv \begin{cases} P_l^m(\cos \theta) \cos(m\phi), & m \geq 0 \\ P_l^{|m|}(\cos \theta) \sin(|m|\phi), & m < 0 \end{cases} \quad (3.32)$$

$P_l^m(\cos \theta)$ are the associated Legendre polynomials. Associating the sin-terms with negative m is not standard, but eliminates the need to refer to two sets of spectral coefficients, one each for the cos-terms and the sin-terms. The radial mapping $X : [R_1, R_2] \rightarrow [-1, 1]$ can be any of the choices in Eq. (3.26). The radial collocation points $r_i, i = 0, \dots, N_r$ are given by Eq. (3.25).

For the angle ϕ , Eq. (3.32) leads to a Fourier series with equally spaced azimuthal collocation points

$$\phi_i = \frac{2\pi i}{N_\phi}, \quad i = 0, 1, \dots, N_\phi - 1. \quad (3.33)$$

There is a total of $N_\theta = L + 1$ angular collocation points θ_i , which are the abscissas of Gauss-Legendre integration. All θ_i are in the interior of the interval $[0, \pi]$, hence no collocation point will be placed on the z -axis of the polar coordinate system.

In order to resolve the full Fourier series in ϕ up to $m = L$, one needs $N_\phi \geq 2L + 1$, since for $N_\phi = 2L$, the term $\sin(L\phi)$ vanishes at all collocation points ϕ_i . We use $N_\phi = 2(L + 1)$ since FFTs are more efficient with an even number of points.

The expansion (3.31) has a total of $(N_r + 1)(L + 1)^2$ spectral coefficients but a total of $(N_r + 1)N_\theta N_\phi = 2(N_r + 1)(L + 1)^2$ collocation points. This means a spherical shell has *more* collocation points than spectral coefficients and the expansion (3.31) approximates the grid point values in a least-square sense only[43]. Performing a spectral transform and its inverse will thus project the grid point values into a subspace with dimension equal to the number of spectral coefficients. The implications of this fact for our code are discussed below in section 3.3.6.

Representation of vectors, tensors and derivatives

In both kinds of subdomains, rectangular blocks and spherical shells, we expand the *Cartesian components* of vectors and tensors, and we compute *Cartesian* derivatives, $\partial/\partial x, \partial/\partial y, \partial/\partial z$. These quantities are smooth everywhere, and thus can be expanded in scalar spherical harmonics. By contrast, the spherical components of a vector field in a spherical shell are discontinuous at the poles and cannot be expanded in scalar spherical harmonics. One would have to use e.g. vector spherical harmonics[43, 44].

For a spherical shell we provide an additional wrapper around the basis functions and the radial mapping that transforms polar derivatives $\partial/\partial r, \partial/\partial \theta, \partial/\partial \phi$ to Cartesian derivatives². This involves multiplications by sines and cosines of the angles θ, ϕ which can be performed grid point by grid point in real space. Alternatively, it can be done spectrally by expressing, e.g. $\sin \theta$ in spherical harmonics, and then using addition theorems to reduce products of spherical harmonics to simple sums. Carrying out the transformation spectrally is slightly better in practice.

Representing vectors and derivatives in Cartesian coordinates in both kinds of subdomains increases flexibility, too. We can use the *same* code to evaluate the residual in *both* kinds of subdomains.

We remark that for given order l exact representation of derivatives of Y_{lm} in Cartesian coordinates requires spherical harmonics up to order $l + 1$. For example, the function $f(\mathbf{x}) = |\mathbf{x}|$ has only a Y_{00} component. However, the z -component of its gradient is $\cos \theta$ which is proportional to Y_{10} . Thus the derivatives of the highest retained l -modes cannot be represented accurately. This is not important, however, as the amplitude of these modes decreases exponentially with resolution.

3.3.3 The operator \mathcal{S}

We now introduce the operator \mathcal{S} , the centerpiece of our method. It combines the solution of the PDE, the boundary conditions and matching between different subdomains.

We introduce \mathcal{S} first with a simple case, a one-dimensional differential equation with a Dirichlet boundary condition at one end and a von Neumann boundary condition at the other end:

²The polar singularity at $\theta = 0, \pi$ is not a problem, as no collocation points are located there.

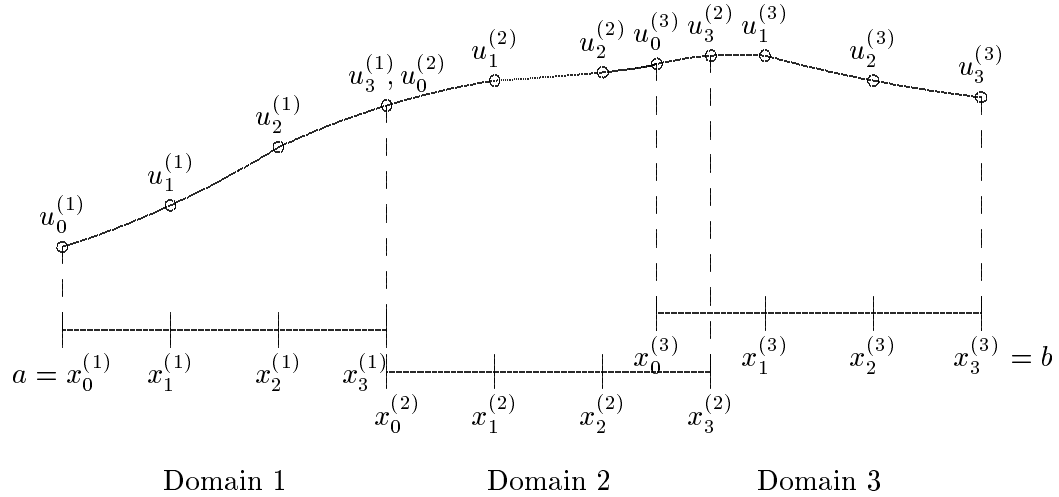


Figure 3.1: Illustration of matching with three subdomains in one dimension. Subdomains 1 and 2 touch each other, and subdomains 2 and 3 overlap. $x_i^{(\mu)}$ denotes the coordinate of the i -th collocation point of the μ -th subdomain, and $u_i^{(\mu)}$ denotes the function values at the grid points.

$$(\mathcal{N}u)(x) = 0, \quad a < x < b, \quad (3.34)$$

$$u(a) = A, \quad (3.35)$$

$$\frac{\partial u}{\partial x}(b) = B. \quad (3.36)$$

To explain our procedure for matching, we assume three domains as depicted in Figure 3.1. N_μ denotes the highest retained expansion order in domain μ ; here $N_\mu = 3$ for all domains. Domains 2 and 3 overlap. Domains 1 and 2 touch so that the collocation points $x_3^{(1)}$ and $x_0^{(2)}$ represent the same physical point. The function value, however, is represented twice, once assigned to domain 1, $u_3^{(1)}$, and once belonging to domain 2: $u_0^{(2)}$. Using just the grid point values within one subdomain, we can expand the function in that subdomain and can evaluate derivatives. We can also interpolate the function to arbitrary positions x . Thus, given values $\{u_i^{(\mu)}, i = 0, \dots, N_\mu\}$, we can compute $u^{(\mu)}(x)$ for $x \in [x_0^{(\mu)}, x_{N_\mu}^{(\mu)}]$.

In order to determine the unknowns $u_i^{(\mu)}$, we need one equation per unknown.

We will first write down these equations and then explain where they come from.

$$(\mathcal{N}u^{(\mu)})(x_i^{(\mu)}) = 0, \quad i = 1, \dots, N_\mu - 1, \quad \mu = 1, \dots, N_{\mathcal{D}} \quad (3.37a)$$

$$u_0^{(1)} - A = 0 \quad (3.37b)$$

$$\frac{\partial u^{(3)}}{\partial x}(x_3^{(3)}) - B = 0 \quad (3.37c)$$

$$u_3^{(1)} - u_0^{(2)} = 0 \quad (3.37d)$$

$$\frac{\partial u^{(1)}}{\partial n}(x_3^{(1)}) + \frac{\partial u^{(2)}}{\partial n}(x_3^{(1)}) = 0 \quad (3.37e)$$

$$u_3^{(2)} - u^{(3)}(x_3^{(2)}) = 0 \quad (3.37f)$$

$$u_0^{(3)} - u^{(2)}(x_0^{(3)}) = 0 \quad (3.37g)$$

Eq. (3.37a) represents the actual pseudo-spectral equation (3.5). It is enforced only for collocation points that are *not* on the boundary of a subdomain. Eqs. (3.37b) and (3.37c) encode the boundary conditions. Eqs. (3.37d) and (3.37e) describe the value and derivative matching at touching subdomain boundaries. These equations follow from Eq. (3.17). Eqs. (3.37f) and (3.37g) perform matching between overlapping subdomains as given by Eq. (3.18).

We will view the left-hand side of Eqs. (3.37) as a non-linear operator \mathcal{S} . This operator acts on the set of grid point values for *all* subdomains $\{u_i^{(\mu)}\}$ ($\mu = 1, 2, 3, i = 0, \dots, N_\mu$ in the example) and returns a residual that incorporates the actual pseudo-spectral condition Eq. (3.5), the boundary conditions, and the matching conditions between different subdomains. If we denote the vector of *all* grid point values by $\underline{\mathbf{u}}$, then the discretized version of the partial differential equation becomes

$$\mathcal{S}\underline{\mathbf{u}} = 0. \quad (3.38)$$

The solution of Eq. (3.38) clearly is the solution of the partial differential equation we want to obtain. By virtue of Eq. (3.38) we thus have condensed the PDE, the boundary conditions and matching into one set of nonlinear equations.

We comment on some implementation issues:

- The action of the operator \mathcal{S} can be computed very easily: Given grid point values $\underline{\mathbf{u}}$, every subdomain is transformed to spectral space and derivatives are computed. Using the derivatives we can compute Eqs. (3.37a), (3.37e) and any boundary conditions that involve derivatives like Eq. (3.37c). The interpolations necessary in Eqs. (3.37f) and (3.37g) are done by summing up the spectral series.

- $\mathcal{S}\underline{\mathbf{u}}$ can be computed in parallel: Everything except the matching conditions depends only on the set of grid point values within *one* subdomain. Therefore the natural parallelization is to distribute subdomains to different processors.
- The code fragments implementing the nonlinear operator \mathcal{N} , the boundary conditions and the matching conditions are independent of each other. In order to change boundary conditions, one has only to modify the code implementing Eqs. (3.37b) and (3.37c). In particular, the code for the matching-equations (3.37d)-(3.37g) can be used for *any* differential operator \mathcal{N} and for *any* boundary condition.

We have now introduced the operator \mathcal{S} in one dimension. Next we address how to solve Eq. (3.38), and then we generalize \mathcal{S} to higher dimensions. We present our method in this order because the generalization to higher dimensions depends on some details of the solution process.

3.3.4 Solving $\mathcal{S}\mathbf{u} = \mathbf{0}$

In this section we describe how we solve the system of nonlinear equations (3.38). Our procedure is completely standard and requires three ingredients: A Newton-Raphson iteration to reduce the nonlinear equations to a linear solve at each iteration, an iterative linear solver, and the preconditioner for the linear solver. For these three steps we employ the software package PETSc[45]. We now comment on each of these three stages.

Newton-Raphson with line searches

PETSc[45] implements a Newton-Raphson method with line searches, similar to the method described in [46]. Given a current guess $\underline{\mathbf{u}}_{\text{old}}$ of the solution, a Newton-Raphson step proceeds as follows: Compute the residual

$$\underline{\mathbf{r}} \equiv \mathcal{S}\underline{\mathbf{u}}_{\text{old}} \quad (3.39)$$

and linearize \mathcal{S} around the current guess $\underline{\mathbf{u}}_{\text{old}}$ of the solution:

$$\mathcal{J} \equiv \frac{\partial \mathcal{S}}{\partial \underline{\mathbf{u}}}(\underline{\mathbf{u}}_{\text{old}}). \quad (3.40)$$

The Jacobian \mathcal{J} is a $N_{DF} \times N_{DF}$ -dimensional matrix, N_{DF} being the number of degrees of freedom. Next compute a correction $\delta \underline{\mathbf{u}}$ by solving the linear system

$$\mathcal{J}\delta \underline{\mathbf{u}} = -\underline{\mathbf{r}}. \quad (3.41)$$

Finally a line-search is performed in the direction of $\delta \underline{\mathbf{u}}$. Parametrize the new solution by

$$\underline{\mathbf{u}}_{\text{new}} = \underline{\mathbf{u}}_{\text{old}} + \lambda \delta \underline{\mathbf{u}} \quad (3.42)$$

and determine the parameter $\lambda > 0$ such that the residual of the new solution,

$$\|\mathcal{S}(\underline{\mathbf{u}}_{\text{new}})\|, \quad (3.43)$$

has sufficiently decreased. Of course, close enough to the true solution, the full Newton-Raphson step $\lambda = 1$ will lead to quadratic convergence. PETSc offers different algorithms to perform this line-search. The default method which employs cubic backtracking worked very well in all our tests. The line search ensures that in each iteration the residual does indeed decrease, which is not guaranteed in Newton-Raphson without line searches.

Linear Solve

In each Newton-Raphson iteration one has to solve Eq. (3.41), a linear system of N_{DF} equations. For large systems of linear equations, iterative linear solvers[34] are most efficient. Such iterative solvers require solely the ability to compute the matrix-vector product $\mathcal{J}\underline{\mathbf{v}}$ for a given vector $\underline{\mathbf{v}}$. Since spectral derivatives and spectral interpolation lead to *full* (i.e. non-sparse) matrices it is impractical to set up the matrix \mathcal{J} explicitly. One can compute these matrix-vector products instead with the linearized variant of the code that computes the operator \mathcal{S} , i.e. equations (3.37a)-(3.37g) and their multidimensional generalizations. Thus our method requires the linearizations of the operator \mathcal{N} [Eq. (3.37a)] and of the boundary conditions [Eqs. (3.37b) and (3.37c)]. The matching equations (3.37d)-(3.37g) are linear anyway, so one can reuse code from \mathcal{S} for these equations. The linearizations are merely Frechet derivatives[32] of the respective operators evaluated at the collocation points, and therefore the Newton-Raphson iteration applied to the discretized equations is equivalent to the Newton-Kantorovitch iteration applied to the PDE.

PETSc includes several different linear iterative solvers (GMRES, TFQR, ...) that can be employed for the linear solve inside the Newton-Raphson iteration. The choice of linear solver and of options for the linear solver and for the Newton-Raphson iteration are made at runtime. This allows one to experiment with different linear solvers and with a variety of options to find an efficient combination.

Note that the matching conditions (3.17) and (3.18) lead to a nonsymmetric matrix \mathcal{J} . Therefore only iterative methods that allow for nonsymmetric matrices can be used.

Preconditioning

In practice one will find that the Jacobian \mathcal{J} is ill-conditioned and thus the iterative method employed to solve Eq. (3.41) will need an increasing number of iterations as the number of collocation points is increased. The *spectral condition number* κ of a matrix is the ratio of largest to smallest eigenvalue of this matrix,

$$\kappa = \frac{\lambda_{max}}{\lambda_{min}}. \quad (3.44)$$

For second order differential equations discretized with Chebyshev polynomials, one finds $\kappa \propto N^4$, N being the number of grid points per dimension. Solving a linear system to given accuracy will require [47, 34] $\mathcal{O}(\kappa)$ iterations of the Richardson method, and $\mathcal{O}(\sqrt{\kappa})$ iterations of modern iterative methods like conjugate gradients or GMRES. Although modern methods are better than Richardson iteration, it is still vital to keep κ close to 1.

This is achieved with *preconditioning*. Instead of solving Eq. (3.41) directly, one solves

$$\mathcal{B}\mathcal{J} \delta \underline{\mathbf{u}} = -\mathcal{B}\underline{\mathbf{r}}, \quad (3.45)$$

with the preconditioning matrix \mathcal{B} . Now the iterative solver deals with the matrix $\mathcal{B}\mathcal{J}$. If \mathcal{B} is a good approximation to \mathcal{J}^{-1} , then $\mathcal{B}\mathcal{J}$ will be close to the identity matrix, the condition number will be close to unity, and the linear solver will converge quickly.

Hence the problem reduces to finding a matrix \mathcal{B} that approximates \mathcal{J}^{-1} sufficiently well and that can be computed efficiently. There exist many different approaches, most notably finite difference preconditioning [29] and finite element preconditioning [48]; we will follow a two-stage process proposed by Orszag [29]. First, initialize a matrix \mathcal{A}_{FD} with a finite difference approximation of the Jacobian \mathcal{J} . Second, approximately invert \mathcal{A}_{FD} to construct \mathcal{B} ,

$$\mathcal{B} \approx \mathcal{A}_{FD}^{-1}. \quad (3.46)$$

In one spatial dimension \mathcal{A}_{FD} is tridiagonal and direct inversion $\mathcal{B} \equiv \mathcal{A}_{FD}^{-1}$ is feasible. In two or more dimensions, direct inversion of \mathcal{A}_{FD} is too expensive; for problems in one two-dimensional subdomain, hardcoded incomplete LU-factorizations

have been developed[40]. In our case we have to deal with the additional complexity that the Jacobian and therefore \mathcal{A}_{FD} contains matching conditions. Since we choose the domain decomposition at runtime, nothing is known about the particular structure of the subdomains.

We proceed as follows: We initialize \mathcal{A}_{FD} with the finite difference approximation of \mathcal{J} . It is sufficient to include those terms of the Jacobian in \mathcal{A}_{FD} that cause the condition number to increase with the expansion order. These are the second spatial derivatives and the first derivatives from matching conditions and boundary conditions, Eqs. (3.37e) and (3.37c). Including the value matching conditions (3.37d), (3.37f), (3.37g) in \mathcal{A}_{FD} improves the ability of the preconditioner to represent modes extending over several subdomains and thus decreases the number of iterations, too. In the first example in section 3.4.1 we demonstrate that preconditioning is indeed necessary, and that one should precondition not only the second order derivatives, but also the matching conditions. Some details about the finite difference approximations are given in appendix 3.7.

Having set up \mathcal{A}_{FD} we then use the software package PETSc[45] for the approximate inversion of Eq. (3.46). PETSc provides many general purpose preconditioners that perform the step (3.46) either explicitly or implicitly, most notably ILU and the overlapping Schwarz method. With PETSc we can explore these to find the most efficient one. We will describe our particular choices for preconditioning below for each example.

3.3.5 \mathcal{S} in higher dimensions

Generalizing \mathcal{S} to multiple dimensions is conceptually straightforward, since Eqs. (3.37) generalize nicely to higher dimensions. In order to simplify the matching between touching subdomains, we require that on a surface shared by touching subdomains, the collocation points are *identical*. If, for example, two three-dimensional rectangular blocks touch along the x -axis, then both blocks must have identical lower and upper bounds of the blocks along the y and z axis and both blocks must use the same mappings and the same number of collocation points along the y - and z -axis. For concentric spherical shells, this restriction implies that all concentric shells must have the same number of collocation points in the angular directions. With this restriction, matching between touching subdomains remains a point-by-point operation.

For overlapping domains, no restriction is needed. If a boundary point of one subdomain happens to be within another subdomain, then an equation analogous to (3.37f) is enforced using spectral interpolation.

The actual implementation of the operator \mathcal{S} involves bookkeeping to keep track of which subdomains overlap or touch, or of what equation to enforce at which grid point. When running in parallel, matching conditions have to be communicated across processors.

3.3.6 Extension of \mathcal{S} to Spherical Shells

Spherical shells have the additional complexity of having more collocation points than spectral coefficients, $N_{col} > N_{spec}$, at least in our formulation. Transforming to spectral space and back to real space projects the real-space values into a N_{spec} -dimensional subspace. Since spectral transforms are used for derivatives and interpolation, a sphere has effectively only N_{spec} degrees of freedom. If we naively try to impose N_{col} equations, one at each collocation point, and if we try to solve for real space values at each collocation point, we find that the linear solver does not converge. This happens because more equations are imposed than degrees of freedom are available. Thus we cannot solve for the real space values u_{ijk} in a spherical shell.

The next choice would be to solve for the spectral coefficients \tilde{u}_{klm} as defined in Eq. (3.31) This is also problematic as it prohibits finite-difference preconditioning. One finds guidance on how to proceed by considering the prototypical elliptic operator, the Laplacian. Application of ∇^2 to an expansion in spherical harmonics yields

$$\nabla^2 \sum_{l,m} a_{lm}(r) Y_{lm} = \sum_{l,m} \left[-\frac{l(l+1)a_{lm}(r)}{r^2} + \frac{1}{r^2} \frac{\partial}{\partial r} \left(r^2 \frac{\partial a_{lm}(r)}{\partial r} \right) \right] Y_{lm}. \quad (3.47)$$

We see that the different (lm) -pairs are uncoupled. The angular derivatives will therefore be diagonal in spectral space (with diagonal elements $-l(l+1)/r^2$). However, one has to precondition the radial derivatives in order to keep the spectral conditioning number low and must therefore keep real-space information about the radial direction. We therefore solve for the coefficients \hat{u}_{ilm} of an expansion defined by

$$u(r_i, \theta, \phi) = \sum_{l=0}^L \sum_{m=-l}^l \hat{u}_{ilm} Y_{lm}(\theta, \phi). \quad (3.48)$$

This mixed real/spectral expansion has N_{spec} coefficients \hat{u}_{ilm} and retains real space information about the radial coordinate necessary for finite difference preconditioning. In order to precondition the flat space Laplacian in a spherical shell, \mathcal{A}_{FD} is initialized with the diagonal matrix $\text{diag}(-l(l+1)/r_i^2)$ for the angular piece of ∇^2 and with finite differences for the radial derivatives. More general differential operators are discussed in the last example, section 3.4.3, and in appendix 3.8.

In order to evaluate $\mathcal{S}\mathbf{u}$ for a spherical shell, we proceed as follows. \mathbf{u} contains the coefficients \hat{u}_{ilm} . Transform these coefficients to real space values. This involves only an angular transform. Compute boundary conditions, matching conditions, and the residual of the nonlinear elliptic operator \mathcal{N} at each collocation point as in rectangular blocks. At this stage we have N_{col} collocation point values, all of which should vanish for the desired solution. We transform these values back into the coefficients of Eq. (3.48) and return these coefficients as the residual of the operator \mathcal{S} .

3.3.7 Implementation Details

Our code is written in C++ and utilizes various software packages extensively. PETSc[45] is used for linear and nonlinear solves as well as for preconditioning. The software package KeLP [49] is used to implement domain decomposition. It provides functionality to iterate over boundary points of a specific subdomain as well as routines for handling the interprocessor communication needed for matching between subdomains. Spherepack[50] provides routines to handle spherical harmonics such as computation of collocation points and spectral transforms. For Fourier transforms we employ DFFTPACK[51].

The object oriented programming language C++ supports the modularity of our code very well. The different elements, e.g. mappings, are represented by polymorphic classes. In total, the code is about 50000 lines long. It shares its infrastructure, i.e. domain decomposition, spectral transforms, mappings, IO, etc., with a separate spectral evolution code that we have written. The code is currently not well documented. However, anyone interested in using it should contact us.

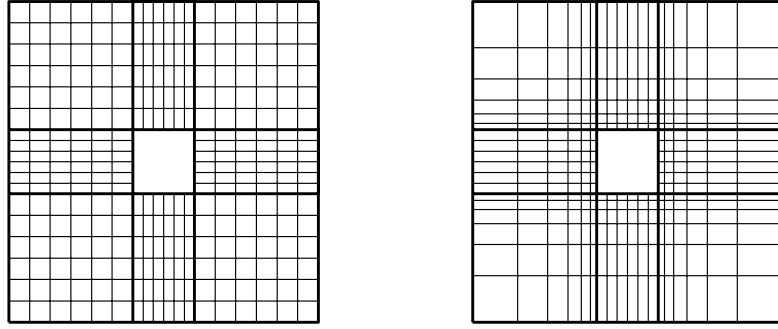


Figure 3.2: Domain decomposition for Laplace equation in a square. The left plot illustrates linear mappings in all subdomains and the right plot shows log-linear-log mappings along each axis.

3.4 Examples

3.4.1 $\nabla^2 u = 0$ in 2-D

As a first test, we solve the Laplace equation in two dimensions with Dirichlet boundary conditions:

$$\nabla^2 u(x, y) = 0 \quad (x, y) \in \mathcal{D} \quad (3.49)$$

$$u(x, y) = \ln(x^2 + y^2) \quad (x, y) \in \partial\mathcal{D} \quad (3.50)$$

The computational domain \mathcal{D} is a square with side $2L$ centered on the origin with a smaller square with side 2 excised:

$$\mathcal{D} = \{(x, y) \mid -L \leq x, y \leq L\} - \{(x, y) \mid -1 < x, y < 1\} \quad (3.51)$$

This domain is decomposed into 8 touching rectangles as shown in figure 3.2. This figure also illustrates the difference between linear mappings and logarithmic mappings. The right plot of figure 3.2 shows that logarithmic mappings move grid points closer to the excised rectangle. For clarity, both plots neglect the fact that the Chebyshev collocation points given in Eq. (3.7) are clustered toward the boundaries.

We solve Eqs. (3.49) and (3.50) for three cases:

- $L = 5$ with linear mappings
- $L = 100$ with linear mappings

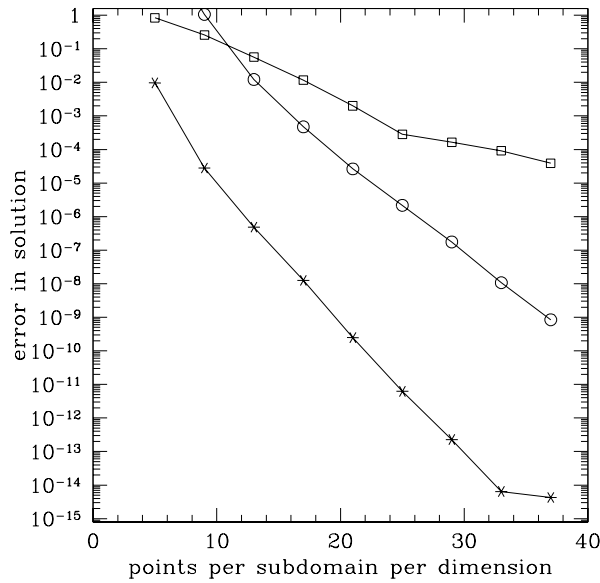


Figure 3.3: Convergence of solution of Laplace equation in a square (rms errors). Stars denote $L = 5$ with linear mappings, squares $L = 100$ with linear mappings, and circles $L = 100$ with log mappings.

- $L = 100$ with logarithmic mappings.

Equation (3.49) is linear, therefore only one Newton-Raphson iteration with one linear solve is necessary. The numerical solution is compared to the analytic solution $u(x, y) = \ln(x^2 + y^2)$. The errors are shown in figure 3.3. In the small computational domain extending only to $x, y = \pm 5$, the accuracy of the solution quickly reaches numerical roundoff. In the larger domain extending to $L = 100$ the achievable resolution with the same number of collocation points is of course lower. With linear mappings we achieve an absolute accuracy of 10^{-4} with a total of ~ 10000 collocation points. This is already better than finite difference codes. However this accuracy can be increased with better adapted mappings. Since the solution $\ln(x^2 + y^2)$ changes much faster close to the origin than far away, one expects better convergence if more collocation points are placed close to the origin. This can be achieved with logarithmic mappings. Figure 3.3 shows that logarithmic mappings roughly double the convergence rate. At the highest resolution the difference is over four orders of magnitude.

Figure 3.4 compares the number of iterations N_{its} in the linear solver for different choices of the finite difference preconditioning matrix \mathcal{A}_{FD} [section 3.3.4].

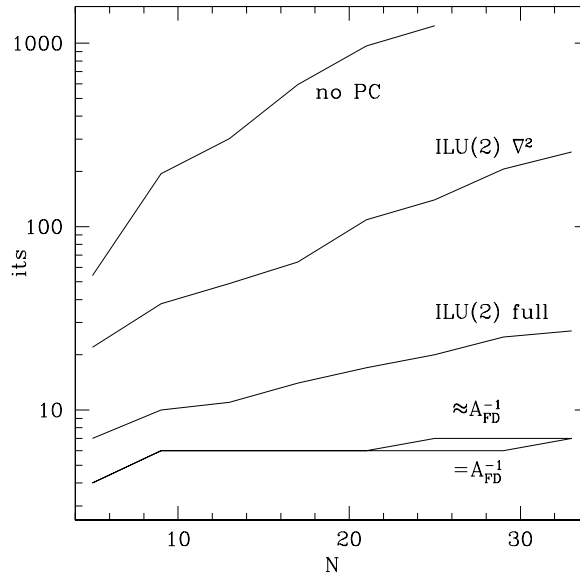


Figure 3.4: Number of iterations in the linear solver for various kinds of preconditioning as a function of the number of collocation points N per dimension per subdomain. “ILU(2) ∇^2 ” denotes ILU(2) preconditioning of only the Laplace operator, whereas in “ILU(2) full” the derivative matching conditions are preconditioned also. “ $= \mathcal{A}_{FD}^{-1}$ ” and “ $\approx \mathcal{A}_{FD}^{-1}$ ” denote exact and approximate inversion of the preconditioning matrix based on Laplace operator and matching conditions.

Without any preconditioning, $\mathcal{A}_{FD} = \mathbf{1}$, N_{its} increases very quickly with the number of collocation points. If only second derivative terms are included in \mathcal{A}_{FD} then N_{its} grows more slowly. Inclusion of both second derivatives and matching conditions (3.37d) and (3.37e) improves the convergence further (see curve labeled “ILU(2) full”). In this case ILU(2) preconditioning completely controls the largest eigenvalue of the preconditioned operator $\mathcal{B}\mathcal{J}$ [cf. Eq. (3.45)], $\lambda_{max} \lesssim 2.6$; however, the smallest eigenvalue λ_{min} approaches zero as N is increased. Hence, the condition number and thus the required number of iteration still increases with resolution. It is typical that ILU has difficulties controlling the long wavelength modes, and the problem is aggravated because the subdomains are only weakly coupled. Figure 3.4 also contains results for exact and approximate inversion of \mathcal{A}_{FD} . These methods control λ_{min} , too, and lead to an iteration count independent of resolution. Direct inversion is computationally expensive and is only feasible for small problems like this one. Approximate inversion of \mathcal{A}_{FD} , our preferred method

for more complex geometries in 3 dimensions, will be explained in detail in the next example.

3.4.2 Quasilinear Laplace equation with two excised spheres

This solver was developed primarily for elliptic problems in numerical relativity. Accordingly we now solve an equation that has been of considerable interest in that field over the last few years (see e.g. [52, 20] and references therein). Readers not familiar with relativity can simply view this problem as another test example for our new solver³. We solve

$$\nabla^2\psi + \frac{1}{8}A^2\psi^{-7} = 0 \quad (3.52)$$

for the function $\psi = \psi(x, y, z)$. $A^2 = A^2(x, y, z)$ is a known, positive function, and the computational domain is \mathbb{R}^3 with two excised spheres,

$$\mathcal{D} = \mathbb{R}^3 - S_1 - S_2. \quad (3.53)$$

The radii $r_{1/2}$ and centers of the spheres are given. The function ψ must satisfy a Dirichlet boundary condition at infinity, and Robin boundary conditions at the surface of each excised sphere:

$$\psi \rightarrow 1 \quad \text{as } r \rightarrow \infty \quad (3.54)$$

$$\frac{\partial\psi}{\partial r} + \frac{\psi}{2r_i} = 0 \quad \vec{r} \in \partial S_i, \quad i = 1, 2 \quad (3.55)$$

$\partial/\partial r$ in Eq. (3.55) denotes the radial derivative in a coordinate system centered at the center of sphere i .

Figure 3.5 sketches the domain decomposition used for the computational domain \mathcal{D} . We surround each excised sphere with a spherical shell. These two spherical shells are matched together with $5 \times 3 \times 3$ rectangular blocks, where the two blocks that contain the excised spheres $S_{1,2}$ are removed. Finally, we surround this structure with a third spherical shell extending to very large outer radius. This gives a total of 46 subdomains, namely 3 shells and 43 rectangular blocks.

³The solution of this problem describes two black holes. The surfaces of the spheres $S_{1,2}$ correspond to the horizons of the black holes, the function A^2 encodes information about spins and velocities of the black holes, and the solution ψ measures the deviation from a flat spacetime. Far away from the black holes one has $\psi \approx 1$ with an almost Minkowski space, close to the holes we will find $\psi \sim 2$ with considerable curvature of spacetime

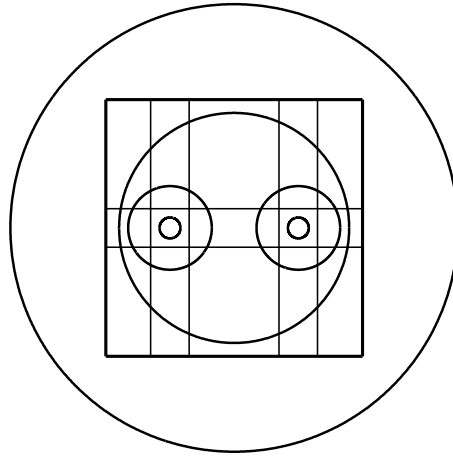


Figure 3.5: Cut through the domain decomposition for the computational domain Eq. (3.53).

In the inner spheres we use a log mapping for the radial coordinate. In the rectangular blocks, a combination of linear and logarithmic mappings is used similar to the 2D example in figure 3.2. In the outer sphere an inverse mapping is used which is well adapted to the fall-off behavior $\psi \sim 1 + ar^{-1} + \dots$ for large radii r . The outer radius of the outer spherical shell is chosen to be 10^9 or 10^{10} and a Dirichlet boundary condition $\psi = 1$ is used to approximate Eq. (3.54). For this particular problem, we could also place the outer boundary *at* infinity without impact on convergence or runtime. We did not do this, because more specialized analysis tools described in [53] currently require a finite outer radius⁴.

We now present two solutions with different sizes and locations of the excised spheres. In sections 3.4.2 to 3.4.2, we then discuss several topics including preconditioning and parallelization.

Equal sized spheres

First we choose two equal sized spheres with radii $r_1 = r_2 = 1$. The separation between the centers of the spheres is chosen to be 10, the outer radius of the outer

⁴One can also approximate (3.54) by a Robin boundary condition at smaller outer radius. This leads to slower convergence, probably because the preconditioning necessary for a Robin boundary condition is less effective in the stretched outer sphere.

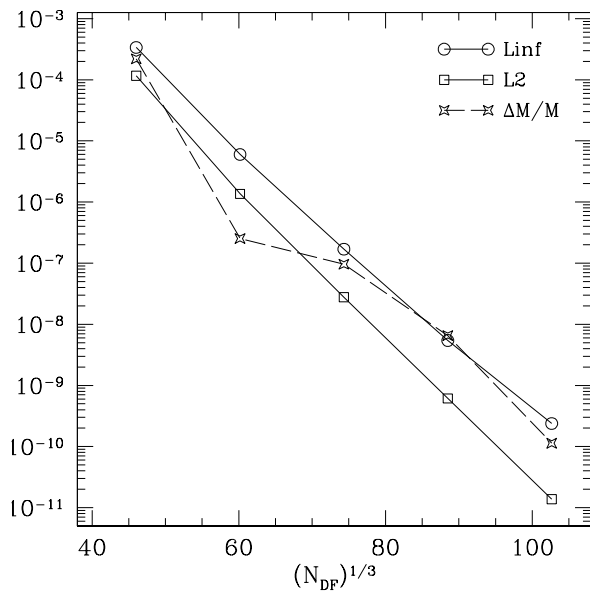


Figure 3.6: Convergence of solution of Eqs. (3.52)-(3.55) with radii of excised spheres $r_1 = r_2 = 1$ at separation 10. N_{DF} , L_{inf} , L_2 , M and ΔM are defined in the text immediately before and after Eq. (3.56).

sphere is 10^9 .

We solve equation (3.52) at several resolutions. The highest resolution uses 29^3 collocation points in each rectangular block, $29 \times 21 \times 42$ collocation points (radial, θ and ϕ directions) in the inner spherical shells and $29 \times 16 \times 32$ in the outer spherical shell. We use the difference in the solutions at neighboring resolutions as a measure of the error. We denote the pointwise maximum of this difference by L_{inf} and the root-mean-square of the grid point values by L_2 . We also compute at each resolution the quantity

$$M = -\frac{1}{2\pi} \int_{\infty} \frac{\partial \psi}{\partial r} d^2 S \quad (3.56)$$

which is the total mass of the binary black hole system. M will be needed in the comparison to a finite difference code below. The difference ΔM between M at neighboring resolutions is again a measure of the error of the solution.

Figure 3.6 shows the convergence of the solution ψ with increasing resolution. Since the rectangular blocks and the spheres have different numbers of collocation points, the cube root of the total number of degrees of freedom, $N_{DF}^{1/3}$ is used to label the x -axis. The exponential convergence is apparent. Because of the exponential convergence, and because Linf, L2 and ΔM utilize differences to the next lower

resolution, the errors given in figure 3.6 are essentially the errors of the next *lower* resolution. Note that at the highest resolutions the approximation of the outer boundary condition (3.54) by a Dirichlet boundary condition at finite outer radius 10^9 becomes apparent: If we move the outer boundary to 10^{10} , M changes by $2 \cdot 10^{-9}$ which is of order $1/10^9$ as expected.

On the coarsest resolution $\psi = 1$ is used as the initial guess. Newton-Raphson then needs six iterations to converge. On the finer resolutions we use the result of the previous level as the initial guess. These initial guesses are so good that one Newton-Raphson iteration is sufficient on each resolution.

Nonequal spheres — Different length scales

With the multidomain spectral method it is possible to distribute resolution differently in each subdomain. This allows for geometries with vastly different length scales. As an example, we again solve equations (3.52)-(3.55). The radii of the spheres are now $r_1 = 1$ and $r_2 = 0.05$, and the separation of the centers of the spheres is 100. The separation of the holes is thus 2000 times the radius of the smaller sphere. A finite difference code based on a Cartesian grid for this geometry would have to use adaptive mesh refinement.

With the spectral solver, we still use the domain decomposition depicted in figure 3.5, but now the inner radii of the two inner spherical shells are different. The outer boundary of the outer sphere is at 10^{10} . The number of collocation points in each subdomain is almost identical to the case with equal sized spheres of figure 3.6, except we add 8 additional radial collocation points to the shell around the small excised sphere. As before we solve on different resolutions and compute the norms of the differences of the solution between different resolutions, as well as of the total mass M . The results are shown in figure 3.7. The exponential convergence shows that the solver can handle the different length scales involved in this problem.

Preconditioning

The finite difference approximation \mathcal{A}_{FD} is initialized with the second derivative terms, the matching conditions in touching domains [cf. Eqs. (3.37d) and (3.37e)], and with a FD approximation of the Robin boundary condition Eq. (3.55). Running on a single processor, we could again define the preconditioner \mathcal{B} via an ILU

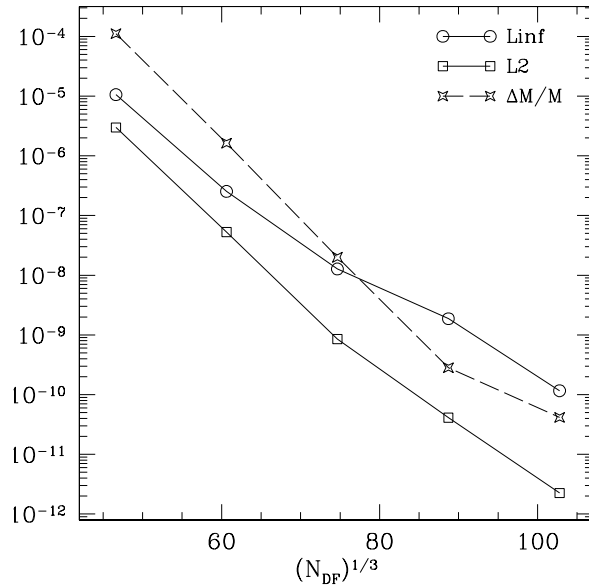


Figure 3.7: Convergence of solution of Eqs. (3.52)-(3.55) for excised spheres of radii $r_1 = 1$, $r_2 = 0.05$ at separation 100. Symbols as in Figure 3.6.

decomposition of \mathcal{A}_{FD} . However, when running on multiple processors, an ILU decomposition requires a prohibitive amount of communication, and block ASM preconditioning[54] with one block per processor becomes favorable. After considerable experimentation, we settled on an implicit definition of \mathcal{B} via its action on vectors. $\mathcal{B}\underline{\mathbf{v}}$ is *defined* to be the approximate solution $\underline{\mathbf{w}}$ of

$$\mathcal{A}_{FD}\underline{\mathbf{w}} = \underline{\mathbf{v}}. \quad (3.57)$$

Equation (3.57) is solved using a second, inner iterative solver, usually GMRES preconditioned with ILU (on a single processor) or a block ASM method (on multiple processors). The inner solver is restricted to a fixed number of iterations. Applying a fixed number of iterations of an iterative solver is *not* a linear operation, hence \mathcal{B} represents no longer a matrix, but a nonlinear operator. In the outer linear solve we therefore use FGMRES[55], a variant of GMRES that does not require that the preconditioner \mathcal{B} is linear. With this preconditioning the outer linear solver needs about 20 iterations to reduce the residual of the linear solve by 10^{-5} .

More inner iterations reduce the number of iterations in the outer linear solve, but increase the computations per outer iteration. We found the optimal number

of inner iterations to be between 15-20. In all the computations given in this paper we use 20 inner iterations, except for the 2-D example in Figure 3.4 where 10 inner iterations sufficed.

Multigrid

We also experimented with multigrid algorithms[40, 46] to improve the runtime. The potential for multigrid is fairly small, since the number of collocation points is so low. In this particular problem, an accuracy of better than 10^{-6} can be achieved with 17^3 grid points per domain, which limits multigrid to at most two coarse levels.

In addition it is not trivial to construct a restriction operator. The obvious and canonical choice for a restriction operator is to transform to spectral space, discard the upper half of the spectral coefficients, and transform back to real space on a coarser grid. This does not work here because the operator \mathcal{S} uses the boundary points of each subdomain to convey information about matching between subdomains and about boundary conditions. Since these boundary points are filled using different equations than the interior points, the residual will typically be *discontinuous* between boundary points of a subdomain and interior points. Information about discontinuities is mainly stored in the high frequency part of a spectral expansion and discarding these will thus result in a loss of information about matching between grids. However, the coarse grid correction of a multigrid algorithm is supposed to handle long wavelength modes of the solution. In our case these extend over several subdomains and thus information about matching is essential. Hence the simple approach of discarding the upper half of the frequencies discards the most vital parts of the information required by the coarse grid solver.

Thus one seems to be compelled to use a real space restriction operator. We examined straight injection[46] which performed fairly well. The execution speed was comparable to the preconditioning with an inner linear solve as described in section 3.4.2. Since we did not achieve a significant code speed-up, there was no reason to keep the increased complexity of the multigrid algorithm.

Comparison to a Finite Difference Code

The computational domain Eq. (3.53) is challenging for standard finite difference codes based on a regular Cartesian grids for two reasons:

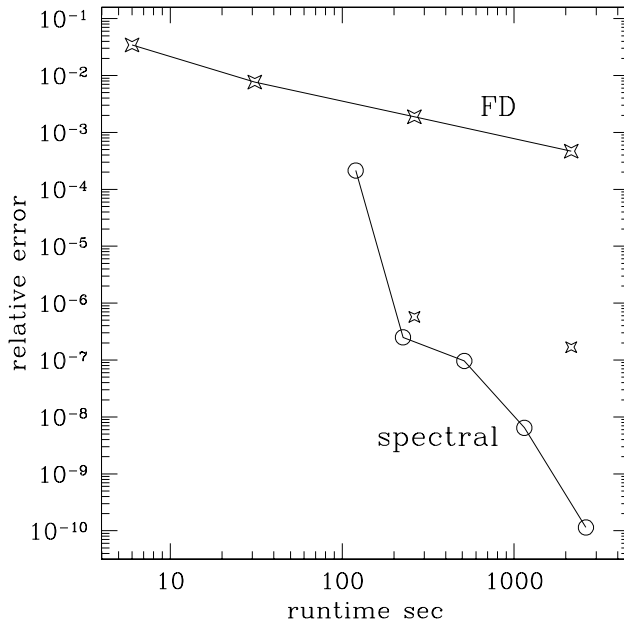


Figure 3.8: Comparison of runtime vs. achieved accuracy for the new spectral solver and the Cadéz code. Plotted is the achieved accuracy of the total mass M vs. runtime needed to solve Eqs. (3.52)-(3.55) for both codes.

1. The boundaries of the excised spheres do not coincide with coordinate boundaries, so complicated interpolation/extrapolation is needed to satisfy the boundary condition (3.55) (This problem led to a reformulation of the underlying physical problem without excised spheres[24]).
2. Resolving both the rapid changes close to the excised spheres *and* the fall-off behavior toward infinity requires a large number of grid points.

In [52] three different methods were developed to solve the boundary value problem (3.52)-(3.55). The best one turned out to be a finite difference code based on a specially adapted coordinate system, the so-called Cadéz coordinates. This code is an FAS-multigrid algorithm developed specifically for the differential equation (3.52). Care was taken that the truncation error is strictly even in grid-spacing h , thus allowing one to take two or three solutions at different resolutions and Richardson extrapolate to $h \rightarrow 0$. The Cadéz code is thus specially built for this equation in this geometry and it is unlikely that it can be significantly improved upon by any finite difference method.

On the other hand, our spectral solver is general purpose. The domain decomposition is not restricted to \mathbb{R}^3 with two excised spheres and we do not employ any specific optimizations for this particular problem.

We compare these two codes for the configuration with equal sized spheres. Figure 3.8 shows a plot of runtime vs. achieved accuracy for both codes. These runs were performed on a single RS6000 processor; the highest resolution runs needed about 1GB of memory. The solid line labeled FD represents the results of the finite difference code without Richardson extrapolation. This line converges quadratically in grid spacing. The two stars represent Richardson extrapolated values. The superiority of the spectral code is obvious. In accuracy, the spectral method outperforms even the finite difference code with Richardson extrapolation by orders of magnitude. Only very few finite difference codes allow for Richardson extrapolation, hence one should also compare the finite difference code without Richardson extrapolation to the spectral code: Then the *lowest* resolution of the spectral code is as accurate as the *highest* resolution of the finite difference code and faster by a factor of 20. Note also that the Cadéz code cannot handle excised spheres of very different sizes or spheres that are widely separated. In particular, it cannot be used for the configuration in section 3.4.2, which is readily solved by our method.

Parallelization

Most computations during a solve are local to each subdomain; the operator \mathcal{S} and the Jacobian \mathcal{J} need communicate only matching information across subdomains. The inner linear solve is a completely standard parallel linear solve with an explicitly known matrix \mathcal{A}_{FD} . The software package PETSc has all the necessary capabilities to solve this system of equations efficiently in parallel. Hence parallelization by distributing different subdomains to different processors is fairly straightforward.

However, different elements of the overall solve scale with different powers of the number of collocation points per dimension. If we denote the number of collocation points per dimension by N , the following scalings hold in three dimensions (the most interesting case): A spectral transform in a rectangular domain requires $\mathcal{O}(N^3 \log N)$ operations; the transform in a sphere—where no useful fast transform for the Legendre polynomials is available—requires $\mathcal{O}(N^4)$ operations; interpolation to *one* point is $\mathcal{O}(N^3)$, so interpolation to *all* $\mathcal{O}(N^2)$ boundary points

Table 3.1: Runtime and scaling efficiency. Three processors host one shell and n_1 blocks each, the remaining processors host n_2 blocks each. The last four columns refer to the Platinum cluster.

Nprocs			SP2		2 procs/node		1 proc/node	
	n_1	n_2	t[sec]	eff.	t[sec]	eff.	t[sec]	eff.
1			2344		1654		1654	
4	10	13	786	0.75	764	0.54	643	0.64
8	4-5	6	384	0.76	381	0.54	304	0.68
18	0	3			198	0.46	156	0.59
26	0	2			140	0.45	111	0.57
46	0	1			87	0.41	73	0.49

scales like $\mathcal{O}(N^5)$. Thus the optimal assignment of subdomains to processors is a function of N . Moreover, assignment of subdomains to processors is a discrete process — it is not possible to move an arbitrary fraction of computations from one processor to the another. One always has to move a whole subdomain with all the computations associated with it. This makes efficient load balancing difficult.

At high resolution, the $\mathcal{O}(N^5)$ interpolation consumes most of the runtime. Note that the outer spherical shell interpolates to 78 block surfaces, whereas the inner shells each interpolate to 6 block surfaces. These interpolations are parallelized by first distributing the data within each sphere to all processors. Then each processor interpolates a fraction of the points and the results are gathered again.

We present scaling results in table 3.1. These results were obtained on the SP2 of the physics department of Wake Forest University, and on NCSA’s Platinum cluster, whose nodes have two Intel Pentium processors each. The listed times are cumulative times for solving at five different resolutions, each solve using the next lower solution as initial guess. Not included in these times is the set up in which the code determines which subdomain is responsible for interpolating which “overlapping” boundary point. Also not included is input/output.

On the SP2 we achieve a scaling efficiency of 75%, whereas the Intel cluster has a lower scaling efficiency between around 54% (8 processors), and 41% (46 processors). Given all the limitations mentioned above these numbers are very encouraging.

Changing from serial to parallel execution degrades performance in two ways:

First, the ILU preconditioner used within the approximate inner linear solve is replaced by an overlapping block ASM preconditioner. Since this preconditioner is less efficient than ILU, the approximate inner linear solve is less accurate after its fixed number of iterations. Therefore the outer linear solve needs more iterations to converge to the required accuracy of 10^{-5} . The single processor code needs 19 outer linear iterations, whereas the parallel codes need 23 or 24. Thus the maximally achievable scaling efficiency is limited to $19/23 \approx 0.83$. The scaling efficiency on the SP2 is close to this limit.

The second reason for low scaling efficiency is that we have not optimized the MPI calls in any way. The fact that the scaling efficiency on the cluster is much better if only one processor per node is used, suggests that the MPI calls are a bottleneck. Using both processors on a node doubles the communication load on that node which doubles the waiting time for MPI communication. The higher scaling efficiency on the SP2 which has faster switches also suggests that the runs on the PC cluster are communication limited.

3.4.3 Coupled PDEs in nonflat geometry with excised spheres

So far we have been considering only PDEs in a single variable. However, the definition of the operator \mathcal{S} is not restricted to this case. In this section we present a solution of four coupled nonlinear PDEs. These equations are

$$\tilde{\nabla}^2 \psi - \frac{1}{8} \psi \tilde{R} - \frac{1}{12} \psi^5 K^2 + \frac{1}{8} \psi^{-7} \sum_{i,j=1}^3 \tilde{A}_{ij} \tilde{A}^{ij} = 0, \quad (3.58)$$

$$\tilde{\Delta}_L V^i - \frac{2}{3} \psi^6 \tilde{\nabla}^i K + \sum_{j=1}^3 \tilde{\nabla}_j \tilde{M}^{ij} = 0, \quad i = 1, 2, 3 \quad (3.59)$$

These equations are important for the binary black hole problem. The exact definitions of the various terms can be found in [53]. For this paper, only the following information is necessary: $\tilde{\nabla}^2$ is the Laplace operator on a nonflat three-dimensional manifold, hence Eq. (3.58) is an elliptic equation for ψ . $\tilde{\Delta}_L$ is a variant of the vector Laplacian, thus Eq. (3.59) is an elliptic equation for the vector $V^i, i = 1, 2, 3$. The variables \tilde{A}_{ij} and \tilde{A}^{ij} are functions of V^i , so that Eqs. (3.58) and (3.59) have to be solved simultaneously. The functions \tilde{R} , K and \tilde{M}^{ij} are given.

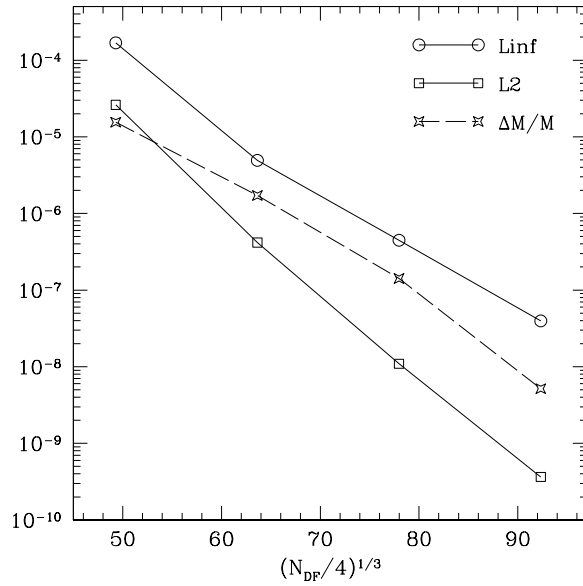


Figure 3.9: Convergence of solution to coupled PDEs (3.58) and (3.59). Definitions as in figure 3.6.

The computational domain again has two spheres $S_{1,2}$ excised,

$$\mathcal{D} = \mathbb{R}^3 - S_1 - S_2. \quad (3.60)$$

The radii of the excised spheres are $r_1 = r_2 = 2$ and the separation between the centers is 10.

We have Dirichlet boundary conditions on all boundaries:

$$\psi = 1, \quad (3.61)$$

$$V^i = 0, \quad i = 1, 2, 3. \quad (3.62)$$

We solve the problem again at several different resolutions. On the coarsest level two Newton-Raphson iterations are necessary, whereas the finer levels need only one Newton-Raphson iteration. The linear solver needs 30 iterations to reduce the residual by 10^5 . Details about constructing \mathcal{A}_{FD} for the nonflat differential operators $\tilde{\nabla}^2$ and $\tilde{\Delta}_L$ are given in appendix 3.8.

The convergence of the solutions is shown in figure 3.9. We again find smooth exponential convergence. Recall that the plotted quantities essentially give the error of the next lower resolution. Hence the next-to-highest resolution run with a total of $78^3 \approx 500000$ collocation points has a maximum pointwise error of

$\sim 0.5 \cdot 10^{-7}$. The wall clock time for that run is less than 2 hours on four RS 6000 processors.

This problem has also been attacked with a finite difference code[56]. The finite difference code required a runtime of 200 CPU hours (on 16 nodes of an Origin 2000). The accuracy of the finite difference code seems to be comparable to the lowest resolution solve of our spectral solver, which took 16 minutes CPU time. Compared to the finite difference code the spectral code is almost embarrassingly fast.

3.5 Improvements

The fact that spherical harmonics have fewer spectral coefficients than collocation points causes a host of complications. We have to solve for mixed real-spectral coefficients, Eq. (3.48). This complicates the operator \mathcal{S} , and severely complicates real space finite difference preconditioning. A double Fourier series[41] for the angular variables might be superior to the expansion in spherical harmonics, since this avoids the necessity for mixed real-spectral coefficients. Moreover one can then use fast transforms for both ϕ and θ which might improve runtime in the spherical shells.

We are working on cylinders as a third possible subdomain type. We also hope to use more general mappings that are no longer restricted to acting on each dimension separately.

In terms of pure runtime, one should try to optimize the interpolation to boundary points of overlapping subdomains. This is the part of the code that has the worst scaling with the number of unknowns. Replacing the explicit summation of the series by one of the faster methods discussed in [32] should speed up the code tremendously. As was seen in the discussion of parallelization in section 3.4.2, the code seems to be communication limited on a PC cluster. One should therefore also optimize the MPI calls. For example, one could overlap communication with subdomain internal computations.

Even without all these improvements our code is already very fast. This indicates the potential of our approach.

3.6 Conclusion

We have presented a new elliptic solver based on pseudo-spectral collocation. The solver uses domain decomposition with spherical shells and rectangular blocks, and can handle nonlinear coupled partial differential equations.

Our method combines the differential operator, the boundary conditions and matching between subdomains in *one* operator \mathcal{S} . The equation $\mathcal{S}\underline{\mathbf{u}} = 0$ is then solved with Newton-Raphson and an iterative linear solver. We show than one can employ standard software packages for nonlinear and linear solves and for preconditioning.

The operator \mathcal{S} has the added benefit that it is modular. Therefore adaption of the method to a new PDE or to new boundary conditions is easy; the user has only to code the differential operator and/or the new boundary conditions. We also discuss our treatment of mappings which decouples mappings from the actual code evaluating the differential operator, and from the code dealing with basis functions and details of spectral transforms. This modularity again simplifies extension of the existing code with e.g. new mappings.

We demonstrated the capabilities of the new method with three examples on non-simply-connected computational domains in two and three dimensions and with one and four variables. We also demonstrated that the domain decomposition allows for vastly different length scales in the problem. During the examples we discussed various practical details like preconditioning and parallelization. Two of these examples were real applications from numerical relativity. We found the spectral code at the *coarsest* resolution to be as accurate as finite difference methods, but faster by one to two orders of magnitude.

Acknowledgements

We thank Gregory Cook for helpful discussions. This work was supported in part by NSF grants PHY-9800737 and PHY-9900672 to Cornell University. Computations were performed on the IBM SP2 of the Department of Physics, Wake Forest University, with support from an IBM SUR grant, as well as on the Platinum cluster of NCSA.

3.7 Appendix A: Preconditioning of inverse mappings

In a subdomain with inverse mapping that extends out to (almost) infinity, the outermost grid points are distributed very unevenly in physical space. This causes finite-difference approximations of derivatives to fail if they are based on the physical coordinate positions. Therefore we difference in the collocation coordinate X and apply the mapping via Eq. (3.24). At the collocation grid point X_i with grid spacing $h_- = X_i - X_{i-1}$ and $h_+ = X_{i+1} - X_i$ we thus use

$$\left(\frac{\partial u}{\partial X}\right)_i = -\frac{h_+ u_{i-1}}{h_-(h_- + h_+)} + \frac{(h_+ - h_-)u_i}{h_+ h_-} + \frac{h_- u_{i+1}}{h_+(h_- + h_+)}, \quad (3.63)$$

$$\left(\frac{\partial^2 u}{\partial X^2}\right)_i = \frac{2u_{i-1}}{h_-(h_- + h_+)} - \frac{2u_i}{h_- h_+} + \frac{2u_{i+1}}{h_+(h_- + h_+)}, \quad (3.64)$$

$$\left(\frac{\partial^2 u}{\partial x^2}\right)_i = X_i'^2 \left(\frac{\partial^2 u}{\partial X^2}\right)_i + X_i'' \left(\frac{\partial u}{\partial X}\right)_i. \quad (3.65)$$

If one substitutes Eqs. (3.63) and (3.64) into (3.65), then the coefficients of u_{i-1} , u_i and u_{i+1} are the values that have to be entered into the FD-approximation matrix \mathcal{A}_{FD} .

Even with this trick, preconditioning of the radial derivatives in an extremely stretched outer sphere is not yet sufficiently good. The preconditioned Jacobian $\mathcal{B}\mathcal{J}$ still contains eigenvalues of size ~ 40 . The eigenmodes are associated with the highest radial mode in the outer sphere. We found that we can suppress these eigenvalues by damping this highest radial mode by a factor of 10 after the PETSc preconditioning is applied.

3.8 Appendix B: Preconditioning the nonflat Laplacian

In a nonflat manifold, the Laplace operator of Eq. (3.58) contains second and first derivatives of ψ ,

$$\tilde{\nabla}^2 \psi = \sum_{i,j=1}^3 g^{ij} \frac{\partial^2 \psi}{\partial x^i \partial x^j} + \sum_{i=1}^3 f^i \frac{\partial \psi}{\partial x^i}. \quad (3.66)$$

The coefficients g^{ij} and f^i are known functions of position. Since our particular manifold is almost flat, we have $g^{ii} \approx 1$, and $g^{ij} \approx 0$ for $i \neq j$. We base our preconditioning only on the diagonal part of (3.66),

$$\sum_{i=1}^3 g^{ii} \frac{\partial^2}{\partial x^{i2}}. \quad (3.67)$$

In rectangular blocks, Eq. (3.67) can be preconditioned without additional fill-in in \mathcal{A}_{FD} . Inclusion of the mixed second derivatives from Eq. (3.66) in \mathcal{A}_{FD} leads to a large fill-in of \mathcal{A}_{FD} . The increase in computation time due to the larger fill-in outweighs the improvement of convergence of the iterative solver in our problems.

For the spherical shells, matters are complicated by the fact that we use mixed real-space/spectral space coefficients [recall Eq. (3.48)]. It is easy to precondition the angular piece of the flat space Laplacian, since our basis functions Y_{lm} are the eigenfunctions of this operator. Derivative operators with angle-dependent coefficients lead to convolutions in spectral space and lead thus to a large fill-in in the preconditioning matrix. Therefore we can only precondition radial derivatives with coefficients that are *independent* of the angles θ, ϕ . We thus need to approximate Eq. (3.67) by a flat space angular Laplacian and constant coefficient radial derivatives. We proceed as follows.

In spherical coordinates Eq. (3.67) takes the form

$$\begin{aligned} \sum_{i=1}^3 g^{ii} \frac{\partial^2}{\partial x^{i2}} = & G^{\theta\theta} \frac{\partial^2}{\partial \theta^2} + G^{\phi\phi} \frac{\partial^2}{\partial \phi^2} + G^{rr} \frac{\partial^2}{\partial r^2} + G^{\theta\phi} \frac{\partial^2}{\partial \theta \partial \phi} \\ & + G^{\theta r} \frac{\partial^2}{\partial \theta \partial r} + G^{\phi r} \frac{\partial^2}{\partial \phi \partial r} + F^\theta \frac{\partial}{\partial \theta} + F^\phi \frac{\partial}{\partial \phi} + F^r \frac{\partial}{\partial r}. \end{aligned} \quad (3.68)$$

The various functions G and F are related to g^{ii} by standard Cartesian-to-polar coordinate transformations. These transformations are singular for $\theta = 0$ and $\theta = \pi$; however, no grid points are located on this axis. Moreover, only $G^{\theta\theta}$, G^{rr} and F^r will be used, and these three quantities are continuous at the pole. We compute $G^{\theta\theta}$, G^{rr} and F^r at each grid point. For each radial grid point r_i , we average over angles to obtain $\bar{G}_i^{\theta\theta}$, \bar{G}_i^{rr} and \bar{F}_i^r . Now precondition as if $\bar{G}_i^{\theta\theta}$ were part of an angular piece of the flat space Laplacian, i.e. enter $-l(l+1)\bar{G}_i^{\theta\theta}/r_i^2$ as the diagonal element belonging to the unknown \hat{u}_{ilm} . Further, precondition $\bar{G}_i^{rr} \partial^2/\partial r^2 + \bar{F}_i^r \partial/\partial r$ with finite differences as described in appendix 3.7. Ignore all other terms in Eq. (3.68).

The operator $\tilde{\Delta}_L$ in Eq. (3.59) is defined by

$$\tilde{\Delta}_L V^i \equiv \tilde{\nabla}^2 V^i + \frac{1}{3} \sum_{k=1}^3 \tilde{\nabla}^i \tilde{\nabla}_k V^k + \sum_{k=1}^3 \tilde{R}_k^i V^k, \quad (3.69)$$

$\tilde{\nabla}$ and \tilde{R}_{ij} being the covariant derivative operator and Ricci tensor associated with the metric of the manifold. $\tilde{\Delta}_L V^i$ contains thus the nonflat Laplace operator acting

on each component V^i separately, plus terms coupling the different components which involve second derivatives, too. We precondition only the Laplace operator $\tilde{\nabla}^2 V^i$ for each component V^i separately as described above and ignore the coupling terms between different components.

Chapter 4

Quasi-circular orbits for spinning binary black holes*

4.1 Introduction

The inspiral and coalescence of binary black hole systems is a prime target for upcoming gravitational wave detectors such as LIGO. Such systems will be circularized by the emission of gravitational waves, and will evolve through a quasi-equilibrium sequence of circular orbits. At the innermost stable circular orbit (ISCO) we expect a transition to a dynamically plunging orbit. It is anticipated that this transition will impart a characteristic signature on the gravitational waveform. It is therefore important to know the orbital frequency at the ISCO, since the corresponding gravitational wave frequency is predominantly just twice this frequency.

Predicting the waveform in detail from the transition at the ISCO to the final merger requires the full machinery of numerical relativity. These calculations require appropriate initial data. Out of the large space of solutions of the initial-value equations of general relativity, we need an algorithm to select solutions corresponding to black holes in quasi-circular orbits. The effective potential method [28] allows one to construct such solutions, and to determine the properties of the ISCO.

The effective potential is based on the fact that minimizing the energy of a system yields an equilibrium solution. This follows from the Hamiltonian equations of motion: If the Hamiltonian \mathcal{H} is minimized with respect to a coordinate q and a momentum p , then $\dot{q} = \partial\mathcal{H}/\partial p = 0$ and $\dot{p} = -\partial\mathcal{H}/\partial q = 0$. The energy of two objects in orbit about each other can be lowered by placing the objects at rest at their center of mass. Therefore minimizing the energy with respect to all coordinates and momenta will not yield a circular orbit. To find circular orbits in Newtonian gravity, one can minimize the energy while holding the angular momentum constant. This procedure works as well for a test-mass orbiting a Schwarzschild black hole, where one minimizes the ADM energy. This can be seen

*H. P. Pfeiffer, S. A. Teukolsky, and G. B. Cook, Phys. Rev. D **62**, 104018 (2000).

as follows. For geodesic motion, one finds [57]

$$\frac{1}{2}\dot{r}^2 + \frac{1}{2}\left(1 - \frac{2M}{r}\right)\left(\frac{\tilde{L}^2}{r^2} + 1\right) = \frac{1}{2}\tilde{E}^2. \quad (4.1)$$

Here M is the mass of the black hole, \tilde{E} is the energy per unit rest mass of the test-particle as seen from infinity and \tilde{L} its orbital angular momentum per unit rest mass. Denote the rest-mass of the test-particle by M' . Then the ADM energy is simply $E_{\text{ADM}} = M + \tilde{E}M'$, and minimizing E_{ADM} is equivalent to minimizing \tilde{E} . Hence minimizing the left hand side of (4.1) with respect to r yields the radius of circular orbits as a function of angular momentum. Minimization of (4.1) with respect to \dot{r} yields $\dot{r} = 0$, which is necessary for a circular orbit. From the minimum one finds the energy of the test-particle as a function of angular momentum. Obviously, one needs to keep M and M' constant during the minimization, so the prescription to compute circular orbits becomes: Minimize E_{ADM} while keeping the angular momentum and the rest masses constant.

These ideas have been formalized as variational principles for finding equilibria for rotating and binary stars in Newtonian gravity. There is also a similar variational principle for rotating stars in general relativity [58]. Binary systems in general relativity are not strictly in equilibrium because they emit gravitational waves. However, for orbits outside the innermost stable circular orbit, the gravitational radiation reaction time scale is much longer than the orbital period. It is therefore a good approximation to treat the binary as an equilibrium system.

In this paper we apply this minimization principle to rotating binary black hole systems. Let the masses of the holes be M_1 and M_2 , the spins be \mathbf{S}_1 and \mathbf{S}_2 , and the total angular momentum of the system be \mathbf{J} . We exploit the invariance under rescaling of the mass by using dimensionless quantities M_1/M_2 , \mathbf{S}_1/M_1^2 , \mathbf{S}_2/M_2^2 , and $\mathbf{J}/\mu m$, where $m = M_1 + M_2$ denotes the total mass and $\mu = M_1M_2/m$ the reduced mass. Then we adopt the following straightforward prescription to locate quasi-circular orbits: Minimize the scaled ADM energy E_{ADM}/m with respect to the separation of the holes, while keeping M_1/M_2 , \mathbf{S}_1/M_1^2 , \mathbf{S}_2/M_2^2 , and $\mathbf{J}/\mu m$ constant.

It is somewhat involved to carry out this simple prescription. The computation of the ADM energy becomes more difficult than for the Schwarzschild example above. More importantly, however, no rigorous definitions exist for the mass or spin of an individual black hole in a spacetime containing two black holes. We

will address these issues in Sec. 4.2. Ultimately, we must use numerical methods to generate and search among the solutions. Our numerical approach involves rootfinding, which is also described in Sec. 4.2.

In Sec. 4.3 we present the results of the effective potential method. For the interpretation of these results, we need to search for common apparent horizons in our binary black hole data sets. These results are included in Sec. 4.3, too. We discuss our results and conclusions in Secs. 4.4 and 4.5. The appendix contains details of the apparent horizon searches.

4.2 Implementation

In order to minimize the ADM energy while keeping M_1/M_2 , $\mathbf{J}/\mu m$, \mathbf{S}_1/M_1^2 and \mathbf{S}_2/M_2^2 constant, we need a method to compute the ADM energy as a function of angular momentum, masses and spins of the holes and separation. As a first step we construct initial data (γ_{ij}, K_{ij}) on a hypersurface as described in [27, 52, 28]. Our particular approach assumes conformal flatness of the 3-metric γ_{ij} , maximal embedding of the hypersurface, as well as inversion symmetry conditions on the 3-metric γ_{ij} and on the extrinsic curvature K_{ij} . The effective potential method is independent of these assumptions and works with all methods that compute initial data. For example, in [59], the effective potential method was used without assuming inversion symmetry. In particular, the assumptions of maximal embedding and conformal flatness are not essential but merely convenient—maximal embedding decouples the Hamiltonian and momentum constraints within the initial-data formalism we use, and conformal flatness allows for an analytic solution of the momentum constraints. One disadvantage of conformal flatness is that Kerr black holes do not admit conformally flat 3-metrics, at least for the simple time slicings we are aware of. In [60] it was shown that the Kerr metric is not conformally flat at second order in the spin parameter S/M^2 . Indeed, in Sec. 4.3.1 we identify this deviation in our results.

Because we assume that the initial hypersurface is maximal, the momentum and Hamiltonian constraints decouple. We follow the Bowen and York [22] prescription to solve the momentum constraint analytically. Then we need only solve one three-dimensional quasi-linear elliptic differential equation, the Hamiltonian constraint. It is solved on a so-called Čadež grid using a multigrid algorithm[52]. The constructed data sets depend on several input parameters, namely the radii

and the positions of the throats of the holes in the flat background space, a_i and \mathbf{C}_i , $i = 1, 2$, respectively, and their linear momenta and spins, \mathbf{P}_i and \mathbf{S}_i , $i = 1, 2$, respectively. We note that in this initial-data prescription, \mathbf{P}_i and \mathbf{S}_i represent the *physical* linear and angular momentum of the black hole if it is isolated. We work in the zero momentum frame, where $\mathbf{P}_2 = -\mathbf{P}_1$, and choose \mathbf{P}_i perpendicular to $\mathbf{C}_2 - \mathbf{C}_1$ in order to realize a circular orbit. Then the magnitude $P \equiv P_1 = P_2$ is sufficient to describe the linear momenta. Choosing a_1 as the fundamental length scale, we are left with the following dimensionless input parameters: the ratio of the throat radii $\alpha = a_1/a_2$, the dimensionless background separation $\beta = |\mathbf{C}_1 - \mathbf{C}_2|/a_1$, and the dimensionless linear momentum and spins, P/a_1 and \mathbf{S}_i/a_1^2 , $i = 1, 2$, respectively.

From the initial data we can rigorously compute the ADM energy E_{ADM} , the total angular momentum \mathbf{J} and the proper separation between the apparent horizons of each hole, ℓ . The total angular momentum is evaluated as in Ref. [28]:

$$\mathbf{J} \equiv (\mathbf{C}_1 - \mathbf{O}) \times \mathbf{P}_1 + (\mathbf{C}_2 - \mathbf{O}) \times \mathbf{P}_2 + \mathbf{S}_1 + \mathbf{S}_2. \quad (4.2)$$

Here \mathbf{O} represents the point about which the angular momentum is defined; it drops out immediately because $\mathbf{P}_1 = -\mathbf{P}_2$. When orbiting black holes have spin, neither the individual spins of the holes nor their orbital angular momentum \mathbf{L} are rigorously defined. We simply take \mathbf{L} to be defined by

$$\mathbf{L} \equiv \mathbf{J} - \mathbf{S}_1 - \mathbf{S}_2, \quad (4.3)$$

with \mathbf{S}_1 and \mathbf{S}_2 defining the individual spins.

Finally, we need to define the masses of the individual holes. As in Ref. [28], we define the mass of each hole via the Christoudoulou formula:

$$M_i^2 = M_{ir,i}^2 + \frac{S_i^2}{4M_{ir,i}^2}, \quad (4.4)$$

$$M_{ir,i}^2 = \frac{A_i}{16\pi}, \quad (4.5)$$

where A_i is the area of the event horizon of the i^{th} hole. Clearly this definition is only rigorous for a stationary spacetime. Moreover, we cannot locate the event horizon from the initial data slice alone. Therefore we must resort to using the apparent horizons areas in equations (4.4) and (4.5) instead. Apparent horizons can be determined from initial data and in the present case their positions are known

to coincide with the throats of the holes [27]. For a stationary spacetime, apparent horizons and event horizons coincide, and in a general, well-behaved spacetime, the event horizon must coincide with or lie outside of the apparent horizon. In the latter case we will underestimate the mass of the black hole by using the apparent horizon area. Some of the results of this work indicate that this happens for very small separations of the holes.

With the individual masses we can finally define the *effective potential* as the non-dimensional binding energy of the system:

$$\frac{E_b}{\mu} \equiv (E_{\text{ADM}} - M_1 - M_2)/\mu. \quad (4.6)$$

Since the mass-ratio M_1/M_2 is kept constant during the minimization, minimizing E_b/μ is equivalent to minimizing E_{ADM}/m .

We construct initial data sets starting from the *input* parameters α , β , P/a_1 and \mathbf{S}_i/a_1^2 , and compute the *physical* parameters E_b/μ , M_1/M_2 , $J/\mu m$ and \mathbf{S}_i/M_i^2 . In order to construct an initial data set with certain physical parameters we have to choose the input parameters appropriately. This requires nonlinear rootfinding.

Within our effective potential approach, we will search for minima in the binding energy as a function of the separation of the black holes. Fortunately, it is not necessary to solve for a specific proper separation ℓ/m . It is sufficient to keep β constant during rootfinding and thus find a binary black hole configuration with some separation ℓ/m . Our goal is to solve the following set of equations [cf. Eqns. (10a-d) of Ref. [28]]:

$$\frac{M_1}{M_2} = \left[\frac{M_1}{M_2} \right] \quad (4.7a)$$

$$\frac{S_1}{M_1^2} = \left[\frac{S_1}{M_1^2} \right] \quad (4.7b)$$

$$\frac{S_2}{M_2^2} = \left[\frac{S_2}{M_2^2} \right] \quad (4.7c)$$

$$\frac{J}{\mu m} = \left[\frac{J}{\mu m} \right]. \quad (4.7d)$$

The bracketed quantities on the right hand sides of (4.7a-4.7c) denote the physical values to be reached, and the expressions on the left-hand side represent functions of the background parameters α , P/a_1 , S_1/a_1^2 and S_2/a_1^2 as well as the fixed β .

For non-rotating holes, equations (4.7b) and (4.7c) are trivially satisfied by $S_1 = S_2 = 0$. For spinning holes this is no longer the case. Hence, it seems one has

to solve the complete set of Eqns. (4.7a–4.7d). However, in any initial data scheme where the physical spins of the black holes are directly parameterized, Eqns. (4.7b) and (4.7c) can be eliminated. First, we note again that if the physical spins are directly parameterized, from Eqn. (4.3) we find that we can replace rootfinding in $J/\mu m$ by rootfinding in $L/\mu m$. Thus Eqn. (4.7d) is replaced by

$$\frac{L}{\mu m} = \left[\frac{L}{\mu m} \right]. \quad (4.8)$$

In the zero momentum frame, Eqns. (4.2) and (4.3) simplify to

$$\frac{L}{a_1^2} = \beta \frac{P}{a_1}. \quad (4.9)$$

Thus we can rewrite S_1 as

$$\frac{S_1}{a_1^2} = \frac{S_1}{M_1^2} \cdot \frac{M_1}{M_2} \cdot \frac{M_1 M_2}{L} \cdot \beta \frac{P}{a_1}. \quad (4.10)$$

For a solution of Eqns. (4.7a–4.7c,4.8), the first three terms on the right hand side of (4.10) take the values of the desired physical parameters, so we can replace them by these parameters throughout the rootfinding. A similar result holds for S_2 . We perform only two-dimensional rootfinding, in α and P/a_1 , and set in each iteration

$$\frac{S_1}{a_1^2} = \left[\frac{S_1}{M_1^2} \right] \left[\frac{M_1}{M_2} \right] \left[\frac{L}{\mu m} \right]^{-1} \beta \frac{P}{a_1}, \quad (4.11a)$$

$$\frac{S_2}{a_1^2} = \left[\frac{S_2}{M_2^2} \right] \left[\frac{M_1}{M_2} \right]^{-1} \left[\frac{L}{\mu m} \right]^{-1} \beta \frac{P}{a_1}. \quad (4.11b)$$

For an important subset of spin configurations, even one-dimensional rootfinding is sufficient as can be seen as follows: Consider equal-sized holes with equal spin magnitudes on both holes. If both spins are parallel to the orbital angular momentum, or both spins are antiparallel, there exists a symmetry under exchange of the two holes. Therefore α must be equal to 1 and we are left with one free parameter, P/a_1 . If one spin is parallel to the orbital angular momentum and the other spin is antiparallel, however, this property is lost. One hole is co-rotating with the orbital motion and the other hole is counter-rotating. The choice $\alpha = 1$ would result in holes with slightly different masses. We thus need two-dimensional rootfinding in α and P/a_1 for this case.

Each “function evaluation” for the rootfinding involves the computation of an initial data set (γ_{ij}, K_{ij}) . High resolution solutions take between 30 minutes and

several hours of CPU time on one RS6000 processor. For maximum efficiency, we first perform rootfinding with a Newton-Raphson method[46] on low resolution data sets. The numerical values for M_1/M_2 and $J/\mu m$ differ slightly between low resolution and high resolution solutions, therefore we solve on low resolution for adjusted values of $[M_1/M_2]$ and $[J/\mu m]$. With the input parameters found in the low resolution rootfinding, a high resolution computation is performed to verify that equations (4.7a) and (4.7d) are indeed satisfied at high resolution, and to adjust the offset used in the next low resolution rootfinding. If necessary, this procedure is repeated. On average each complete rootfinding takes fewer than two high resolution computations.

Following our prescription, we now minimize the binding energy with respect to separation while keeping M_1/M_2 , $L/\mu m$ and \mathbf{S}_i/M_i^2 constant. The binding energy of a sequence of solutions with these quantities held constant represents a contour of the effective potential. Our code starts at large separation β and reduces β until a minimum in E_b/μ is bracketed. Then the minimum is located with Brent's method [46], yielding a quasi-circular orbit for the prescribed values of $J/\mu m$, M_1/M_2 , and \mathbf{S}_i/M_i^2 . Note that each computation of E_b/μ during the minimization along an effective potential contour requires rootfinding.

By computing quasi-circular orbits for different $J/\mu m$, but fixed M_1/M_2 and \mathbf{S}_i/M_i^2 , a *sequence* of quasi-circular orbits is obtained. A binary black hole that radiates away energy and angular momentum will follow such a sequence approximately, assuming that the spin on each hole remains constant. We step towards smaller $J/\mu m$, and compute only as many points along each effective potential contour as are required for the minimization. As soon as we do not find a minimum in the effective potential contours anymore we expect to be beyond the innermost stable circular orbit. We trace out some complete effective potential contours around the last value of $J/\mu m$ to check the behavior of these curves.

Finally, from the binding energy E_b/μ and the angular momentum $J/\mu m$ along the sequence, we compute the orbital angular frequency as

$$\Omega = \left. \frac{\partial E_b}{\partial J} \right|_{\text{sequence}} \quad (4.12)$$

4.3 Results

The parameter space of spinning binary black holes is large – one can vary the mass ratio of the holes as well as spin directions and magnitudes. Astrophysically

most interesting are holes that co-rotate with the orbital motion, i.e. with both spins \mathbf{S}_i parallel to the orbital angular momentum \mathbf{L} . In addition to these co-rotating configurations, we examine configurations with one co-rotating hole and one counter-rotating hole, and configurations with two counter-rotating holes. We have the following three families of sequences:

- The “++ sequences” with two co-rotating holes.
- The “+- sequences” with one co-rotating and one counter-rotating hole.
- The “-- sequences” with two counter-rotating holes.

We restrict ourselves to equal mass holes, $M_1 = M_2 \equiv M$ with equal spin magnitudes $S_1 = S_2 \equiv S$. As we will see, the assumption of conformal flatness becomes questionable at high spins, so we consider only spin magnitudes $S/M^2 \leq 0.50$. We denote a spin configuration by two plus or minus signs together with a number specifying the spin magnitude on the holes. Thus “++0.25” denotes a configuration with two co-rotating holes and spin magnitudes $S_1/M^2 = S_2/M^2 = 0.25$.

Quasi-circular orbits were computed for various values of $J/\mu m$ along each sequence. In Fig. 4.1 the binding energy E_b/μ along each sequence is plotted as a function of the angular momentum $J/\mu m$. A binary black hole that loses energy and angular momentum through gravitational radiation moves along such a sequence if the spins of the individual holes remain constant. The dashed lines in Fig. 4.1 represent the results of (post)²-Newtonian theory which we describe in Sec. 4.3.1.

Using equation (4.12) we compute the orbital angular frequency. In Figs. 4.2 and 4.3, the binding energy and the angular momentum along the sequences are plotted as a function of orbital frequency.

4.3.1 Behavior at large separations

We compare our results to the (post)²-Newtonian expansions for spinning holes in quasi-circular orbit that were kindly provided by L. Kidder. The expressions for arbitrary spins and masses are lengthy. If one restricts attention to equal-mass holes, $M_1 = M_2 = M$, $m = 2M$, $\mu = M/2$, it turns out that only the *sum* of the spins enters the (post)²-Newtonian expansions. In terms of

$$\mathbf{s} \equiv \frac{\mathbf{S}_1 + \mathbf{S}_2}{M^2}, \quad (4.13)$$

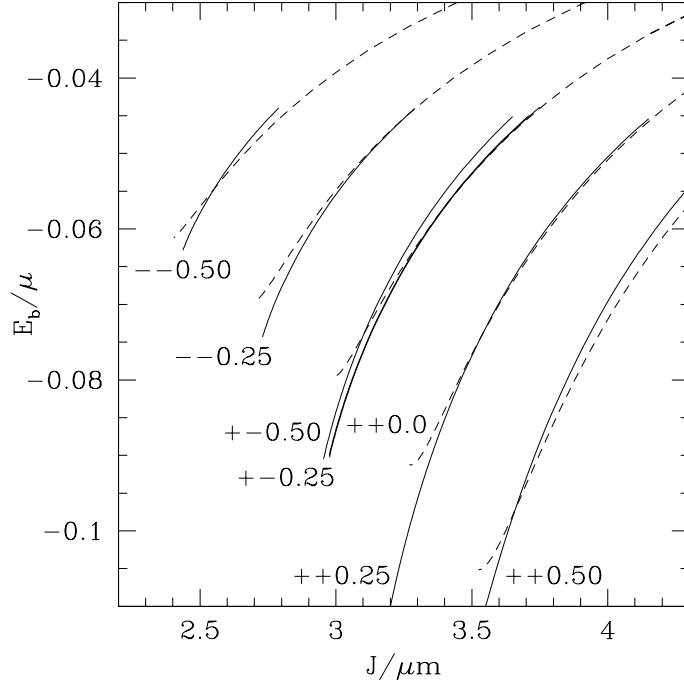


Figure 4.1: Sequences of quasi-circular orbits for different spin configurations. Plotted is the binding energy E_b/μ vs. the angular momentum $J/\mu m$ along the sequences. The solid lines represent the data, the dashed lines are the results based on $(\text{post})^2$ -Newtonian theory. As discussed later in this paper, the effective potential method could not locate an ISCO for the $++0.25$ and $++0.50$ sequences, although we believe each sequence should terminate in one.

and with $\hat{\mathbf{L}}$ being the unit-vector parallel to \mathbf{L} , the $(\text{post})^2$ -Newtonian expansions become

$$\frac{E_b}{\mu} = -\frac{1}{2}(m\Omega)^{2/3} \left\{ 1 - \frac{37}{48}(m\Omega)^{2/3} + \frac{7}{6}(\hat{\mathbf{L}} \cdot \mathbf{s})(m\Omega) - \left(\frac{1069}{384} + \frac{1}{8} [3(\hat{\mathbf{L}} \cdot \mathbf{s})^2 - \mathbf{s}^2] \right) (m\Omega)^{4/3} \right\}, \quad (4.14a)$$

$$\left(\frac{J}{\mu m} \right)^2 = (m\Omega)^{-2/3} \left\{ 1 + 2(\hat{\mathbf{L}} \cdot \mathbf{s})(m\Omega)^{1/3} + \left(\frac{37}{12} + \mathbf{s}^2 \right) (m\Omega)^{2/3} + \frac{1}{6}(\hat{\mathbf{L}} \cdot \mathbf{s})(m\Omega) + \left(\frac{143}{18} - \frac{37}{24}(\hat{\mathbf{L}} \cdot \mathbf{s})^2 - \frac{7}{8}\mathbf{s}^2 \right) (m\Omega)^{4/3} \right\}. \quad (4.14b)$$

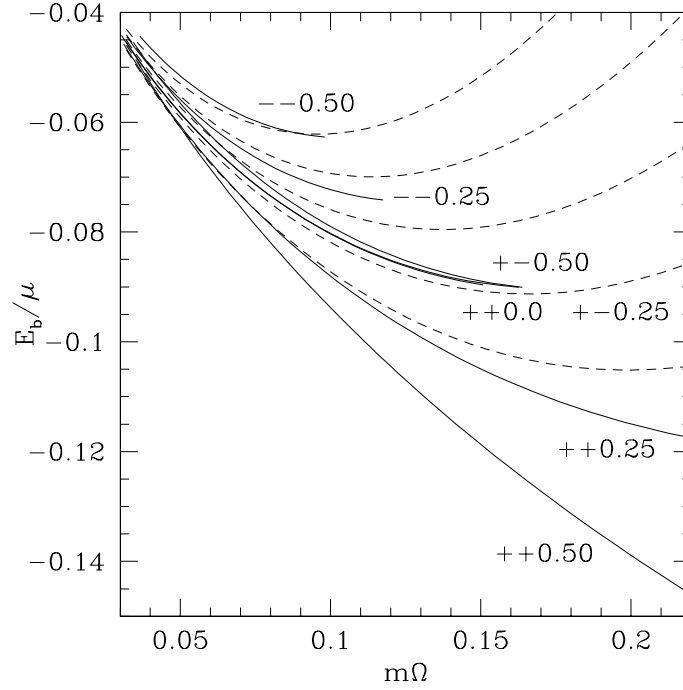


Figure 4.2: Sequences of quasi-circular orbits for different spin configurations. Plotted is the binding energy E_b/μ vs. the orbital angular frequency $m\Omega$ along the sequences. The solid lines represent the data, the dashed lines are the results based on $(\text{post})^2$ -Newtonian theory. As discussed later in this paper, the effective potential method could not locate an ISCO for the $++0.25$ and $++0.50$ sequences, although we believe each sequence should terminate in one.

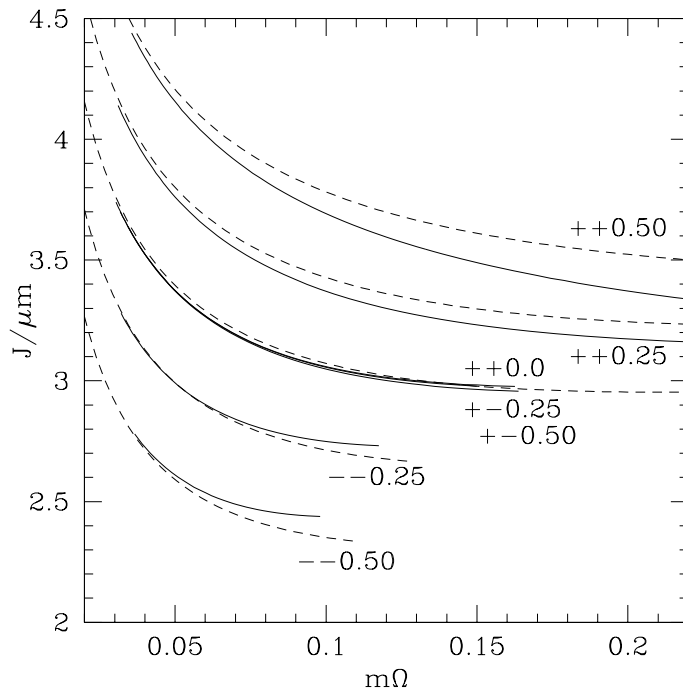


Figure 4.3: Sequences of quasi-circular orbits for different spin configurations. Plotted is the angular momentum $J/\mu m$ vs. the orbital angular frequency $m\Omega$ along the sequences. The solid lines represent the data, the dashed lines are the results based on $(\text{post})^2$ -Newtonian theory. As discussed later in this paper, the effective potential method could not locate an ISCO for the $++0.25$ and $++0.50$ sequences, although we believe each sequence should terminate in one.

These expressions are plotted in Figs. 4.1–4.3 together with our results from the effective potential method. There is remarkable agreement.

The sum $\mathbf{S}_1 + \mathbf{S}_2$ is zero for all $+ -$ sequences with equal spin magnitudes, so $(\text{post})^2$ -Newtonian theory predicts that the $+ -$ sequences are identical to the non-rotating sequence. This is remarkable, and indeed, in Figs. 4.1–4.3 the $+ -$ sequences are close to the $++0.0$ sequence. However, a closer look reveals a systematic behavior from which we can gain some insight into our assumptions. For fixed angular momentum $J/\mu m$, consider the difference in binding energy between a point on a $+ -$ sequence and a point on the non-rotating 0.0 sequence,

$$\Delta E_b/\mu(S) = \frac{E_b}{\mu}(+-S) - \frac{E_b}{\mu}(0). \quad (4.15)$$

In Fig. 4.4, $\Delta E_b/\mu(S)$ is plotted as a function of spin for several values of an-

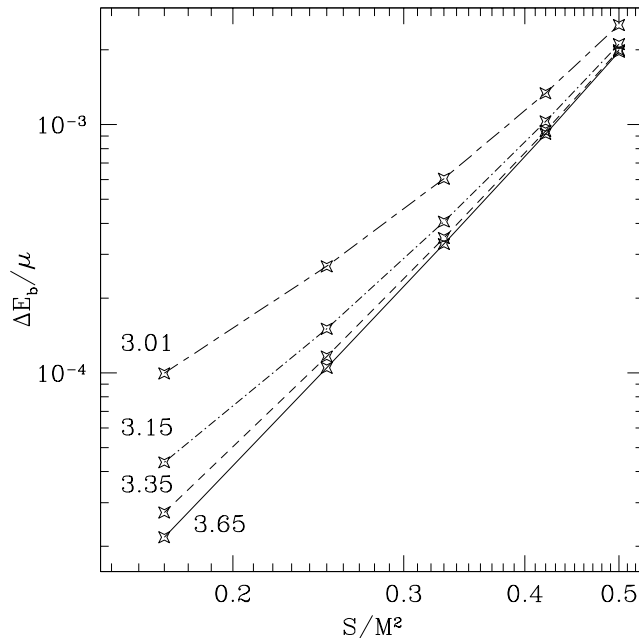


Figure 4.4: Difference in binding energy $\Delta E_b/\mu$ between $+-$ sequences and non-rotating sequence as a function of spin of the $+-$ sequence for fixed angular momentum $J/\mu m$. Each curve is labeled by its value of $J/\mu m$. $J/\mu m = 3.01$ is very close to the ISCOs that have $J/\mu m \approx 2.98$. $J/\mu m = 3.65, 3.35, 3.15$ and 3.01 correspond to a separation of $\ell/m \approx 12.3, 9.6, 7.7$ and 6.1 , respectively.

gular momentum $J/\mu m$. $\Delta E_b/\mu$ varies as the fourth power of spin. This might be a physical effect beyond (post)²-Newtonian expansions, but for the following reason it seems likely that one of our assumptions introduces a non-physical contribution to $\Delta E_b/\mu$, too. Figure 4.4 strongly suggests that $\Delta E_b/\mu$ is converging to a non-zero value as $J/\mu m$ (and thus separation) increase, indicating that there is a contribution to ΔE_b that is independent of the separation of the holes. For all spin configurations, E_b must approach zero in the limit of large separation, therefore any physical contribution to ΔE_b should decrease with separation. Moreover, a coupling between the holes, physical or unphysical, will give rise to a separation-dependent contribution to $\Delta E_b/\mu$. Therefore the separation-independent contribution must be a non-physical effect due to properties of each *isolated* hole. A likely candidate is the underlying assumption of conformal flatness. At large separations each hole should resemble a Kerr black hole, which is *not* conformally flat.

Since the Kerr metric is the unique stationary state for a spinning black hole,

if the conformally flat initial data for a single hole were evolved, the metric would relax to the Kerr metric and emit some gravitational radiation. Therefore the total energy contained in our initial data slices is larger than in a more faithful conformally non-flat data slice and $\Delta E_b/\mu$ should be positive, which it indeed is.

We conclude that at large separations ΔE_b is contaminated by an unphysical contribution because of the conformal flatness assumption. At small separation there might be additional physical contributions beyond the (post)²-Newtonian order.

4.3.2 Behavior at small separations – ISCO

In this section we report the key results of this work – the spin dependence of the innermost stable circular orbit. As we will see, the interpretation of our data at small separations is somewhat complicated. At large separations, the assumptions and approximations we have used are reasonable, except for the assumption of conformal flatness when the holes are spinning. At small separations, the interaction between the two black holes becomes relatively strong, and our approximations begin to break down. Near the ISCO, we must evaluate the quality of our assumptions to determine how reliable our results are.

In the neighborhood of each tentative ISCO, we compute a set of complete effective potential contours. These are shown in Fig. 4.5. In each plot, the binding energy E_b/μ is shown as a function of separation ℓ/m for several different values of angular momentum $J/\mu m$. Also plotted is the sequence of quasi-circular orbits passing through the minima of the effective potential. Figure 4.5 shows the non-rotating sequence ++0.0, one example each of a -- and a +- sequence, and three ++ sequences with different spin magnitudes.

Examining the constant J contours of the effective potential for *fixed* spin configurations, we find that they fall into three regimes separated by critical values that we will label J_A and J_B . Contours with $J > J_A$ exhibit a single minimum positioned at large separation ℓ/m . This minimum moves inward as the angular momentum decreases, i.e. the holes approach each other as angular momentum and energy are radiated away. We call this the “outer” minimum. As J passes through the critical value J_A , a new “inner” minimum appears inside the outer minimum. In this region, contours of the effective potential have two minima separated by a local maximum. The maximum corresponds to the well known unstable circular

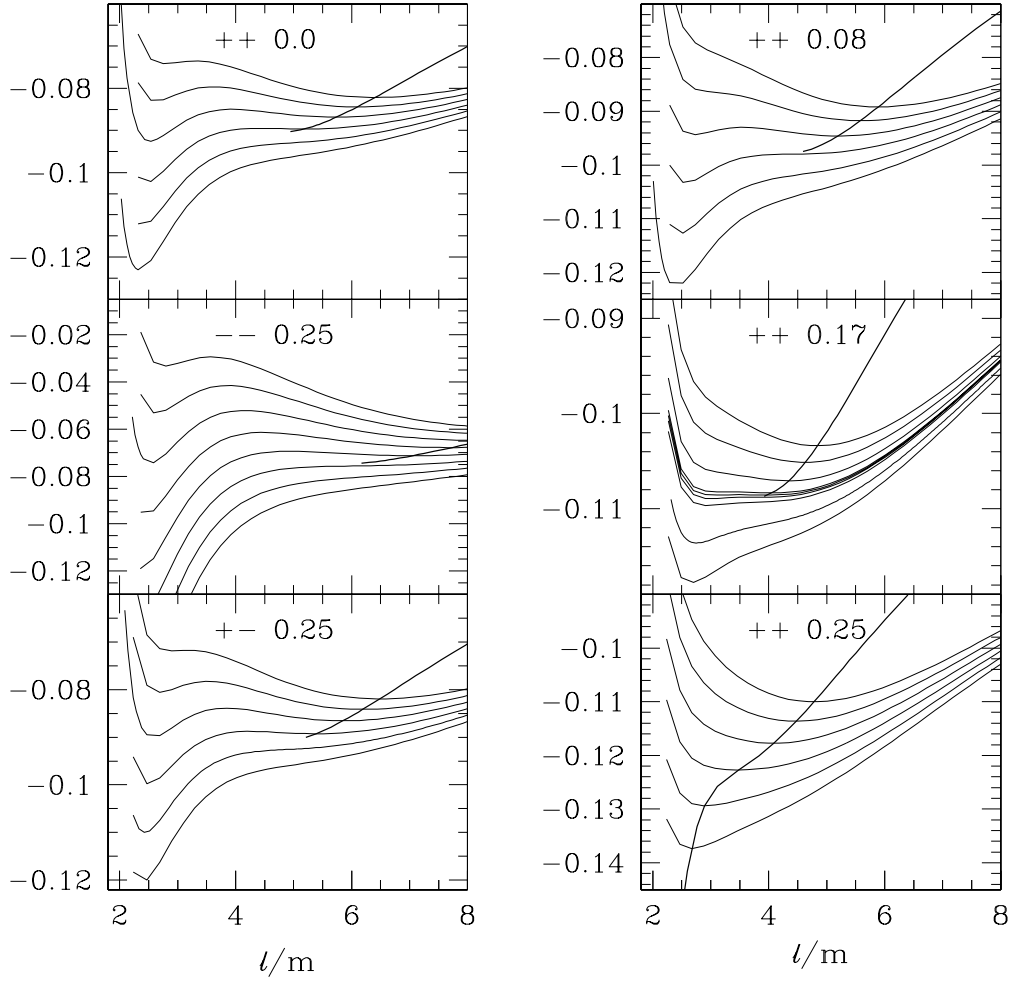


Figure 4.5: Constant $J/\mu m$ contours of the effective potential E_b/μ as a function of separation ℓ/m for various spin configurations. The curves are spaced in steps of $\Delta J/\mu m = 0.02$ except for the $--0.25$ and the $++0.17$ configurations, which have steps of 0.04 and 0.01, respectively. Also plotted is the sequence of quasi-circular orbits connecting the minima of the effective potential.

orbit of a Schwarzschild black hole. As J decreases further, $J_A > J > J_B$, the maximum moves outward whereas the outer minimum continues to move inward – the quasi-circular orbit associated with the outer minimum continues to shrink. As J passes through the second critical value J_B the outer minimum and the maximum meet in an inflection point and disappear. The quasi-circular orbit associated with the outer minimum disappears and this inflection point is identified with the ISCO. For $J < J_B$, only the inner minimum remains.

This behavior for the non-rotating sequence was already found in [28]. There, the inner minimum was dismissed as unphysical, since the underlying assumptions become weaker at small separations of the holes, and since a common event horizon might form. We will discuss this “unphysical” region and the possibility and consequences of the formation of a common event horizon below. But first we continue discussing the behavior of the effective potential for different spin configurations.

As we increase the spin magnitude for the $--$ configurations, the two critical angular momentum values J_A and J_B move away from each other. We see a more pronounced local maximum and the E_b curves look similar to the effective potential of Schwarzschild for a larger interval of angular momenta. The ISCO moves outward to larger separations as spin increases.

Conversely, as we increase the spin magnitude for the $++$ configurations the interval (J_B, J_A) , where two minima and a local maximum exist becomes smaller. Slightly above $S/M^2 = 0.17$, J_A and J_B merge and for $S/M^2 \gtrsim 0.17$, the regime with two minima and a maximum is *not* present. Figure 4.6 illustrates the small interval (J_B, J_A) with an enlargement of the $++0.17$ sequence. As long as the regime with two minima and a maximum is present, we can still define the ISCO by the inflection point. It moves towards smaller separation of the holes as the spin is increased. However, since the inflection point ceases to exist at some spin magnitude, we cannot define an ISCO for all S/M^2 . Therefore the $++$ sequences displayed in Figs. 4.1–4.3 do not terminate. Furthermore, we need a more careful analysis to determine whether the ISCO properties for spin magnitudes close to the critical value $S/M^2 \approx 0.17$ are reliable.

The $+ -$ configurations are very similar to the non-rotating one. Given the weak dependence on spin within the $+ -$ sequences, this is not surprising. We do not consider the $+ -$ configurations further.

Figure 4.7 and Table 4.1 summarize the orbital parameters at the ISCO as a function of spin for the $--$ sequences and the $++$ sequences. The numerical

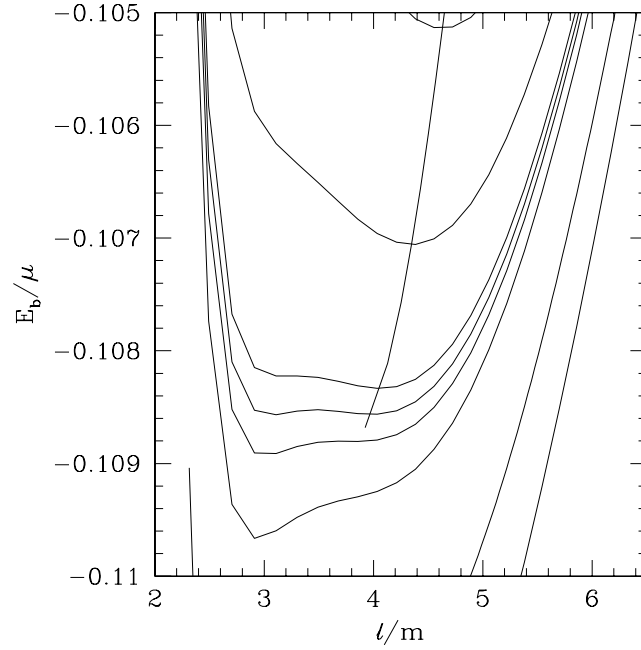


Figure 4.6: Enlargement of the ++0.17 sequence of Fig. 4.5. The displayed effective potential contours (top to bottom) correspond to angular momenta $J/\mu m = 3.12, 3.11, 3.104, 3.103, 3.102, 3.10, 3.09$ and 3.08 . Also shown is the sequence of quasi-circular orbits.

Table 4.1: Orbital parameters of the innermost stable circular orbit for equal-mass spinning holes. The second through sixth columns give the data obtained in this work, the three columns to the right give the data for a test mass orbiting a Kerr black hole. The results for the ++0.08 and ++0.17 sequences will have larger systematic errors than the other cases (see text).

Sequence	ℓ/m	E_b/μ	$m\Omega$	$J/\mu m$	$L/\mu m$	E_b/μ	$L/\mu m$	$m\Omega$
--0.50	7.05	-0.0628	0.100	2.438	3.438	-0.04514	3.8842	0.04935
--0.37	6.68	-0.0687	0.107	2.595	3.335	-0.04767	3.7834	0.05319
--0.25	6.17	-0.0743	0.120	2.730	3.230	-0.05032	3.6856	0.05727
--0.12	5.58	-0.0815	0.139	2.865	3.105	-0.05363	3.5738	0.06242
++0.0	4.94	-0.0901	0.166	2.976	2.976	-0.05719	3.4641	0.06804
++0.08	4.59	-0.0975	0.186	3.042	2.882	-0.05991	3.3870	0.07237
++0.17	3.93	-0.1087	0.235	3.103	2.763	-0.06337	3.2957	0.07793

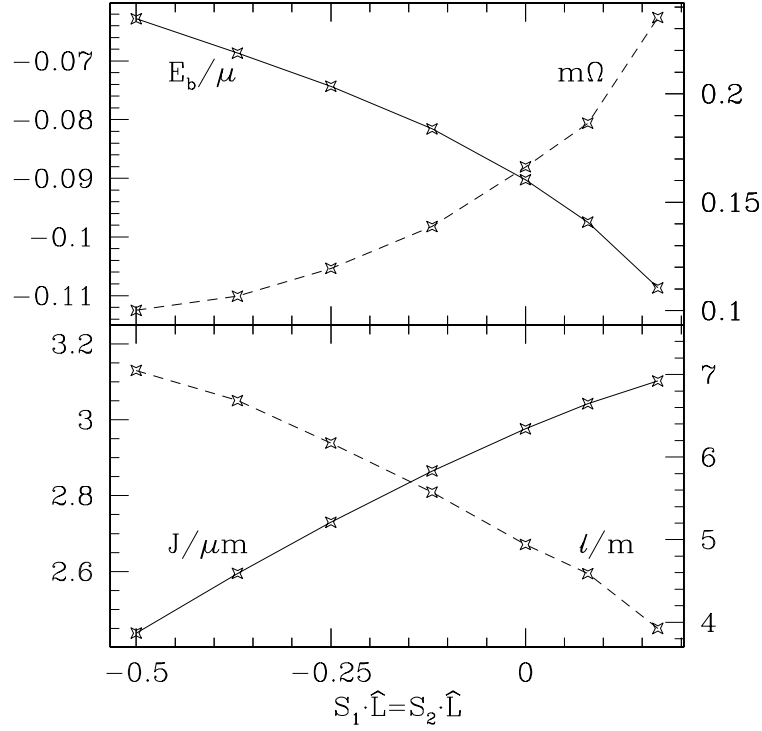


Figure 4.7: Values of several physical parameters at the ISCO of the $++$ and $--$ sequences. Plotted are the binding energy E_b/μ , the orbital angular frequency $m\Omega$, the total angular momentum $J/\mu m$ and the proper separation between the holes, ℓ/m as a function of spin S/M^2 on the holes. The $++$ sequences are plotted along the positive part of the horizontal axis, the $--$ sequences along the negative part as $-S/M^2$. The vertical axes on the left side belong to E_b/μ and $J/\mu m$.

Table 4.2: Summary of the common apparent horizon searches. Listed are the sequences and values of orbital angular momentum for which an apparent horizon search was carried out. The apparent horizon was found to form at a separation $\ell_1/m < \ell/m < \ell_2/m$. (a): From [62], which found a critical separation $\beta = 4.17$. This corresponds to a proper separation of $\ell/m \approx 1.89$.

Sequence	$L/\mu m$	ℓ_1/m	ℓ_2/m
--0.37	3.38	2.32	2.38
--0.25	3.10	2.20	2.25
--0.25	3.34	2.24	2.29
++0.0	0.0	1.89 ^(a)	
++0.0	2.94	2.08	2.13
++0.0	3.00	2.08	2.13
++0.08	2.84	2.03	2.08
++0.08	2.92	2.03	2.08
++0.17	2.79	1.98	2.03
++0.25	2.70	1.96	2.01

errors in E_b/μ , $L/\mu m$ and $J/\mu m$ are less than 1 per cent, while $m\Omega$ and ℓ/m are accurate to a few percent. However, for the ++ sequences the systematic errors of our approach might be much larger. The table also includes ISCO parameters for a test mass orbiting a Kerr black hole obtained from formulas in [61].

4.3.3 Common apparent horizons

A common event horizon might be responsible for the strange behavior of the effective potential at small separations, because once a common event horizon forms, there are no longer two distinct black holes. It would be helpful to know the critical separation where a common event horizon first forms. However, in order to locate the event horizon, knowledge of the complete spacetime is needed. In the present case, only data on one time-slice is available, and so we can only search for common apparent horizons. Since the event horizon must lie outside the apparent horizon, the formation of a common apparent horizon places a firm bound on the formation of an event horizon.

Searches for a common apparent horizon were carried out for several spin configurations. Details of the apparent horizon finder and the method used to discern

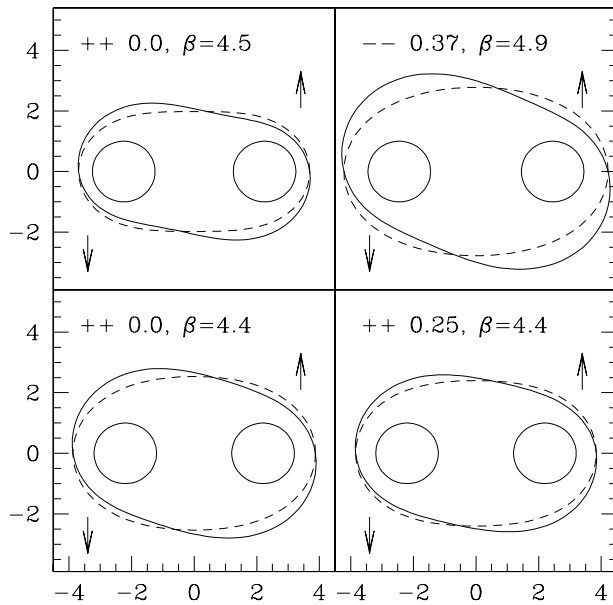


Figure 4.8: Shapes of the common apparent horizons for different spin configurations. Circles denote the throats of the holes. The solid lines are cuts in the plane of orbital motion (arrows indicating the direction of motion), the dashed lines represent cuts normal to the plane of motion.

the formation of a common apparent horizon are given in the Appendix. In Table 4.2, the results of the apparent horizon searches are listed.

For fixed spin configurations the common apparent horizon forms at larger separation for larger angular momentum. This can be seen from the $--0.25$ and $++0.0$ sequences. For varying spins and angular momentum close to the ISCO values, the proper separation between the throats at the formation of the common apparent horizon depends weakly on the spin. It decreases from $\ell/m \approx 2.3$ for the $--0.37$ sequence down to $\ell/m \approx 2.0$ for the $++0.17$ sequence.

Notice that the segment of parameter space where common apparent horizons form does not include the sequence of quasi-circular orbit configurations. Indeed, the common apparent horizons form at a separation inside the inner minimum where the effective potential *increases* with decreasing separation.

The search for the onset of common apparent horizons also provides the actual surfaces. In Fig. 4.8 some apparent horizon surfaces just inside the formation of a common apparent horizon are plotted. The circles represent the throats of

the holes. The solid lines represent a cut through the plane of orbital motion of the holes, arrows indicating the direction of linear momentum of the holes. The dashed lines are cuts through the plane perpendicular to the plane of motion and parallel to the spins of the holes. We find that the apparent horizons lag behind the orbital motion, with the amount of lag being larger for counter-rotating than for co-rotating holes.

4.4 Discussion

We found that the effective potential contours at very small separation *increase* with decreasing separation. This is in contrast to the usual shape of the effective potential for a Schwarzschild or a Kerr black hole, which tends to $-\infty$ at sufficiently small separations.

This behavior can be interpreted in the light of the common apparent horizon searches. The common apparent horizon that was found to form at a small separation of the holes might influence the observed effective potential as follows: The event horizon must lie outside the apparent horizon. Therefore a common event horizon must form before a common apparent horizon forms. To accomplish this the event horizons around the individual holes must grow towards this common event horizon. Thus, even before formation of a common event horizon, the individual event horizons will no longer be close to the individual apparent horizons and the areas of the event horizons of the individual holes must be larger than the areas of their apparent horizons. Therefore, equations (4.4) and (4.5) will *underestimate* the mass of the holes. We denote this underestimate by ΔM . Consider the effect this underestimate of M has on the binding energy. The numerator of (4.6) will be *over*-estimated by a relative amount of

$$\frac{2\Delta M}{|E_{\text{ADM}} - 2M|} = \frac{4}{|E_b/\mu|} \frac{\Delta M}{M} \gg \frac{\Delta M}{M}. \quad (4.16)$$

At the same time, the denominator of (4.6) and the denominator of the scaled angular momentum (4.7d) change too, leading to an underestimate of the binding energy E_b/μ . However, the relative changes of these denominators are only of the order of $\Delta M/M$, so that the overestimate from Eqn. (4.16) dominates. It might well be that this overestimate is so large that it counter-balances the decreasing effective potential that one might expect in analogy to Schwarzschild or Kerr black holes.

This idea leads to the following picture to explain the observed effective potential curves: At large separation of the holes, the masses of the holes and the effective potential are reliable and we see an effective potential that looks similar to a Schwarzschild black hole. Consider, for example, the $++0.0$ sequence: For J slightly above its ISCO value we see the (outer) minimum of the stable quasi-circular orbit and a maximum corresponding to an unstable circular orbit. As J increases, the stable circular orbit moves outwards and the unstable one moves inwards. Once the maximum corresponding to the unstable orbit moves too far in, the $\Delta M/M$ contamination of the effective potential “eats up” the maximum and it disappears.

Now we turn on spin. We found that a common apparent horizon forms at approximately the same proper separation, independent of the spin of the holes. It seems reasonable that the $\Delta M/M$ error is also weakly dependent on the spin, and also the separation of the holes, where $\Delta M/M$ becomes significant. For the $--$ sequences the ISCO moves to larger separations. Thus the maximum in the effective potential (the unstable orbit) will survive for a larger range of separations and angular momenta J . Conversely, for the $++$ sequences, the ISCO moves inwards, closer to the separation where $\Delta M/M$ becomes significant. The maximum in E_b/μ is lost almost immediately, and in the extreme limit of $S/M^2 > 0.17$, it does not show up at all.

This scenario is sufficient to capture the complete behavior of the effective potential as a function of J and spin. What does this picture imply for the validity of our ISCO results from Table 4.1? We expect that $\Delta M/M$ decays rapidly with increasing separation, so the ISCO data for the non-rotating sequence $++0.0$ as well as for the $--$ sequences should be sound. However, because ΔM changes the characteristic behavior for the $++$ configurations even for $S/M^2 < 0.17$, the $++$ sequences will be affected. Let us consider how these changes affect our estimates of circular orbits.

Figure 4.9 illustrates the effect of the $\Delta M/M$ contamination on the effective potential contours. As we noted above, the $\Delta M/M$ contaminations of the binding energy overestimates the binding energy of an effective potential contour. Since this error increases as the separation decreases, our estimates for the separation at a given value of angular momentum are also too high, and our estimates of the orbital angular velocity $m\Omega$ are too low. Unfortunately, we cannot determine whether our estimates for the location of the ISCO are too high or too low. While

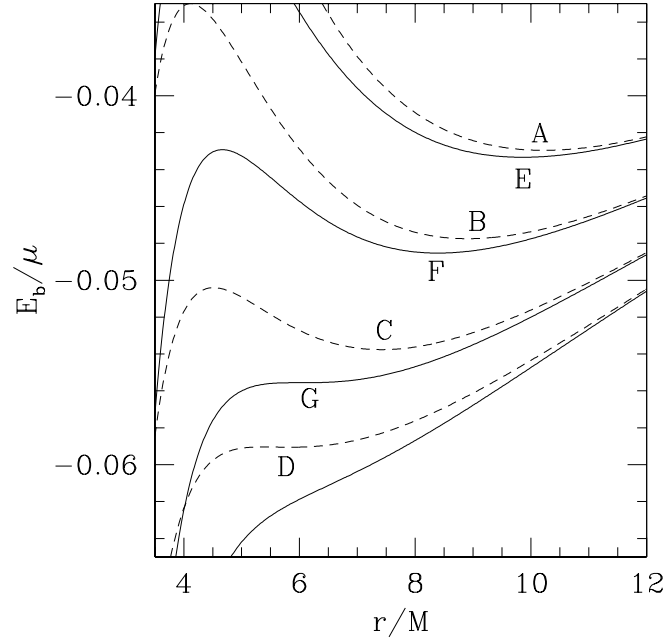


Figure 4.9: Illustration of the effects of a systematic underestimation of E_b/μ . The dashed lines represent the observed effective potential contours for some values of J . The points A, B, and C correspond to circular orbits. The ISCO is at D. Assuming that the true binding energy is smaller, with the deviation increasing as the separation decreases, yields true effective potential contours similar to the solid lines. The true circular orbits are at E and F and the true ISCO is at G. We find that the minima of the true contours will lie at smaller separation (for the same J). The angular frequency is given by $\Omega = dE_b/dJ$. Using the points A and B, we see that the observed dE_b is smaller than the true one, so we under-estimate $m\Omega$. For fixed J , true circular orbits will occur at smaller separation, but the true ISCO will appear at larger J than we have observed. These effects counteract each other, making it impossible to predict their effect on the true ISCO.

our estimates for the separation of a given orbit are too high, we see that the true ISCO will occur at a larger value of the total angular momentum than we estimate. These effects oppose each other.

The angular momentum at the ISCO, $J/\mu m$, increases with spin for the $++$ configurations. It is interesting to examine whether the final black hole resulting from a merger of such a spinning binary black hole can violate the Kerr limit on spin of a black hole. From (4.4) we find

$$M_{ir}^2 = \frac{M^2}{2} \left(1 + \sqrt{1 - \frac{S^2}{M^4}} \right). \quad (4.17)$$

By the area theorem, the final irreducible mass must satisfy $M_{ir,f}^2 \geq 2M_{ir}^2$, where equal mass holes were assumed. The final angular momentum cannot exceed the angular momentum at the ISCO, $J_f \leq J$. With these two constraints and by virtue of the Christoudoulou formula (4.4), we find

$$\frac{M_f^2}{M_{ir,f}^2} \leq 1 + \frac{(J/\mu m)^2}{4 \left(1 + \sqrt{1 - (S/M^2)^2} \right)^2} \quad (4.18)$$

A Kerr black hole has always $M^2/M_{ir}^2 \leq 2$ with equality in the extreme Kerr limit. With data from Table 4.1 we find for the $--0.50$ sequence $M_f^2/M_{ir,f}^2 \leq 1.43$ and for the $++0.17$ sequence $M_f^2/M_{ir,f}^2 \leq 1.61$. These values correspond to spin parameters of $J/M_f^2 \leq 0.92$ and $J/M_f^2 \leq 0.97$, respectively. Hence the merged black hole might be close to the Kerr limit, but will not violate it.

+– Sequences and conformal flatness

The (spin)⁴ effect illustrated in Fig. 4.4 suggests that the assumption of conformal flatness might lead to inaccurate results. This is particularly important for analysis of gravitational waves. As seen in Fig. 4.4, for spinning holes with $S/M^2 \sim 0.50$ the assumption of conformal flatness results in an unphysical gravitational wave content of the order of $\sim 2 \cdot 10^{-3} \mu \sim 5 \cdot 10^{-4} m$. This is less than 0.1 percent of the total mass and a few percent of the binding energy E_b . If the gravitational energy radiated away is less than 1% of the total mass, then the gravitational wave content due to an unsuitable initial data slice is a significant contamination.

4.5 Conclusion

In this work, we have constructed sequences of quasi-circular orbits for equal-sized, spinning black holes. At large separations, the results we have obtained match well with (post)²-Newtonian expansions, although there is a clear contamination of the data because of the assumption of conformal flatness. The main results of this paper, displayed in Table 4.1 and Fig. 4.7, reveal the behavior of the ISCO for the cases where the spins of the holes are either both co-rotating (++) or counter-rotating (--) with respect to the orbital motion. For co-rotation, the ISCO moves inwards with increasing spin and the orbital angular frequency increases. For counter-rotation the ISCO moves outward and the orbital angular frequency decreases. In fact, we find that the orbital angular frequency changes by almost a factor of 2 between the --0.50 sequence and the ++0.08 sequence. We have noted a systematic error in our results that has its origins in an underestimation of the mass of each black hole when they are close together. For the ISCO, this implies that our results are most accurate (ignoring the errors due to conformal flatness) when the holes have large counter-rotating spins, and the error increases as we move to configurations with large co-rotating spins. In fact, the error becomes so large in the ++ sequences that our method cannot locate the ISCO when $S/M^2 \gtrsim 0.17$.

Our results clearly show the need to give up the simplifying assumption of conformal flatness if we are to construct astrophysically realistic black hole initial data. This is certainly not a new realization, but this is the first time that the effects of the conformal flatness assumption have been seen so clearly in the context of black hole binaries. Work toward more astrophysically realistic initial data has begun [63]. This improvement in the initial data is needed for all separations. It remains to be seen what impact this improvement will have on the process of locating quasi-circular orbits when the holes are close together. It is likely that the systematic underestimate of the mass will still be significant. If so, an improved method for locating quasi-circular orbits and the ISCO will be useful.

Acknowledgements

We thank Larry Kidder and Mark Scheel for helpful discussions. This work was supported in part by NSF grants PHY-9800737 and PHY-9900672 and NASA

Grant NAG5-7264 to Cornell University, and NSF grant PHY-9988581 to Wake Forest University. Computations were performed on the IBM SP2 at Cornell Theory Center, and on the Wake Forest University Department of Physics IBM SP2 with support from an IBM SUR grant.

4.6 Appendix: Common apparent horizons

Here we provide details of the apparent horizon (AH) finder. We use the AH finder described in [64]. The AH surface is expanded in spherical harmonics up to some order L . The apparent horizon, as a marginally outer trapped surface, has everywhere vanishing expansion and is located by minimizing the square of the expansion over the surface. We use convergence with increasing expansion order L to diagnose the formation of a common AH. Therefore high expansion orders L are needed as well as reliable convergence of the minimization routine to the true minimum of the square of the expansion.

The Powell minimization used in [64] is too slow for high-order expansions. We replaced it by a DFP method with finite difference approximations of the Jacobian [46]. For the modest expansion order $L = 6$, DFP is already ten times faster than Powell's method.

Furthermore, we take advantage of the symmetries of the AH surface. The holes are located along the \hat{z} -axis at $z = \pm\beta/2$. Their linear momenta point in the $\pm\hat{x}$ -direction and the spins are directed along the $\pm\hat{y}$ -axis. It is straightforward to show that these choices imply that the AH surface is invariant under reflection at the xz -plane, $y \rightarrow -y$. This symmetry constrains the coefficients A_{lm} of the expansion in spherical harmonics to be real. Moreover, for the $++$ and $--$ configurations with equal sized holes and equal spin magnitudes, the configuration is symmetric under rotation by 180° around the \hat{y} -axis, this is $(x, y, z) \rightarrow (-x, y, -z)$. Both symmetries together force $A_{lm} = 0$ for odd l and A_{lm} to be real for even l . Hence the number of free parameters in the minimization routine can be reduced by almost a factor of four.

To prevent convergence to spurious local minima, it is vital that the function that is minimized be as smooth as possible. Therefore we use second order spline interpolation to provide the required data for the AH finder. Compared to bicubic interpolation, the spline interpolation somewhat decreased the number of iterations needed in the minimization routine, but more importantly it significantly reduced

the probability of getting stuck in a local minimum. In addition, many rays were used to reduce the anisotropies introduced by the discrete position of the rays. Finally, we distribute the rays *non*-uniformly in solid angle. The reason for this is simple: The common AH surface will be very oblate along the \hat{z} -axis, since it must encompass the two throats located along the \hat{z} -axis. The polar regions of the AH surface are close to the throats and the conformal factor changes rapidly. These regions are particularly important, but the standard distribution uniform in $\cos\theta$ places relatively few rays in the polar regions. Therefore we implemented a procedure that distributes the rays in proportion to an arbitrary ray-density function $f(\theta)$. A uniform distribution of rays is represented by $f(\theta) = \text{const.}$, whereas we used $f(\theta) = 1 + \cos^2\theta$, resulting in a doubled density of rays close to the poles.

With the improved AH finder, we performed extensive tests with various numbers of rays. As a rule of thumb, about ten times more rays as free minimization parameters are necessary to ensure reliable convergence to the true minimum of the square-sum of the expansion.

We used expansions up to order $L = 16$ and up to 64x48 rays (64 in θ direction, 48 in ϕ). We perform a set of AH searches, starting at $L = 2$ and increasing L by 2 between searches. The result of the previous search is used as the initial guess for the next higher expansion order. Such a set of expansions from $L = 2$ to $L = 16$ takes typically about 2 hours CPU time on a RS6000 processor.

A disadvantage of an AH finder based on a minimization routine is that the minimization routine will *always* find a minimum. It does not matter whether there actually is a “true” apparent horizon, or whether there is only a surface with small but non-zero expansion. And even for a true AH, the result of the minimization will be non-zero because of the finite grid resolution in the underlying elliptic solver and finite expansion order in spherical harmonics. Therefore we need a method to discern a “true” AH from a mere minimum in the square of the expansion.

For a true AH, the square of the expansion is exactly zero, therefore we expect that the residual of the minimization tends to zero as the resolution of the elliptic solver and the expansion order L are increased. With increasing L , the error in the approximation of the surface by spherical harmonics should decrease *exponentially*. On the other hand, for a mere minimum in the expansion, we expect that the residual of the minimization tends towards a *non-zero* limit as the resolution of the elliptic solver and the expansion order L is increased. We use this signature to

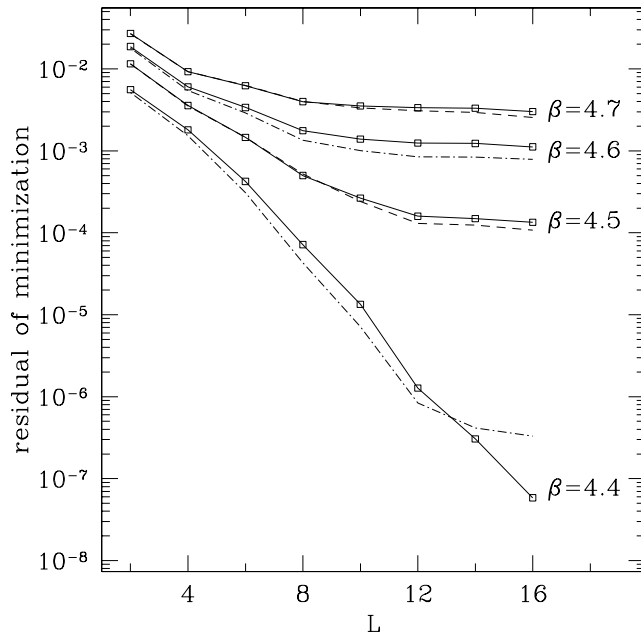


Figure 4.10: Residual of the minimization in the apparent horizon finder as a function of expansion order L . The number of rays used was $N_\theta = 64$, $N_\phi = 48$. The different solid lines represent different separations of the holes along an effective potential contour with $J/\mu m = 3.29$ on the $++0.25$ sequence. The dashed lines are the results of minimizations with $N_\theta = 48$, $N_\phi = 32$. The dotted-dashed lines show examples of minimizations at lower grid resolution and $N_\theta = 64$, $N_\phi = 48$.

discern the formation of a common apparent horizon.

Figure 4.10 shows the residual of the minimization for various values of L and different separations β . The solid lines represent configurations at different separations of the holes. They are labeled by the background separation of the holes, β . Each solid line represents a set of minimizations with varying expansion order $2 \leq L \leq 16$ on the *same* initial data set. At large separations, $\beta \geq 4.5$, the residual of the minimization becomes independent of L for large L . At small separation, $\beta = 4.4$, the residual decreases exponentially through all computed expansion orders up to $L = 16$ – a common AH has formed.

Neither reducing the number of rays, nor decreasing the resolution of the Hamiltonian solver changes the convergence behavior significantly. This is illustrated by some examples in Fig. 4.10. We conclude that for this particular example a com-

mon AH first forms between $\beta = 4.4$ and $\beta = 4.5$.

Expansions to high order in L are essential for discerning the formation of a common AH. If one had Fig. 4.10 only up to expansions up to $L = 8$, it would be impossible to decide where the common AH first forms. One would probably conclude that the common AH forms at larger separations than it actually does.

Chapter 5

Quasi-circular orbits in the test-mass

limit

5.1 Introduction

For the test-mass limit, in which the second black hole (or particle) has much smaller mass M_2 than the first one (with mass M_1), many analytical or semi-analytical results are available. For example, a point-particle in circular orbits around a Schwarzschild black hole satisfies [6, 57]

$$\frac{L}{\mu m} = \frac{r/m}{\sqrt{r/m - 3}}, \quad (5.1)$$

$$\frac{E_b}{\mu} = \frac{r/m - 2}{\sqrt{(r/m)^2 - 3r/m}} - 1, \quad (5.2)$$

$$m\Omega = \left(\frac{r}{m}\right)^{-3/2}. \quad (5.3)$$

Here, $m = M_1 + M_2$ and $\mu = M_1 M_2 / m$ are total mass and reduced mass, respectively (or, to leading order, mass of the big hole and the small hole, respectively), r is the areal radius, and Ω denotes the orbital angular frequency as seen by an observer at infinity.

Pushing numerical relativity calculations toward this limit is interesting, because one can compare against analytic results, and because many approximations involved in constructing black holes in quasi-circular orbits become exact. Thus, more stringent tests of the remaining approximations emerge.

However, the test-mass limit is also computationally more challenging, as the required resolution is set by the size of the smaller object, which we are trying to shrink as far as possible. This is one reason why fully numerical initial data calculations so far usually assume equal mass binaries (see e.g. [28, 24, 59, 65, 56, 66, 67, 68]). The restriction to equal mass reduces also the size of the parameter space under consideration.

The ideas on which these numerical calculations are based do *not* usually require equal mass objects; for example, the effective potential method [28, 65] which we apply in chapter 4 is completely general: It can be used to construct quasi-circular orbits for any choice of masses and spins. The multi-domain elliptic solver developed in chapter 3 can handle very different length scales as was demonstrated

in Figure 3.7. It is also sufficiently fast to allow calculations approaching the test-mass limit. Consequently, I will now employ this solver to examine quasi-circular orbits for non-spinning black holes of *unequal* mass.

5.2 Implementation & Results

The effective potential method is outlined in section 4.1 and explained in detail in reference [28]. Application to non-equal mass binaries is straightforward. The root-finder and the remaining infrastructure developed in chapter 4 can handle non-equal mass holes anyway (this was necessary for treating one co- and one counter-rotating hole), and were reused. Simply the elliptic solver had to be upgraded from Cook's finite-difference code [52] to the pseudo-spectral code. In order to ensure a uniform accuracy of the pseudo-spectral code, solves of the Hamiltonian constraint were performed for mass-ratios between unity and ~ 40 , and for separations $6 \lesssim \beta \lesssim 100$, to ensure that the number of collocation points in the various subdomains is well-balanced (it turned out that only the number of radial collocation points in the spherical shell surrounding the smaller excised sphere had to be adjusted).

We traced out sequences of quasi-circular orbits for mass-ratios $X = M_1/M_2$ up to 32. Figure 5.1 presents sequences for $X = 4, 8, 16, 32$. As the mass-ratio increases, the sequences move closer to the curve denoting the point-mass result (cf. Eqs. (5.1) and (5.2)), as we expect. The figure includes post-Newtonian results taken from [28]:

$$\frac{E_b}{\mu} = -\frac{1}{2} \left(\frac{L}{\mu m} \right)^{-2} \left[1 + \frac{9 + \eta}{4} \left(\frac{L}{\mu m} \right)^{-2} + \frac{81 - 7\eta + \eta^2}{8} \left(\frac{L}{\mu m} \right)^{-4} + \dots \right], \quad (5.4)$$

$$\frac{E_b}{\mu} = -\frac{1}{2} (m\Omega)^{2/3} \left[1 - \frac{9 + \eta}{12} (m\Omega)^{2/3} - \left(\frac{27}{8} - \frac{19\eta}{8} + \frac{\eta^2}{24} \right) (m\Omega)^{4/3} + \dots \right], \quad (5.5)$$

$$\left(\frac{L}{\mu m} \right)^2 = (m\Omega)^{-2/3} \left[1 + \frac{9 + \eta}{3} (m\Omega)^{2/3} + \left(9 - \frac{17\eta}{4} + \frac{\eta^2}{9} \right) (m\Omega)^{4/3} + \dots \right]. \quad (5.6)$$

Here, $\eta = \mu/m$, so that equal mass binaries correspond to $\eta = 1/4$, and the test-mass limit is $\eta = 0$.

Figure 5.2 shows the angular momentum $L/\mu m$ as a function of orbital angular frequency [cf. Eq. (4.12)]

$$m\Omega = \frac{dE_b/\mu}{dL/\mu m}. \quad (5.7)$$

For this Figure, $m\Omega$ was computed by simple first order finite differencing between

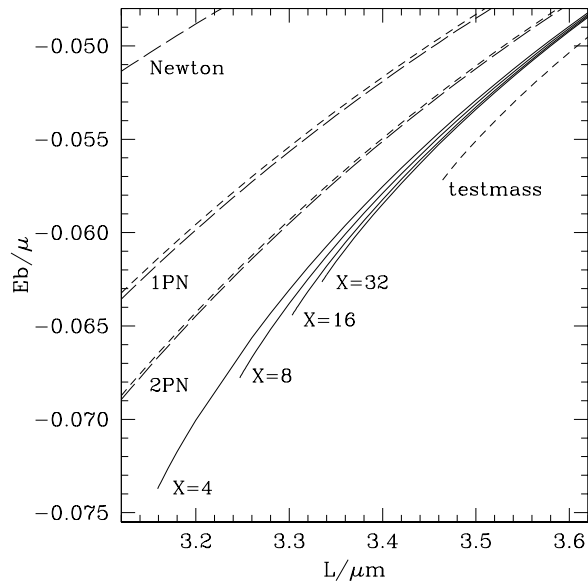


Figure 5.1: Sequences of quasi-circular orbits for different mass-ratios obtained with inversion symmetric Bowen-York initial data. The sequences terminate at the location of the ISCO. Also shown is the sequence of circular orbits for a test-mass orbiting a black hole, as well as (post-)Newtonian results. For the latter, the long-dashed lines correspond to $X = 1$, whereas the short-dashed lines represent the test-mass limit, $X \rightarrow \infty$.

neighboring points along each sequence. This is sufficiently accurate for plotting but leads to fairly inaccurate ISCO locations in this plot.

Figure 5.3 plots the binding energy E_b/μ along the sequences for large separation. To facilitate plotting, the binding energy in the test-mass limit was *subtracted* from each curve. The computed sequences, labelled $X = 4$ to $X = 32$ reverse their relative ordering around $L/\mu m \approx 4$: At small angular momenta (i.e. at small separation), $|E_b/\mu|$ increases with increasing mass-ratio X . At large angular momenta, however, $|E_b/\mu|$ decreases with increasing X . This behavior matches the second post-Newtonian results, although the crossover occurs at a different separation.

In Figures 5.1 and 5.2, the sequences of quasi-circular orbits terminate simply at the smallest quasi-circular orbit that was found, which is outside the ISCO by definition. The location of the ISCO is determined with greater accuracy with the following procedure:

For several quasi-circular orbits close to the tentative ISCO, labeled by “ a ”, we

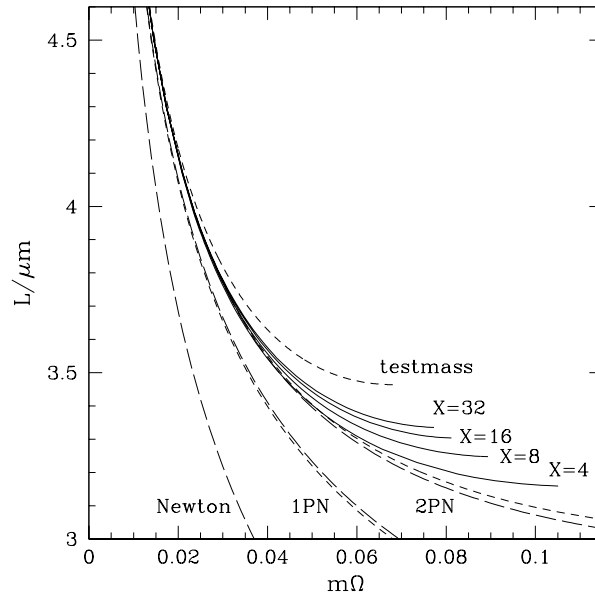


Figure 5.2: Sequences of quasi-circular orbits for different mass-ratios obtained with inversion symmetric Bowen-York initial data. Symbols as in Figure 5.1.

recorded the parameters characterizing the orbit: β_a , $(L/\mu m)_a$, $(E_b/\mu)_a$. The Appendix shows that L behaves *quadratically* in separation β close to ISCO, the ISCO coinciding with the *minimum* of the parabola. Consequently, we fit a parabola through the points

$$\left(\beta_a, (L/\mu m)_a\right); \quad (5.8)$$

its minimum gives β_{ISCO} and $(L/\mu m)_{\text{ISCO}}$. Further, we fit a parabola through the points

$$\left((L/\mu m)_a, (E_b/\mu)_a\right). \quad (5.9)$$

Evaluation of this parabola at $(L/\mu m)_{\text{ISCO}}$ yields $(E_b/\mu)_{\text{ISCO}}$, evaluation of the *derivative* at $(L/\mu m)_{\text{ISCO}}$ yields $(m\Omega)_{\text{ISCO}}$. We ensure that the ISCO-parameters are insensitive to the number of points used in the quadratic fit; usually, five or six points were used.

The results are presented in Figure 5.4. The data point at $X = 1$ has been computed before, both in [28], and in chapter 4. Close to $X = 1$, the physical parameters $L/\mu m$, E_b/μ and $m\Omega$ behave quadratically in X , as they must due to the $X \rightarrow 1/X$ symmetry (exchange of the two black holes). We confirmed that the physical ISCO-parameters for $X = 1.1$ and $X = 1/1.1$ are identical, as they should

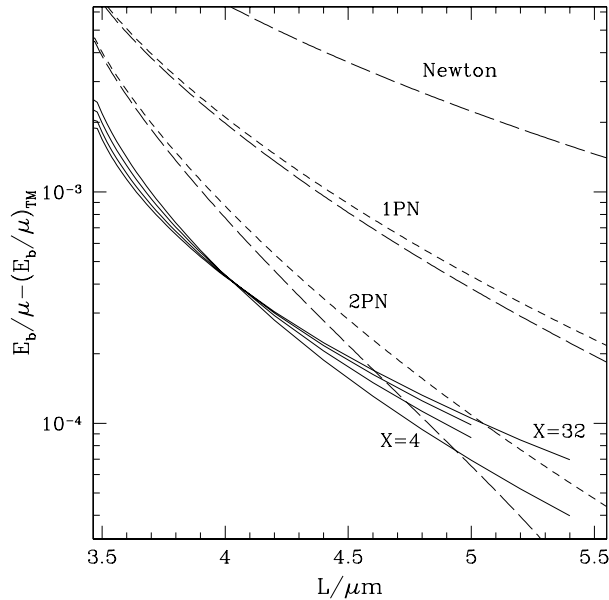


Figure 5.3: Sequences of quasi-circular orbits for different mass-ratios obtained with inversion symmetric Bowen-York initial data. Plotted is the difference of E_b/μ along the sequence to its value in the test-mass limit. Symbols as in Figure 5.1. The computed sequences terminate at some large ($L/\mu m$) simply because no further data was computed; in reality they should continue.

(of course, the *unscaled* background separation β differs). β_{ISCO} and $(m\Omega)_{\text{ISCO}}$ are less accurate, as can already be seen by the noise in Figure 5.4. The values of β for each quasi-circular orbit are obtained as the abscissas of a minimization, which is inherently inaccurate, whereas $m\Omega$ is obtained by differentiation of numerical data.

For $1/X \lesssim 0.2$, the ISCO parameters appear to depend linearly on $1/X$. We have reached the linear regime so that we can confidently extrapolate the results to the test-mass limit, $1/X \rightarrow 0$. Table 5.1 contains the numerical values at ISCO, as well as an extrapolation to $X = \infty$. Analytic values for the test-mass limit are obtained from Eqs. (5.1)–(5.3) with $r = 6m$. In this limit, β approximates the isotropic radius so that $\beta_{\text{ISCO}} = \frac{1}{2} (5 + \sqrt{24}) m \approx 9.899$ (the mass $m \approx 2$ because the large throat has radius 1 and not $1/2$).

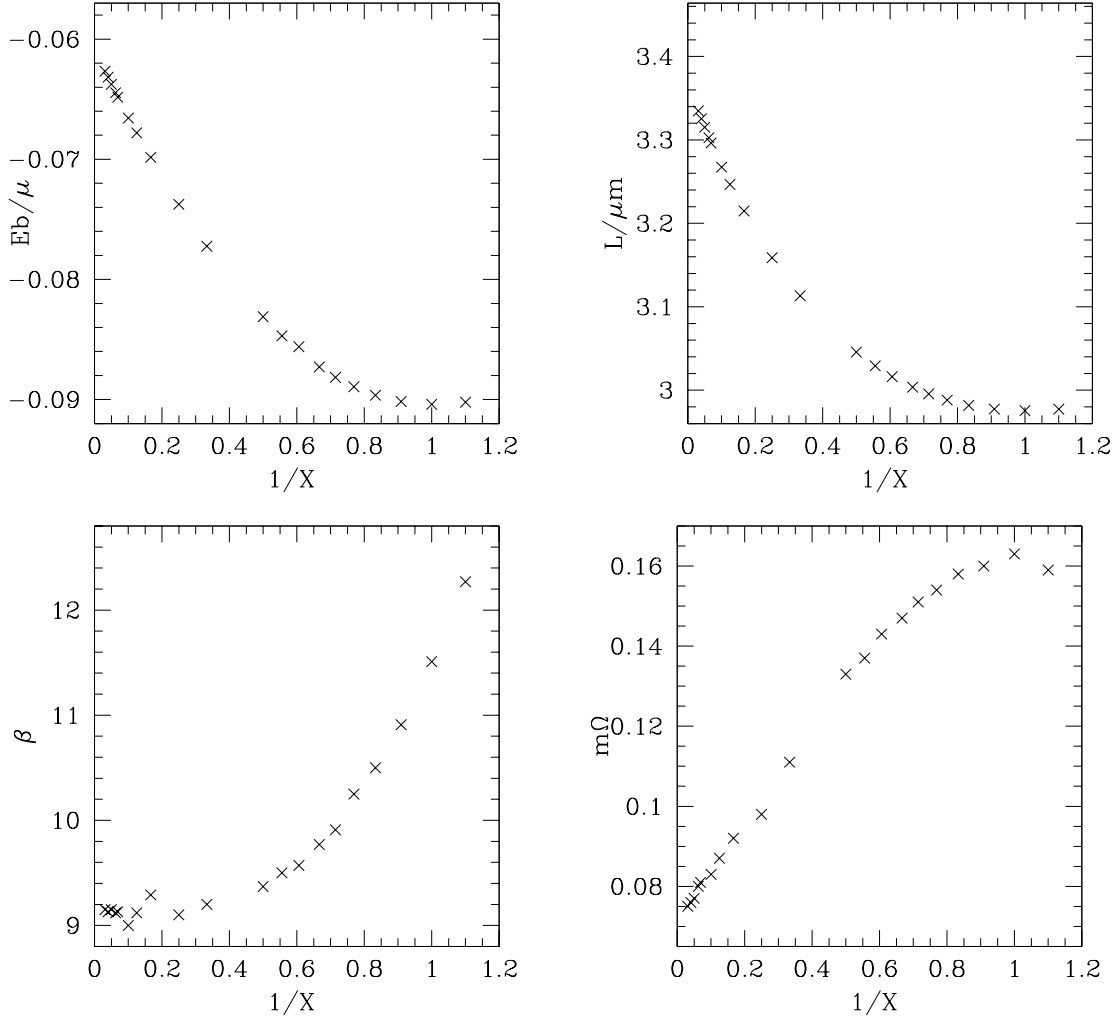


Figure 5.4: ISCO's for different mass-ratios obtained with inversion symmetric Bowen-York initial data. Plotted are the values of several quantities at ISCO vs. the mass-ratio.

Table 5.1: ISCO parameters for different mass-ratios obtained with the effective potential method, “ ∞ ” denoting extrapolation to the test-mass limit.

X	$L/\mu m$	E_b/μ	$m\Omega$	β	α	\bar{P}
0.909	2.9772	-0.09022	0.159	12.27	0.8847	1.867
1.0	2.9755	-0.09040	0.163	11.51	1.0000	1.77
1.1	2.9774	-0.09017	0.160	10.91	1.1301	1.639
1.2	2.9818	-0.08965	0.158	10.50	1.2622	1.512
1.3	2.9881	-0.08893	0.154	10.25	1.38	1.395
1.4	2.9955	-0.08815	0.151	9.91	1.531	1.302
1.5	3.0036	-0.08728	0.147	9.77	1.666	1.204
1.65	3.0162	-0.08560	0.143	9.57	1.869	1.081
1.8	3.0292	-0.0847	0.137	9.5	2.070	0.975
2.0	3.0457	-0.08310	0.133	9.37	2.338	0.855
3.0	3.1132	-0.07724	0.111	9.2	3.675	0.538
4.0	3.1588	-0.07375	0.098	9.1	5.00	0.394
6.0	3.2149	-0.06984	0.092	9.29	7.63	0.251
8.0	3.2467	-0.06780	0.087	9.12	10.32	0.189
10	3.2680	-0.06657	0.083	9	12.96	0.152
14.5	3.2963	-0.06483	0.081	9.13	18.94	0.1029
16	3.3026	-0.06446	0.080	9.12	20.94	0.0933
20	3.3151	-0.06376	0.077	9.15	26.21	0.0774
25	3.3255	-0.06317	0.076	9.13	32.9	0.059
32	3.3348	-0.06267	0.075	9.15	42.1	0.046
∞	3.370	-0.0607	0.071	9.15		
analytic	3.463	-0.0572	0.0680	9.899		

5.3 Discussion

Extrapolation $X \rightarrow \infty$ in Table 5.1 shows that in this limit, the ISCO parameters computed with the effective potential method differ by a few per cent from the analytical results; the computed ISCOs are too tightly bound.

In the test-mass limit, many assumptions of the effective potential method become exact: The radiation reaction time-scale grows with the mass-ratio X so that the adiabatic approximation becomes increasingly good. As the inspiral time-scale increases and the configuration moves closer to stationarity, the deviation between apparent horizons and event horizons should diminish, and the apparent horizon masses should increasingly well represent the “true” mass of each black hole. Moreover, the underlying idea of minimizing E_b/μ is equivalent to the method used to find circular orbits analytically, as the discussion just before and after Eq. (4.1) shows.

The remaining assumptions include conformal flatness, inversion symmetry, and the Bowen-York solution of the momentum constraint. Regarding conformal flatness, the space time will be dominated by the large black hole (which is at rest for infinite mass-ratio) so that we should recover the Schwarzschild metric in isotropic coordinates. Close to the small hole, however, the assumption of conformal flatness might still break down. I did not analyze or estimate possible errors associated with conformal flatness.

The major uncertain approximation remains the Bowen-York solution for the extrinsic curvature. This is just a *convenient* solution of the momentum constraint, as it is analytical, but there is no reason for it to be the *correct* solution. In chapter 6, we show that initial data sets computed with the extrinsic curvature formulation are very sensitive to the choice of background extrinsic curvature, hence it is likely that the present results are also sensitive to the choice of extrinsic curvature.

How would a “wrong” choice for the extrinsic curvature manifest itself? Cook [26] examines single black holes constructed using the Bowen-York solution and inversion symmetry. For a black hole with linear momentum, he finds that the ADM-energy of the spacetime *exceeds* the apparent horizon mass times the Lorentz-factor. The difference increases with increasing linear momentum of the hole, and can be attributed to gravitational radiation outside the hole, which might fall into the hole, or escape to infinity. It seems reasonable that the binary black hole solutions behave similarly, this is, that the ADM-energy is contaminated by “gravitational

radiation” outside the holes, such that the contamination increases with increasing linear momentum \bar{P} . Along a single effective potential contour, the momentum parameter \bar{P} *increases* as the separation decreases: the observed values of E_{ADM} and E_b/μ will be systematically too large for smaller separations. This is exactly the situation we discussed in Figure 4.9 on page 85, and offers an explanation why the numerical calculation yields $(L/\mu m)_{\text{ISCO}}$ smaller than the analytical result.

If the contamination is indeed induced by the Bowen-York extrinsic curvature, then it will *not* disappear in the test-mass limit. In this limit, the large black hole is simply at rest; unphysical gravitational radiation will be associated with the small hole, which moves with a significant fraction of the speed of light. For given velocity, the gravitational wave contamination introduced by the small hole is proportional to its mass M_2 . The binding energy E_b is also proportional to M_2 , so that M_2 scales out of the effective potential E_b/μ .

This discussion shows that the notion that the Bowen-York extrinsic curvature contaminates the initial data sets is consistent with the numerical results. The same effect might also contribute to the disappearance of the ISCO for spinning equal mass black holes in chapter 4. In that chapter, we attributed the failure of the effective potential method to a break down of the apparent horizon mass, but given the current result and the sensitive dependence of the initial data sets on the extrinsic curvature (cf. chapter 6), it seems plausible that the Bowen-York extrinsic curvature plays also a role for the spinning black holes in chapter 4.

The ISCO for equal mass nonspinning black holes has also been computed with post-Newtonian methods [69, 70, 71, 68, 72] and with the helical Killing vector approximation [67, 68, 72]. Both these methods find consistently the ISCO to be *less* tightly bound than the effective potential method with Bowen-York extrinsic curvature [28, 65, 59]. As the effective potential method results in too tightly bound ISCOs for the test-mass limit, it seems likely that its results for equal mass binary black holes are too tightly bound, too, thus explaining at least part of the discrepancy between the different ISCO results.

The results of this chapter point again toward the importance of the choice of extrinsic curvature, here in the form of the Bowen-York extrinsic curvature.

5.4 Appendix: L depends quadratically on β close to ISCO

Let x be some measure of the separation of the black holes, e. g., β or the proper separation ℓ/m . Denote $\delta x = x - x_{\text{ISCO}}$, $\delta L = (L/\mu m) - (L/\mu m)_{\text{ISCO}}$, and expand the effective potential as a power series in separation around ISCO:

$$E_b/\mu = a(\delta L)\delta x^3 + b(\delta L)\delta x^2 + c(\delta L)\delta x + d(\delta L). \quad (5.10)$$

The coefficients $a(\delta L), \dots, d(\delta L)$ depend on the angular momentum δL . The function $d(\delta L)$ merely shifts the energy and is irrelevant for determining the sequence of quasi-circular orbits in the $(\delta x, \delta L)$ -plane. By definition of ISCO,

$$\left. \frac{\partial E_b/\mu}{\partial \delta x} \right|_{\delta x=0, \delta L=0} = 0 \quad \Rightarrow \quad c(0) = 0, \quad (5.11)$$

$$\left. \frac{\partial^2 E_b/\mu}{\partial \delta x^2} \right|_{\delta x=0, \delta L=0} = 0 \quad \Rightarrow \quad b(0) = 0, \quad (5.12)$$

$$\left. \frac{\partial^3 E_b/\mu}{\partial \delta x^3} \right|_{\delta x=0, \delta L=0} > 0 \quad \Rightarrow \quad a(0) \equiv a_0 > 0. \quad (5.13)$$

Thus, the lowest order behavior of the coefficients is

$$a(\delta L) \approx a_0, \quad b(\delta L) \approx b_1 \delta L, \quad c(\delta L) \approx c_1 \delta L, \quad (5.14)$$

with constants a_0, b_1 and c_1 . For $\delta L > 0$, two extrema exist, therefore the determinant of the quadratic equation

$$\left. \frac{\partial E_b/\mu}{\partial \delta x} \right|_{\delta L} = 3a_0 \delta x^2 + 2b_1 \delta L \delta x + c_1 \delta L = 0 \quad (5.15)$$

must be positive,

$$4(b_1 \delta L)^2 + 12a_0 c_1 \delta L = 12a_0 c_1 \delta L + \mathcal{O}(\delta L^2) > 0, \quad (5.16)$$

so that $c_1 < 0$. Solving Eq. (5.15) for δL , we find that, along the sequence,

$$\delta L = -\frac{3a_0 \delta x^2}{2b_1 \delta x + c_1} = -\frac{3a_0}{c_1} \delta x^2 + \mathcal{O}(\delta x^3), \quad (5.17)$$

so that $(L/\mu m)$ depends quadratically on the separation and is extremal at x_{ISCO} . Because $a_0 > 0$ and $c_1 < 0$, $L/\mu m$ has a minimum at x_{ISCO} . We have also established that the energy can be expanded close to ISCO as

$$E_b/\mu = a_0 \delta x^3 + b_1 \delta L \delta x^2 - c_1 \delta L \delta x + d(\delta L), \quad (5.18)$$

with $a_0 > 0$ and $c_1 < 0$. The sign of b_1 is undetermined.

Chapter 6

Comparing initial-data sets for binary

black holes*

6.1 Introduction

Numerical evolutions of black holes have been improved slowly but steadily over the last few years and now first attempts are being made to extract physical information from these evolutions. Most notably one wants to predict the gravitational radiation emitted during black hole coalescence [73, 74, 75].

The quality of the initial data will be crucial to the success of the predictions of the gravitational wave forms. Unphysical gravitational radiation present in the initial data will contribute to the gravitational waves computed in an evolution and might overwhelm the true gravitational wave signature of the physical process under consideration. Therefore an important question is how to control the gravitational wave content of initial-data sets, and how to specify *astrophysically* relevant initial data with the appropriate gravitational wave content, for e.g. two black holes orbiting each other. Unfortunately, assessing and controlling the gravitational wave content of initial-data sets is not well understood at all.

The mere *construction* of an initial-data set alone is fairly involved, since every initial-data set must satisfy a rather complicated set of four partial differential equations, the so-called constraint equations of general relativity. The question of how to solve these equations, and how to specify initial data representing binary black holes in particular, has received considerable attention.

We consider in this paper three different approaches that transform the constraint equations into elliptic equations: The *conformal transverse-traceless (TT) decomposition*[4], the *physical TT decomposition* [19, 76, 77] and the *conformal thin sandwich decomposition*[1]. These decompositions split the variables on the initial-data surface into various pieces in such a way that the constraint equations determine some of the pieces while not restricting the others. After these freely specifiable pieces are chosen, the constraint equations are solved and the results are combined with the freely specifiable pieces to yield a valid initial-data set.

*H. P. Pfeiffer, G. B. Cook, and S. A. Teukolsky, Pys. Rev. D **66**, 024047 (2002).

Any reasonable choice for the freely specifiable pieces will lead to a valid initial-data set. Furthermore, any one of these decompositions can generate any desired initial-data set, given the *correct* choices of the freely specifiable pieces. However, it is not clear *what* choices of freely specifiable pieces lead to initial-data sets with the desired properties.

The decompositions we consider here lead to four coupled nonlinear elliptic partial differential equations. Since such equations are difficult to solve, the early approach to constructing initial data was pragmatic: One used the conformal TT decomposition with additional restrictions on the freely specifiable pieces, most notably conformal flatness and maximal slicing. These assumptions decouple the constraints and allow for analytical solutions to the momentum constraints, the so-called *Bowen-York extrinsic curvature*[21, 22, 23]. All that remains is to solve a single elliptic equation, the Hamiltonian constraint. This approach has been used in several variations[78, 52, 24].

However, these numerical simplifications come at a cost. The freely specifiable pieces have been restricted to a small subset of all possible choices. One therefore can generate only a subset of all possible initial-data sets, one that might not contain the desired astrophysically relevant initial-data sets.

Over the last few years there have been additional developments: Post-Newtonian results have indicated that binary black hole metrics are not conformally flat[79, 70]. With certain restrictions on the slicing, it has also been shown that a single stationary spinning black hole cannot be represented with a conformally flat spatial metric [80, 60]. In [65], it was shown that conformally flat initial data sets for spinning binary black holes contain an unphysical contamination. Moreover, computations in spherical symmetry[81] indicated that initial-data sets depend strongly on the choice of the extrinsic curvature and that the use of the Bowen-York extrinsic curvature might be problematic.

Therefore it is necessary to move beyond conformally flat initial data and to explore different choices for the extrinsic curvature. Matzner et al[63] proposed a non-flat conformal metric based on the superposition of two Kerr-Schild metrics; a solution based on this proposal was obtained in [56]. This work demonstrated the existence of solutions to the 3D set of equations, but did not examine the data sets in any detail. Refs. [67, 68] obtained solutions to a similar set of equations during the computation of quasi-circular orbits of binary black holes. However, these works assumed conformal flatness.

In this paper we present a code capable of solving the three above-mentioned decompositions of the constraint equations for arbitrary choices of the freely specifiable pieces. This code is based on spectral methods which have been used successfully for several astrophysical problems (see e.g. [82, 83, 84, 66, 15, 85, 68]). Our code is described in detail in a separate paper[86].

We compute solutions of the different decompositions for the non-flat conformal metric proposed in Ref. [63]. Each decomposition has certain choices for the freely specifiable pieces and boundary conditions that seem “natural” and which we use in our solutions. We compare the computed initial-data sets with each other and with the “standard” conformally-flat solution using the Bowen-York extrinsic curvature. Our major results confirm that

1. the different decompositions generate different physical initial-data sets for seemingly similar choices for the freely specifiable pieces.
2. the choice of extrinsic curvature is critical.

The first result is certainly not unexpected, but each of these factors can cause relative differences of several per cent in gauge-invariant quantities like the ADM-energy.

We also find that the conformal TT/physical TT decompositions generate initial-data sets with ADM-energies 2 – 3% higher than data sets of the conformal thin sandwich decomposition. We demonstrate that this higher ADM-energy is related to the choice of the freely specifiable part of the extrinsic curvature. In addition, we find that the solutions depend significantly on the boundary conditions used.

The paper is organized as follows. In the next section we describe the three decompositions. Section 6.3 explains how we choose the freely specifiable data within each decomposition. In section 6.4 we describe and test our elliptic solver. Section 6.5 presents our results, which we discuss in section 6.6.

6.2 Decompositions of Einstein's equations and the constraint equations

6.2.1 3+1 Decomposition

In this paper we use the standard 3+1 decomposition of Einstein's equations. We foliate the spacetime with $t = \text{const}$ hypersurfaces and write the four-dimensional metric as

$${}^{(4)}ds^2 = -N^2 dt^2 + \gamma_{ij}(dx^i + N^i dt)(dx^j + N^j dt), \quad (6.1)$$

where γ_{ij} represents the induced 3-metric on the hypersurfaces, and N and N^i represent the lapse function and the shift vector, respectively. We define the extrinsic curvature K_{ij} on the slice by

$$\mathbf{K} = -\frac{1}{2} \perp \mathcal{L}_n {}^{(4)}\mathbf{g} \quad (6.2)$$

where ${}^{(4)}\mathbf{g}$ is the space-time metric, n the unit normal to the hypersurface, and \perp denotes the projection operator into the $t = \text{const}$ slice. Einstein's equations divide into constraint equations, which constrain the data (γ_{ij}, K^{ij}) on each hypersurface, and into evolution equations, which determine how the data (γ_{ij}, K^{ij}) evolve from one hypersurface to the next. The constraint equations are

$$R + K^2 - K_{ij}K^{ij} = 16\pi G\rho \quad (6.3)$$

$$\nabla_j (K^{ij} - \gamma^{ij}K) = 8\pi Gj^i. \quad (6.4)$$

Eq. (6.3) is called the *Hamiltonian constraint*, and Eq. (6.4) is referred to as the *momentum constraint*. $K = \gamma_{ij}K^{ij}$ is the trace of the extrinsic curvature, ∇ and R denote the three dimensional covariant derivative operator and the Ricci scalar compatible with γ_{ij} . ρ and j^i are the energy and momentum density, respectively. Both vanish for the vacuum spacetimes considered here.

The evolution equation for γ_{ij} is

$$\partial_t \gamma_{ij} = -2NK_{ij} + \nabla_i N_j + \nabla_j N_i, \quad (6.5)$$

which follows from Eq. (6.2). There is a similar albeit longer equation for $\partial_t K_{ij}$ which we will not need in this paper. The choices of N and N^i are arbitrary. One can in principle use any lapse and shift in the evolution off the initial-data surface, although some choices of lapse and shift are better suited to numerical implementation than others.

Later in this paper we will often refer to the trace-free piece of Eq. (6.5). Denote the tracefree piece of a tensor by $\text{TF}(\cdot)$, and define $\gamma \equiv \det \gamma_{ij}$. From Eq. (6.5) and the fact that $\delta \ln \gamma = \gamma^{kl} \delta \gamma_{kl}$, it follows that

$$\text{TF}(\partial_t \gamma_{ij}) = \gamma^{1/3} \partial_t (\gamma^{-1/3} \gamma_{ij}) = -2N A_{ij} + (\mathbb{L}N)_{ij}. \quad (6.6)$$

Here $A_{ij} = K_{ij} - \frac{1}{3} \gamma_{ij} K$ denotes the trace-free extrinsic curvature, and

$$(\mathbb{L}N)^{ij} \equiv \nabla^i N^j + \nabla^j N^i - \frac{2}{3} \gamma^{ij} \nabla_k N^k. \quad (6.7)$$

\mathbb{L} always acts on a vector, so the 'N' in $(\mathbb{L}N)^{ij}$ denotes the shift vector N^i and not the lapse N .

6.2.2 Decomposition of the constraint equations

Equations (6.3) and (6.4) constrain four degrees of freedom of the 12 quantities (γ_{ij}, K^{ij}) . However, it is not immediately clear which pieces of γ_{ij} and K^{ij} are constrained and which pieces can be chosen at will. Several decompositions have been developed to divide the 12 degrees of freedom into freely specifiable and constrained pieces. We will now review some properties of the three decompositions we consider in this paper.

All three decompositions follow the York-Lichnerowicz approach and use a conformal transformation on the physical 3-metric γ_{ij} ,

$$\gamma_{ij} = \psi^4 \tilde{\gamma}_{ij}. \quad (6.8)$$

ψ is called the *conformal factor*, $\tilde{\gamma}_{ij}$ the *background metric* or *conformal metric*. We will denote all conformal quantities with a tilde. In particular, $\tilde{\nabla}$ is the covariant derivative operator associated with $\tilde{\gamma}_{ij}$, and \tilde{R}_{ij} and \tilde{R} are the Ricci tensor and Ricci scalar of $\tilde{\gamma}_{ij}$.

The extrinsic curvature is split into its trace and trace-free part,

$$K^{ij} = A^{ij} + \frac{1}{3} \gamma^{ij} K. \quad (6.9)$$

The three decompositions of the constraint equations we discuss in this paper differ in how A^{ij} is decomposed. For each decomposition, we discuss next the relevant equations, and describe how we choose the quantities one has to specify before solving the equations. We use the conventions of [20].

Conformal TT Decomposition

In this decomposition one first conformally transforms the traceless extrinsic curvature,

$$A^{ij} = \psi^{-10} \tilde{A}^{ij}, \quad (6.10)$$

and then applies a TT decomposition with respect to the background metric $\tilde{\gamma}_{ij}$:

$$\tilde{A}^{ij} = \tilde{A}_{TT}^{ij} + (\tilde{\mathbb{L}}X)^{ij}. \quad (6.11)$$

The operator $\tilde{\mathbb{L}}$ is defined by Eq. (6.7) but using the conformal metric $\tilde{\gamma}_{ij}$ and derivatives associated with $\tilde{\gamma}_{ij}$. \tilde{A}_{TT}^{ij} is transverse with respect to the conformal metric, $\tilde{\nabla}_j \tilde{A}_{TT}^{ij} = 0$, and is traceless.

Substituting Eqs. (6.10) and (6.11) into the momentum constraint (6.4), one finds that it reduces to an elliptic equation for X^i , whereas \tilde{A}_{TT}^{ij} is unconstrained.

In order to specify the transverse-traceless tensor \tilde{A}_{TT}^{ij} one usually has to *construct* it from a general symmetric trace-free tensor \tilde{M}^{ij} by subtracting the longitudinal piece. As described in [20] one can incorporate the construction of \tilde{A}_{TT}^{ij} from \tilde{M}^{ij} into the momentum constraint, arriving at the following equations:

$$\tilde{\nabla}^2 \psi - \frac{1}{8} \psi \tilde{R} - \frac{1}{12} \psi^5 K^2 + \frac{1}{8} \psi^{-7} \tilde{A}_{ij} \tilde{A}^{ij} = -2\pi G \psi^5 \rho, \quad (6.12)$$

$$\tilde{\Delta}_L V^i - \frac{2}{3} \psi^6 \tilde{\nabla}^i K + \tilde{\nabla}_j \tilde{M}^{ij} = 8\pi G \psi^{10} j^i, \quad (6.13)$$

where \tilde{A}^{ij} and the operator $\tilde{\Delta}_L$ are defined by

$$\tilde{A}^{ij} = (\tilde{\mathbb{L}}V)^{ij} + \tilde{M}^{ij} \quad (6.14)$$

and

$$\tilde{\Delta}_L V^i \equiv \tilde{\nabla}_j (\tilde{\mathbb{L}}V)^{ij}. \quad (6.15)$$

After solving these equations for ψ and V^i , one obtains the physical metric γ_{ij} from (6.8) and the extrinsic curvature from

$$K^{ij} = \psi^{-10} \tilde{A}^{ij} + \frac{1}{3} \psi^{-4} \tilde{\gamma}^{ij} K. \quad (6.16)$$

We will refer to Eqs. (6.12) and (6.13) together with (6.14), (6.16) and (6.8) as the *conformal TT equations*. In these equations we are free to specify the background metric $\tilde{\gamma}_{ij}$, the trace of the extrinsic curvature K , and a symmetric traceless tensor

\tilde{M}^{ij} . The solution V^i will contain a contribution that removes the longitudinal piece from \tilde{M}^{ij} and the piece that solves the momentum constraint if \tilde{M}^{ij} were transverse-traceless.

This decomposition has been the most important in the past, since if one chooses a constant K and if one considers vacuum spacetimes then the momentum constraint (6.13) decouples from the Hamiltonian constraint (6.12). Moreover, if one assumes conformal flatness and $\tilde{M}^{ij} = 0$, it is possible to write down analytic solutions to Eq. (6.13), the so-called Bowen-York extrinsic curvature. In that case one has to deal with only one elliptic equation for ψ . The Bowen-York extrinsic curvature can represent multiple black holes with arbitrary momenta and spins. One can fix boundary conditions for ψ by requiring that the initial-data slice be inversion symmetric at both throats[9, 27]. In that case one has to modify the extrinsic curvature using a method of images. We will include initial-data sets obtained with this approach below, where we will refer to them as *inversion symmetric* initial data.

Reasonable choices for the freely specifiable pieces $\tilde{\gamma}_{ij}$, K , \tilde{M}^{ij} will lead to an initial-data set (γ_{ij}, K^{ij}) that satisfies the constraint equations. How should we choose all these functions in order to obtain a desired physical configuration, say a binary black hole with given linear momenta and spins for the individual holes? We can gain insight into this question by considering how the conformal TT decompositions can recover a known solution.

Suppose we have a known solution (γ_{0ij}, K_0^{ij}) of the constraint equations. Denote the trace and trace-free parts of this extrinsic curvature by K_0 and A_0^{ij} , respectively. If we set

$$\tilde{\gamma}_{ij} = \gamma_{0ij}, \quad K = K_0, \quad \tilde{M}^{ij} = A_0^{ij} \quad (6.17)$$

then

$$\psi = 1, \quad V^i = 0 \quad (6.18)$$

trivially solve Eqs. (6.12-6.13). Note that we have to set \tilde{M}^{ij} equal to the trace-free part of the extrinsic curvature.

Now suppose we have a guess for a metric and an extrinsic curvature, which—most likely—will not satisfy the constraint equations (6.3) and (6.4). Set $\tilde{\gamma}_{ij}$ to the guess for the metric, and set K and \tilde{M}^{ij} to the trace and trace-free piece of the guess of the extrinsic curvature. By solving the conformal TT equations we can compute (γ_{ij}, K^{ij}) that satisfy the constraint equations. If our initial guess is

“close” to a true solution, we will have $\psi \approx 1$ and $V^i \approx 0$, so that γ_{ij} and K^{ij} will be close to our initial guess.

Thus one can guess a metric and extrinsic curvature as well as possible and then solve the conformal TT equations to obtain corrected quantities that satisfy the constraint equations.

An artifact of the conformal TT decomposition is that one has no direct handle on the transverse traceless piece with respect to the *physical* metric. For any vector X^i ,

$$(\mathbb{L}X)^{ij} = \psi^{-4}(\tilde{\mathbb{L}}X)^{ij}. \quad (6.19)$$

Thus, Eqs. (6.10) and (6.11) imply

$$A^{ij} = \psi^{-10}\tilde{A}_{TT}^{ij} + \psi^{-6}(\mathbb{L}X)^{ij}. \quad (6.20)$$

For any symmetric traceless tensor S^{ij}

$$\nabla_j S^{ij} = \psi^{-10}\tilde{\nabla}_j(\psi^{10}S^{ij}). \quad (6.21)$$

Therefore the first term on the right hand side of Eq. (6.20) is transverse-traceless with respect to the physical metric,

$$\nabla_j(\psi^{-10}\tilde{A}_{TT}^{ij}) = 0. \quad (6.22)$$

However, the second term on the right hand side of Eq. (6.20) is conformally weighted. Therefore, Eq. (6.20) does not represent the usual TT decomposition.

Physical TT Decomposition

In this case one decomposes the physical traceless extrinsic curvature directly:

$$A^{ij} = A_{TT}^{ij} + (\mathbb{L}X)^{ij}. \quad (6.23)$$

As above in the conformal TT decomposition, the momentum constraint becomes an elliptic equation for X^i . We can again incorporate the construction of the symmetric transverse traceless tensor A_{TT}^{ij} from a general symmetric tensor \tilde{M}^{ij} into the momentum constraint. Then one obtains the *physical TT equations*:

$$\tilde{\nabla}^2\psi - \frac{1}{8}\psi\tilde{R} - \frac{1}{12}\psi^5K^2 + \frac{1}{8}\psi^5\tilde{A}_{ij}\tilde{A}^{ij} = -2\pi G\psi^5\rho, \quad (6.24)$$

$$\tilde{\Delta}_L V^i + 6(\tilde{\mathbb{L}}V)^{ij}\tilde{\nabla}_j \ln \psi - \frac{2}{3}\tilde{\nabla}^i K + \psi^{-6}\tilde{\nabla}_j \tilde{M}^{ij} = 8\pi G\psi^4 j^i, \quad (6.25)$$

where \tilde{A}^{ij} is defined by

$$\tilde{A}^{ij} = (\tilde{\mathbb{L}}V)^{ij} + \psi^{-6}\tilde{M}^{ij}. \quad (6.26)$$

When we have solved (6.24) and (6.25) for ψ and V^i , the physical metric is given by (6.8), and the extrinsic curvature is

$$K^{ij} = \psi^{-4} \left(\tilde{A}^{ij} + \frac{1}{3}\tilde{\gamma}^{ij}K \right). \quad (6.27)$$

We are free to specify the background metric $\tilde{\gamma}_{ij}$, the trace of the extrinsic curvature K , and a symmetric traceless tensor \tilde{M}^{ij} . As with the conformal TT equations, the solution V^i will contain a contribution that removes the longitudinal piece from \tilde{M}^{ij} and a piece that solves the momentum constraint if \tilde{M}^{ij} were transverse-traceless.

These equations can be used in the same way as the conformal TT equations. Guess a metric and extrinsic curvature, set $\tilde{\gamma}_{ij}$ to the guess for the metric, and K and \tilde{M}^{ij} to the trace and trace-free pieces of the guess for the extrinsic curvature. Then solve the physical TT equations to obtain a corrected metric γ_{ij} and a corrected extrinsic curvature K^{ij} that satisfy the constraint equations.

The transverse traceless piece of K^{ij} (with respect to γ_{ij}) will be the transverse traceless piece of $\psi^{-10}\tilde{M}^{ij}$. One can also easily rewrite the physical TT equations such that $\psi^{-10}\tilde{M}^{ij}$ can be freely chosen instead of \tilde{M}^{ij} . So, in this decomposition we can directly control the TT piece of the physical extrinsic curvature. We have chosen to follow [20] since it seems somewhat more natural to specify two conformal quantities, $\tilde{\gamma}_{ij}$ and \tilde{M}^{ij} than to specify one conformal and one physical quantity.

Conformal thin sandwich decomposition

The conformal and physical TT decompositions rely on a tensor splitting to decompose the trace-free part of the extrinsic curvature. In contrast, the conformal thin sandwich decomposition simply defines A^{ij} by Eq. (6.10) and the decomposition

$$\tilde{A}^{ij} \equiv \frac{1}{2\tilde{\alpha}} \left((\tilde{\mathbb{L}}\beta)^{ij} - \tilde{u}^{ij} \right), \quad (6.28)$$

where \tilde{u}^{ij} is symmetric and tracefree. Eq. (6.28) is motivated by Eq. (6.6): If one evolves an initial-data set with A^{ij} of the form (6.28) using as lapse and shift

$$\begin{aligned} N &= \psi^6\tilde{\alpha}, \\ N^i &= \beta^i, \end{aligned} \quad (6.29)$$

then

$$\text{TF}(\partial_t \gamma_{ij}) = \psi^4 \tilde{u}_{ij}. \quad (6.30)$$

Therefore, the decomposition (6.28) is closely related to the kinematical quantities in an evolution. Although $\tilde{\alpha}$ and β^i are introduced in the context of initial data, one usually refers to them as the “conformal lapse” and “shift”. While the form of Eq. (6.28) is similar in form to the conformal and physical TT decompositions, there are differences. In particular, \tilde{u}^{ij} is *not* divergenceless.

Within the *conformal thin sandwich decomposition*, the constraint equations take the form:

$$\tilde{\nabla}^2 \psi - \frac{1}{8} \psi \tilde{R} - \frac{1}{12} \psi^5 K^2 + \frac{1}{8} \psi^{-7} \tilde{A}_{ij} \tilde{A}^{ij} = -2\pi G \psi^5 \rho \quad (6.31)$$

$$\begin{aligned} \tilde{\Delta}_L \beta^i - (\tilde{\mathbb{L}}\beta)^{ij} \tilde{\nabla}_j \ln \tilde{\alpha} - \frac{4}{3} \tilde{\alpha} \psi^6 \tilde{\nabla}^i K \\ - \tilde{\alpha} \tilde{\nabla}_j \left(\frac{1}{\tilde{\alpha}} \tilde{u}^{ij} \right) = 16\pi G \tilde{\alpha} \psi^{10} j^i \end{aligned} \quad (6.32)$$

Having solved Eqs. (6.31) and (6.32) for ψ and the vector β^i , one obtains the physical metric from (6.8) and the extrinsic curvature from

$$K^{ij} = \psi^{-10} \tilde{A}^{ij} + \frac{1}{3} \psi^{-4} \tilde{\gamma}^{ij} K. \quad (6.33)$$

In this decomposition we are free to specify a conformal metric $\tilde{\gamma}_{ij}$, the trace of the extrinsic curvature K , a symmetric trace-free tensor \tilde{u}^{ij} and a function $\tilde{\alpha}$.

It seems that the conformal thin sandwich decomposition contains additional degrees of freedom in the form of the function $\tilde{\alpha}$ and three additional unconstrained components of \tilde{u}^{ij} . This is not the case. The longitudinal piece of \tilde{u}^{ij} corresponds to the gauge choice of the actual shift vector used in an evolution. Thus \tilde{u}^{ij} really only contributes two degrees of freedom, just like \tilde{M}^{ij} in the conformal and physical TT decompositions. Furthermore, we can reach any *reasonable* physical solution (γ_{ij}, K^{ij}) with any *reasonable* choice of $\tilde{\alpha}$; each choice of $\tilde{\alpha}$ simply defines a new decomposition. A forthcoming article by York[2] will elaborate on these ideas. Note that for $\tilde{\alpha} = 1/2$ we recover the conformal TT decomposition.

Let us now turn to the question of how one should pick the freely specifiable data in the conformal thin sandwich approach. We motivate our prescription again by considering how to recover a known spacetime: Assume we are given a full four-dimensional spacetime with 3+1 quantities γ_{0ij} , K_0^{ij} , N_0^i and N_0 . Further assume the spacetime is stationary and the slicing is such that $\partial_t \gamma_{ij} = \partial_t K_{ij} = 0$. An

example for such a situation is a Kerr black hole in Kerr-Schild or Boyer-Lindquist coordinates.

Using $\partial_t \gamma_{0ij} = 0$ in Eq. (6.6) yields a relation for the trace-free extrinsic curvature

$$A_0^{ij} = \frac{1}{2N_0} (\mathbb{L}N_0)^{ij}. \quad (6.34)$$

This is a decomposition of the form (6.28) with $\tilde{u}^{ij} = 0$. Therefore, if we choose the freely specifiable data for the conformal thin sandwich equations as

$$\begin{aligned} \tilde{\gamma}_{ij} &= \gamma_{0ij}, & \tilde{\alpha} &= N_0, \\ K &= K_0, & \tilde{u}^{ij} &= 0, \end{aligned} \quad (6.35)$$

and if we use appropriate boundary conditions, then the solution of the conformal thin sandwich equations will be $\psi = 1$ and $\beta^i = N_0^i$. As part of the solution, we obtain the shift vector needed for an evolution to produce $\text{TF}(\partial_t \gamma_{ij}) = 0$. Not needing a guess for the trace-free extrinsic curvature, and having the solution β^i automatically provide an initial shift for evolution, make the conformal thin sandwich equations very attractive.

In order to generate initial-data slices that permit an evolution with zero time derivative of the conformal metric — a highly desirable feature for quasi-equilibrium data, or for a situation with holes momentarily at rest — one can proceed as follows: Set $\tilde{\gamma}_{ij}$ and K to the guess for the metric and trace of extrinsic curvature, respectively. Set $\tilde{\alpha}$ to the lapse function that one is going to use in the evolution, and set $\tilde{u}^{ij} = 0$. If these guesses are good, the conformal factor ψ will be close to 1, and $N = \psi^6 \tilde{\alpha}$ as well as $N^i = \beta^i$ give us the actual lapse function and shift vector to use in the evolution.

6.3 Choices for the freely specifiable data

6.3.1 Kerr-Schild coordinates

We base our choice for the freely specifiable data on a superposition of two Kerr black holes in Kerr-Schild coordinates. In this section we describe the Kerr-Schild solution and collect necessary equations. We also describe how we compute the 3-metric, lapse, shift and extrinsic curvature for a boosted black hole with arbitrary spin.

A Kerr-Schild metric is given by

$$g_{\mu\nu} = \eta_{\mu\nu} + 2Hl_\mu l_\nu, \quad (6.36)$$

where $\eta_{\mu\nu}$ is the Minkowski metric, and l_μ is a null-vector with respect to both the full metric and the Minkowski metric: $g^{\mu\nu}l_\mu l_\nu = \eta^{\mu\nu}l_\mu l_\nu = 0$. The 3-metric, lapse and shift are

$$\gamma_{ij} = \delta_{ij} + 2Hl_i l_j, \quad (6.37)$$

$$N = (1 + 2Hl^t l^t)^{-1/2}, \quad (6.38)$$

$$N^i = -\frac{2Hl^t l^i}{1 + 2Hl^t l^t}. \quad (6.39)$$

For a black hole at rest at the origin with mass M and angular momentum $M\vec{a}$, one has

$$H = \frac{Mr^3}{r^4 + (\vec{a} \cdot \vec{x})^2}, \quad (6.40)$$

$$l_\mu^{\text{rest}} = (1, \vec{l}_{\text{rest}}), \quad (6.41)$$

$$\vec{l}_{\text{rest}} = \frac{r\vec{x} - \vec{a} \times \vec{x} + (\vec{a} \cdot \vec{x})\vec{a}/r}{r^2 + a^2}, \quad (6.42)$$

with

$$r^2 = \frac{\vec{x}^2 - \vec{a}^2}{2} + \left(\frac{(\vec{x}^2 - \vec{a}^2)^2}{4} + (\vec{a} \cdot \vec{x})^2 \right)^{1/2}. \quad (6.43)$$

For a nonrotating black hole with $\vec{a} = 0$, H has a pole at the origin, whereas for rotating black holes, r has a ring singularity. We will therefore have to excise from the computational domain a region close to the center of the Kerr-Schild black hole.

Under a boost, a Kerr-Schild coordinate system transforms into a Kerr-Schild coordinate system. Applying a Lorentz transformation with boost velocity v^i to l_μ^{rest} , we obtain the null-vector l_μ of the boosted Kerr-Schild coordinate system. Eqs. (6.37-6.39) give then the boosted 3-metric, lapse, and shift. Since all time-dependence is in the uniform motion, evolution with lapse N and shift N^i yields $\partial_t \gamma_{ij} = -v^k \partial_k \gamma_{ij}$, and from Eq. (6.5) one can compute the extrinsic curvature

$$K_{ij} = \frac{1}{2N} (v^k \partial_k \gamma_{ij} + \nabla_i N_j + \nabla_j N_i). \quad (6.44)$$

If this initial-data set is evolved with the shift N^i , the black hole will move through the coordinate space with velocity v^i . However, if the evolution uses the

shift vector $N^i + v^i$, the coordinates will move with the black hole, and the hole will be at rest in coordinate space. The spacetime is nonetheless different from a Kerr black hole at rest. The ADM-momentum will be $P_{ADM}^i = \gamma M v^i$, where M is the rest-mass of the hole and $\gamma = (1 - \bar{v}^2)^{-1/2}$.

6.3.2 Freely specifiable pieces

We want to generate initial data for a spacetime containing two black holes with masses $M_{A,B}$, velocities $\vec{v}_{A,B}$ and spins $M_A \vec{a}_A$ and $M_B \vec{a}_B$.

We follow the proposal of Matzner et al [63, 56] and base our choices for the freely specifiable choices on two Kerr-Schild coordinate systems describing two individual black holes. The first black hole with label A has an associated Kerr-Schild coordinate system with metric

$$\gamma_{Aij} = \delta_{ij} + 2H_A l_{Ai} l_{Aj}, \quad (6.45)$$

and with an extrinsic curvature K_{Aij} , a lapse N_A and a shift N_A^i . The trace of the extrinsic curvature is K_A . All these quantities can be computed as described in the previous section, 6.3.1. The second black hole has a similar set of associated quantities which are labeled with the letter B.

For all three decompositions, we need to choose a conformal metric and the trace of the extrinsic curvature. We choose

$$\tilde{\gamma}_{ij} = \delta_{ij} + 2H_A l_{Ai} l_{Aj} + 2H_B l_{Bi} l_{Bj} \quad (6.46)$$

$$K = K_A + K_B \quad (6.47)$$

The metric is singular at the center of each hole. Therefore we have to excise spheres around the center of each hole from the computational domain. We now specify for each decomposition the remaining freely specifiable pieces and boundary conditions.

Conformal TT and physical TT decompositions

For the conformal TT and physical TT decompositions we will be solving for a correction to our guesses. As guess for the trace-free extrinsic curvature, we use a superposition

$$\tilde{M}^{ij} = \left(K_{Ak}^{(i} + K_{Bk}^{(i} - \frac{1}{3} \delta_k^{(i} (K_A + K_B) \right) \tilde{\gamma}^{j)k}. \quad (6.48)$$

\tilde{M}^{ij} is symmetric and trace-free with respect to the conformal metric, $\tilde{\gamma}_{ij}\tilde{M}^{ij} = 0$. Solving for a correction only, we expect that $\psi \approx 1$ and $V^i \approx 0$, hence we use Dirichlet boundary conditions

$$\psi = 1, \quad V^i = 0. \quad (6.49)$$

Conformal thin sandwich

For conformal thin sandwich, we restrict the discussion to either two black holes at rest, or in a quasi-circular orbit in corotating coordinates. In these cases, one expects small or even vanishing time-derivatives, $\partial_t \gamma_{ij} \approx 0$, and so Eq. (6.30) yields the simple choice

$$\tilde{u}^{ij} = 0. \quad (6.50)$$

The conformal 3-metric and the trace of the extrinsic curvature are still given by Eqs. (6.46) and (6.47). Orbiting black holes in a corotating frame will not move in coordinate space, therefore we do not boost the individual Kerr-Schild metrics in this decomposition: $v_{A/B}^i = 0$. The lapse functions $N_{A/B}$ and the shifts $N_{A/B}^i$ are also for unboosted Kerr-Schild black holes.

We use Dirichlet boundary conditions:

$$\psi = 1 \quad \text{all boundaries} \quad (6.51a)$$

$$\beta^i = N_A^i \quad \text{sphere inside hole A} \quad (6.51b)$$

$$\beta^i = N_B^i \quad \text{sphere inside hole B} \quad (6.51c)$$

$$\beta^i = \vec{\Omega} \times \vec{r} \quad \text{outer boundary} \quad (6.51d)$$

Eq. (6.51d) ensures that we are in a corotating reference frame; the cross-product is performed in flat space, and $\vec{\Omega} = 0$ corresponds to two black holes at rest. Close to the holes we force the shift to be the shift of a single black hole in the hope that this choice will produce a hole that is at rest in coordinate space.

For the conformal lapse we use

$$\tilde{\alpha} = N_A + N_B - 1 \quad (6.52)$$

or

$$\tilde{\alpha} = N_A N_B. \quad (6.53)$$

The first choice of $\tilde{\alpha}$ follows the philosophy of adding quantities of each individual hole. However, $\tilde{\alpha}$ of Eq. (6.52) becomes negative sufficiently close to the center of

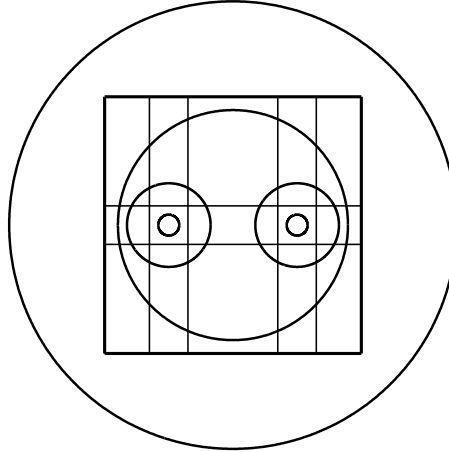


Figure 6.1: Structure of domains. Spherical shells around each excised sphere are surrounded by 43 rectangular blocks and another spherical shell. The rectangular blocks touch each other and overlap with all three spherical shells.

each hole and is therefore a bad choice if the excised spheres are small. The choice (6.53) does not change sign and has at large distances the same behavior (same $1/r$ term) as (6.52).

6.4 Numerical Implementation

We implemented an elliptic solver that can solve all three decompositions we described above in complete generality. The solver uses domain decomposition and can handle nontrivial topologies. It is based on pseudospectral collocation, that is, it expresses the solution in each subdomain as an expansion in basis functions. This elliptic solver is described in detail in a separate paper [86].

From the computational domain we excise two spheres containing the singularities of the Kerr-Schild metric close to the center of each hole. Around each of the excised spheres we place a spherical shell. These shells are patched together with $5 \times 3 \times 3 = 45$ rectangular blocks, with the two blocks at the location of the spheres removed. Around these 43 blocks, another spherical shell is placed that extends far out, typically to an outer radius of $10^7 M$. In the rectangular blocks, we expand in Chebyshev polynomials, while in the spheres we use Chebyshev polynomials radially and spherical harmonics for the angular variables. This setup is depicted in Fig. 6.1.

The domain decomposition in Fig. 6.1 is fairly complicated. Even if the shells were made as large as possible, they do not cover the full computational domain when the excised spheres are close together. Thus additional subdomains are needed in any case. Choosing the 43 cubes as depicted allows for relatively small inner shells and for a relatively large inner radius of the outer shell. Thus each shell covers a region of the computational domain in which the angular variations of the solution are fairly low, allowing for comparatively few angular basis-functions.

The code can handle a general conformal metric. In principle, the user needs to specify only $\tilde{\gamma}_{ij}$. Then the code computes $\tilde{\gamma}^{ij}$, and —using numerical derivatives— the Christoffel symbols, Ricci tensor and Riemann scalar. For the special case of the Kerr-Schild metric of a single black hole and the superposition of two Kerr-Schild metrics, Eq. (6.46), we compute first derivatives analytically and use numerical derivatives only to compute the Riemann tensor.

The solver implements Eqs. (6.12) and (6.13) for the conformal TT decomposition, Eqs. (6.24) and (6.25) for the physical TT decomposition, and Eqs. (6.31) and (6.32) for the conformal thin sandwich decomposition.

After solving for (ψ, V^i) [conformal TT and physical TT], or (ψ, β^i) [thin sandwich] we compute the physical metric γ_{ij} and the physical extrinsic curvature K^{ij} of the solution. Utilizing these physical quantities (γ_{ij}, K^{ij}) , we implement several analysis tools. We evaluate the constraints in the form of Eq. (6.3) and (6.4), we compute ADM-quantities and we search for apparent horizons. Note that these analysis tools are completely independent of the particular decomposition; they rely only on γ_{ij} and K^{ij} .

Next we present tests ensuring that the various systems of equations are solved correctly. We also include tests of the analysis tools showing that we can indeed compute constraints, ADM-quantities and apparent horizons with good accuracy.

6.4.1 Testing the conformal TT and physical TT decompositions

We can test the solver by conformally distorting a known solution of the constraint equations. Given a solution to the constraint equations (γ_{0ij}, K_0^{ij}) pick functions

$$\Psi > 0, \quad W^i \tag{6.54}$$

and set

$$\tilde{\gamma}_{ij} = \Psi^{-4} \gamma_{0ij}, \quad (6.55)$$

$$K = K_0, \quad (6.56)$$

and

$$\tilde{M}^{ij} = \Psi^{10} \left(K_0^{ij} - \frac{1}{3} \gamma_0^{ij} K_0 \right) - \Psi^4 (\mathbb{L}_0 W)^{ij} \quad (6.57)$$

for conformal TT or

$$\tilde{M}^{ij} = \Psi^{10} \left(K_0^{ij} - \frac{1}{3} \gamma_0^{ij} K_0 - (\mathbb{L}_0 W)^{ij} \right) \quad (6.58)$$

for physical TT. With these freely specifiable pieces and appropriate boundary conditions, a solution of the conformal TT equations (6.12), (6.13) or the physical TT equations (6.24), (6.25) will be

$$\psi = \Psi \quad (6.59)$$

$$V^i = W^i. \quad (6.60)$$

From Eq. (6.8) we recover our initial metric γ_{0ij} , and from Eq. (6.16) [conformal TT] or Eq. (6.27) [physical TT] we recover the extrinsic curvature K_0^{ij} .

In our tests we used the particular choices

$$\Psi = 1 + \frac{8(r-2)}{36 + x^2 + 0.9y^2 + 1.3(z-1)^2} \quad (6.61)$$

$$W^i = \frac{50(r-2)}{(6^4 + r^4)} (-y, x, 1). \quad (6.62)$$

These functions are plotted in Fig. 6.2. Ψ varies between 0.8 and 1.5, W^i varies between ± 0.5 , and both take their maximum values around distance ~ 7 from the center of the hole. We used for $(\tilde{\gamma}_{0ij}, K_0^{ij})$ a single, boosted, spinning black hole in Kerr-Schild coordinates.

Figure 6.3 shows results of testing the conformal TT decomposition on a single spherical shell. The numerical solution (ψ, V^i) converges to the analytic solutions (Ψ, W^i) exponentially with the number of basis functions as expected for a properly constructed spectral method. Moreover, the reconstructed metric and extrinsic curvature satisfy the constraints.

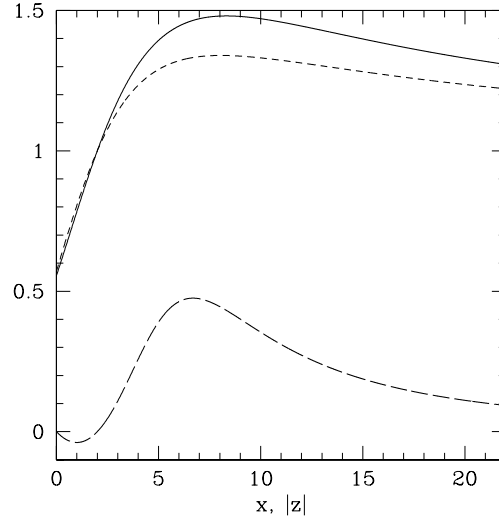


Figure 6.2: Plot of the functions Ψ and W^i from Eqs. (6.61) and (6.62). The solid line depicts Ψ along the positive x -axis, the short dashed line depicts Ψ along the negative z -axis. The long dashed line is a plot of W^y along the positive x -axis.

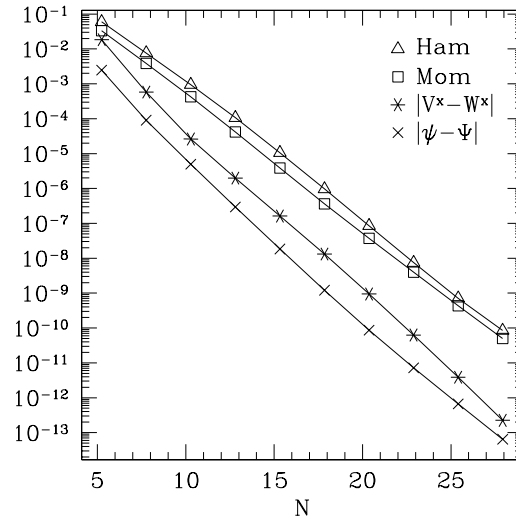


Figure 6.3: Testing the solver for the conformal TT decomposition. Eqs. (6.12-6.13) with freely specifiable data given by Eqs. (6.55-6.57) are solved in a single spherical shell with $1.5M < r < 10M$. N is the cube root of the total number of unknowns. Plotted are the L2-norms of $\psi - \Psi$, $V^x - W^x$, and the residuals of Hamiltonian and momentum constraints, Eqs. (6.3) and (6.4).

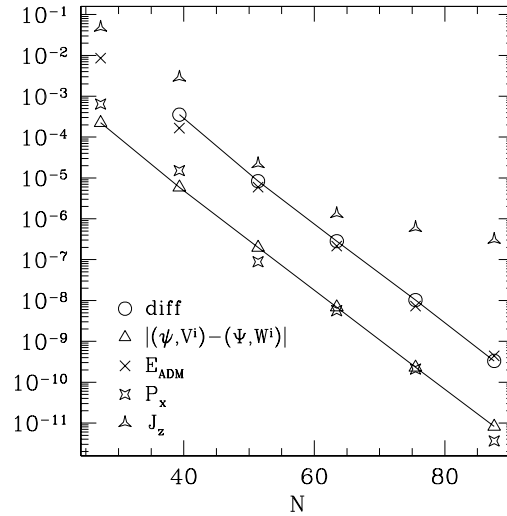


Figure 6.4: Physical TT decomposition with domain decomposition. Eqs. (6.24), (6.25) with freely specifiable data given by Eq. (6.55, 6.56, 6.58) are solved in multiple domains (one inner spherical shell, 26 rectangular blocks, one outer spherical shell). N is the cube root of the total number of grid-points. *diff* denotes the L_2 -norm of the difference of the solution and the solution at next lower resolution. Triangles denote the L_2 -norm of the difference to the analytic solution. The remaining symbols denote the errors of numerically extracted ADM-quantities.

Now we test the solver for the physical TT decomposition, and demonstrate that we can correctly deal with multiple domains. In this example the computational domain is covered by an inner spherical shell extending for $1.5M \leq r \leq 10M$. This shell is surrounded by 26 rectangular blocks that overlap with the shell and extend out to $x, y, z = \pm 25M$. Finally another spherical shell covers the region $20M \leq r \leq 10^6M$. As can be seen in Fig. 6.4, the solution converges again exponentially.

For realistic cases we do not know the analytic solution and therefore need a measure of the error. Our major tool will be the change in results between different resolution. In particular we consider the L_2 norm of the point-wise differences of the solution at some resolution and at the next lower resolution. This diagnostic is labeled by circles in Fig. 6.4. Since the solution converges exponentially, these circles essentially give the error of the *lower* of the two resolutions.

In addition to testing the equations, this example tests domain decomposition

and the integration routines for the ADM quantities. The ADM quantities are computed by the standard integrals at infinity in Cartesian coordinates,

$$E_{ADM} = \frac{1}{16\pi} \int_{\infty} (\gamma_{ij,j} - \gamma_{jj,i}) d^2 S_i, \quad (6.63)$$

$$J_{(\xi)} = \frac{1}{8\pi} \int_{\infty} (K^{ij} - \gamma^{ij} K) \xi_j d^2 S_i. \quad (6.64)$$

For the x -component of the linear ADM-momentum, $\xi = \hat{e}_x$ in Eq. (6.64). The choice $\xi = x\hat{e}_y - y\hat{e}_x$ yields the z -component of the ADM-like angular momentum as defined by York [4]. Since the space is asymptotically flat there is no distinction between upper and lower indices in Eqs. (6.63) and (6.64). Note that Eq. (6.63) reduces to the familiar monopole term

$$-\frac{1}{2\pi} \int_{\infty} \partial_r \psi dA \quad (6.65)$$

only for quasi-isotropic coordinates. Our outer domain is large, but since it does not extend to infinity, we extrapolate $r \rightarrow \infty$.

For a Kerr black hole with mass M and spin \vec{a} , that is boosted to velocity \vec{v} , the ADM-quantities will be

$$E_{ADM} = \gamma M, \quad (6.66)$$

$$\vec{P}_{ADM} = \gamma M \vec{v}, \quad (6.67)$$

$$\vec{J}_{ADM} = \left[\gamma \vec{a} - (\gamma - 1) \frac{(\vec{a} \vec{v}) \vec{v}}{v^2} \right] M, \quad (6.68)$$

where $\gamma = (1 - v^2)^{-1/2}$ denotes the Lorentz factor. Eq. (6.68) reflects the fact that under a boost, the component of the angular momentum perpendicular to the boost-direction is multiplied by γ .

The example in Fig. 6.4 uses $\vec{v} = (0.2, 0.3, 0.4)$, and $\vec{a} = (-1/4, 1/4, 1/6)M$. The evaluation of the angular momentum J_z seems to be less accurate since our current procedure to extrapolate to infinity magnifies roundoff. We plan to improve this in a future version of the code. Until then we seem to be limited to an accuracy of $\sim 10^{-6}$.

6.4.2 Testing conformal thin sandwich equations

The previous decompositions could be tested with a conformally distorted known solution. In order to test the conformal thin sandwich decomposition we need to

find an analytic decomposition of the form (6.28). To do this, we start with a stationary solution of Einstein's equations and boost it with uniform velocity v^i . Denote the metric, extrinsic curvature, lapse and shift of this boosted spacetime by $\tilde{\gamma}_{0ij}$, $K_0^{ij} = A_0^{ij} + \frac{1}{3}\gamma_0^{ij}K_0$, N_0 and N_0^i , respectively. Since we boosted the static solution, we will *not* find $\partial_t\gamma_{ij} = 0$ if we evolve it with the shift N_0^i . However, all time-dependence of this spacetime is due to the uniform motion, so in the comoving reference frame specified by the shift $N_0^i + v^i$, we will find $\partial_t\gamma_{ij} = 0$. In this case, Eq. (6.6) yields

$$A_0^{ij} = \frac{1}{2N_0}(\mathbb{L}(N_0 + v))^{ij}. \quad (6.69)$$

If we choose $\tilde{\alpha} = N_0$ and $\tilde{u}^{ij} = 0$, the thin sandwich equations (6.31) and (6.32) will thus be solved by $\psi = 1$ and $\beta^i = N_0^i + v^i$. Similar to the conformal TT and physical TT decomposition above, we can also conformally distort the metric γ_{0ij} . Furthermore, we can consider nonvanishing \tilde{u}^{ij} . We arrive at the following method to test the solver for the conformal thin sandwich equations:

Given a boosted version of a stationary solution with shift N_0^i , lapse N_0 , 3-metric γ_{0ij} , trace of extrinsic curvature K_0 , and boost-velocity v^i . Pick any functions

$$\Psi > 0 \quad (6.70)$$

$$W^i \quad (6.71)$$

and set

$$\tilde{\gamma}_{ij} = \Psi^{-4}\gamma_{0ij} \quad (6.72)$$

$$K = K_0 \quad (6.73)$$

$$\tilde{\alpha} = \Psi^{-6}N_0 \quad (6.74)$$

$$\tilde{u}^{ij} = \Psi^4(\mathbb{L}_0W)^{ij} \quad (6.75)$$

Then a solution to the thin sandwich equations (6.31-6.32) will be

$$\psi = \Psi \quad (6.76)$$

$$\beta^i = N_0^i + v^i + W^i \quad (6.77)$$

assuming boundary conditions respecting this solution.

Figure 6.5 shows results of this test for a single spherical shell and a Kerr black hole with $\vec{v} = (0.2, -0.3, 0.1)$, $\vec{a} = (0.4, 0.3, 0.1)M$. The solution converges to the

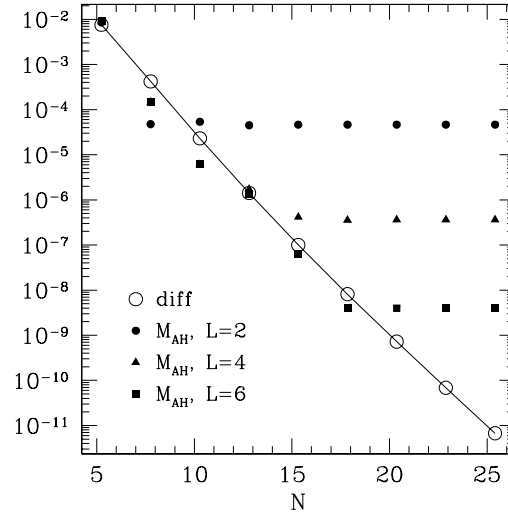


Figure 6.5: Testing thin sandwich decomposition with apparent horizon searches. Equations (6.31) and (6.32) with freely specifiable data given by Eqs. (6.72)–(6.75) are solved in a single spherical shell. N and $diff$ as in Fig. 6.4. Apparent horizon searches with different surface expansion order L were performed, and the errors of the apparent horizon mass M_{AH} are plotted.

expected analytical result exponentially. In addition, apparent horizon searches were performed. For the numerically found apparent horizons, the apparent horizon area A_{AH} as well as the apparent horizon mass

$$M_{AH} = \sqrt{\frac{A_{AH}}{16\pi}} \quad (6.78)$$

were computed. The figure compares M_{AH} to the expected value

$$M \left(\frac{1}{2} + \frac{1}{2} \sqrt{1 - \frac{\vec{a}^2}{M^2}} \right)^{1/2}. \quad (6.79)$$

As described in [64, 65], the apparent horizon finder expands the apparent horizon surface in spherical harmonics up to a fixed order L . For fixed L , the error in the apparent horizon mass is dominated by discretization error of the elliptic solver at low resolution N . As N is increased, the discretization error of the elliptic solver falls below the error due to finite L . Then the error in M_{AH} becomes independent of N . Since the expansion in spherical harmonics is *spectral*, the achievable resolution increases exponentially with L . Note that for exponential

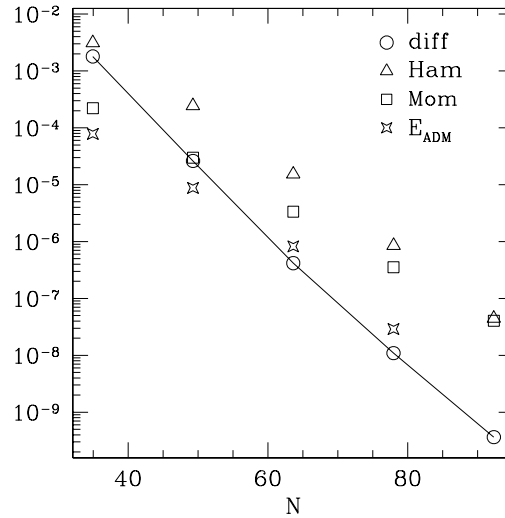


Figure 6.6: Binary black hole with conformal TT decomposition. The residuals of several quantities are plotted as a function of the cube root of the total number of grid points. *diff* as in Fig. 6.4, *Ham* and *Mom* are the residuals of Hamiltonian and momentum constraints. E_{ADM} denotes the difference between ADM-energy at resolution N and ADM-energy at highest resolution.

convergence it is necessary to position the rays in the apparent horizon finder at the abscissas of Gauss-Legendre integration.

6.4.3 Convergence of binary black hole solutions

Figure 6.6 present the convergence of the solver in the binary black hole case. In this particular example, the conformal TT equations were solved for two black holes at rest with coordinate separation of $10M$. The computational domain is structured as in Fig. 6.1. The excised spheres have radius $r_{exc} = 2M$, the inner spherical shells extend to radius $4M$. The rectangular blocks cover space up to $x, y, z = \pm 25M$, and the outer spherical shell extending from inner radius $20M$ to an outer radius of $R = 10^7M$.

We do not use fall-off boundary conditions at the outer boundary; we simply set $\psi = 1$ there. This limits the computations presented in this paper to an accuracy of order $1/R \sim 10^{-7}$. Figure 6.6 shows that even for the next to highest resolution ($N \approx 80$) the solution will be limited by the outer boundary condition. All results presented in the following section are obtained at resolutions around $N \approx 80$. If

the need arises to obtain solutions with higher accuracy, one can easily change to a fall-off boundary condition, or just move the outer boundary further out.

6.5 Results

The purpose of this paper is to compare the initial-data sets generated by different decompositions using simple choices for the freely specifiable pieces in each decomposition. We solve

- **ConfTT:** Conformal TT equations (6.12) and (6.13) with freely specifiable pieces and boundary conditions given by Eqs. (6.46), (6.47), (6.48) and (6.49).

- **PhysTT:** Physical TT equations (6.24) and (6.25) with same freely specifiable pieces and boundary conditions as ConfTT.

- **CTS:** Conformal thin sandwich equations (6.31) and (6.32) with freely specifiable pieces and boundary conditions given by Eqs. (6.46), (6.47), (6.50) and (6.51). The lapse $\tilde{\alpha}$ is given by either Eq. (6.52), or by Eq. (6.53).

We will apply the terms “ConfTT”, “PhysTT” and “CTS” only to these particular choices of decomposition, freely specifiable pieces and boundary conditions. When referring to different freely specifiable pieces, or a decomposition in general, we will not use these shortcuts. If we need to distinguish between the two choices of $\tilde{\alpha}$ in CTS, we will use “CTS-add” for the additive lapse Eq. (6.52) and “CTS-mult” for the multiplicative lapse Eq. (6.53). Below in section 6.5.3 we will also introduce as a fourth term “mConfTT”.

6.5.1 Binary black hole at rest

We first examine the simplest possible configuration: Two black holes at rest with equal mass, zero spin, and with some fixed proper separation between the apparent horizons of the holes. We solve

- ConfTT
- PhysTT
- CTS (with both choices of $\tilde{\alpha}$).

In the comparisons, we also include inversion symmetric conformally flat initial data obtained with the conformal-imaging formalism.

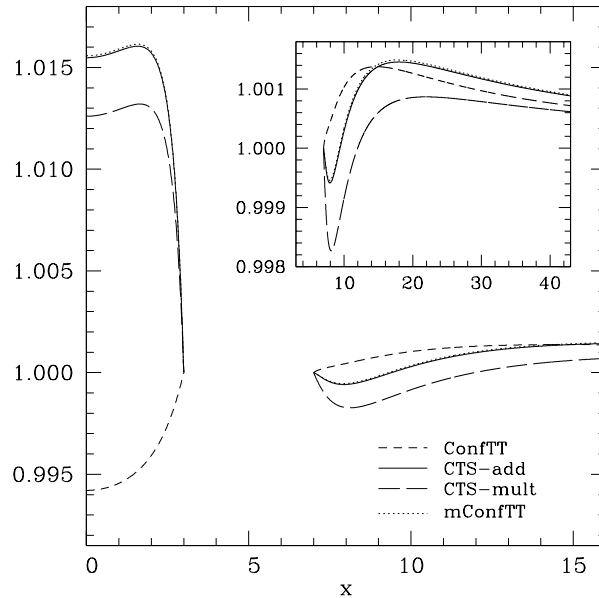


Figure 6.7: The conformal factor ψ along the axis connecting the holes for several decompositions. x measures the distance from the center of mass, so that the excised sphere is located between $3 < x < 7$. mConfTT is explained below in section 6.5.3. The solution of PhysTT is not plotted since it is within the line thickness of ConfTT. The insert shows an enlargement for large x .

We excised spheres with radius $r_{exc} = 2M$, which is close to the event horizon for an individual Eddington-Finkelstein black hole. This results in the boundary conditions being imposed close to, but within the apparent horizons of the black holes. The centers of the excised spheres have a coordinate separation of $d = 10M$.

We now discuss the solutions. The conformal factor ψ is very close to 1 for each of the three decompositions. It deviates from 1 by less than 0.02, indicating that a conformal metric based of a superposition of Kerr-Schild metrics does not deviate far from the constraint surface.

Figure 6.7 presents a plot of the conformal factor along the axis through the centers of the holes. One sees that ψ is close to 1; however, between the holes ConfTT and CTS force ψ in *opposite* directions. For CTS, $\psi > 1$ between the holes, for ConfTT, $\psi < 1$! The contour plots in Fig. 6.8 also show this striking difference between the decompositions.

The result of PhysTT was found to be almost identical with ConfTT. This is reasonable, since these two decompositions differ only in that in one case the TT

Table 6.1: Solutions of different decompositions for two black holes at rest. Ham and Mom are the rms residuals of the Hamiltonian and momentum constraint, ℓ is the proper separation between the apparent horizons. *mConfTT* represents the modified conformal TT decomposition which is explained in section 6.5.3. *inv. symm.* represents a conformally flat, time symmetric and inversion symmetric solution of the Hamiltonian constraint.

	Ham	Mom	E_{ADM}	A_{AH}	M_{AH}	ℓ	ℓ/m	E_{ADM}/m	E_{MPRC}/E_{ADM}	E_b/μ
ConfTT	9×10^{-7}	4×10^{-7}	2.06486	57.7369	1.07175	8.062	3.761	0.9633	0.2660	-0.1467
PhysTT	9×10^{-7}	3×10^{-7}	2.06490	57.7389	1.07176	8.062	3.761	0.9633	0.2660	-0.1467
CTS-add	2×10^{-6}	4×10^{-7}	2.08121	62.3116	1.11340	8.039	3.610	0.9346	0.2434	-0.2615
CTS-mult	2×10^{-6}	5×10^{-7}	2.05851	60.8113	1.09991	8.080	3.672	0.9358	0.2444	-0.2569
mConfTT	3×10^{-6}	1×10^{-6}	2.0827	62.404	1.1142			0.9346	0.2434	-0.2617
inv. symm.	-	-	4.36387	284.851	2.38053	17.731	3.724	0.9166	0.2285	-0.3337

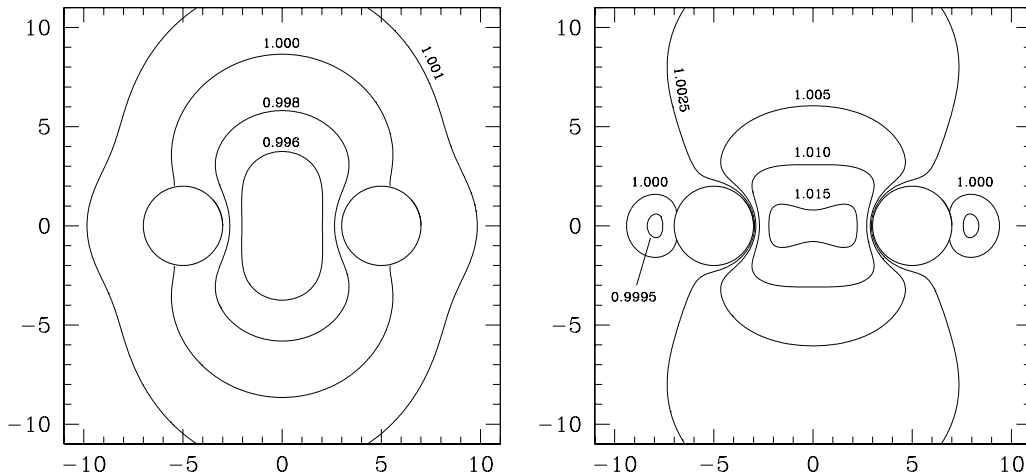


Figure 6.8: Black holes at rest: Contour plots of the conformal factor ψ for ConfTT (left) and CTS-add (right). The circles denote the excised spheres of radius 2.

decomposition is with respect to the conformal metric, and in the other case the TT decomposition it is with respect to the physical metric. Since $\psi \approx 1$, the conformal metric is almost identical to the physical metric, and only minor differences arise. In the following we will often use ConfTT/PhysTT when referring to both data sets.

We performed apparent horizon searches for these cases. For all data sets, the apparent horizon is outside the sphere with radius $2M$, that is outside the coordinate location for the apparent horizon in a single hole spacetime. For ConfTT/PhysTT, the radius of the apparent horizon surface is $\approx 2.05M$, for CTS it is $\approx 2.15M$. We computed the apparent horizon area A_{AH} , the apparent horizon mass

$$M_{AH} = \sqrt{\frac{A_{AH}}{16\pi}} \quad (6.80)$$

of either hole, and the combined mass of both holes,

$$m = 2M_{AH}. \quad (6.81)$$

There is no rigorous definition of the mass of an individual black hole in a binary black hole spacetime, and Eq. (6.80) represents the true mass on an individual black hole only in the limit of wide separation of the black holes. A hard upper limit on the possible gravitational radiation emitted to infinity during the coalescence

process of a binary will be

$$E_{MPRC} = E_{ADM} - \sqrt{\frac{2A_{AH}}{16\pi}}, \quad (6.82)$$

where $2A_{AH}$ is the combined apparent horizon area of both holes. Thus, E_{MPRC} represents the maximum possible radiation content (MPRC) of the initial data. This, of course, makes the unlikely assumption that the binary radiates away all of its angular momentum.

We also compute the proper separation ℓ between the apparent horizon surfaces along the straight line connecting the centers of the excised spheres. In order to compare different data sets we consider the dimensionless quantities ℓ/E_{ADM} , E_{ADM}/m and E_{MPRC}/E_{ADM} . We will also use E_b/μ which will be defined shortly.

Table 6.1 summarizes these quantities for all three decompositions. It also includes results for inversion symmetric initial data, which for black holes at rest reduces to the Misner data[9]¹. The results in Table 6.1 are intended to represent nearly the *same* physical configuration.

From Table 6.1, one finds that the black holes have roughly the same dimensionless proper separation. However, the scaled ADM-energy E_{ADM}/m differs by as much as 4.7% between the different data sets. E_{MPRC}/E_{ADM} , which does not depend on any notion of individual black hole masses at all, differs by 16% between the different data sets.

The inversion symmetric data has lowest E_{ADM}/m and E_{MPRC}/E_{ADM} , CTS has somewhat larger values, and ConfTT/PhysTT lead to the biggest values for E_{ADM}/m and E_{MPRC}/E_{ADM} . This indicates that, relative to the sizes of the black holes, ConfTT/PhysTT and CTS probably contain some excess energy.

A slightly different argument uses the binding energy which is defined as

$$\frac{E_b}{\mu} \equiv \frac{E_{ADM} - 2M_{AH}}{\mu}, \quad (6.83)$$

where $\mu = M_{AH}/2$ is the reduced mass. Two Newtonian point masses at rest satisfy

$$\frac{E_b}{\mu} = -\frac{1}{\ell/m}. \quad (6.84)$$

¹Although the Misner solution can be obtained analytically, we found it more convenient to solve the Hamiltonian constraint numerically. The configuration in Table 6.1 corresponds to a separation $\beta = 12$ in terms of [27].

From Table 6.1 we see that for ConfTT/PhysTT, $|E_b/\mu| > (l/m)^{-1}$, and for CTS, $|E_b/\mu| \approx (l/m)^{-1}$. Since gravity in general relativity is typically *stronger* than Newtonian gravity, we find again that CTS and ConfTT/PhysTT contain too much energy relative to the black hole masses, ConfTT/PhysTT having even more than CTS.

The proper separation between the apparent horizons ℓ/m is about 4% smaller for CTS than for ConfTT/PhysTT. By Eq. (6.84) this should lead to a relative difference in binding energy of the same order of magnitude. Since E_b/μ differs by almost a factor of two between the different decompositions, the differences in ℓ/m play only a minor role.

6.5.2 Configurations with angular momentum

Now we consider configurations which are approximating two black holes in orbit around each other. The conformal metric is still a superposition of two Kerr Schild metrics. The black holes are located along the x -axis with a coordinate separation d . For ConfTT/PhysTT, we boost the individual holes to some velocity $\pm v\hat{e}_y$ along the y -axis. For CTS we go to a co-rotating frame with an angular frequency $\vec{\Omega} = \Omega\hat{e}_z$. Thus, for each decomposition we have a two parameter family of solutions, the parameters being (d, v) for ConfTT and PhysTT, and (d, Ω) for CTS.

By symmetry, these configuration will have an ADM angular momentum parallel to the z -axis which we denote by J . In order to compare solutions among each other, and against the conformally flat inversion symmetric data sets, we adjust the parameters (d, v) and (d, Ω) , such that each initial-data set has angular momentum $J/\mu m = 2.976$ and a proper separation between the apparent horizons of $l/m = 4.880$. In Ref. [28], these values were determined to be the angular momentum and proper separation of a binary black hole at the innermost stable circular orbit.

Table 6.2 lists the parameters corresponding to this situation as well as results for each initial-data set². As with the configuration with black holes at rest, we find again that ConfTT/PhysTT and CTS lead to different ADM-energies. Now,

²Because of the Lorentz contraction, the apparent horizons for ConfTT/PhysTT intersect the sphere with radius 2. In order to have the full apparent horizon inside the computational domain, the radius of the excised spheres was reduced to 1.9 for these data sets.

Table 6.2: Initial-data sets generated by different decompositions for binary black holes with the same angular momentum $J/\mu m$ and separation ℓ/m . The mConfTT dataset is explained in section 6.5.3. It should be compared to CTS-add.

	parameters	M_{AH}	E_{ADM}	$J/\mu m$	ℓ/m	E_{ADM}/m	E_{MPRC}/E_{ADM}	E_b/μ
ConfTT	$d = 11.899, v = 0.26865$	1.06368	2.12035	2.9759	4.879	0.9967	0.2906	-0.0132
PhysTT	$d = 11.899, v = 0.26865$	1.06369	2.12037	2.9757	4.879	0.9967	0.2906	-0.0132
CTS-add	$d = 11.860, \Omega = 0.0415$	1.07542	2.10391	2.9789	4.884	0.9782	0.2771	-0.0873
CTS-mult	$d = 11.750, \Omega = 0.0421$	1.06528	2.08436	2.9776	4.880	0.9783	0.2772	-0.0867
mConfTT	$d = 11.860, \Omega = 0.0415$	1.0758	2.1061	3.011	4.883	0.979	0.278	-0.085
inv. symm. ^a				2.976	4.880	0.9774	0.2766	-0.09030

^aData taken from [28]

E_{ADM}/m and E_{MPRC}/E_{ADM} differ by 0.02 and 0.013, respectively, between CTS and ConfTT/PhysTT. However, in contrast to the cases where the black holes at rest, now CTS and the inversion symmetric data set have very similar values for E_{ADM}/m and E_{MPRC}/E_{ADM} .

6.5.3 Reconciling conformal TT and thin sandwich

We now investigate further the difference between ConfTT/PhysTT and CTS. Since the resulting initial-data sets for PhysTT and ConfTT are very similar, we restrict our discussion to ConfTT.

Motivation

The construction of binary black hole data for the ConfTT/PhysTT cases produces an extrinsic curvature that almost certainly contains a significant TT component. It would be interesting to know how significant this component is to the value of the various physical parameters we are comparing. Ideally, we would like to completely eliminate the TT component and see what effect this has on the resulting data sets. Unfortunately, this is a difficult, if not impossible, task.

The TT component of a symmetric tensor M^{ij} is defined as

$$M_{TT}^{ij} \equiv M^{ij} - (\mathbb{L}Y)^{ij}, \quad (6.85)$$

where the vector Y^i is obtained by solving an elliptic equation of the form

$$\Delta_{\mathbb{L}} Y^i = \nabla_j M^{ij}. \quad (6.86)$$

The problem resides in the fact that the meaning of the TT component depends of the boundary conditions used in solving (6.86).

For the ConfTT/PhysTT cases we are actually solving for a vector V^i that is a linear combination of two components, one that solves an equation of the form of (6.86) to obtain the TT component of \tilde{M}^{ij} and one that solves the momentum constraint. But by imposing inner-boundary conditions of $V^i = 0$, we don't specify the boundary conditions on either part independently. Nor is it clear what these boundary conditions should be. Since we cannot explicitly construct the TT component of the extrinsic curvature, we cannot eliminate it. Although it is not ideal, there is an alternative we can consider that does provide some insight into the importance of the initial choice of \tilde{M}^{ij} .

Black holes at rest

Consider the following numerical experiment for two black holes at rest: Given \tilde{M}^{ij} from Eq. (6.48), make a transverse traceless decomposition by setting

$$2N\tilde{M}^{ij} = \tilde{M}_{TT}^{ij} + (\tilde{\mathbb{L}}Y)^{ij} \quad (6.87)$$

where $\tilde{\nabla}_j \tilde{M}_{TT}^{ij} = 0$ and $N = N_A + N_B - 1$. Notice that we are decomposing $2N\tilde{M}^{ij}$, not \tilde{M}^{ij} . Taking the divergence of Eq. (6.87) one finds

$$\tilde{\Delta}_L Y^i = \tilde{\nabla}_j (2N\tilde{M}^{ij}). \quad (6.88)$$

The decomposition chosen in Eq. (6.87) is motivated by the conformal thin sandwich decomposition. With this decomposition we can, in fact, use the shift vector N^i to fix boundary conditions on Y^i , just as it was used to fix the boundary conditions in Eqs. (6.51b—6.51d). For the black holes at rest in this case, we have $\Omega = 0$. After solving Eq. (6.88) for Y^i , we can construct a new conformal extrinsic curvature by

$$\tilde{M}'^{ij} = \frac{1}{2N} (\tilde{\mathbb{L}}Y)^{ij} \quad (6.89)$$

which is similar to what would result if we could eliminate \tilde{M}_{TT}^{ij} from \tilde{M}^{ij} . Using \tilde{M}'^{ij} in place of \tilde{M}^{ij} , we can again solve the conformal TT equations. The result of this modified conformal TT decomposition “**mConfTT**” is striking: Figure 6.7 shows that mConfTT generates a conformal factor ψ that is very similar to ψ of CTS. mConfTT is also included in Table 6.1 where it can be seen that the quantities E_{ADM}/m and E_{MPRC}/E_{ADM} differ only slightly between mConfTT and CTS.

The fact that modification of the extrinsic curvature changes the ADM-energy by such a large amount underlines the importance of a careful choice for the extrinsic curvature \tilde{M}^{ij} in ConfTT/PhysTT. The extremely good agreement between CTS and mConfTT is probably caused by our procedure to determine \tilde{M}'^{ij} . We force the extrinsic curvature of mConfTT into the form Eq. (6.89). This is precisely the form of the extrinsic curvature in CTS, Eq. (6.28), even using the same function N and the same boundary conditions on the vectors Y^i and β^i .

Black holes with angular momentum

We now apply the modified conformal TT decomposition to the orbiting configurations of section 6.5.2. In the corotating frame, the black holes are at rest, and

we start with $\tilde{\gamma}_{ij}$ and \tilde{M}^{ij} of two black holes *at rest* with coordinate separation $d = 11.860$. We now solve Eq. (6.88) with

$$N = N_A + N_B - 1 \quad (6.90)$$

and corotating boundary conditions on Y^i [cf. Eqs. (6.51b)–(6.51d)]:

$$Y^i = N_A^i \quad \text{sphere inside hole A,} \quad (6.91a)$$

$$Y^i = N_B^i \quad \text{sphere inside hole B,} \quad (6.91b)$$

$$Y^i = \vec{\Omega} \times \vec{r} \quad \text{outer boundary.} \quad (6.91c)$$

$N_{A/B}$ and $N_{A/B}^i$ are lapse and shift of individual Kerr-Schild black holes at rest. \tilde{M}^{ij} is again constructed by Eq. (6.89) and used in solving the conformal TT equations.

Results from this procedure are included in Table 6.2. Again, mConfTT generates results very close to CTS. E_{ADM}/m changes by 1.8% of the total mass between ConfTT and mConfTT, again highlighting the importance of the extrinsic curvature.

6.5.4 Dependence on the size of the excised spheres

The framework presented in this paper requires the excision of the singularities at the centers of each hole³. So far we have used $r_{exc} = 2M$ or $r_{exc} = 1.9M$ in order to impose boundary conditions close to the apparent horizons, but different choices can be made. Indeed, one might expect that the boundary conditions (6.49) and (6.51) become “better” farther inside the apparent horizon, where the metric and extrinsic curvature of that black hole dominate the superposed metric $\tilde{\gamma}_{ij}$ and superposed extrinsic curvature \tilde{M}^{ij} .

In order to test this assumption, we solve the constraint equations for two black holes at rest for different radii r_{exc} . We find that for all three decompositions, the data sets depend strongly on the radius of the excised spheres.

Figure 6.9 presents plots of the conformal factor ψ and V^x for ConfTT with different r_{exc} . There is no clear sign of convergence of ψ as $r_{exc} \rightarrow 0$. For $r_{exc} = 0.2M$, the conformal factor ψ even oscillates close to the excised sphere. Table 6.3 displays various quantities for the ConfTT decomposition for different r_{exc} . As

³Marronetti and Matzner[56] effectively excised the centers, too, by using “blending functions”.

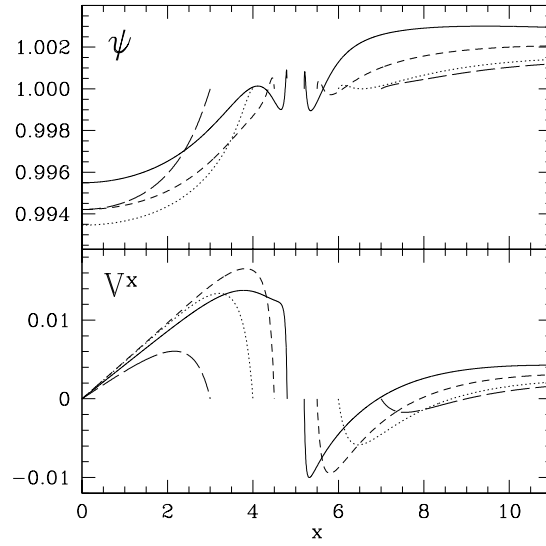


Figure 6.9: Plots of ψ and V^x along the positive x -axis for ConfTT for different radii $r_{exc} = 2M, M, 0.5M, 0.2M$. The excised spheres are centered on the x -axis at $x = \pm 5$. The position where a line terminates gives r_{exc} for that line.

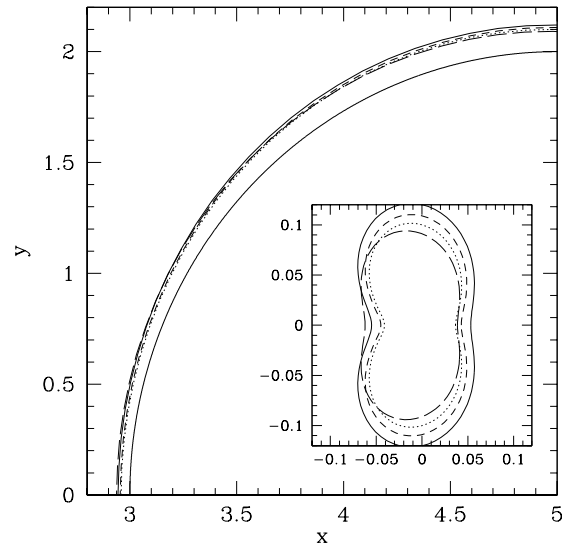


Figure 6.10: Apparent horizons for ConfTT with different radii of excised spheres. Results shown are for $r_{exc} = 2M$ (long dashed line), M (dotted line), $0.5M$ (short dashed line) and $0.2M$ (outer solid line). The inner solid line is a circle with radius 2. The insert shows a parametric plot of $r(\phi) - 2$, which emphasizes the differences between the different apparent horizons.

Table 6.3: Solutions of ConfTT for different radii of the excised spheres, r_{exc} . The results for PhysTT are nearly identical.

r_{exc}	E_{ADM}	A_{AH}	ℓ	E_{ADM}/m	ℓ/E_{ADM}
Conformal TT					
2.0	2.0649	57.737	8.062	0.9633	3.904
1.0	2.0682	57.825	8.101	0.9641	3.917
0.5	2.0808	58.520	8.101	0.9642	3.893
0.2	2.0978	59.514	8.093	0.9640	3.858
0.1	2.1064	60.025	8.089	0.9638	3.840

r_{exc} varies between $2.0M$ and $0.1M$, the ADM-energy varies between 2.065 and 2.106, whereas the apparent horizon area changes by nearly 4%. The apparent horizons move around somewhat as r_{exc} changes. Figure 6.10 shows the location of the apparent horizons for different r_{exc} .

For CTS-add (with $\tilde{\alpha} = N_A + N_B - 1$), the initial-data sets seem to diverge as r_{exc} is decreased. This has to be expected, since this choice for $\tilde{\alpha}$ changes sign if the excised spheres become sufficiently small. Changing to $\tilde{\alpha} = N_A N_B$ so that the lapse does not change sign reduces this divergent behavior. Von Neumann boundary conditions on ψ at the excised spheres,

$$\frac{\partial \psi}{\partial r} = 0, \quad (6.92)$$

lead to an increase in A_{AH} especially for large excised spheres. This combination of lapse $\tilde{\alpha}$ and boundary conditions exhibits the smallest variations in E_{ADM}/m ; cuts through ψ , β^x and through the apparent horizons are shown in Figs. 6.11 and 6.12. From the three examined combinations of lapse and boundary conditions, the one shown behaves best, but there is still no convincing sign of convergence.

Table 6.4 presents ADM-energies and apparent horizon areas and masses for CTS with different r_{exc} and different choices of lapse and boundary condition. From the unscaled ADM-energy E_{ADM} it is apparent that $\tilde{\alpha} = N_A + N_B - 1$ diverges most strongly. Note that between all choices of lapse, boundary conditions and r_{exc} , the unscaled quantities E_{ADM} , M_{AH} , and ℓ exhibit a much broader variation than the scaled quantities E_{ADM}/m and ℓ/E_{ADM} .

Table 6.4: Solutions of CTS as a function of radius of excised spheres, r_{exc} . Different choices of the lapse $\tilde{\alpha}$ and boundary conditions for ψ at the excised spheres are explored.

r_{exc}	E_{ADM}	A_{AH}	ℓ	E_{ADM}/m	ℓ/E_{ADM}
$\tilde{\alpha} = N_A + N_B - 1, \psi = 1$					
2.0	2.0812	62.312	8.039	0.9346	3.863
1.0	2.1846	68.279	8.000	0.9372	3.662
0.5	2.3085	76.253	7.925	0.9371	3.433
0.2	2.5463	93.534	7.750	0.9333	3.044
0.1	2.8543	118.834	7.489	0.9282	2.624
$\tilde{\alpha} = N_A N_B, \psi = 1$					
2.0	2.0585	60.811	8.080	0.9358	3.925
1.0	2.1216	64.080	8.044	0.9395	3.792
0.5	2.1696	66.790	8.017	0.9411	3.695
0.2	2.2120	69.456	7.991	0.9409	3.613
0.1	2.2326	70.809	7.978	0.9405	3.573
$\tilde{\alpha} = N_A N_B, \partial\psi/\partial r = 0$					
2.0	2.1110	64.229	8.085	0.9337	3.830
1.0	2.1533	66.128	8.030	0.9387	3.729
0.5	2.1794	67.427	8.011	0.9409	3.676
0.2	2.2136	69.559	7.990	0.9409	3.609
0.1	2.2330	70.836	7.978	0.9405	3.573

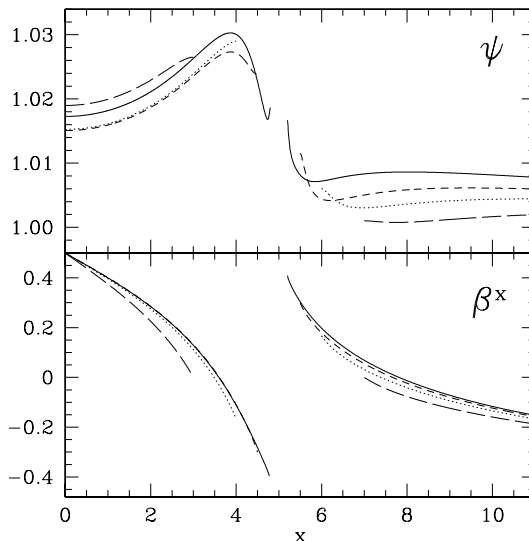


Figure 6.11: Cuts through ψ and β^x for CTS-mult for different radii r_{exc} . Here $\tilde{\alpha} = N_A N_B$ and the boundary condition on ψ at the excised spheres is $d\psi/dr = 0$. The curves for β^x are shifted up by 0.5 for $x < 5$, and are shifted down by 0.5 for $x > 5$ to allow for better plotting. $d\psi/dr$ approaches zero at the inner boundary on scales too small to be seen in this figure.

6.6 Discussion

Our results clearly show that different decompositions lead to different initial-data sets, even when seemingly similar choices for the freely specifiable pieces are used. From Tables 6.1 and 6.2, one sees that E_{ADM}/m changes by as much as 0.029 between ConfTT/PhysTT and CTS. The difference between ConfTT/PhysTT and the inversion symmetric data is even larger, 0.047. These numbers seem to be small; however, current evolutions of binary data usually find the total energy emitted in gravitational radiation E_{GW}/m to be between 0.01 and 0.03 [73, 74, 87], which is the same order of magnitude as the changes in E_{ADM}/m we find. This means that, in principle, most of the energy radiated in these simulations could originate from “spurious” energy in the system and not from the dynamics of the binary system we are interested in.

These findings highlight the fact that current binary black hole initial data sets are inadequate for the task of accurately describing realistic binary systems. We see that the choices of the conformal 3-geometry $\tilde{\gamma}_{ij}$ and the freely specifiable portions

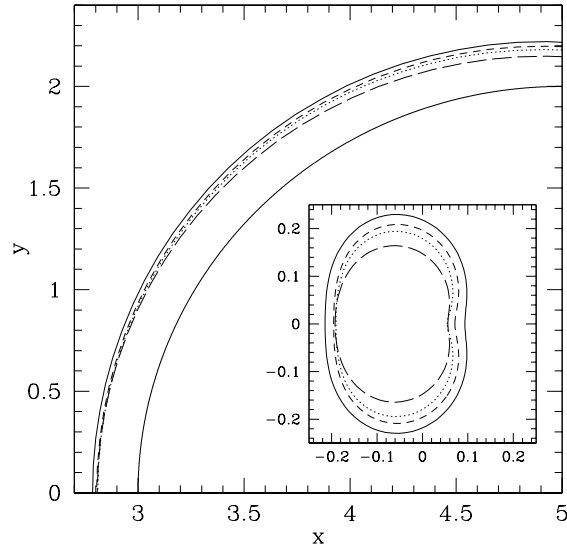


Figure 6.12: Apparent horizons for CTS with $\tilde{\alpha} = N_A N_B$ and inner boundary condition $d\psi/dr = 0$. The different curves belong to different r_{exc} as explained in Fig. 6.10

of the extrinsic curvature, embedded in \tilde{M}^{ij} , influence the content of the initial data at a significant level. Furthermore, the results suggest that small changes in the free data associated with the extrinsic curvature are more significant than small changes in the choice of $\tilde{\gamma}_{ij}$.⁴ This assertion is supported by the fact that E_{ADM}/m is consistently larger for the ConfTT solutions than for the CTS solutions but the two approaches can be made to produce quite consistent results by using the modified extrinsic curvature of the mConfTT method. All of these decompositions use the same non-flat conformal metric, but differ in the extrinsic curvature. On the other hand, results for the conformally-flat inversion-symmetric data agree rather well with the results from the CTS method when we consider orbiting black holes. For black holes at rest, CTS differs from the inversion symmetric data, which seems to contradict our conclusion. However, this difference is likely due to the time-symmetric nature of the inversion symmetric data, which is especially adapted to the time-symmetry of the particular configuration of “two black holes at rest”.

⁴Following submission of this paper, a preprint by Damour et al.[72] has appeared that lends support to our idea that the extrinsic curvature plays a key role in constructing quasi-equilibrium binary black hole initial data.

Improved binary black hole initial data will require choices for the freely specifiable data that are physically motivated, rather than chosen for computational convenience. The same is true for the boundary conditions used in solving the constraints. The boundary conditions used in this paper carry the implicit assumptions that the approximate metric and extrinsic curvature are correct at the excision boundaries and that the value of the single-hole Kerr-Schild shift at the excision boundary is correct in a multi-hole situation. This is clearly not true, but we might hope that the impact of the error in this choice would diminish as we decrease the radius of the excision boundary. However, our results presented in Tables 6.3 and 6.4 do not support this conjecture. Examining the change in E_{ADM}/m as we vary r_{exc} shows only a small change, but more importantly, it shows no sign of converging as we decrease r_{exc} . The effects of changing r_{exc} are much more significant for ℓ/E_{ADM} , changing its value by as much as 10% in the case of CTS-mult for the range of values considered. Furthermore, as with the energy, we see no sign of convergence in ℓ/E_{ADM} as r_{exc} decreases. Interestingly, although the solutions show no sign of convergence as we shrink the excision radius, we do find that the dimensionless quantities E_{ADM}/m and ℓ/E_{ADM} do become independent of the choice of the inner-boundary condition as r_{exc} decreases. This can be seen in comparing the result in Table 6.4 for the cases using $\psi = 1$ and $\partial\psi/\partial r = 0$ as inner-boundary conditions. Additional tests, not reported in this paper, further support this assertion.

6.7 Conclusion

Using a new elliptic solver capable of solving the initial-value problem of general relativity for any of three different decompositions and any choice for the freely specifiable data, we have examined data sets representing binary black hole spacetimes. We find that the choices for the freely specifiable data currently in use are inadequate for the task of simulating the gravitational radiation produced in astrophysically realistic situations. In particular, we studied the results of using a superposition of two Kerr-Schild black holes to fix the freely specifiable data and compared them to the results obtained from conformally flat initial data.

Although the new Kerr-Schild based data provide a valuable point of comparison, it is not clear that the data produced are significantly superior to previous conformally-flat data. What is clear is that the choice of the freely specifiable data

will be very important in constructing astrophysically realistic binary black hole initial data. Progress will require that these data, *and* the boundary conditions needed to solve the constraints, must be chosen based on physical grounds rather than computational convenience.

How can better initial data be achieved and how can the quality of initial data be measured? We believe that the conformal thin sandwich decomposition will be especially useful. Genuine radiative degrees of freedom cannot *in principle* be recognized on a single time slice. The conformal thin sandwich method uses in effect two nearby surfaces, giving it a potential advantage over other methods. Also, it avoids much of the uncertainty related to specifying a conformal extrinsic curvature. Moreover, the conformal thin sandwich approach is especially well suited for the most interesting configurations, a black-hole binary in a quasi-equilibrium orbit. In this case time derivatives of all quantities are small and the choice $\tilde{u}^{ij} = 0$ is physically motivated. One should exploit the condition of quasi-equilibrium as fully as possible, i.e. one should use the conformal thin sandwich approach together with the constant K equation, $\partial_t K = 0$. The latter yields another elliptic equation for the lapse which removes the arbitrariness inherent in choosing a conformal lapse $\tilde{\alpha}$. One will also need more physical boundary conditions. Work in this direction was begun in [67, 68] and refined in [88].

Ultimately, the gravitational wave content of an initial-data set can be determined only by long term evolutions. One must compute an initial-data set representing a binary black hole in quasi-circular orbit and evolve it. Then one must repeat this process with an initial-data set representing the *same* binary black hole, say, one orbital period earlier, and evolve that data set, too. If both evolutions lead to the same gravitational waves (modulo time offset) then one can be confident that the gravitational radiation is indeed astrophysically realistic. This approach has recently been used for the first time in conjunction with conformally flat puncture data, where it proved remarkably successful [75].

Acknowledgements

We thank Lawrence Kidder, Mark Scheel, and James York for helpful discussions. This work was supported in part by NSF grants PHY-9800737 and PHY-9900672 to Cornell University, and by NSF grant PHY-9988581 to Wake Forest University. Computations were performed on the IBM SP2 of the Department of Physics,

Wake Forest University, with support from an IBM SUR grant.

Chapter 7

Quasi-equilibrium initial data

In this chapter we explore another route to initial data for binary black holes in circular orbits. The basic idea is that if a black hole binary were in an exact circular orbit, then in a *corotating* frame, the configuration would be *time-independent*. Thus, for an exact circular orbit,

$$\partial_t g_{ij} = 0, \quad \partial_t K_{ij} = 0 \tag{7.1}$$

in a corotating coordinate system. Of course, in reality, a binary system slowly spirals in due to gravitational wave emission, and therefore all 12 equations (7.1) cannot be satisfied¹. However, one can still try to enforce as many of these equations as possible. Moreover, the radiation reaction time-scale increases very rapidly with separation, so that at large separations it should be possible to satisfy Eq. (7.1) to a very good approximation.

The quasi-equilibrium idea was first used by Wilson & Mathews [90, 91] and later by many others to construct binary neutron stars. Later, it was applied byourgoulhon, Grandclément & Bonazzola [67, 68] to construct black hole binaries in circular orbits.ourgoulhon et al’s work is slightly deficient in that their initial data sets violate the constraints [88], although at a very small level. Also, their boundary conditions require the lapse to vanish on the apparent horizons of the black holes. Evolutions with black hole excision, however, need initial data that extends smoothly *through* the horizon.

The conformal thin sandwich formalism very clearly displays *which* of the time-derivatives in (7.1) are freely specifiable, namely $\partial_t \tilde{g}_{ij} = \tilde{u}_{ij}$ and $\partial_t K$. It therefore provides a unified and general framework for quasi-equilibrium initial data. Accordingly, we use the conformal thin sandwich equations with

$$\tilde{u}_{ij} = 0, \quad \partial_t K = 0, \tag{7.2}$$

throughout this chapter. Since we only enforce Eq. (7.2), the quasi-equilibrium method has a built-in consistency check: For the “correct” quasi-equilibrium solution, *all* time-derivatives in Eq. (7.1) should be small.

¹Unless the emitted gravitational radiation is balanced with an equal amount of *ingoing* radiation [89].

In section 7.1 we consider the consequences of (7.2) for stationary spacetimes. This will lead us to the question of *boundary conditions* in section 7.2. After some implementation details (section 7.3), we present solutions for single black hole spacetimes in section 7.4, and binary black hole spacetimes in section 7.5. We close with a brief discussion in section 7.6. The appendices contain details of the calculations, tests, and remarks on how to prepare these initial data sets for an evolution.

7.1 Stationary spacetimes

Let Σ be a spacelike hypersurface with future pointing unit normal n^μ through a spacetime with Killing vector l such that $-n \cdot l$ is strictly positive. Denote by g_{ij}^0 , K_0^{ij} , and $K_0 = g_{ij}^0 K_0^{ij}$ the induced metric, extrinsic curvature and mean curvature of Σ . Furthermore, drag the coordinates along the Killing vector, i.e.

$$\begin{aligned}\beta_0 &= \perp l, \\ N_0 &= -n \cdot l,\end{aligned}\tag{7.3}$$

where \perp is the projection operator into Σ . The gauge (7.3) evolves along the Killing vector, so the 3+1-quantities will be time-independent: $\partial_t g_{ij} = \partial_t K_{ij} = 0$.

We now set up this hypersurface for a solution of the conformal thin sandwich equations (2.28), (2.29) and (2.34). If we choose as free data (2.31)

$$\tilde{g}_{ij} = \Psi^{-4} g_{ij}^0, \quad \tilde{u}_{ij} = 0, \quad K = K_0, \quad \partial_t K = 0,\tag{7.4}$$

(where Ψ is some uniformly positive function), then by construction,

$$\psi = \Psi, \quad \beta^i = \beta_0^i, \quad \tilde{N} = \Psi^{-6} N_0,\tag{7.5}$$

will solve the conformal thin sandwich equations, given boundary conditions compatible with Eq. (7.5). We point out that in Eq. (7.4) we specify only the conformal equivalence class of g_{ij} and the mean curvature of Σ ; the determinant of g_{ij} and the tracefree extrinsic curvature are recovered by the conformal thin sandwich equations.

Assuming that the conformal thin sandwich equations have a unique solution, we can reverse these considerations:

If the free data \tilde{g}_{ij} , and K as well as the boundary conditions are compatible with a time-independent solution of Einstein's equations, then the choice $\tilde{u}^{ij} = 0$,

$\partial_t K = 0$ will generate complete initial data on Σ , as well as lapse and shift such that the evolution is completely time independent. The Killing vector of the spacetime is then given by $l = Nn + \beta$.

This result is very useful in two ways: First, the only non-trivial free data is \tilde{g}_{ij} and K . In particular, one need not provide a guess for the trace-free extrinsic curvature A^{ij} , on which solutions of the extrinsic curvature decomposition depend very sensitively (see chapter 6). In addition, any spherically symmetric slice can be written in conformally flat coordinates, so that $\tilde{g}_{ij} = f_{ij}$ is a completely general choice for spherical symmetry.

Second, one is generally interested in *evolving* the initial data, which requires lapse and shift. We see that the conformal thin sandwich equations not only yield lapse and shift, but, for stationary spacetimes, yield the *optimal* lapse and shift.

Of course, the present discussion depends on *boundary conditions*. The conformal thin sandwich equations generally will have a solution even if the boundary conditions are not compatible with (7.3). In such a case, however, the time-vector of the evolution will not coincide with the Killing vector, and the evolution will not be time-independent. Thus we are led to consider boundary conditions next.

7.2 Quasi-equilibrium boundary conditions

The idea of quasi-equilibrium is also very useful for deriving boundary conditions at interior boundaries of the computational domain which surround the singularities inside each black hole. Here, I present the proposal of Cook [88] in my own words, with some improvements and simplifications which have been found since publication of [88] by Cook and by myself.

Our goal is to construct initial data for either a single black hole, or a binary black hole in quasi-circular orbit. For a binary, the orbital angular frequency is denoted by Ω . For a single black hole one should replace Ω by zero in what follows. Thus we seek initial data (g_{ij}, K^{ij}) on a hypersurface Σ as well as lapse N and shift β^i so that the configuration is initially as time-independent as possible.

The initial data should contain one or two black holes which are “time-independent.” Therefore, we require that Σ contains one or two *apparent horizons*,²

²Technically, a “marginally outer trapped surface” (MOTS) – the apparent horizon is defined as the outermost MOTS, and we do not rigorously show that no other MOTS exists outside \mathcal{S} .

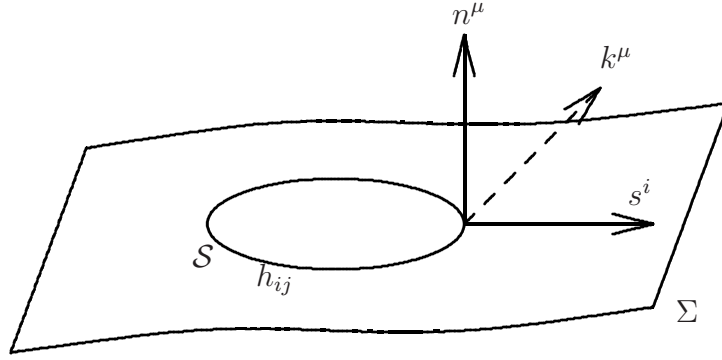


Figure 7.1: Inner boundary for quasi-equilibrium boundary conditions. The 2-surface \mathcal{S} has the induced metric h_{ij} .

denoted by \mathcal{S} , and that these apparent horizons have constant area as one moves to the neighboring hypersurfaces. The situation is illustrated in Figure 7.1, which also introduces several vectors on \mathcal{S} : n^μ denotes as usual the future pointing unit normal to Σ , s^μ is the unit-normal to \mathcal{S} within Σ , and

$$k^\mu = s^\mu + n^\mu \quad (7.6)$$

denotes the outgoing null normal to \mathcal{S} with a convenient normalization. Furthermore, the induced metric h_{ij} on \mathcal{S} is

$$h_{ij} = g_{ij} - s_i s_j. \quad (7.7)$$

For the apparent horizon \mathcal{S} , by definition, the expansion of k^μ vanishes:

$$\theta = 0 \quad \text{on } \mathcal{S}. \quad (7.8)$$

Therefore, if \mathcal{S} is moved along k^μ , initially, the surface area of \mathcal{S} will not change. Of course, so far there is no guarantee that the apparent horizon moves along k^μ .

We consider Raychaudhuri's equation

$$\frac{d\theta}{d\lambda} = -\frac{1}{2}\theta^2 - \sigma_{\mu\nu}\sigma^{\mu\nu} + \omega_{\mu\nu}\omega^{\mu\nu} - R_{\mu\nu}k^\mu k^\nu, \quad (7.9)$$

where $\sigma_{\mu\nu}$, and $\omega_{\mu\nu}$ denote shear and twist of k^μ , respectively, and λ is the affine parameter along the null-geodesics tangent to k^μ such that $k = d/d\lambda$. Since $\theta = 0$ (on \mathcal{S}), $R_{\mu\nu} = 0$ in vacuum and $\omega_{\mu\nu} = 0$ (because k^μ is surface-forming by construction), Eq. (7.9) simplifies to

$$\frac{d\theta}{d\lambda} = -\sigma_{ij}\sigma^{ij} \quad \text{on } \mathcal{S}. \quad (7.10)$$

Therefore, the expansion will stay zero along k^μ (initially), if

$$\sigma_{ij} = 0 \quad \text{on } \mathcal{S}. \quad (7.11)$$

The apparent horizon is defined by $\theta = 0$; Eq. (7.11) thus ensures that the apparent horizon moves along k^μ and that its area is (initially) constant during an evolution.

We remark that the conditions on \mathcal{S} we have derived so far are in close contact to the *isolated horizon framework* (see, e.g. [92], or [93] for an easily accessible introduction). This framework tries to capture the concept of a black hole that is not changing for a certain period of time in a spacetime, which is otherwise allowed to change. Within this framework, one can then define *locally* mass and angular momentum of the hole. One of the defining properties of an isolated horizon is that it can be foliated by null-geodesics with zero expansion, which is very similar to our requirement that $\theta = 0$ and $d\theta/d\lambda = 0$ on \mathcal{S} .

So far we have been concerned with coordinate independent conditions on the spacetime; we now consider coordinate choices which make the configuration as time-independent as possible in the specific coordinate system we are constructing.

It will be convenient to know where the apparent horizon \mathcal{S} is located in Σ . We achieve this by simply *choosing* the surface \mathcal{S} in our coordinate system, and then *demanding* that \mathcal{S} is an apparent horizon. In Appendix 7.7 we show that from Eq. (7.8) it follows that

$$\tilde{s}^k \tilde{\nabla}_k \ln \psi = -\frac{1}{4} \left(\tilde{h}^{ij} \tilde{\nabla}_i \tilde{s}_j - \psi^2 J \right) \quad \text{on } \mathcal{S}. \quad (7.12)$$

Here, \tilde{s}^k and \tilde{h}_{ij} are the conformal unit-normal to \mathcal{S} and the conformal induced metric of \mathcal{S} ,

$$s_i = \psi^2 \tilde{s}_i, \quad h_{ij} = \psi^4 \tilde{h}_{ij}, \quad (7.13)$$

and $J = h_{ij} K^{ij}$. Equation (7.12) has already been expressed in conformal quantities which are known before the conformal thin sandwich equations are solved.

Equations (7.10) and (7.11) ensure that the apparent horizon is a null surface; we now require that the set of *coordinate* points that coincide with \mathcal{S} in the initial hypersurface Σ coincides with a null surface during the evolution (initially). This ensures that the apparent horizons will not move through coordinate space in the evolution (at least initially). We decompose the shift β^μ into pieces perpendicular and tangential to \mathcal{S} ,

$$\beta^\mu = \beta_\perp s^\mu + \beta_\parallel^\mu \quad \text{on } \mathcal{S}, \quad (7.14)$$

with $\beta_{\perp} = s_{\mu}\beta^{\mu}$ and $s_{\mu}\beta_{\parallel}^{\mu} = 0$. The time-vector then splits into

$$t = Nn + \beta_{\perp}s + \beta_{\parallel} = \zeta + \beta_{\parallel} \quad \text{on } \mathcal{S}, \quad (7.15)$$

where $\zeta^{\mu} \equiv Nn^{\mu} + \beta_{\perp}s^{\mu}$ describes the radial motion of the boundary whereas β_{\parallel}^{μ} shifts coordinates *tangential* to \mathcal{S} . In order for the inner boundary to coincide with a null surface, ζ^{μ} must be null,

$$\zeta^2 = -N^2 + \beta_{\perp}^2 = 0 \quad \text{on } \mathcal{S}, \quad (7.16)$$

so that

$$\beta_{\perp} = N \quad \text{on } \mathcal{S}, \quad (7.17)$$

(which also implies that ζ^{μ} is proportional to k^{μ}). This condition relates the radial part of the shift-vector to the lapse. The overall scaling of ζ^{μ} is not fixed by the requirement of ζ^{μ} being null.

Having the results of the last two pages, we analyze the condition (7.11). We show in Appendix 7.7 that $\sigma_{ij} = 0$ together with (7.14) and (7.17) implies that

$$(\tilde{\mathbb{L}}_{\mathcal{S}}\beta_{\parallel})^{ij} = 0. \quad (7.18)$$

The operator on the left-hand side of (7.18) is the two-dimensional longitudinal operator (the *conformal Killing operator*), given by Eq. (2.17), acting in \mathcal{S} . The solutions of (7.18) are therefore conformal Killing vectors of \mathcal{S} (or on each connected component of \mathcal{S} , for a binary black hole). For the special case of a sphere in conformal flatness, we note that a rotation centered on the sphere satisfies Eq. (7.18) for any choice of rotation-angle and orientation of the axis of rotation.

Cook [88, 94] suggests to use the freedom in β_{\parallel}^i to construct *spinning* black holes. The choice $\beta_{\parallel}^i = 0$ corresponds to corotating black holes, whereas any other solution of (7.17) would impart an additional rotation on the hole. In the special case of conformal flatness with excised spheres, for example, the choice

$$\beta_{\parallel}^i = \Omega \left(\frac{\partial}{\partial\phi_H} \right)^i \quad (7.19)$$

with $\partial/\partial\phi_H$ the rotational conformal Killing vector centered on the excised sphere with rotation axis parallel to the orbital angular momentum, should generate irrotational black holes.

Looking back we see that Eqs. (7.12), (7.14) and (7.17) have the character of boundary conditions on ψ and β^i , which are four of the five unknowns of the

conformal thin sandwich equations (the fifth one is the lapse \tilde{N}). Therefore, we can guarantee that these equations are satisfied by using them as boundary conditions in the elliptic solve of the conformal thin sandwich equations³.

At the *outer* boundary, the boundary conditions are dictated by asymptotic flatness:

$$\psi \rightarrow 1 \quad \text{as } r \rightarrow \infty, \quad (7.20)$$

$$N \rightarrow 1 \quad \text{as } r \rightarrow \infty, \quad (7.21)$$

both in an inertial frame and in the rotating frame. In the inertial frame, furthermore, $\beta^i \rightarrow 0$. In the corotating frame, therefore

$$\beta^i \rightarrow \Omega \left(\frac{\partial}{\partial \phi} \right)^i \quad \text{as } r \rightarrow \infty, \quad (7.22)$$

where $\partial/\partial\phi$ represents a rotation in the asymptotically flat region around the orbital axis (for a single black hole, $\Omega = 0$).

We can summarize the *quasi-equilibrium method* as follows:

1. Pick a conformal metric \tilde{g}_{ij} , mean curvature K , and a two-surface \mathcal{S} consisting of one or two topologically spherical components.
2. Solve the conformal thin sandwich equations with $\tilde{u}_{ij} = \dot{K} = 0$ in the exterior of \mathcal{S} with boundary conditions
 - on \mathcal{S} given by Eqs. (7.12), (7.14) and (7.17), and $\beta_{||}^i$ satisfying (7.18),
 - at infinity given by Eqs. (7.20), (7.21) and (7.22).

We have not yet specified a boundary condition on the lapse on \mathcal{S} . Cook [88] proposed to require that along the inner boundary, the expansion of the *ingoing* null geodesics be constant in time. This translates to a very complicated condition, namely

$$\mathcal{R} \equiv J\tilde{s}^i\partial_i N + \psi^2(J^2 - JK + \tilde{\mathcal{D}})N = 0, \quad (7.23)$$

with

$$\tilde{\mathcal{D}} \equiv \psi^{-4} \left(-\frac{1}{2} {}^{(2)}\tilde{R} + 2\tilde{D}^2 \ln \psi + \tilde{h}^{ij}(\tilde{D}_i - J_i)(\tilde{D}_j - J_j) \right), \quad (7.24)$$

where $J_i = h_{ik} s_l K^{kl}$. (Note that $\tilde{\mathcal{D}}$ involves second two-dimensional covariant derivatives within the surface \mathcal{S}).

³The apparent horizon equation was first used as a boundary condition in [78].

In spherical symmetry, however, I show that (7.23) is degenerate with the quasi-equilibrium boundary conditions on ψ and β^i , and cannot be used. Furthermore, for non-spherical symmetric situations, I present evidence in section 7.4.3 that Eq. (7.23) is ill-posed due to a term that vanishes identically in spherical symmetry.

Consequently, I do not believe that Eq. (7.23) represents a usable boundary condition. Instead I will use Dirichlet or von Neumann boundary conditions on the lapse. But although Eq. (7.23) cannot be used as a boundary condition, $\mathcal{R} = 0$ must nonetheless hold for *time-independent* slicings; therefore, we will use the residual \mathcal{R} as a diagnostic of the time-independence of computed initial data sets.

7.3 Implementation details

In the code, we always excise *spheres*. For a binary, the centers of the spheres are located on the x -axis at $x = \pm s/2$. We also choose $\vec{\Omega}$ parallel to the z -axis, $\vec{\Omega} = \Omega \hat{e}_z$.

For equal mass black holes in a configuration that is symmetric under exchange of the two holes, the center of the corotating frame must coincide with the origin. For *unequal* mass black holes the center will no longer be halfway between the holes and therefore not at the origin. Moreover, the $+y$ direction is different from the $-y$ direction, as the holes moving in either direction differ in mass. Thus it seems possible that the center of the corotating frame is not on the x -axis, although we would expect it to be close to it. Accordingly we center the corotating frame at $\vec{R} = (R_x, R_y, 0)$ in Cartesian coordinates.

The shift boundary condition Eq. (7.22) reads in Cartesian coordinates

$$\beta^i \rightarrow (\vec{\Omega} \times (\vec{r} - \vec{R}))^i = \xi^i + (\Omega R_y, -\Omega R_x, 0), \quad (7.25)$$

where

$$\xi^i \equiv (\vec{\Omega} \times \vec{r})^i = (-\Omega y, \Omega x, 0) \quad (7.26)$$

denotes the divergent part of the shift, and $\vec{r} = (x, y, z)$.

The outer sphere of the domain decomposition extends to very large outer radius and expands functions in inverse powers of r (via the inverse mapping of Eq. (3.26) on p. 34). The shift is proportional to r for large radii, and therefore cannot be represented as an expansion in $1/r$. Instead of solving for β^i directly, we write

$$\beta^i = B^i + \xi^i \quad (7.27)$$

and solve for B^i (which is finite as $r \rightarrow \infty$).

With these changes, the conformal thin sandwich equations are

$$\tilde{\nabla}_j \left(\frac{1}{2\tilde{N}} (\tilde{\mathbb{L}}B)^{ij} \right) + \tilde{\nabla}_j \left(\frac{1}{2\tilde{N}} (\tilde{\mathbb{L}}\xi)^{ij} \right) - \frac{2}{3} \psi^6 \tilde{\nabla}^i K = 0, \quad (7.28a)$$

$$\tilde{\nabla}^2 \psi - \frac{1}{8} \psi \tilde{R} - \frac{1}{12} \psi^5 K^2 + \frac{1}{8} \psi^{-7} \tilde{A}_{ij} \tilde{A}^{ij} = 0, \quad (7.28b)$$

$$\begin{aligned} \tilde{\nabla}^2 (\tilde{N} \psi^7) - (\tilde{N} \psi^7) \left[\frac{1}{8} \tilde{R} + \frac{5}{12} \psi^4 K^2 + \frac{7}{8} \psi^{-8} \tilde{A}_{ij} \tilde{A}^{ij} \right] \\ - \psi^5 B^k \partial_k K - \psi^5 \xi^k \partial_k K = 0, \end{aligned} \quad (7.28c)$$

where

$$\tilde{A}^{ij} = (2\tilde{N})^{-1} \left((\tilde{\mathbb{L}}B)^{ij} + (\tilde{\mathbb{L}}\xi)^{ij} \right). \quad (7.28d)$$

The quasi-equilibrium boundary conditions are

$$\tilde{s}^k \tilde{\nabla}_k \ln \psi = -\frac{1}{4} \left(\tilde{h}^{ij} \tilde{\nabla}_i \tilde{s}_j - \psi^2 J \right) \quad \text{on } \mathcal{S}, \quad (7.28e)$$

$$B^i = N \psi^{-2} \tilde{s}^i + \beta_{\parallel}^i - \xi^i \quad \text{on } \mathcal{S}, \quad (7.28f)$$

$$\psi \rightarrow 1 \quad \text{as } r \rightarrow \infty, \quad (7.28g)$$

$$B^i \rightarrow (\Omega R_y, -\Omega R_x, 0) \quad \text{as } r \rightarrow \infty, \quad (7.28h)$$

$$N \rightarrow 1 \quad \text{as } r \rightarrow \infty, \quad (7.28i)$$

with β_{\parallel}^i satisfying Eq. (7.18). Equation (7.28c) is coded as an equation for $\tilde{N} \psi^7 = N \psi$, so that, in the code, we impose boundary conditions on $N \psi$. We will loosely refer to these boundary conditions as ‘‘lapse boundary conditions,’’ nonetheless.

We finally note that one can absorb the $(\tilde{\mathbb{L}}\xi)^{ij}$ -terms in a redefinition of \tilde{u}^{ij} : If one uses $\tilde{u}^{ij} = -(\tilde{\mathbb{L}}\xi)^{ij}$, then Eqs. (7.28a) and (7.28b) for B^i take the same form as the original thin sandwich equations (2.28) and (2.29) for β^i ; ξ^i only appears in the advection term in (7.28c) and in the boundary conditions. Also, in the important case of conformal flatness, $(\tilde{\mathbb{L}}\xi)^{ij} = 0$. We report on some code tests in Appendix 7.8, and proceed now to compute initial data sets.

7.4 Single black hole solutions

We will first apply the quasi-equilibrium ideas to a spherically symmetric spacetime with a single black hole. This demonstrates the practicability of the formalism, and tests the code.

7.4.1 Eddington-Finkelstein coordinates

The Eddington-Finkelstein coordinate system is well suited for numerical relativity, as it is *horizon penetrating* and comparatively simple. We collect here some relevant formulae and a few useful numbers. The standard Eddington-Finkelstein coordinate system is given by

$$g_{ij}^{EF} = \delta_{ij} + \frac{2M}{r} n^i n^j, \quad (7.29a)$$

$$N_{EF} = \left(1 + \frac{2M}{r}\right)^{-1/2}, \quad (7.29b)$$

$$\beta_{EF}^i = \left(1 + \frac{2M}{r}\right)^{-1} \frac{2M}{r} n^i, \quad (7.29c)$$

where $n^i = x^i/r$, and $r^2 = \delta_{ij} x^i x^j$. The mean curvature is

$$K_{EF}(r) = \frac{2M}{r^2} \left(1 + \frac{2M}{r}\right)^{-3/2} \left(1 + \frac{3M}{r}\right). \quad (7.30)$$

The tracefree piece of the extrinsic curvature is not needed here; it could be obtained via $A_{EF}^{ij} = (2N_{EF})^{-1}(\mathbb{L}\beta_{EF})^{ij}$ if necessary.

The 3-metric (7.29a) in spherical coordinates reads

$${}^{(3)}ds^2 = \left(1 + \frac{2M}{r}\right) dr^2 + r^2 d\Omega^2 \quad (7.31)$$

where $d\Omega^2$ is the metric on the sphere. As with any spherically symmetric metric a suitable radial coordinate transformation $r \rightarrow \hat{r}(r)$ will transform (7.31) into conformally flat form,

$${}^{(3)}ds^2 = \psi^4 \left(d\hat{r}^2 + \hat{r}^2 d\Omega^2 \right). \quad (7.32)$$

Comparing the coefficients of $d\Omega^2$ in (7.31) and (7.32) yields $r^2 = \psi^4 \hat{r}^2$, so that $\psi^2 = r/\hat{r}$. Comparison of coefficients along the radial direction gives then

$$\left(1 + \frac{2M}{r}\right)^{1/2} dr = \frac{r}{\hat{r}} d\hat{r}, \quad (7.33)$$

with solution (subject to the boundary condition $\hat{r} \rightarrow r$ as $r \rightarrow \infty$) [88]

$$\hat{r} = \frac{r}{4} \left(1 + \sqrt{1 + \frac{2M}{r}}\right)^2 e^{2-2\sqrt{1+2M/r}}. \quad (7.34)$$

The conformal factor is therefore

$$\psi = \sqrt{\frac{r}{\hat{r}}} = \frac{2e^{\sqrt{1+2M/r}-1}}{1 + \sqrt{1+2M/r}}. \quad (7.35)$$

The mean curvature K behaves as a scalar under such a spatial coordinate transformation,

$$K_{EFCF}(\hat{r}) = K_{EF}(r(\hat{r})). \quad (7.36)$$

The coordinate transformation (7.34) maps the radius of the horizon from $r_{AH}/M = 2$ to

$$\frac{\hat{r}_{AH}}{M} = \frac{e^{2-2\sqrt{2}}}{2} (1 + \sqrt{2})^2 \approx 1.27274, \quad (7.37)$$

whereas, on the horizon,

$$\psi(\hat{r}_{AH}) = \frac{2e^{\sqrt{2}-1}}{1 + \sqrt{2}} \approx 1.25356, \quad (7.38)$$

$$(N\psi)(\hat{r}_{AH}) = \sqrt{\frac{1}{2}} \psi(\hat{r}_{AH}) \approx 0.88640. \quad (7.39)$$

These three numerical values will be used below. We confirm in Appendix 7.8 that the Eddington-Finkelstein metric indeed satisfies the quasi-equilibrium equations (7.28).

7.4.2 Solving for spherically symmetric spacetimes

We now employ the quasi-equilibrium method to solve for the standard Eddington-Finkelstein slice. We set the conformal metric equal to Eq. (7.29a), so that the solution should have $\psi = 1$, choose the mean curvature by Eq. (7.30), and set $\beta_{\parallel}^i = 0$. Furthermore, we use a Dirichlet boundary condition on the lapse,

$$N\psi = \frac{1}{\sqrt{2}} \quad \text{on } \mathcal{S}, \quad (7.40)$$

which follows from Eq. (7.29b) and $\psi = 1$.

With the most primitive initial guess, $\psi = 1$, $\beta^i = 0$, and $N\psi = 1$, the Newton-Raphson method inside the elliptic solver does not converge. A suitable initial guess can be obtained by performing an elliptic solve with *Dirichlet* boundary condition on the conformal factor, $\psi = 1$ on \mathcal{S} , and then using the result of this solve as initial guess for the “real” solve. Similar convergence problems of the Newton-Raphson procedure are encountered sometimes for binary black hole solutions. In practice, a similar “preprocessing solve” with Dirichlet boundary conditions $\psi = \psi_{\mathcal{S}}$ resolves this difficulty (this procedure is fairly insensitive to the exact value of the constant $\psi_{\mathcal{S}}$ —choosing it based on the underlying single black

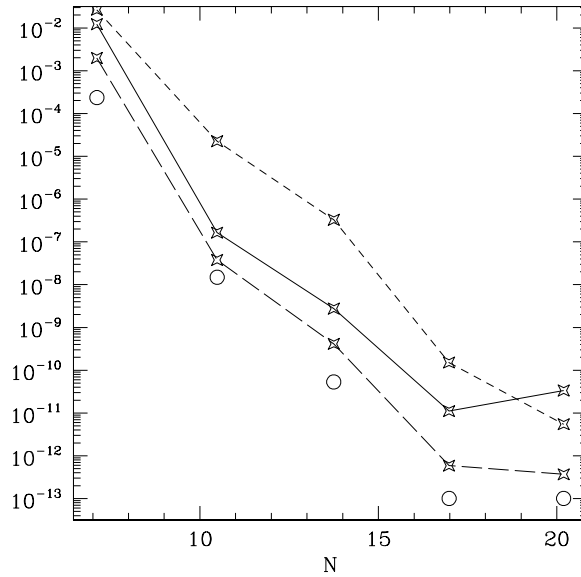


Figure 7.2: Solving the quasi-equilibrium equations (7.28) on an Eddington-Finkelstein slice. The lines denote the L_∞ residuals of the Hamiltonian constraint (solid), $\partial_t \ln \psi$ (long-dashed) and the lapse condition (7.23) (short-dashed). The circles give the deviation of the ADM-energy from the expected value 1.

hole solutions is sufficient). For binary black hole solves, using the underlying single black hole solutions as initial guess usually results in fast convergence of the Newton-Raphson method, too.

With a suitable initial guess, the Newton-Raphson method converges nicely for each resolution. The solutions converge exponentially with increasing resolution, as they should (see Figure 7.2), and reproduce the standard Eddington-Finkelstein slice.

If we replace the Dirichlet boundary condition on the lapse by the lapse condition $\mathcal{R} = 0$, Eq. (7.23), then the elliptic solver does *not* converge. To gain further insight, we perform nine solves for spherically symmetric single black hole spacetimes. For all solves, we choose conformal flatness, $\tilde{g}_{ij} = \delta_{ij}$, and vary the lapse boundary condition as well as the mean curvature:

1. For the lapse, we use two different Dirichlet boundary conditions (as indicated in Table 7.1) and the von Neumann boundary condition $\partial_r(N\psi) = 0$.
2. For K , we use $K = K_{EFCF}(\hat{r})$ (Eddington-Finkelstein with conformally flat

radial coordinate), $K = 2/r^2$ and $K = 0$.

The radius of the excised sphere is $\hat{r}_{AH}/M \approx 1.2727$ as given by Eq. (7.37), so that the first of the nine solutions should recover the Eddington-Finkelstein solution with conformally flat radial coordinate.

The runs are summarized in Table 7.1. For each run we compute the apparent horizon mass

$$M_{AH} = \sqrt{\frac{A_{AH}}{16\pi}}, \quad (7.41)$$

the ADM-energy

$$E_{ADM} = -\frac{1}{8\pi} \int_{r=\infty} \frac{\partial\psi}{\partial r} d^2A, \quad (7.42)$$

and the Komar mass⁴

$$M_K = \frac{1}{4\pi} \int_{r=\infty} \frac{\partial N}{\partial r} d^2A. \quad (7.43)$$

We also evaluate $\partial_t \ln \psi$ and \mathcal{R} . For single hole solutions, we can push the accuracy of the pseudo-spectral method close to round-off, as can be seen by the residuals of the constraints (these are L_∞ -norms; the L_2 norms are smaller by roughly one order of magnitude). E_{ADM} and M_K are determined by surface integrals extrapolated to infinite radius, which makes them less accurate. Nonetheless, we can compute them to better than 10^{-6} . We also remark that the data sets with $K = 2/r^2$ display a slower exponential convergence; although more collocation points are used for these solves, they are still somewhat less accurate.

The first data set in Table 7.1 has a mass of exactly one, as it should, because it *is* just Eddington-Finkelstein with unit-mass with the radial coordinate transformation (7.34). It is not surprising that the time-derivative of the conformal factor vanishes and that this dataset also satisfies the lapse condition \mathcal{R} , Eq. (7.23).

Perhaps more surprising is that *all* datasets presented in Table 7.1 apparently satisfy the lapse condition (7.23). This explains why the lapse condition (7.23) fails as a boundary condition together with the other quasi-equilibrium boundary conditions: *Any* value of the lapse (with the other quasi-equilibrium boundary conditions) leads to a data set satisfying (7.23). Equation (7.23) is degenerate with the other quasi-equilibrium boundary conditions and cannot be used to single out a unique value of the lapse on the horizon.

⁴These definitions for E_{ADM} and M_K are valid only in conformal flatness. More general definitions can be found in [4] and [95].

Table 7.1: Spherically symmetric single black hole solutions with \tilde{g}_{ij} =flat and different choices for the lapse boundary condition and for K . Radius of the excised sphere is \hat{r}_{AH} .

lapse BC	K	Hamilt. (upper limits)	moment. (upper limits)	M_{AH}	E_{ADM}	M_K	$L_\infty(\partial_t \ln \psi)$ (upper limits)	$L_\infty(\mathcal{R})$ (upper limits)
$(N\psi)(\hat{r}_{AH})$	K_{EFCF}	$1.3 \cdot 10^{-11}$	$6.1 \cdot 10^{-12}$	1.0000000	1.000000	1.000000	$1.0 \cdot 10^{-13}$	$2.5 \cdot 10^{-12}$
$(N\psi)(\hat{r}_{AH})$	$2/r^2$	$3.3 \cdot 10^{-9}$	$1.9 \cdot 10^{-8}$	0.772329	0.77235	0.77236	$2.2 \cdot 10^{-10}$	$9.3 \cdot 10^{-10}$
$(N\psi)(\hat{r}_{AH})$	0	$1.5 \cdot 10^{-10}$	$1.5 \cdot 10^{-11}$	1.2897483	1.289748	1.28975	$2.0 \cdot 10^{-12}$	$5.7 \cdot 10^{-11}$
3/4	K_{EFCF}	$1.9 \cdot 10^{-10}$	$2.0 \cdot 10^{-9}$	1.085413	1.08541	1.08541	$2.5 \cdot 10^{-11}$	$1.4 \cdot 10^{-10}$
3/4	$2/r^2$	$1.0 \cdot 10^{-9}$	$1.2 \cdot 10^{-8}$	0.8351808	0.83518	0.8352	$5.1 \cdot 10^{-11}$	$2.2 \cdot 10^{-10}$
3/4	0	$5.3 \cdot 10^{-11}$	$1.1 \cdot 10^{-11}$	1.3998627	1.39986	1.39986	$6.2 \cdot 10^{-13}$	$1.7 \cdot 10^{-11}$
$\partial_r(N\psi) = 0$	K_{EFCF}	$3.0 \cdot 10^{-11}$	$5.2 \cdot 10^{-11}$	0.9942475	0.994247	0.994247	$4.3 \cdot 10^{-13}$	$6.4 \cdot 10^{-12}$
$\partial_r(N\psi) = 0$	$2/r^2$	$2.0 \cdot 10^{-10}$	$2.9 \cdot 10^{-9}$	0.6828056	0.68281	0.68281	$1.7 \cdot 10^{-11}$	$1.1 \cdot 10^{-10}$
$\partial_r(N\psi) = 0$	0	$3.4 \cdot 10^{-11}$	$1.6 \cdot 10^{-11}$	1.4807928	1.480792	1.480793	$1.0 \cdot 10^{-11}$	$2.7 \cdot 10^{-11}$

From Table 7.1 we see further, that *all* datasets apparently have vanishing $\partial_t \ln \psi$, indicating that all these data sets might be time-independent. Moreover, for each dataset, apparent horizon mass, ADM energy and Komar mass agree up to the numerical accuracy of those numbers. E_{ADM} measures the total energy of the hypersurface, including gravitational waves, whereas M_{AH} just includes the black hole mass. As the apparent horizon mass is a lower bound of the event horizon mass, which in turn must be smaller than the ADM energy, we find that none of these datasets contains gravitational radiation. Finally, $E_{ADM} = M_K$ for stationary spacetimes [96, 95], hence equality of these masses once again hints toward a stationary spacetime.

The fact that the quasi-equilibrium equations in spherical symmetry seem to generate stationary slices for all our choices of the lapse boundary condition and the mean curvature can be understood as follows: The apparent horizon boundary condition guarantees the existence of a black hole in the spherically symmetric space time; by Birkhoff's theorem, the generated initial data set must therefore be a slice through a Schwarzschild black hole. Schwarzschild is stationary, and we recall from the discussion about stationary spacetimes in section 7.1 that lapse and shift along the Killing vector solve the conformal thin sandwich equations *if compatible* with the free data.

Any spherically symmetric hypersurface is conformally flat, so that $\tilde{g}_{ij} = \text{flat}$ cannot lead to incompatibilities. The inner boundary is an apparent horizon (by Eq. (7.28e)) and the time vector t^μ is radial and null there (because of Eq. (7.28f) together with $\beta_{||}^i = 0$), therefore at the inner boundary, t^μ is proportional to the Killing vector. At the outer boundary, the time vector is identical to the Killing vector by the outer boundary conditions (7.28g)–(7.28i). So the only incompatibility left could be a different constant of proportionality between t^μ and the Killing vector on the boundaries. But for the data sets contained in Table 7.1, apparently no such inconsistency exists. Thus it seems likely that for all (reasonable) mean curvatures K and values of the lapse on the apparent horizon, there exists a spherically symmetric slice through Schwarzschild. In each case, the black hole mass will have some value, based on the radius of the excised sphere, the lapse boundary condition and K .

This interpretation is also consistent with the fact that there exists a one-parameter family of spherically symmetric maximal slices through Schwarzschild [94,

97]⁵, given by

$${}^{(3)}ds^2 = \left(1 - \frac{2M}{r} + C^2 \frac{M^4}{r^4}\right)^{-1} dr^2 + r^2 d\Omega^2, \quad (7.44a)$$

$$N = \left(1 - \frac{2M}{r} + C^2 \frac{M^4}{r^4}\right)^{1/2}, \quad (7.44b)$$

$$\beta^r = \left(1 - \frac{2M}{r} + C^2 \frac{M^4}{r^4}\right)^{-1/2}, \quad (7.44c)$$

where M is the mass of the black hole and C is a dimensionless constant ($C = 0$ yields the standard Schwarzschild slice). Substituting $r = 2M$ into (7.44b) we find the value of the lapse on the horizon to be $C/4$, so that the slicings differ indeed by the value of the lapse on the horizon.

A suitable radial coordinate transformation $r \rightarrow \hat{r}(r)$ will make the metric (7.44a) conformally flat⁶. Picking values for M and C in Eqs. (7.44a)–(7.44c) and transforming to conformally flat coordinates will result in an initial data set with apparent horizon at $\hat{r}_{AH} = \hat{r}(2M)$ and lapse on the horizon of $N(\hat{r}_{AH}) = C/4$. Conversely, picking the radius of the excised sphere r_{exc} (which is an apparent horizon due to the quasi-equilibrium boundary conditions) and a lapse boundary condition on the excised sphere will determine some numerical values for M and C in Eq. (7.44a): M will simply be the ADM-energy, and $C = 4N(r_{exc})$.

Finally, we remark, that Table 7.1 suggests that for any value of the mean curvature datasets with $\partial_t \ln \psi = 0$ exist. This implies that we cannot use quasi-equilibrium ideas to single out a unique K . One cannot, for example, use $\partial_t \ln \psi = 0$ to fix K . This is perfectly consistent with the result in section 2.2.4 that using $\partial_t \psi = 0$ to fix K leads to a non-invertible differential operator in the momentum constraint.

7.4.3 The lapse boundary condition

In the last section we have seen that the lapse condition (7.23) is degenerate with the other quasi-equilibrium boundary conditions in *spherical symmetry*. For binary black hole configurations which are *not* strictly stationary, this degeneracy

⁵Estabrook et al. [97] use $T = CM^2$ instead of C . Equations (7.44) can be obtained by substituting a *time-independent* T into their more general results.

⁶This coordinate transformation is not available in closed form; it must be obtained by numerical integration [94].

might disappear. In that case, Eq. (7.23) might represent a valid lapse boundary condition which sets one additional time derivative to zero, bringing the solution even closer to stationarity.

However, in the limit of large separation, we recover two isolated black holes, and therefore the boundary conditions must become degenerate. Therefore it is likely that even at finite separation the lapse condition will be nearly degenerate with the remaining quasi-equilibrium boundary conditions, resulting in a system of equations which is difficult to solve numerically.

Nonetheless, I have put considerable effort into using the lapse condition (7.23) for solutions representing binary black hole spacetimes, or non-spherically symmetric single black hole spacetimes, but *without success*.

The rest of this subsection demonstrates one further problematic point regarding the lapse condition (7.23) in non-spherically symmetric single black hole solutions: We excise a sphere with radius $\hat{r}_{AH} \approx 1.2727$, choose conformal flatness $\tilde{g}_{ij} = \delta_{ij}$, and use K_{EFCF} as mean curvature centered at $(x, y, z) = (0.02, 0, 0.01)$ so that the center of K does not coincide with the center of the excised sphere. We use the quasi-equilibrium boundary conditions (7.28e)–(7.28i), where we set β_{\parallel}^i to a rotation around the z-axis with angular frequency 0.1 to further break spherical symmetry.

With these free data and boundary conditions, and with the lapse-condition as boundary condition on $N\psi$, the linear solver inside the Newton-Raphson procedure fails to converge.

From spherically symmetric spacetimes, we recall that the lapse boundary condition was degenerate with the remaining quasi-equilibrium boundary conditions; the overall mass-scale had to be set. Similarly, we now try to fix the value of $N\psi$ at one point on the surface of the excised sphere, in the hope that the lapse condition (7.23) will then determine it at all other points. Since we solve for the spherical harmonic coefficients (cf. Eq. (3.48) on p. 43), it is difficult to fix $N\psi$ at one point in real-space. Instead, we require that the *average* value of $N\psi$ on the surface equals 0.866, which translates to a condition on the coefficient of Y_{00} . This average-fixing condition replaces the Y_{00} component of the lapse condition (7.23), i.e. we do not enforce the monopole component $\mathcal{R} = 0$, but require only that all higher spherical harmonic pieces of \mathcal{R} vanish.

This fairly elaborate procedure alone does not yet cure the convergence problems of the linear solver. In addition, we need to consider the lapse boundary

condition (7.23) in more detail. Expanding Eq. (7.23) yields the version of this equation which is actually implemented in the code:

$$0 = \left(\frac{\psi}{2N\psi} \tilde{J} + \frac{2}{3} K \right) \tilde{s}^i \tilde{\nabla}_i (N\psi) + \frac{3\psi^4}{16N\psi} \tilde{J}^2 - \frac{1}{3} \psi^2 (N\psi) K^2 + \left(\frac{\psi}{8} \tilde{J} + \frac{N\psi}{6} K \right) \tilde{h}^{ij} \tilde{\nabla}_j \tilde{s}_i + \psi^3 \tilde{\mathcal{D}}N, \quad (7.45)$$

where

$$\begin{aligned} \psi^3 \tilde{\mathcal{D}}N &= \frac{1}{\psi^2} \tilde{D}^2 (N\psi) + \frac{N\psi}{\psi^3} \tilde{D}^2 \psi - \frac{N\psi}{2\psi^2} {}^{(2)}R - \frac{2}{\psi^3} \tilde{D}^i (N\psi) \tilde{D}_i \psi \\ &\quad - \frac{\psi}{2N\psi} \tilde{h}^{ij} \tilde{J}_i \tilde{D}_j (N\psi) - \frac{1}{2} \tilde{h}^{ij} \tilde{J}_i \tilde{D}_j \psi + \frac{\psi^4}{4N\psi} \tilde{h}^{ij} \tilde{J}_i \tilde{J}_j - \frac{\psi}{2} \tilde{h}^{ij} \tilde{D}_i \tilde{J}_j, \end{aligned} \quad (7.46)$$

and

$$J = h_{ij} K^{ij} = \frac{1}{2\alpha} \tilde{J} + \frac{2}{3} K, \quad (7.47)$$

$$\tilde{J}_i = \tilde{h}_{ik} \tilde{s}_l \left((\tilde{\mathbb{L}}\beta)^{kl} - \tilde{u}^{kl} \right). \quad (7.48)$$

We will refer to the last term of Eq. (7.46), $-\frac{\psi}{2} \tilde{h}^{ij} \tilde{D}_i \tilde{J}_j$ as “the divergence term.” We multiply this term by a coefficient Ξ ; $\Xi = 1$ recovers Eq. (7.23). We find, that for $\Xi \neq 1$, we *can* solve the system of equations (albeit the linear solver converges very slowly). For $\Xi = 1$, we recover the original formulation where the solver fails.

Figure 7.3 plots the minimum of N of the solution versus the coefficient Ξ in the modified lapse boundary condition. Every data point in this figure represents a convergent solution (in the number of basis functions⁷) of the quasi-equilibrium equations with the modified lapse condition. Close to $\Xi = 1$, the solution depends very sensitively on the parameter Ξ , apparently with a singularity for $\Xi = \Xi_{crit} \approx 1$. This observation shows that the lapse-condition with $\Xi = 1$ is probably ill-posed.

We note that the divergence term under consideration vanishes identically in spherical symmetry. Moreover, the divergence term contains *second* derivatives of the shift β^i . Thus it is possible that the lapse condition somehow interferes with the *second order* elliptic equation for β^i .

⁷For given resolution, the linear solve inside the Newton-Raphson method converges very slowly. This might be caused by either insufficient preconditioning of the lapse condition (which is not preconditioned at all), or by a nearly degenerate system of equations.

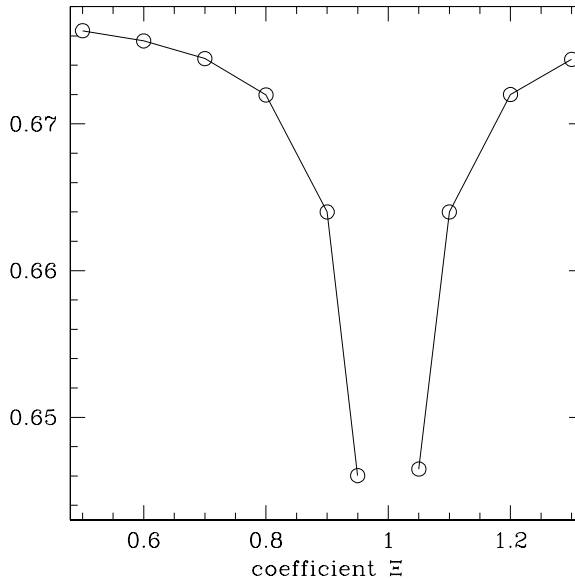


Figure 7.3: Minimum of N as a function of the coefficient Ξ multiplying the last term in Eq. (7.46).

7.5 Binary black hole solutions

7.5.1 Choices for the remaining free data

We consider initial data sets with two black holes labeled A and B . The quasi-equilibrium framework requires excision of two topologically spherical regions, which we choose to be spheres of radius $r_{A/B}$. We need further choices for the conformal metric \tilde{g}_{ij} , the mean curvature K , and a lapse boundary condition.

In the spirit of Matzner et al [63, 56] and chapter 6 of this thesis, we will continue to base these free data on a superposition of single black hole quantities. For convenience, we reproduce here Eqs. (6.46)–(6.48), which are the choices advocated by Matzner et al:

$$\tilde{g}_{ij} = \delta_{ij} + 2H_A l_{Ai} l_{Aj} + 2H_B l_{Bi} l_{Bj} \quad (7.49)$$

$$K = K_A + K_B \quad (7.50)$$

$$\tilde{M}^{ij} = \left(K_A^{(i} K_B^{j)} - \frac{1}{3} \delta_k^{(i} (K_A + K_B) \right) \tilde{g}^{j)k}. \quad (7.51)$$

We focus here on non-spinning black holes as the first step in understanding binary black hole data sets within the quasi-equilibrium framework. For non-spinning black holes, we have seen in the previous section that a multitude of

single black hole solutions exist that are *conformally flat* (namely all spherically symmetric solutions, after an appropriate radial coordinate transformation). Basing the superposition on conformally flat single black hole slices, the equivalent of (7.49) is simply

$$\tilde{g}_{ij} = \delta_{ij}. \quad (7.52)$$

For the mean curvature, we will explore two different choices:

- Eddington-Finkelstein slices with “conformally flat” radial coordinate,

$$K(x^i) = K_{EFCA}(r_A) + K_{EFB}(r_B). \quad (7.53)$$

The functions $K_{EFCA/B}$ are given by Eqs. (7.36) and (7.30) with parameters appropriate for hole A/B . The radii of the excised spheres are given by \hat{r}_{AH} from Eq. (7.37).

- maximal slices with a “conformally flat” radial coordinate. Each slice has $K_{A/B} = 0$, hence trivially

$$K = 0. \quad (7.54)$$

As mentioned already, the quasi-equilibrium approach based on the conformal thin sandwich equations does not require specification of a background extrinsic curvature analogous to (7.51). The choice (7.52) looks certainly much simpler than (7.49), however, both of these choices are inherently ambiguous in that both are based on a *specific* coordinate system within the Eddington-Finkelstein slice.

As lapse boundary condition on the excised spheres, we use a von Neumann condition,

$$\tilde{s}^k \tilde{\nabla}_k (N\psi) = 0. \quad (7.55)$$

The reasons for this condition are rather heuristic: With Dirichlet boundary condition, fairly often steep gradients arise in N close to the inner boundary. Using a von Neumann condition allows the lapse to adjust itself to reduce these gradients, and to better adjust to tidal distortion due to the other hole. We choose $\partial_t(N\psi) = 0$ rather than $\partial_t N = 0$ to mimic single black hole solutions, which often have a lapse that *increases* as one moves away from the horizon, for example, Eqs. (7.29b) and (7.44b).

Finally, the quasi-equilibrium framework presented so far does not yet fix the orbital angular frequency Ω which appears in the outer boundary condition (7.22). Gourgoulhon et al [67, 68] suggest that Ω be chosen such that the $1/r$ -terms of g_{ij}

and N behave as for a Schwarzschild black hole; in conformal flatness, this implies that

$$\psi \sim 1 + \frac{M}{2r} \quad \text{and} \quad N \sim 1 - \frac{M}{r} \quad (7.56)$$

for the same constant M . Equation (7.56) is equivalent to requiring that the ADM-energy Eq. (7.42) equals the quantity M_K defined in Eq. (7.43).⁸ Below, we take the approach of computing several data sets for different Ω and we will find that $E_{ADM} = M_K$ indeed singles out a unique Ω .

7.5.2 Eddington-Finkelstein slicings

We solve the quasi-equilibrium equations (7.28) with lapse boundary condition (7.55) for equal mass black holes. According to the discussion in the previous paragraphs, we choose a *flat* conformal metric and give the mean curvature by (7.53) with $M_A = M_B = 1$. We excise two spheres with radius $\hat{r}_{AH} \approx 1.27$ [cf. Eq. (7.37)] with centers separated by $s = 10$. By symmetry, the rotation axis of the corotating frame must pass through the origin, $R_x = R_y = 0$.

We perform several solves with different values for the last free parameter, Ω , and compute several diagnostic quantities, in particular $M_{AH} = \sqrt{A_{AH}/16\pi}$ (the apparent horizon mass of one black hole), E_{ADM} and M_K , as well as the time-derivative of the conformal factor, $\partial_t \ln \psi$ and the violation of the lapse condition, \mathcal{R} . Figure 7.4 presents these quantities as a function of Ω . We see that there is indeed a unique Ω_{EQ} such that $E_{ADM} = M_K$; in this case $\Omega_{EQ} \approx 0.04266$.

Turning our attention to the lower panel of Figure 7.4, we see that the maximal value of $|\partial_t \ln \psi|$ is smaller than $2 \cdot 10^{-3}$ for all considered values of Ω . This time derivative is smallest for $\Omega = 0$. Finally, we note that the average value of the lapse condition \mathcal{R} , Eq. (7.23) passes through zero at Ω close to Ω_{EQ} , exhibiting consistency between Eq. (7.23) and the stationarity condition $E_{ADM} = M_K$. Of course, an *average* value of \mathcal{R} of zero does not imply that $\mathcal{R} \equiv 0$, for example, for $\Omega = 0.04$, \mathcal{R} has an average of only $\mathcal{R}_{avg} = 5 \cdot 10^{-5}$, but a maximum value of $|\mathcal{R}|_{\infty} = 8 \cdot 10^{-3}$.

⁸The Komar-mass is only defined for stationary spacetimes which have a time-like Killing vector at infinity, whereas the helical Killing vector is spacelike at infinity. Hence, for binary black holes in the corotating frame M_K is, strictly speaking, not the Komar-mass.

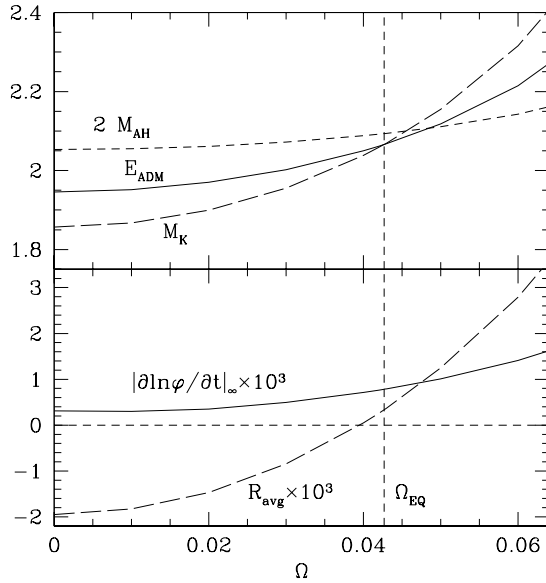


Figure 7.4: Quasi-equilibrium binary black hole initial data sets on Eddington-Finkelstein slices. Plotted are several quantities as a function of the orbital angular velocity Ω . R_{avg} denotes the residual of \mathcal{R} averaged over the boundary \mathcal{S} .

Figure 7.5 examines the solution with $\Omega = \Omega_{EQ}$ in more detail. The conformal factor around each hole is spherically symmetric to a good approximation, whereas the lapse is very asymmetric, varying on the horizon between 0.53 and 0.75. Another interesting feature is that $\partial_t \ln \psi$ is more than ten times bigger *between* the holes than anywhere else.

The results in this section confirm that it is feasible to solve the quasi-equilibrium equations on a slice that is a superposition of two Eddington-Finkelstein slices. The condition $E_{ADM} = M_K$ indeed singles out a unique Ω .

7.5.3 Maximal slices

We now repeat the computations of the last section for maximal slices. Again, the quasi-equilibrium equations (7.28) are solved with lapse boundary condition (7.55) for equal mass black holes. The conformal metric is *flat*, and the mean curvature is $K = 0$.

Table 7.1 includes a single black hole solve with these free data. It shows that an excised sphere with radius $r_{exc} \approx 1.2727$ leads to a black hole mass of

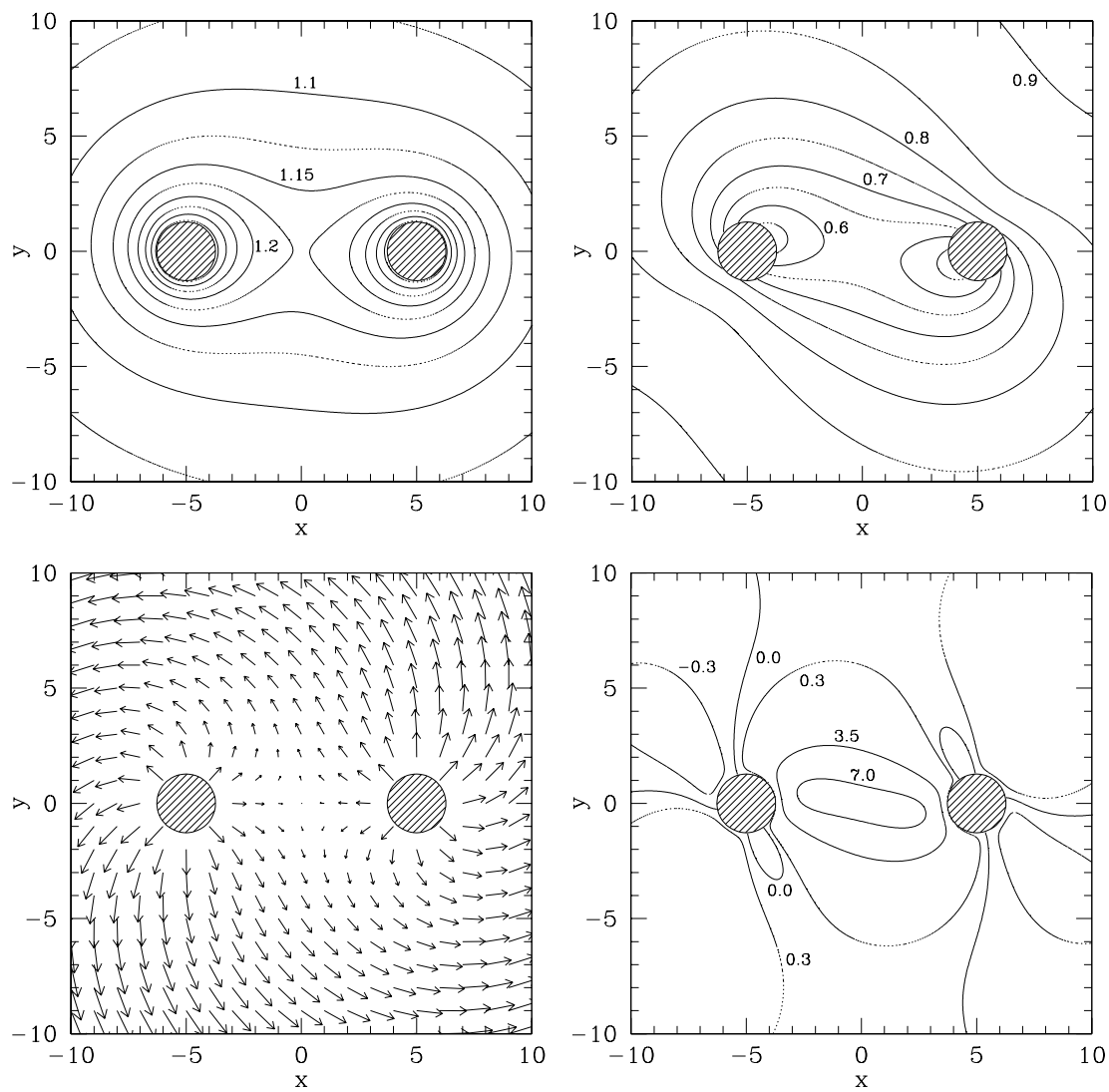


Figure 7.5: Quasi-equilibrium binary black hole initial data set on an *Eddington-Finkelstein slice*. From top right, counter-clockwise: lapse N , conformal factor ψ , shift β^i (in arbitrary units), and $\partial_t \ln \psi$ (in units of 10^{-4}).

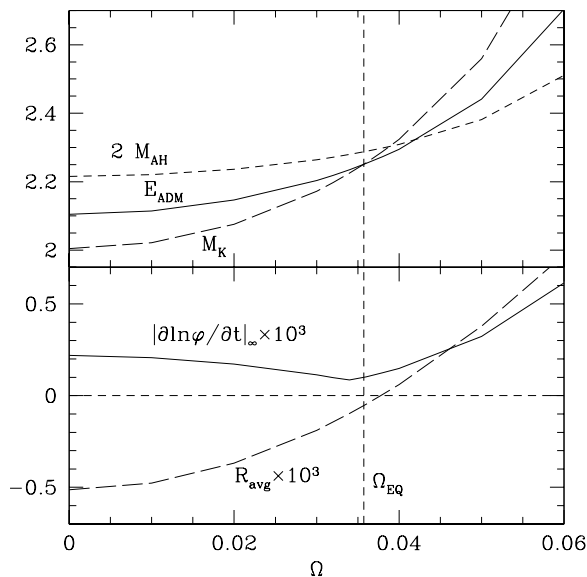


Figure 7.6: Quasi-equilibrium binary black hole initial data sets on *maximal slices*. Plotted are several quantities as a function of the orbital angular velocity Ω . R_{avg} denotes the residual of \mathcal{R} averaged over the boundary \mathcal{S} . Compare to Figure 7.4.

$M_{AH} \approx 1.4808$. Thus, $r_{exc} = 1.27274103/1.4807928 \approx 0.8594997$ in a single hole solve will result in a black hole of unit mass⁹. For ease of comparing with the previous section we therefore excise spheres with radius $r_{exc} = 0.8594997$. Although the excised spheres here and for the Eddington-Finkelstein slices considered earlier have the same conformal separation 10, the resulting initial data sets will nonetheless have black holes at different *physical* separation. For example, we will find that on maximal slices, the conformal factor tends to be larger resulting in a larger separation.

Figure 7.6 presents several quantities as functions of Ω . There is a unique $\Omega_{EQ} \approx 0.03572$, such that $E_{ADM} = M_K$. We also note that the average value of the lapse condition \mathcal{R} passes through zero close to Ω_{EQ} , and $\partial_t \ln \psi$ is closest to zero around Ω_{EQ} , too. These findings again strongly indicate that $E_{ADM} = M_K$ is a reasonable condition to select Ω .

Figure 7.7 presents cuts through the data set with $\Omega = \Omega_{EQ}$. The lapse N varies

⁹One can show analytically, that $\partial_r(N\psi) = 0$ corresponds to $C = \frac{2}{3}(\sqrt{13} - 1)$ in Eqs. (7.44). Numerical integration of the coordinate transformation to conformal flatness yields the same horizon radius as we find here [94].

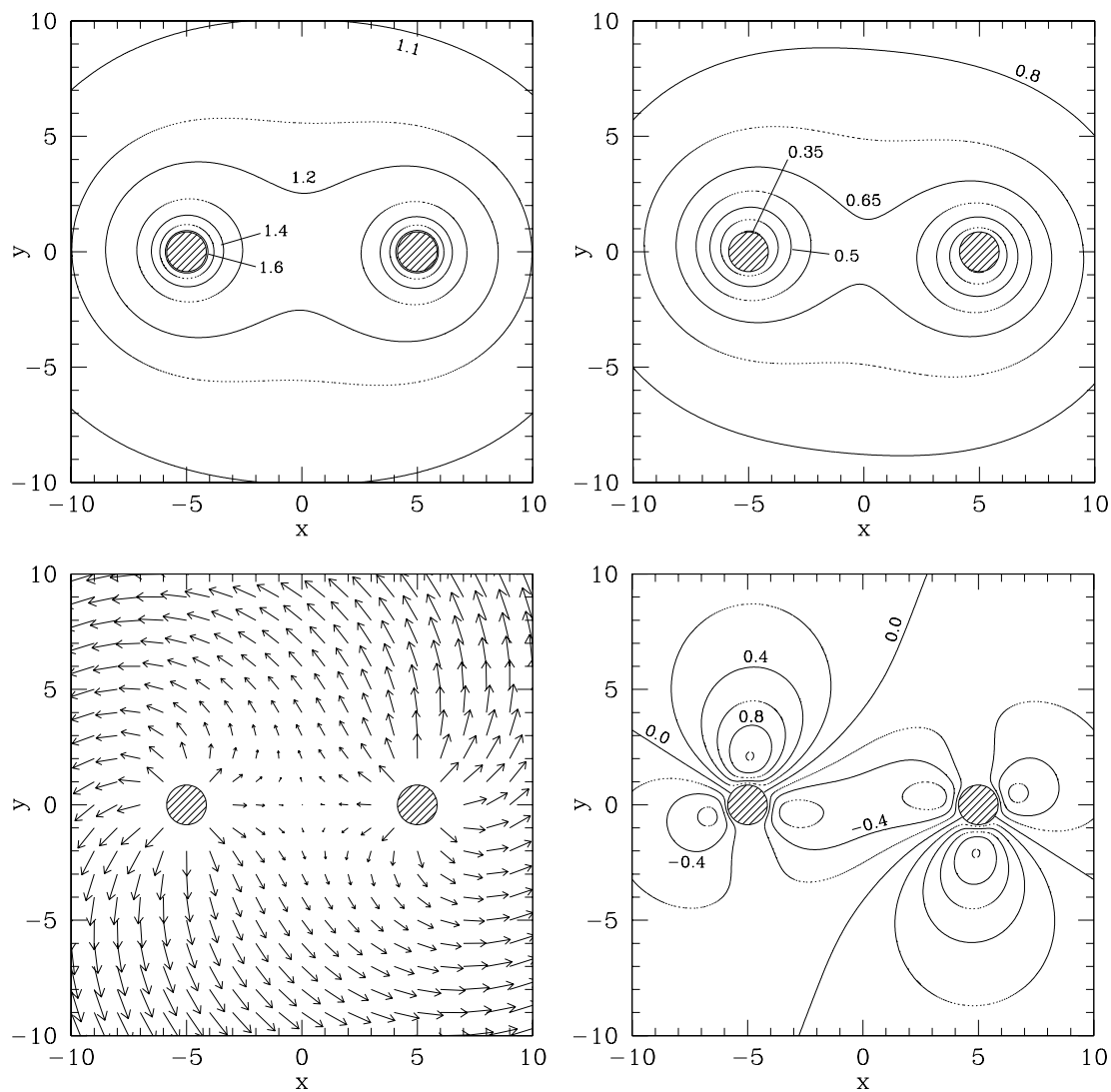


Figure 7.7: Quasi-equilibrium binary black hole initial data set on a *maximal slice*. From top right, counter-clockwise: lapse N , conformal factor ψ , shift β^i (in arbitrary units), and $\partial_t \ln \psi$ (in units of 10^{-4}). Compare to Figure 7.5.

between 0.345 and 0.395 on the horizon, a smaller variation than for the Eddington-Finkelstein slice. The time-derivative of the conformal factor is approximately one order of magnitude smaller than for the Eddington-Finkelstein slice (Figure 7.5) and exhibits more complex behavior: Along the axis connecting the black holes, $\partial_t \ln \psi$ is negative, whereas in the wake of each hole, it is positive. As a function of Ω , the extrema of $\partial_t \ln \psi$ change in a complicated way: As Ω increases, the minimum between the holes and the peaks behind the holes increase whereas the minima outside the holes on the x -axis decrease. All five extrema change sign at angular frequencies close to Ω_{EQ} .

7.5.4 Toward the test mass limit

We now attempt to compute initial data sets for unequal mass black holes. From the computational domain, we excise two spheres with radii r_1 and r_2 , centered on the x -axis at location $x = \pm s/2$, s being the separation between the centers of the excised spheres. r_1 is fixed depending on K such that the resulting hole has approximately unit-mass (e.g. $r_1 = \hat{r}_{AH}$ for K based on Eddington-Finkelstein, cf. Eq. (7.37)).

We place the center of the rotating frame at $\vec{R} = (R_x, R_y, 0)$, and choose the orbital angular frequency along the z -axis, $\vec{\Omega} = \Omega \hat{e}_z$. As before, Ω will be determined by the requirement

$$E_{ADM} = M_K. \quad (7.57a)$$

To fix R_x and R_y , we require that the linear ADM momentum vanishes,

$$P_{ADM}^i = 0. \quad (7.57b)$$

Finally, we choose the radius of the second hole such that the ratio of the apparent horizon masses equals a specified mass-ratio X ,

$$\frac{M_1}{M_2} = \frac{\sqrt{A_1/16\pi}}{\sqrt{A_2/16\pi}} = X. \quad (7.57c)$$

(In the present exploratory work, we do not take into account the black hole spins in defining $M_{1,2}$ for corotating configurations.) This procedure leads to four-dimensional rootfinding in $\Omega, r_2/r_1, R_x$, and R_y which is performed with Broyden's method [46].

We take $s = 10$ throughout this section, and perform solves (including rootfinding to satisfy Eqs. (7.57a)–(7.57c)) for $X = 1, 2, 4, 8, 16$. We explore four families of solutions, with two different slicings (Eddington-Finkelstein slicing and maximal slicing) and corotating black holes as well as irrotational black holes. In the latter case, $\beta_{\parallel}^i = \Omega(\partial/\partial\phi)^i$ on each excised sphere, with the axis of rotation centered on the respective hole.

Figure 7.8 presents results as a function of X . We see that, as $X \rightarrow \infty$, the orbital angular frequency Ω approaches a constant value for each of the four families (the families will lead to different values in the limit). The angular momentum appears to be approximately linear in the smaller mass, as it should be. The enlargement of the J_{ADM} -plot shows that at large mass-ratios for *irrotational* families, J_{ADM} is proportional to $1/X$ as expected. For *corotating* families, J_{ADM} has an additional contribution due to the intrinsic spin of the large black hole. We also find that the residual \mathcal{R} of the lapse condition on the *large* black hole tends to zero as $X \rightarrow \infty$. These findings are so far consistent with the expectation that for $X \rightarrow \infty$, we should recover a spacetime with an exact helical Killing vector.

However, two more indicators of time-independence fail: The maximum of $\partial_t \ln \psi$ seems to increase linearly with X , and the residual of \mathcal{R} on the small black hole appears to diverge even faster with X , probably quadratically. These results do not depend on the choice of slicing, or on the choice between corotation or irrotation. The maximum of $\partial_t \ln \psi$ occurs very close to the small black hole as Figure 7.9 confirms.

The behavior of $\partial_t \ln \psi$ in the vicinity of the small black hole seems to be self-similar: Scaled to the radius r_2 of the small black hole, the shape of $\partial_t \ln \psi$ appears to be independent of r_2 for sufficiently large mass-ratio, while the amplitude grows linearly with X . So far we have not scaled the time-coordinate in $\partial_t \ln \psi$. The large black hole has approximately unit mass in all solutions, so that $X = M_1/M_2 \approx 1/M_2$, from which we see that the conformal factor ψ changes on the time-scale of the small black hole.

Figure 7.9 also presents plots of the shift close to the small black hole. At the horizon, the shift points radially outward, consistent with the boundary condition (7.28f), whereas far away from the small hole, the Keplerian shift of the corotating frame dominates. The cross-over between these two regimes depends on the slicing: For Eddington-Finkelstein slices, the shift of the hole is larger than for maximal slices, hence the cross-over occurs at a larger distance. We also note that the

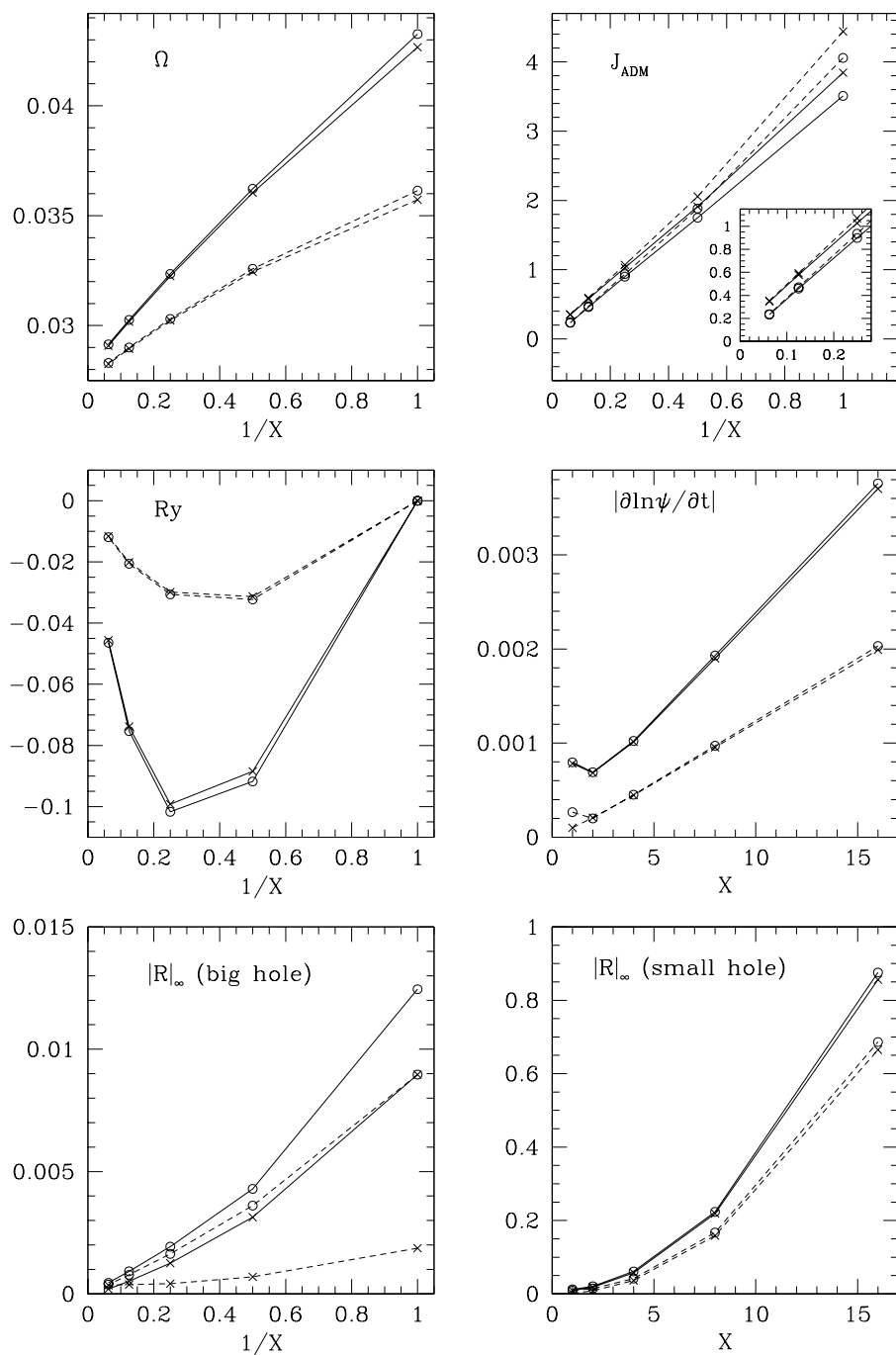


Figure 7.8: Quasi-equilibrium method in the test-mass limit: Various quantities as a function of the mass-ratio. Solid lines denote Eddington-Finkelstein slices, dashed lines maximal slices. Crosses stand for corotation, circles for irrotation.

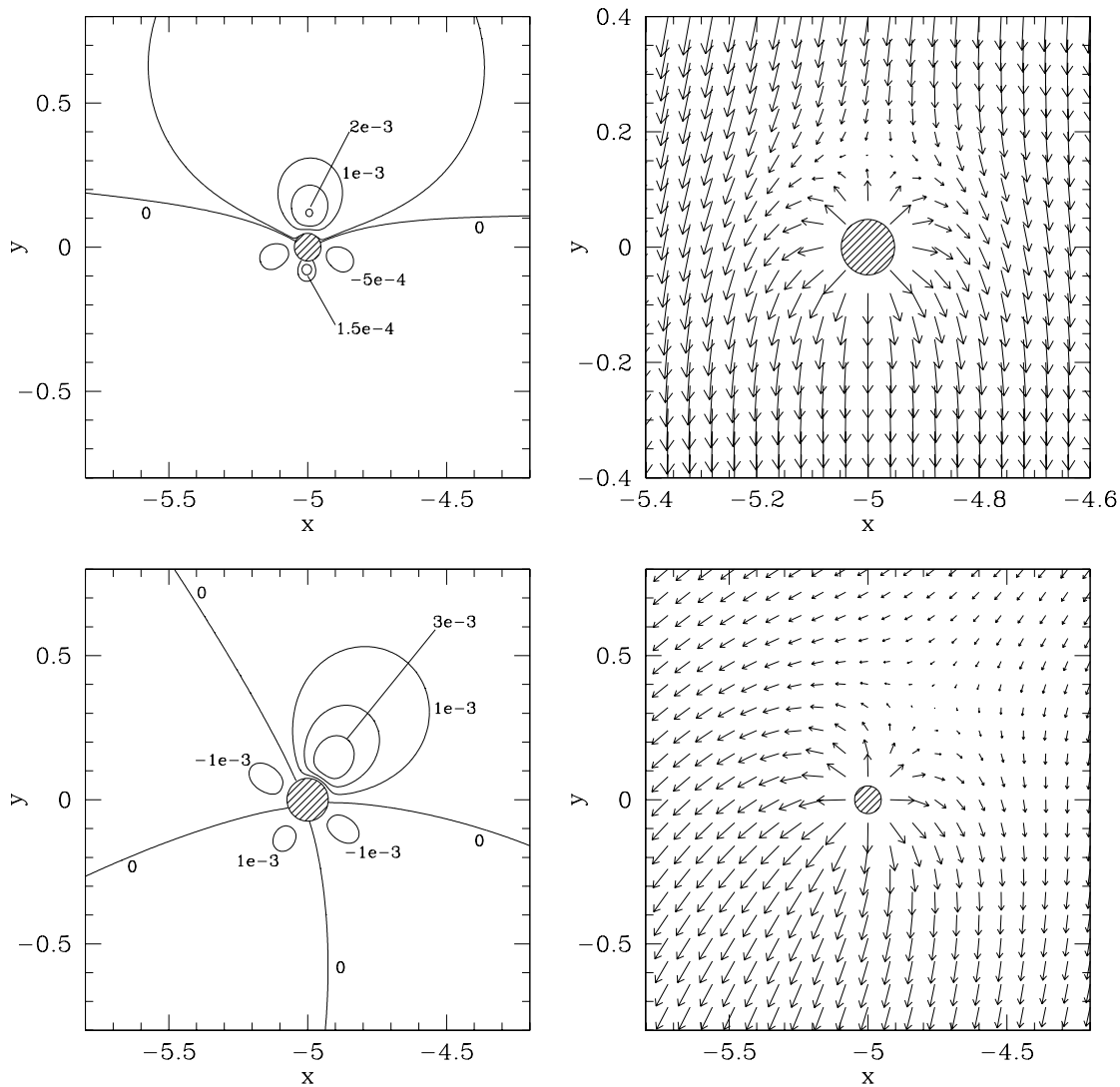


Figure 7.9: $\partial_t \ln \psi$ (left plots) and shift β^i (right plots) for the $X = 16$ initial data sets on a maximal slice (top plots) and Eddington-Finkelstein slice (bottom plots). Only a small region in the xy plane around the small black hole is shown. The upper right plot has a different scale.

maximum of $\partial_t \ln \psi$ seems to be in the vicinity of the stagnation point of the shift.

The apparent self-similarity of $\partial_t \ln \psi$ for $X \rightarrow \infty$, suggests that the small black hole influences the overall solution only in a small region around it; one can think of the small black hole as “immersed” in the “background” generated from the large black hole. If we place a sphere S around the small black hole with radius r satisfying $M_2 \ll r \ll s$, then on this surface the solution (ψ, β^i, N) of the conformal thin sandwich equations will be the solution of the large hole alone, i.e. it will not depend on M_2 (as long as $M_2 \ll r$ holds).

The values $(\psi|_S, \beta^i|_S, N|_S)$ constitute now *outer boundary conditions* for the local solution around the small black hole, which thus can be interpreted as a quasi-equilibrium solution for *one* black hole. However, in contrast to the single hole solutions in section 7.4, the outer boundary condition on the shift β^i is here *not* zero, but the Keplerian shift of the large black hole. (The conformal factor $\psi|_S$ and lapse $N|_S$ will also slightly differ from 1, however, an overall shift in those quantities corresponds merely to an overall scaling of the spatial coordinates and the time-coordinate, respectively.) As the outer boundary is far away ($M_2 \ll r \approx \infty$), the solution scales with the size M_2 of the small hole, explaining why $\partial_t \ln \psi$ is self-similar and changes on the time-scale of M_2 . The lapse condition (7.23) is essentially the time-derivative of the ingoing expansion. The ingoing expansion is proportional to $1/M_2$, and the time-derivative scales as $1/M_2$, too, thus $\mathcal{R} \propto M_2^{-2}$, as observed in Figure 7.8.

We confirm this picture by performing a single black hole solve that mimics the situation around the small black hole: We solve the quasi-equilibrium equations (7.28) on a maximal slice with inner boundary condition on the lapse $\partial_r(N\psi) = 0$, and outer boundary conditions

$$\psi = 1, \quad \beta^i = (0, -0.22, 0), \quad N = 1, \quad \text{as } r \rightarrow \infty. \quad (7.58)$$

The particular value for β^i (in Cartesian coordinates) is the ambient Keplerian shift in the top-right panel of Figure 7.9. The radius of the excised sphere is taken to be 0.8594997, appropriate for unit-mass if the outer shift boundary condition were $\beta^i \rightarrow 0$. Note that this solve differs from the spherical symmetric single black hole solves of section 7.4 only in the outer boundary condition of the shift. Figure 7.10 presents $\partial_t \ln \psi$ and shift for this solve; it is strikingly similar to the binary black hole solution in Figure 7.9.

In essence, a quasi-equilibrium solve with outer boundary conditions (7.58)

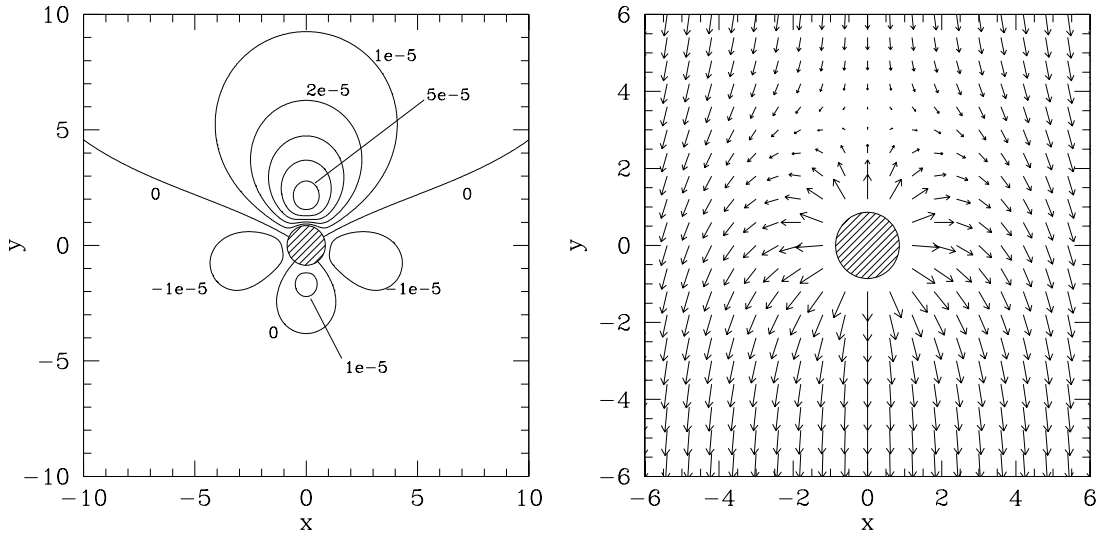


Figure 7.10: $\partial_t \ln \psi$ (left) and shift β^i (right) for a single black hole with outer boundary conditions (7.58). Compare to the upper panels of Figure 7.9.

attempts to generate a time-independent solution with a constant shift β_∞^i toward infinity – a boosted black hole in a co-moving frame. These considerations lead to two conclusions:

1. The free quantities in the quasi-equilibrium approach (\tilde{g}_{ij} , K , the lapse-boundary condition on \mathcal{S} and the shape of \mathcal{S}) must be consistent with a stationary boosted black hole in a co-moving coordinate system.
2. The free quantities we use so far do not satisfy this requirement (because $\partial_t \ln \psi \neq 0$ in Figure 7.10).

In sections 6.4.1 and 6.4.2, we use Eddington-Finkelstein initial data sets of boosted black holes in co-moving coordinates. Those data sets would be appropriate here. Due to the Lorentz-contraction, the apparent horizons of those data sets are ellipsoids, indicating that in a fully consistent quasi-equilibrium approach, one might have to abandon exactly spherical surfaces \mathcal{S} . Once we abandon spherical surfaces, however, we have to find a means to pick the shape. An ellipsoid might be appropriate for the test-mass limit $M_2 \ll M_1$, but for comparable sized black holes tidal forces might deform \mathcal{S} even further. In addition, even in the test-mass limit, one has to fix the eccentricity of the ellipsoid (i.e. the Lorentz-factor of the boost).

7.5.5 Toward the post-Newtonian limit

For binary black holes at large separations, the post-Newtonian approximation to general relativity becomes increasingly accurate. Moreover, the inspiral time-scale set by radiation-reaction forces increases much more rapidly with separation than the orbital period, so that the approximation of quasi-stationarity should more accurately reflect reality.

We therefore perform calculations at larger separations on a maximal slice (cf. section 7.5.3), which was found to have a smaller $\partial_t \ln \psi$ than the superposed Eddington-Finkelstein slice. At separations $s = 30$ and $s = 100$, we adjust Ω such that $E_{ADM} = M_K$, and examine the resulting data sets. Our results are summarized in Table 7.2. As this table contains a wealth of information we will spend quite some time discussing it (the table contains additional information about the data sets discussed in sections 7.5.2 and 7.5.3 as well).

The first block of Table 7.2 lists the two parameters s and Ω , on which the solution depends, as well as several raw numbers extracted from the computed initial data set. The second block in Table 7.2 lists dimensionless quantities in commonly used scalings.

In order to make contact with post-Newtonian theory, e.g. Eqs. (4.14a) and (4.14b), we need to accommodate the fact that the quasi-equilibrium solutions are *corotating*. From the initial data set, we know Ω (which equals the angular frequency of the horizon), and the apparent horizon mass $M_{AH} = \sqrt{A_{AH}/16\pi}$. However, in order to use Eq. (4.14b), we need the full mass M (including the rotational contribution) of each black hole as well as its spin S . For a Kerr black hole, irreducible mass and angular frequency of the horizon are given by [6]

$$M_{irr} = \frac{1}{2} \sqrt{\left(1 + \sqrt{1 - (S/M^2)^2}\right)^2 + (S/M^2)^2}, \quad (7.59)$$

$$M\Omega = \frac{S/M^2}{2 + 2\sqrt{1 - (S/M^2)^2}}. \quad (7.60)$$

Approximating $M_{irr} \approx M_{AH}$, and inverting these two relations, we find the desired quantities,

$$M = \frac{M_{AH}}{\sqrt{1 - (2M_{AH}\Omega)^2}}, \quad (7.61)$$

$$\frac{S}{M^2} = 4M_{AH}\Omega\sqrt{1 - (2M_{AH}\Omega)^2}. \quad (7.62)$$

Table 7.2: Parameters for equal mass binary black hole solutions. The $s = 10$ data sets were presented in Figures 7.5 and 7.7. M is given by Eq. (7.61), $m = 2M$ and $\mu = M/2$ are combined mass of both black holes, and reduced mass, respectively, and $E_b = E_{ADM} - 2M$.

	EF	Maximal slice		
s	10	10	30	100
Ω	0.0426633	0.0357221	0.0080078	0.0013840
E_{ADM}	2.0659	2.2506	2.06299	2.01751
M_K	2.0659	2.2506	2.06299	2.01751
M_{AH}	1.0466	1.1436	1.03934	1.011223
J_{ADM}	3.8443	4.4406	4.75536	7.49276
M	1.0508	1.1474	1.03948	1.011223
dimensionless parameters of the data-sets				
$E_{ADM}\Omega$	0.08813	0.08040	0.01652	0.00279
J_{ADM}/E_{ADM}^2	0.9007	0.8767	1.1174	1.8408
S/M^2	0.1779	0.1629	0.033287	0.0055982
$m\Omega$	0.0897	0.0820	0.016648	0.0027991
$J_{ADM}/\mu m$	3.4816	3.3730	4.40100	7.32737
E_b/μ	-0.0679	-0.0770	-0.03073	-0.00976
Comparison to post-Newtonian expansions				
J-Newton	0.642	0.682	0.8899	0.9684
J-PN-1	0.899	0.937	0.9890	0.9991
J-PN-2	0.968	1.004	1.0025	1.0005
E-Newton	1.475	1.225	1.0609	1.0172
E-PN-1	1.247	1.047	1.0076	1.0017
E-PN-2	1.135	0.962	0.9964	1.0006
relevant time-scales				
$2\pi/\Omega \equiv P$	$71E_{ADM}$	$78E_{ADM}$	$380E_{ADM}$	$2300E_{ADM}$
$1/ \partial_t \ln \psi _\infty$	$9P$	$66P$	$68P$	$52P$
$\frac{ K_{ij} _\infty}{ \partial_t K_{ij} _\infty}$	$0.2P$	$0.6P$	$0.8P$	$0.7P$
$\frac{\sqrt{ (K_{ij})^2 _\infty}}{\sqrt{ (\partial_t K_{ij})^2 _\infty}}$	$0.2P$	$0.5P$	$0.9P$	$0.7P$

The total mass and the reduced mass are $m = 2M$ and $\mu = M/2$, respectively. The black hole spins are parallel to the orbital angular momentum, so that Eq. (4.14b) reduces to

$$\left(\frac{J}{\mu m}\right)^2 = (m\Omega)^{-2/3} \left\{ 1 + \frac{4S}{M^2} (m\Omega)^{1/3} + \left(\frac{37}{12} + \frac{4S^2}{M^4}\right) (m\Omega)^{2/3} + \frac{S}{3M^2} (m\Omega) + \left(\frac{143}{18} - \frac{29S^2}{3M^4}\right) (m\Omega)^{4/3} \right\}. \quad (7.63)$$

We define the quantities

$$\text{J-Newton} \equiv \frac{(m\Omega)^{-1/3}}{J/\mu m}, \quad (7.64a)$$

$$\text{J-PN-1} \equiv \frac{(m\Omega)^{-1/3}}{J/\mu m} \left\{ 1 + \frac{4S}{M^2} (m\Omega)^{1/3} + \left(\frac{37}{12} + \frac{4S^2}{M^4}\right) (m\Omega)^{2/3} \right\}^{1/2}, \quad (7.64b)$$

$$\text{J-PN-2} \equiv \frac{(m\Omega)^{-1/3}}{J/\mu m} \left\{ 1 + \frac{4S}{M^2} (m\Omega)^{1/3} + \left(\frac{37}{12} + \frac{4S^2}{M^4}\right) (m\Omega)^{2/3} + \frac{S}{3M^2} (m\Omega) + \left(\frac{143}{18} - \frac{29S^2}{3M^4}\right) (m\Omega)^{4/3} \right\}^{1/2}. \quad (7.64c)$$

Furthermore, Eq. (4.14a) reduces in the present context to

$$\frac{E_b}{\mu} = -\frac{1}{2}(m\Omega)^{2/3} \left\{ 1 - \frac{37}{48}(m\Omega)^{2/3} + \frac{7S}{3M^2}(m\Omega) - \left(\frac{1069}{384} + \frac{S^2}{M^4}\right) (m\Omega)^{4/3} \right\} \quad (7.65)$$

so that we can examine the ratios

$$\text{E-Newton} \equiv -\frac{(m\Omega)^{2/3}}{2E_b/\mu}, \quad (7.66a)$$

$$\text{E-PN-1} \equiv -\frac{(m\Omega)^{2/3}}{2E_b/\mu} \left\{ 1 - \frac{37}{48}(m\Omega)^{2/3} \right\}, \quad (7.66b)$$

$$\text{E-PN-2} \equiv -\frac{(m\Omega)^{2/3}}{2E_b/\mu} \left\{ 1 - \frac{37}{48}(m\Omega)^{2/3} + \frac{7S}{3M^2}(m\Omega) - \left(\frac{1069}{384} + \frac{S^2}{M^4}\right) (m\Omega)^{4/3} \right\} \quad (7.66c)$$

Deviation of these numbers from unity will measure the disagreement of the quasi-equilibrium solution with predictions of post-Newtonian theory.

Table 7.2 shows that the post-Newtonian expansions are in good agreement with the quasi-equilibrium calculations. At $s = 100$, the quasi-equilibrium method and post-Newtonian expansions differ by less than 0.1 per cent. For $s = 10$ on

a maximal slice, angular momentum and binding energy agree to better than 1 per cent and a few per cent, respectively. On the Eddington-Finkelstein slice, deviations are larger, indicating that such a slicing might be less suited for quasi-equilibrium initial data.

As a final consistency check of the quasi-equilibrium method, we evaluate $\partial_t \ln \psi$ and $\partial_t K_{ij}$. The characteristic time-scale on which ψ changes is

$$\frac{1}{|\partial_t \ln \psi|_\infty}, \quad (7.67)$$

where $|\cdot|_\infty$ denotes the maximum norm. For the tensor-quantity $\partial_t K_{ij}$ it is more difficult to define a time-scale. We use the maximum value of any Cartesian component of K_{ij} and $\partial_t K_{ij}$, as well as the maximum value of $K_{ij}K_{kl}g^{il}g^{jl}$ and $\partial_t K_{ij}\partial_t K_{kl}g^{il}g^{jl}$. Thus, we estimate the characteristic time-scale for changes in K_{ij} by

$$\frac{|K_{ij}|_\infty}{|\partial_t K_{ij}|_\infty} \quad \text{and} \quad \frac{\sqrt{|K_{ij}K_{kl}g^{il}g^{jl}|_\infty}}{\sqrt{|\partial_t K_{ij}\partial_t K_{kl}g^{il}g^{jl}|_\infty}}. \quad (7.68)$$

Table 7.2 compares these three time-scales to the orbital period $P = 2\pi/\Omega$. For maximal slicing, the conformal factor changes on a fairly long timescale, about 50 orbital periods. However, the extrinsic curvature changes much faster, within half an orbital period. Both of these time scales increase approximately linearly with the orbital period.

While the time-scale of ψ is satisfactory, the time-scale associated with the extrinsic curvature is shorter than expected. For a binary in “quasi-circular orbit,” changes should occur on time-scales much longer than the orbital period. This is especially true at large separations where the radiation reaction time-scale is much longer than the orbital period.

A close inspection of the $s = 100$ data set indicates that the comparatively large time-derivatives have the same cause as in the test-mass limit: The free data of the quasi-equilibrium approach is not compatible with a boosted black hole in a comoving frame. Because the velocity of Keplerian orbits decays very slowly with separation, namely as $s^{-1/2}$, this effect dominates at large separations. When comparing a single black hole solution with appropriate nonzero shift at infinity (cf. Figure 7.10) with the region close to one black hole in the binary black hole solution (with $s = 100$), we find:

1. Very good agreement in the form and amplitude of $\partial_t \ln \psi$.

2. Good agreement in the form and amplitude of $\sqrt{(\partial_t K_{ij})^2}$.

Furthermore, very close to the horizons, the binary black hole solution exhibits tidal effects: On the hemisphere of the horizon which points away from the other black hole, $\sqrt{(\partial_t K_{ij})^2}$ is *twice* as big as on the hemisphere pointing toward the companion.

Given the good agreement of orbital parameters with the post-Newtonian expansions, it seems likely that the data sets are only contaminated locally around each black hole.

7.6 Discussion

We have presented the quasi-equilibrium method and demonstrated that it provides a viable method to construct single and binary black hole initial data.

For single non-rotating black holes, this method is spectacularly successful. Only the mean curvature K and the lapse boundary condition remain as freely specifiable data, and any (reasonable) choice for these results in a completely time-independent slicing of Schwarzschild.

Binary black hole initial data was constructed with two different choices for K . Apart from a proposed lapse boundary condition—which we found to be ill-posed—no difficulties arose when solving the coupled partial differential equations with the quasi-equilibrium boundary conditions. Furthermore, the condition $E_{ADM} = M_K$ singles out a unique orbital frequency.

We examined the test-mass limit and the limit of widely separated black holes. In both limits, we found time-derivatives $\partial_t \ln \psi$, $\partial_t K_{ij}$ significantly larger than expected based on the long inspiral time-scales in these limits. We identified one cause for these large time-derivatives, namely the apparent inconsistency of our choices for the remaining free data with a boosted black hole in co-moving coordinates.

Future work should be directed toward resolving this issue. Indeed, the demonstration that time-derivatives approach zero in these limiting cases consistent with the inspiral time-scale would be a major success. One might also continue to search for a physically motivated boundary condition for the lapse. One could consider, for example, a quantity κ defined analogous to the surface gravity by $\zeta \cdot \nabla \zeta^\mu = \kappa \zeta^\mu$ [ζ^μ is given in Eq. (7.15)]. As κ scales linearly with ζ^μ , the requirement that κ take the value appropriate for a Kerr black hole might fix the scaling of ζ^μ , i.e. the

lapse N . Finally, work is already underway to construct sequences of quasi-circular orbits based on the initial data presented in this chapter, and to determine the location of the ISCO.

Although the quasi-equilibrium initial data was found not to be perfect, it nonetheless represents a significant improvement. It is superior to initial data constructed with the Bowen-York approach in many aspects:

- The quasi-equilibrium approach avoids ambiguities regarding the choice of extrinsic curvature.
- It sets certain time-derivatives explicitly to zero, whereas with the effective potential method no rigorous statement can be made about time-derivatives.
- The quasi-equilibrium method has a natural consistency check, evaluation of the remaining time-derivatives $\partial_t \ln \psi$ and $\partial_t K_{ij}$.
- Locating quasi-circular orbits is computationally simpler than with the effective potential method because no minimization is necessary.
- The initial data solve also yields lapse and shift which can be used in the evolution of the initial data.
- The apparent horizon boundary condition and the shift boundary condition guarantee that the apparent horizons initially do not move in coordinate space. This allows evolution with black hole excision to proceed for some time without regridding.

Given all these advantages, I believe that one should aggressively attempt to evolve the equal-mass initial data sets constructed in this chapter. This is especially true in the light of the significant improvements in black hole evolutions over the last few years. The initial data based on maximal slices has somewhat smaller time-derivatives and agrees better with post-Newtonian theory than the data based on Eddington-Finkelstein slices. One should therefore evolve initial data constructed on maximal slices.

The research in this chapter illustrates that numerics has reached a level of maturity which makes it not only feasible to implement complex proposals for constructing initial data, but also to perform consistency checks and guide further analytical work.

7.7 Appendix A: Detailed quasi-equilibrium calculations

We define the extrinsic curvature of \mathcal{S} along the outward-going null rays by

$$\Sigma_{\mu\nu} = \frac{1}{2}h_\mu^\alpha h_\nu^\beta \mathcal{L}_k^{(4)} \mathbf{g}_{\alpha\beta} = h_\mu^\alpha h_\nu^\beta \underline{\nabla}_{(\alpha} k_{\beta)}, \quad (7.69)$$

where $\underline{\nabla}$ is the spacetime derivative. The trace and trace-free (symmetric) parts of $\Sigma_{\mu\nu}$ are expansion and shear, which we want to compute. Use $k^\mu = (n^\mu + s^\mu)$ and insert a redundant projection operator to find

$$\Sigma_{\mu\nu} = h_\mu^\alpha h_\nu^\beta \underbrace{g_{\alpha'}^{\alpha'} g_{\beta'}^{\beta'} \underline{\nabla}_{(\alpha'} n_{\beta')}}_{-K_{\alpha\beta}} + h_\mu^\alpha h_\nu^\beta \underline{\nabla}_{(\alpha} s_{\beta)}. \quad (7.70)$$

The first term contains the extrinsic curvature of Σ , the second term is the extrinsic curvature of \mathcal{S} as embedded in Σ . All tensors in Eq. (7.70) are purely spatial, so we can switch to Latin (spatial) indices:

$$\Sigma_{ij} = -h_i^k h_j^l K_{kl} + h_i^k h_j^l \nabla_{(k} s_{l)}. \quad (7.71)$$

The trace of Eq. (7.71) gives the expansion,

$$\theta = \Sigma_{ij} h^{ij} = -h^{ij} K_{ij} + h^{ij} \nabla_i s_j. \quad (7.72)$$

Use $h^{ij} \nabla_i s_j = \psi^{-4} \tilde{h}^{ij} \nabla_i (\psi^2 \tilde{s}_j) = \psi^{-2} \tilde{h}^{ij} \nabla_i \tilde{s}_j$ (because $\tilde{h}^{ij} \tilde{s}_i = 0$), and transform the derivative into conformal space with Eq. (2.8):

$$\begin{aligned} h^{ij} \nabla_i s_j &= \psi^{-2} \tilde{h}^{ij} (\partial_i \tilde{s}_j - \Gamma_{ij}^k \tilde{s}_k) \\ &= \psi^{-2} \tilde{h}^{ij} \left(\partial_i \tilde{s}_j - \tilde{\Gamma}_{ij}^k \tilde{s}_k - 2 (\delta_i^k \partial_j \ln \psi + \delta_j^k \partial_i \ln \psi - \tilde{g}_{ij} \tilde{g}^{kl} \partial_l \ln \psi) \tilde{s}_k \right) \\ &= \psi^{-2} \left(\tilde{h}^{ij} \tilde{\nabla}_i \tilde{s}_j + 4 \tilde{s}^l \partial_l \ln \psi \right). \end{aligned} \quad (7.73)$$

Combining Eqs. (7.72) and (7.73), and setting $\theta = 0$ gives

$$\tilde{s}^k \partial_k \ln \psi = -\frac{1}{4} \left(\tilde{h}^{ij} \tilde{\nabla}_i \tilde{s}_j - \psi^2 h^{ij} K_{ij} \right), \quad (7.74)$$

which is Eq. (7.12) from the main text.

To compute the shear, it is easiest to return to Eq. (7.71) and use the conformal thin sandwich decomposition of K_{ij} , Eqs. (2.11) and (2.25). The first term of (7.71) gives (with $\tilde{u}_{ij} = 0$)

$$\begin{aligned} h_i^k h_j^l K_{kl} &= h_i^k h_j^l \left(\frac{1}{3} g_{kl} K + \frac{1}{2N} (\mathbb{L}\beta)_{kl} \right) \\ &= \frac{1}{3} h_{ij} \left(K - \frac{1}{N} \nabla_k \beta^k \right) + \frac{1}{N} h_i^k h_j^l \nabla_{(k} \beta_{l)}. \end{aligned} \quad (7.75)$$

Now substitute the boundary condition $\beta^k = \beta_\perp s^k + \beta_\parallel$ into the second term of Eq. (7.71). It suffices that the boundary condition holds only on \mathcal{S} , because the derivative is projected into \mathcal{S} . Using $h_i^k s_k = 0$, we find

$$h_i^k h_j^l K_{kl} = \frac{1}{3} h_{ij} \left(K - \frac{1}{N} \nabla_k \beta^k \right) + \frac{\beta_\perp}{N} h_i^k h_j^l \nabla_{(k} s_{l)} + \frac{1}{N} D_{(i} \beta_{j)}, \quad (7.76)$$

where D_i denotes the induced two-dimensional covariant derivative in \mathcal{S} . Equation (7.71) becomes

$$\Sigma_{ij} = -\frac{1}{3} h_{ij} \left(K - \frac{1}{N} \nabla_k \beta^k \right) + \left(1 - \frac{\beta_\perp}{N} \right) h_i^k h_j^l \nabla_{(k} s_{l)} - \frac{1}{N} D_{(i} \beta_{j)}. \quad (7.77)$$

The first term of (7.77) is purely trace and the second term vanishes because of the boundary condition $\beta_\perp = N$. Therefore, the shear is simply

$$\sigma_{ij} = \Sigma_{ij} - \frac{1}{2} h_{ij} h^{kl} \Sigma_{kl} = -\frac{1}{N} \left(D_{(i} \beta_{j)} - \frac{1}{2} h_{ij} D_k \beta_\parallel^k \right) = -\frac{1}{2N} (L_S \beta_\parallel)_{ij}, \quad (7.78)$$

where L_S denotes the two-dimensional longitudinal operator within \mathcal{S} . Thus, the shear vanishes if $(L_S \beta_\parallel)^{ij} = 0$, or, using the conformal scaling behavior of the longitudinal operator, Eq. (2.18), if

$$(\tilde{L}_S \beta_\parallel)^{ij} = \tilde{D}^i \beta_\parallel^j + \tilde{D}^j \beta_\parallel^i - \tilde{h}^{ij} \tilde{D}_k \beta_\parallel^k = 0, \quad (7.79)$$

which is Eq. (7.18) from the main text.

7.8 Appendix B: Code Tests

We set the conformal metric \tilde{g}_{ij} and the mean curvature K to their values for Eddington-Finkelstein, Eqs. (7.29a) and (7.30), and verify that the conformal factor $\psi \equiv 1$ and lapse and shift given by Eqs. (7.29b) and (7.29c) indeed solve the quasi-equilibrium equations (7.28). We also perform the variable transformation (7.34) to a conformally flat metric, and verify that a flat background metric, $\tilde{g}_{ij} = \delta_{ij}$, transformed lapse and shift and the now non-trivial conformal factor (7.35) still satisfy Eqs. (7.28). (In the latter case, one has to change the radius of the excised sphere to \hat{r}_{AH} as given by (7.37)). Convergence of the residuals to zero is demonstrated in Figure 7.11.

The lapse boundary condition (7.23) is very complicated, and was implemented only for spherically symmetric conformal metrics \tilde{g}_{ij} , which includes conformal

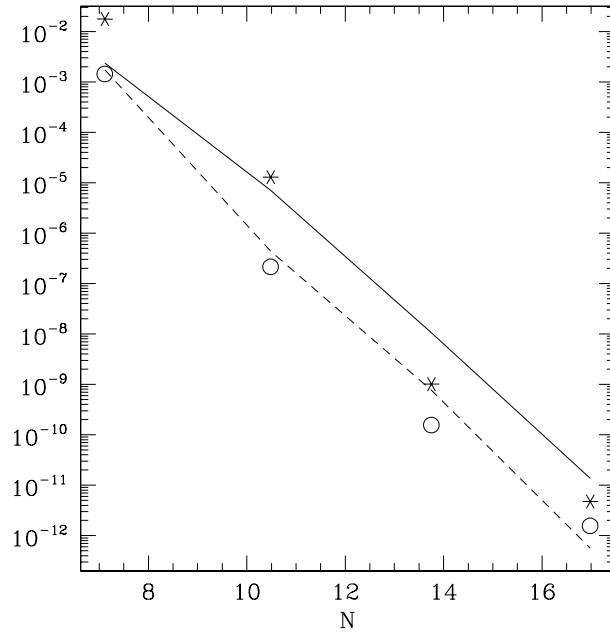


Figure 7.11: Residuals of the quasi-equilibrium boundary conditions (7.28) and the lapse quasi-equilibrium condition (7.23) for an Eddington-Finkelstein slice in the standard coordinates (solid line) and the “conformally flat” coordinates (dashed line). The stars and circles denote the violation of the Hamiltonian constraint for both cases. All norms are L_∞ -norms.

flatness, and the usual Eddington-Finkelstein slicing (7.29). (The *solutions* ψ , β^i and N are not required to be spherically symmetric). The lapse condition is included in the residuals shown Figure 7.11, already providing a first test of Eq. (7.23). However, many terms in Eqs. (7.23) and (7.24) vanish identically for spherically symmetric solutions like Eqs. (7.29b) and (7.29c).

We therefore test the code implementing Eq. (7.23) against a separate analytical calculation with Mathematica. We choose a flat background metric $\tilde{g}_{ij} = \text{flat}$, and set

$$\begin{aligned}
 \psi &= 1 + \frac{a_0}{|\vec{r} - \vec{r}_0|}, & \vec{\beta} &= \hat{e}_r \frac{1}{r} + \hat{e}_x \frac{a_1}{|\vec{r} - \vec{r}_1|} + \hat{e}_z \frac{a_2}{|\vec{r} - \vec{r}_2|}, \\
 N\psi &= 1 + \frac{a_3}{|\vec{r} - \vec{r}_3|}, & K &= \frac{a_4}{|\vec{r} - \vec{r}_4|}, & \tilde{u}_{ij} &= \frac{U_{ij}}{|\vec{r} - \vec{r}_u|},
 \end{aligned} \tag{7.80}$$

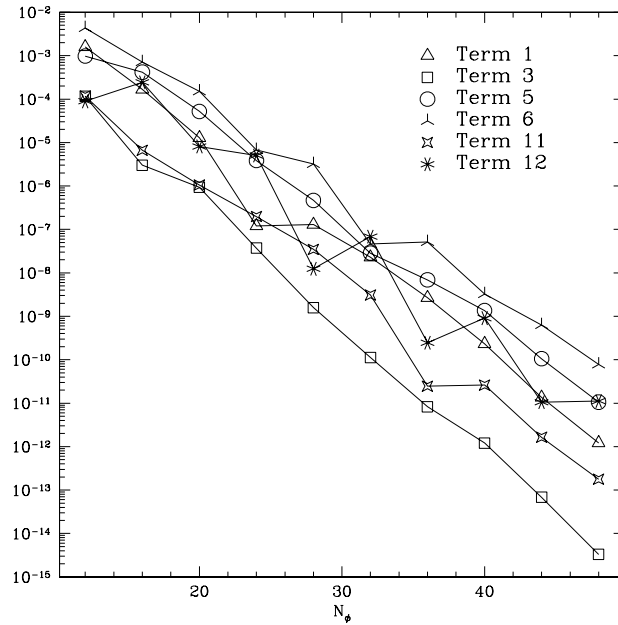


Figure 7.12: Convergence of selected terms of the lapse boundary condition Eq. (7.23).

with constants

$$\begin{aligned}
 a_0 &= -0.2, & \vec{r}_0 &= (-0.1, 0.2, 0.3), & a_1 &= 0.3, & \vec{r}_1 &= (0.3, 0.0, -0.1), \\
 a_2 &= -0.2, & \vec{r}_2 &= (0.3, -0.1, 0.2), & a_3 &= -0.3, & \vec{r}_3 &= (0.3, 0.1, -0.2), \\
 a_4 &= 1, & \vec{r}_4 &= (0.3, 0.1, 0.1), & U_{ij} &= 0.1(i + j), & \vec{r}_u &= (0.3, 0, -0.1).
 \end{aligned}$$

\mathcal{S} was taken as a sphere centered at the origin with radius 1.2. These data do not satisfy Eq. (7.23), of course. However, we can nonetheless compare the computed values of various terms in (7.23) against the results obtained with Mathematica. Figure 7.12 confirms that these results converge exponentially with resolution, as expected. (In the implementation, Eq. (7.23) has been expanded into smaller terms, see Eq. (7.45). The numbering of terms in Figure 7.12 corresponds to the terms in the code).

7.9 Appendix C: Extrapolation into the interior of the excised spheres

The quasi-equilibrium method yields initial data *up to* the apparent horizon. Evolutions with black hole excision, however, place the inner boundary *inside* the

apparent horizon, so that one needs to extrapolate the initial data set a small distance into the interior of \mathcal{S} . Simple summation of the spectral series outside its domain is very unstable as the high frequency modes blow up very quickly. A function f given in the inner spherical shell is extrapolated into the excised region with the following method:

1. For each grid point on the inner surface of the shell, compute radial derivatives up to order N_{extrp} ; we denote these derivatives by $f_{jk}^{(n)}$, where j and k label the angular grid-points.
2. To extrapolate to a point (r, θ, ϕ) with $r < r_{exc}$, first spectrally interpolate $f_{jk}^{(n)}$ to the direction (θ, ϕ) . This is done by summing up the expansion in spherical harmonics, and results in $f^{(n)}(\theta, \phi)$, $n = 0, \dots, N_{extrp}$. Then use a Taylor series in radius to find

$$f(r, \theta, \phi) = \sum_{n=0}^{N_{extrp}} \frac{f^{(n)}(\theta, \phi)}{n!} (r_{exc} - r)^n. \quad (7.81)$$

By construction, this procedure leads to an extrapolation that is smooth up to and including the N_{extrp} -th derivative. Note that this procedure is *not* equivalent to just truncating the spectral series after N_{extrp} terms; it rather takes polynomials up to order N_{extrp} from *all* terms in the spectral series. Extrapolation by a truncated spectral series, i.e.

$$f(r) = \begin{cases} \sum_0^N \tilde{f}_k \Phi_k(r), & \text{for } r \geq r_{exc} \\ \sum_0^{N_{extrp}} \tilde{f}_k \Phi_k(r), & \text{for } r < r_{exc} \end{cases} \quad (7.82)$$

results in a discontinuous function,

$$\lim_{\varepsilon \rightarrow 0} (f(r_{exc}) - f(r_{exc} - \varepsilon)) = \sum_{N_{extrp}+1}^N \tilde{f}_k \Phi_k(r_{exc}) \neq 0. \quad (7.83)$$

Two considerations influence the choice of N_{extrp} . If it is too big, then the Taylor series is dominated by the very fast growing highest radial derivatives, which in turn depend on high-order spectral coefficients. These coefficients are small and have a comparatively large (relative) error so that the extrapolation

becomes inaccurate. On the other hand, using a Taylor series up to order N_{extrp} implies that the $(N_{extrp} + 1)$ -st derivative of the extrapolated function will be discontinuous at the location of the inner boundary. If N_{extrp} is too small, this discontinuity will destroy exponential convergence.

In practice, we found that $N_{extrp} = 10$ is satisfactory. For example, evolutions run for roughly the same evolution time [98] with completely analytic Eddington-Finkelstein initial data, or with initial data that is the analytic Eddington-Finkelstein just *up to* the horizon, while the grid-points inside the horizon are filled by extrapolation.

Chapter 8

Initial data with superposed gravitational waves

8.1 Introduction

The goal of this chapter is to construct initial data sets that contain a strong gravitational wave where one can control certain characteristics like shape, location and direction of propagation.

Spacetimes containing some component of gravitational radiation are very interesting for several reasons. One can, for example, investigate perturbed black holes [99, 100], or examine critical collapse to a black hole [101, 102]. Moreover, an initial data set with gravitational radiation is non-stationary and is therefore a good test for numerical evolution codes and gravitational wave extraction in a setting computationally much simpler than a full binary black hole evolution.

Numerical work on perturbed black holes is either done on spacelike hypersurfaces (the formalism we use throughout this thesis), or on null surfaces, with so-called characteristic formulations. Characteristic formulations are very well adapted to studying gravitational radiation, since gravitational radiation moves along null-cones which coincide with coordinate surfaces. Bishop et al [103] demonstrate their characteristic code by scattering a strong ingoing pulse of radiation on a Schwarzschild black hole. Papadopoulos [100] perturbs a Schwarzschild black hole with an outgoing pulse centered on the potential barrier at $r = 3M$ and examines the power emitted into different modes. Characteristic formulations, however, are limited by formation of caustics; in particular, a binary black hole coalescence most likely cannot be computed with a characteristic formulations alone (see for example the discussion in [104]). Therefore we now turn our attention back to the initial value problem on spacelike surfaces, where we will recover some aspects of work already done using the characteristic formulation.

Perturbed spacetimes represented on *spacelike surfaces* dates back to Brill [8]. He pointed out that, for time-symmetry, a certain axisymmetric form of the metric,

$$ds^2 = \psi^4 [e^{2q} (d\rho^2 + dz^2) + \rho^2 d\phi^2], \quad (8.1)$$

allows the Hamiltonian constraint (2.55) to be written as a very simple *flat space*

Laplace equation for the conformal factor ψ . Here, (ρ, z, ϕ) are cylindrical coordinates, and the function $q(\rho, z)$ can be freely specified (subject to certain regularity and fall-off conditions), encoding the perturbation of the spacetime. Brill used (8.1) for a positivity of energy proof.

Since then, so-called ‘‘Brill-waves’’ with various choices for q have been used. Perturbations of *flat space* were obtained, for example, with ([105, 106, 107, 108])

$$q = \frac{A\rho^2}{1 + (r/\lambda)^n}, \quad (8.2)$$

$$q = Ar^2 \exp \left[- \left(\frac{\rho}{a} \right)^2 - \left(\frac{z}{b} \right)^2 \right], \quad (8.3)$$

$$q = A\rho^2 e^{-r^2} \left[1 + c \frac{\rho^2}{1 + \rho^2} \cos^2(m\varphi) \right], \quad (8.4)$$

$$(8.5)$$

with constants A, λ, a, b, c, n and integer m . For perturbations around flat space, there are no singularities or inner boundaries in the computational domain, and the conformal factor ψ will be close to unity; in particular, $q \equiv 0$ yields the solution $\psi \equiv 1$: flat space. Shibata [109] generalized (8.1) to compute three-dimensional time-symmetric initial data sets.

Black hole solutions with superposed Brill waves can be obtained by excising a sphere from the computational domain and applying an isometry boundary condition on ψ . Then the conformal factor will significantly differ from unity close to the inner boundary. This approach has been used, for example, in [110, 111, 112]. These authors also modify the conformal metric (8.1) and abandon time-symmetry to incorporate spin. They choose the extrinsic curvature in such a way that it satisfies the momentum constraint, so that only the Hamiltonian constraint has to be solved for ψ . In the spirit of Brill, a function q still parametrizes the distortion, for example [112],

$$q = A \sin^n \theta \left(e^{-(\eta+b)^2/w^2} + e^{-(\eta-b)^2/w^2} \right) (1 + c \cos^2 \varphi). \quad (8.6)$$

Here, η is a radial coordinate (the horizon is at $\eta = 0$), and A, b, c, w, n are constants. b was set to zero in the computations in [110, 111, 112], so that the Brill distortion is located *on the throat*, making it difficult to distinguish between effects of the initial perturbation from subsequent interaction of the black hole with the gravitational wave.

This short and non-exhaustive survey illustrates that a lot of work is based on Brill’s original idea. The different choices for q show that there is considerable freedom in this approach. It appears that, generally, the function q is chosen rather ad hoc, its purpose mainly being to perturb the spacetime in *some* way. Every one of these choices for q leads to a perturbed initial data set containing a “blob” of gravitational radiation. However, it is not clear what properties the gravitational radiation has nor how to control them.

Part of the motivation to use the Brill metric (8.1) was certainly that the resulting elliptic equation is relatively simple. As we have a robust elliptic solver for the coupled constraint equations, computational complexity is no longer a concern.

We describe here a different approach, which is based on *linear* gravitational waves. By choosing the underlying linear wave one can construct initial data sets with very specific properties. This approach is related to and generalizes work by Abrahams & Evans [113, 102]. Their axisymmetric work sets a certain component of the extrinsic curvature (namely K_θ^r in spherical coordinates) equal to the value appropriate for the linear wave, and solves the momentum constraints for the remaining components of K_{ij} ; this procedure singles out a preferred coordinate system. Our method here, in contrast, is three-dimensional, and covariant with respect to spatial coordinate transformations. Moreover, we use the conformal thin sandwich formalism and not an extrinsic curvature decomposition.

8.2 Method

We first recall some properties of linear gravitational waves. In linear gravity, one writes the spacetime metric as

$${}^{(4)}\mathbf{g}_{\mu\nu} = \eta_{\mu\nu} + A h_{\mu\nu}, \quad (8.7)$$

where $\eta_{\mu\nu}$ is the Minkowski-metric, $A \ll 1$ a constant, and $h_{\mu\nu} = \mathcal{O}(1)$ the linear gravitational wave. (We separate the amplitude A from $h_{\mu\nu}$ for later convenience.) In the *transverse-traceless* gauge [6], $h_{\mu\nu}$ is purely spatial, $h_{\mu 0} = 0$, transverse with respect to Minkowski space, $\nabla^i h_{ij} = 0$, and traceless, $\eta^{ij} h_{ij} = 0$. To first order in the amplitude A , Einstein’s equations reduce to

$$\square h_{ij} = 0. \quad (8.8)$$

The 3+1 decomposition of the metric (8.7) in transverse-traceless gauge is

$$g_{ij} = f_{ij} + A h_{ij} \quad (8.9a)$$

$$\beta^i = 0, \quad (8.9b)$$

$$N = 1, \quad (8.9c)$$

where f_{ij} denotes the flat metric. The evolution equation for g_{ij} , Eq. (2.3), yields the extrinsic curvature

$$K_{ij} = -\frac{A}{2} \dot{h}_{ij}. \quad (8.9d)$$

The spacetime metric (8.7) satisfies Einstein's equations to first order in A . Consequently, (g_{ij}, K^{ij}) from Eqs. (8.9a) and (8.9d) will satisfy the constraints to linear order in A , also. Since we will increase A to order unity later on, this is not sufficient, and we must solve the constraint equations. But which formalism and what free data should we use?

Given a linear wave h_{ij} it is straightforward to compute the three-dimensional metric $g_{ij} = f_{ij} + A h_{ij}$ and its *time-derivative* $A \dot{h}_{ij}$. In the conformal thin sandwich decomposition (section 2.2), we are free to specify a conformal metric \tilde{g}_{ij} and its *time-derivative* $\partial_t \tilde{g}_{ij} = \tilde{u}_{ij}$. This suggests using the conformal thin sandwich equations with the choices

$$\tilde{g}_{ij} = f_{ij} + A h_{ij}, \quad (8.10a)$$

$$\tilde{u}_{ij} = A \dot{h}_{ij} - \frac{1}{3} \tilde{g}_{ij} \tilde{g}^{kl} A \dot{h}_{kl}. \quad (8.10b)$$

The second term in (8.10b) ensures that \tilde{u}_{ij} is tracefree with respect to \tilde{g}_{ij} . Because h_{ij} and \dot{h}_{ij} are both traceless, Eq. (8.9d) suggests the choice

$$K = 0. \quad (8.10c)$$

The free data Eq. (2.31) is completed by setting

$$\dot{K} = 0. \quad (8.10d)$$

We now have a prescription to construct a slice through perturbed flat space with an arbitrarily strong gravitational wave: Pick a gravitational wave in TT gauge, h_{ij} , and solve the conformal thin sandwich equations with free data given by Eqs. (8.10).

We generalize this prescription to an arbitrary background spacetime as follows:

Let g_{ij}^0 and K^0 be the 3-metric and mean curvature of a slice through a stationary spacetime (for example flat space or a Kerr black hole). Solve the conformal thin sandwich equations with the free data

$$\tilde{g}_{ij} = g_{ij}^0 + A h_{ij}, \quad (8.11a)$$

$$\tilde{u}_{ij} = A \dot{h}_{ij} - \frac{1}{3} \tilde{g}_{ij} \tilde{g}^{kl} A \dot{h}_{kl}, \quad (8.11b)$$

$$K = K^0, \quad (8.11c)$$

$$\dot{K} = 0. \quad (8.11d)$$

We consider a few limiting cases

- $A \rightarrow 0$ recovers the underlying stationary spacetime in time-independent coordinates (if appropriate boundary conditions were used).
- For $A \ll 1$ with linear wave “far away” where the spacetime is approximately flat, $g_{ij}^0 \approx f_{ij}$, $K^0 \approx 0$ the linear theory is valid and the properties of the linear wave are well defined and well known¹.
- Finally, for large A we will have a nonlinearly perturbed spacetime, our primary interest. Due to the nonlinearity of Einstein’s equations, the properties of such a strongly perturbed spacetime will differ from the linear wave, however, we would expect that the qualitative properties still agree.

We remark that this formalism is covariant; any suitable three dimensional coordinate system can be used. Furthermore, the conformal thin sandwich equations have to be solved in a general conformal background, cf. Eqs. (8.10a) and (8.11a), which requires an elliptic solver capable of handling this situation.

¹If h_{ij} is a linear wave on the curved background g_{ij}^0 , then the $A \ll 1$ case is well-defined even for a wave in the strong curvature region. However, we consider here only the simpler case of h_{ij} being a flat space wave.

8.3 Quadrupole waves

We use for h_{ij} quadrupole waves as described by Teukolsky [114]. The even parity outgoing wave is [114]

$$\begin{aligned}
 ds^2 = & -dt^2 + (1 + Af_{rr})dr^2 + (2Bf_{r\theta})rdrd\theta + (2Bf_{r\theta})r \sin \theta drd\phi \\
 & + \left(1 + Cf_{\theta\theta}^{(1)} + Af_{\theta\theta}^{(2)}\right) r^2 d\theta^2 + [2(A - 2C)f_{\theta\phi}] r^2 \sin \theta d\theta d\phi \quad (8.12) \\
 & + \left(1 + Cf_{\phi\phi}^{(1)} + Af_{\phi\phi}^{(2)}\right) r^2 \sin^2 \theta d\phi^2.
 \end{aligned}$$

with radial dependence given by

$$A = 3 \left[\frac{F^{(2)}}{r^3} + \frac{3F^{(1)}}{r^4} + \frac{3F}{r^5} \right], \quad (8.13)$$

$$B = - \left[\frac{F^{(3)}}{r^2} + \frac{3F^{(2)}}{r^3} + \frac{6F^{(1)}}{r^4} + \frac{6F}{r^5} \right], \quad (8.14)$$

$$C = \frac{1}{4} \left[\frac{F^{(4)}}{r} + \frac{2F^{(3)}}{r^2} + \frac{9F^{(2)}}{r^3} + \frac{21F^{(1)}}{r^4} + \frac{21F}{r^5} \right], \quad (8.15)$$

$$F^{(n)} \equiv \left[\frac{d^n F(x)}{dx^n} \right]_{x=t-r}. \quad (8.16)$$

$F(x) = F(t-r)$ describes the shape of the wave. The functions $f_{rr}, \dots, f_{\phi\phi}^{(2)}$ depend only on angles (θ, ϕ) ; they are given explicitly in Ref. [114] for azimuthal quantum number $m = -2, \dots, 2$. *Ingoing* quadrupole waves are obtained by replacing $F(t-r)$ with a function of $t+r$, and reversing the signs in front of odd derivatives of F in Eq. (8.16). Reference [114] gives also the metric for odd parity waves. From Eq. (8.12), one can easily extract h_{ij} and \dot{h}_{ij} in spherical coordinates, which we transform to the Cartesian coordinates used in the code.

8.4 Results

8.4.1 Flat space with ingoing pulse

We first consider a perturbation of flat space, $g_{ij}^0 = f_{ij}$, $K^0 = 0$. We choose the even parity, $m = 0$ ingoing mode. The shape of the pulse is taken as a Gaussian

$$F(x) = e^{-(x-x_0)^2/w^2} \quad (8.17)$$

of width $w = 1$ and with an initial radius of $x_0 = 20$.

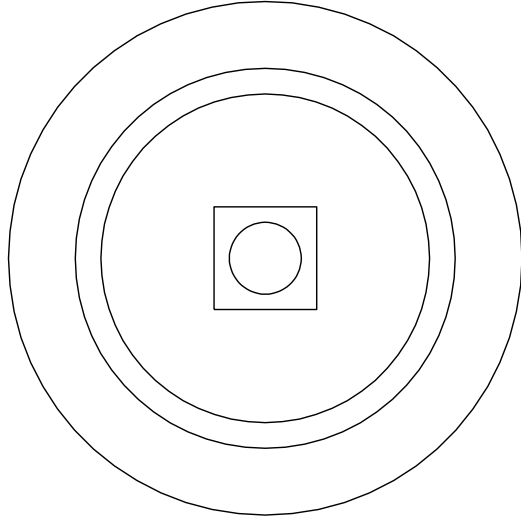


Figure 8.1: Domain decomposition used for elliptic solves in full R^3 . A cube covers the central region which is not covered by the spherical shells.

The domain decomposition used during the solve is shown in Figure 8.1. We use three spherical shells with boundaries at $r = 1.5, 16, 24, 10^6$. The middle shell is centered on the gravitational wave and has higher radial resolution than the other shells. The inner shell does not extend down to the origin, since the regularity conditions at the origin of a sphere are not implemented. Instead, we place a cube on the origin which overlaps with the innermost spherical shell.

As a first step, we verify that such a linear wave does satisfy the constraints to first order in A . Figure 8.2 shows the constraint violation of (g_{ij}, K_{ij}) given by Eqs. (8.9a) and (8.9d), or, equivalently to linear order in A , by the free data Eqs. (8.11) *without* solving the conformal thin sandwich equations.

We now solve the conformal thin sandwich equations with the free data (8.11) for different A . For small A , we find that $\psi - 1$ is proportional to A^2 . This is expected, because $\psi - 1$ corrects the conformal metric to satisfy the Hamiltonian constraint. As the constraint violation is proportional to A^2 , so is this correction. Figure 8.3 presents the ADM-energy of the resulting hypersurfaces as a function of A . One can clearly achieve initial data sets with a significant energy content. At low amplitudes, E_{ADM} is proportional to A^2 , as one expects given that $\psi - 1$ is proportional to A^2 . At high amplitudes, however, E_{ADM} grows faster than A^2 , indicating that the non-linear regime with self-interaction is reached. For $A > 0.3$, the elliptic solver fails to converge.

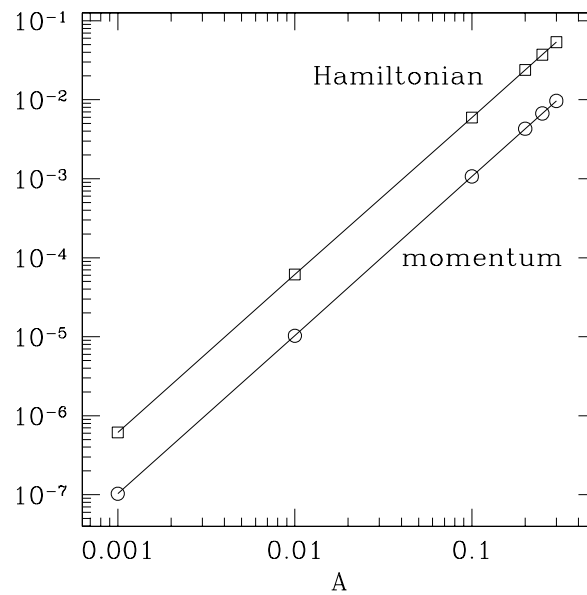


Figure 8.2: Constraint violation of linear gravitational wave in flat background.

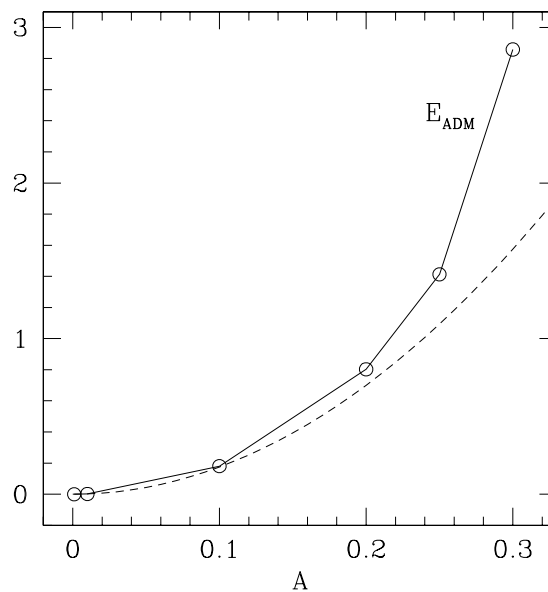


Figure 8.3: ADM energy of an ingoing Gaussian pulse in flat space. The dashed line indicates the low-amplitude quadratic behavior.

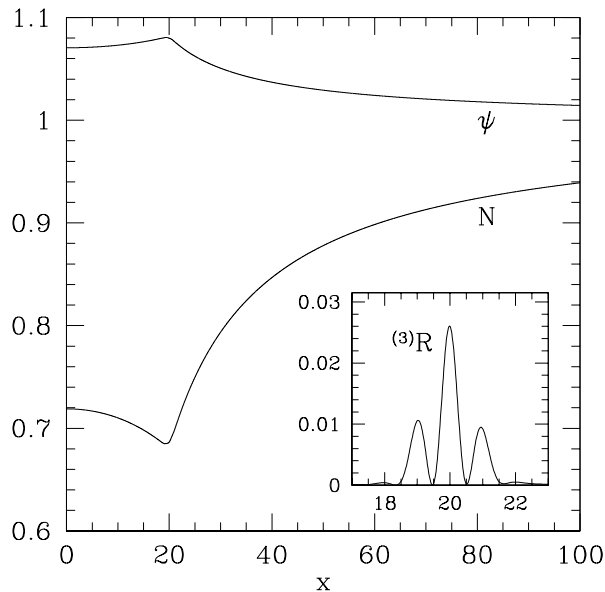


Figure 8.4: Cuts through the equatorial plane of the $A = 0.3$ data set of Fig. 8.3. The large plot shows lapse and conformal factor, the insert shows the scalar curvature of the 3-metric.

We now examine the highest amplitude data set with $A = 0.3$, having $E_{ADM} = 2.858$. Figure 8.4 presents cuts through the conformal factor ψ , lapse N and the scalar curvature of the physical 3-metric, ${}^{(3)}R$. Conformal factor and lapse deviate significantly from unity confirming that the solution is indeed deep in the nonlinear regime. The scalar curvature is virtually zero everywhere except within a spherical shell with $18 \lesssim r \lesssim 20$.

The gravitational wave is concentrated in a spherical shell of width $w = 1$. The underlying *linear* wave is purely ingoing, so it seems reasonable that the gravitational perturbation in the physical, *nonlinear* spacetime is also predominantly ingoing. Neglecting dispersion, the wave will concentrate in a sphere centered at the origin with radius $r \sim w$. Black holes usually form for systems with mass to size ratio of order unity; here, $E_{ADM}/w \approx 2.8$, so that black hole formation appears very likely once the pulse is concentrated at the origin.

These data sets could be used to examine critical collapse to a black hole, repeating Abrahams & Evans [102] and extending it to genuinely three-dimensional collapse by choosing $m \neq 0$ in the underlying quadrupole wave. These datasets also provide a testbed for evolution codes in situations where the *topology* of the horizons changes.

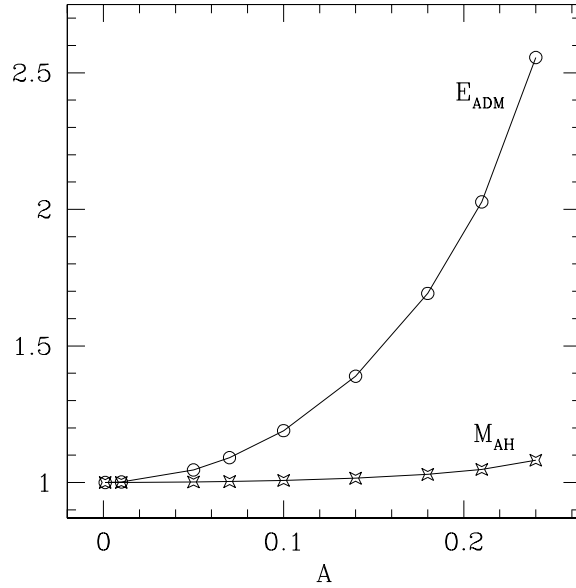


Figure 8.5: Black hole with superposed gravitational wave.

8.4.2 Black hole with gravitational wave

As a second example of the flexibility of our method, we now superpose a gravitational wave on a black hole background. For the metric g_{ij}^0 and mean curvature K^0 in Eqs. (8.11), we use a Schwarzschild black hole in Eddington-Finkelstein coordinates, Eqs. (7.29a) and (7.30). (We do not apply the radial coordinate transformation to make it conformally flat; instead, we use the deviation of the conformal factor from unity as a diagnostic).

We choose an odd, ingoing $m = 0$ quadrupole wave with Gaussian shape, Eq. (8.17) at location $x_0 = 15$ and width $w = 1$. The metric is singular at the origin, therefore we excise a inner sphere with radius $1.5M$ inside the horizon. At this inner boundary, we impose simple Dirichlet boundary conditions appropriate for the unperturbed black hole: $\psi = 1$, and N and β^i given by Eqs. (7.29b) and (7.29c), respectively.

Figure 8.5 shows the ADM-energy and the apparent horizon mass of the central black hole as a function of the amplitude of the gravitational wave. The apparent horizon mass changes only slowly with A indicating that the central black hole is only slightly perturbed by the gravitational wave. However, the ADM-energy changes drastically; for large amplitudes it is over twice as large as the apparent horizon mass, indicating a huge amount of energy in the gravitational wave outside

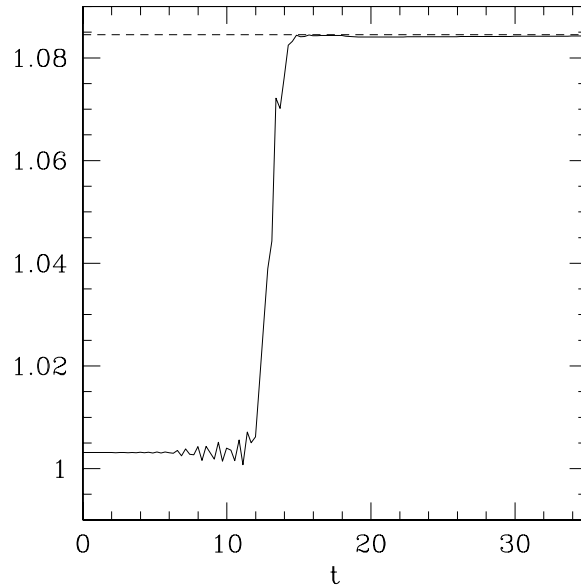


Figure 8.6: Apparent horizon mass during an evolution of a perturbed black hole spacetime. The dashed line indicates E_{ADM} from the initial data set.

the black hole.

We finally present an evolution of a black hole with superposed ingoing gravitational wave [115]. The initial data for the evolution is identical to the data sets used in Figure 8.5 with the one exception that the gravitational wave has even parity. Figure 8.6 shows the apparent horizon mass as a function of evolution time. For $t \lesssim 12$, M_{AH} is constant, its value being that from the initial data set. Between $12 \lesssim t \lesssim 16$, M_{AH} increases rapidly to an asymptotic value of $M_{AH} \approx 1.084$. The ADM-energy of the initial data set was $E_{ADM} = 1.0845$. Apparently, the ingoing gravitational wave outside the black hole falls into it, increasing the area of the apparent horizon. The final apparent horizon mass is very close to the ADM-energy, and the growth of M_{AH} happens during a time-interval of roughly the width of the initial pulse. Thus it appears that a large fraction of the wave is coherently ingoing and falls into the black hole.

8.5 Discussion

We propose a new method to construct spacetimes containing gravitational radiation. Since our method is based on a *linear* wave, it allows for easy physical

interpretation of the generated data set in the limit of small amplitude. For strong amplitudes, the initial data sets are very nonlinear, but we expect that the solutions still retain qualitatively the properties of the underlying linear wave.

Two examples illustrate that the method is capable of generating initial data surfaces containing a large amount of gravitational energy.

There are many possible uses for these initial data sets: For example, data analysis of gravitational wave experiments would benefit from knowing in how many different frequencies a black hole radiates significantly, i.e., whether a nonlinearly perturbed black hole settles down into the lowest frequency eigenmode very quickly, or whether higher frequency eigenmodes are important for an intermediate period of time. This question could be addressed by hitting a black hole with one of the very strong pulses presented in section 8.4.2.

The example in section 8.4.2 can also be generalized to spinning black holes, off-centered gravitational waves, or gravitational waves with $m \neq 0$. Interesting questions would include, whether one can impart linear or angular momentum on the black hole, and which fraction of the gravitational wave is scattered at the black hole potential and reaches infinity.

Numerically, these initial data sets provide test-beds of evolution codes in situations far away from stationarity. The mass of a central black hole changes when a large gravitational wave falls into it; can today's gauge conditions handle this situation? If a gravitational wave collapses to a black hole, horizons appear, and evolution codes using black hole excision must accommodate this change. Furthermore, such spacetimes are ideal test-beds for gravitational wave extraction.

BIBLIOGRAPHY

- [1] J. W. York, Jr. *Phys. Rev. Lett.*, 82(7), pp. 1350–1353, 1999.
- [2] H. P. Pfeiffer and J. W. York Jr. *Phys. Rev. D*, 67, p. 044022, 2003.
- [3] R. Arnowitt, S. Deser and C. W. Misner. In L. Witten, ed., *Gravitation: An introduction to current research*. Wiley, New York, 1962.
- [4] J. W. York, Jr. In L. L. Smarr, ed., *Sources of Gravitational Radiation*, p. 83. Cambridge University Press, Cambridge, England, 1979.
- [5] P. A. Lichnerowicz. *J. Math. Pures Appl.*, 23, pp. 37–63, 1944.
- [6] C. W. Misner, K. S. Thorne and J. A. Wheeler. *Gravitation*. W. H. Freeman, New York, 1973.
- [7] L. P. Eisenhart. *Riemannian Geometry*. Princeton University Press, Princeton, New Jersey, 1925.
- [8] D. R. Brill. *Annals of Physics*, 7, pp. 466–483, 1959.
- [9] C. W. Misner. *Annals of Physics*, 24, pp. 102–17, 1963.
- [10] D. R. Brill and R. W. Lindquist. *Phys. Rev.*, 131(1), pp. 471–476, 1963.
- [11] S. Deser. *Ann. Inst. Henri Poincaré, Section A*, 7(2), pp. 149–188, 1967.
- [12] J. W. York, Jr. *J. Math. Phys.*, 14(4), pp. 456–464, 1973.
- [13] J. W. York, Jr. *Ann. Inst. Henri Poincaré, Section A*, 21(4), p. 319, 1974.
- [14] Y. Choquet-Bruhat and J. W. York. *Banach Center Publ.*, 41(Part 1), p. 119, 1997.
- [15] L. E. Kidder, M. A. Scheel and S. A. Teukolsky. *Phys. Rev. D*, 64, p. 064017, 2001.
- [16] L. Smarr and J. W. York, Jr. *Phys. Rev. D*, 17(8), pp. 1945–1956, 1978.
- [17] W. Tichy, B. Brügmann, M. Campanelli and P. Diener. *Phys. Rev. D*, 67, p. 064008, 2003.
- [18] J. W. York, Jr. *Phys. Rev. Lett.*, 28(16), pp. 1082–1085, 1972.
- [19] N. Ó. Murchadha and J. W. York. *Phys. Rev. D*, 10, pp. 428–436, 1974.
- [20] G. B. Cook. *Living Rev. Relativity*, 3(5), 2000. <http://livingreviews.org/Articles/Volume3/2000-5cook/> [Online Article]: cited on Aug 11, 2001.

- [21] J. M. Bowen. *Gen. Relativ. Gravit.*, 11(3), pp. 227–231, 1979.
- [22] J. M. Bowen and J. W. York, Jr. *Phys. Rev. D*, 21(8), pp. 2047–2056, 1980.
- [23] A. D. Kulkarni, L. C. Shepley and J. W. York, Jr. *Phys. Lett. A*, 96A(5), pp. 228–230, 1983.
- [24] S. Brandt and B. Brügmann. *Phys. Rev. Lett.*, 78(19), pp. 3606–3609, 1997.
- [25] M. D. Hannam, C. R. Evans, G. B. Cook and T. W. Baumgarte. *gr-qc/0306028*, 2003.
- [26] G. B. Cook. *Initial Data for the Two-Body Problem of General Relativity*. Ph.D. thesis, University of North Carolina at Chapel Hill, 1990.
- [27] G. B. Cook. *Phys. Rev. D*, 44(10), pp. 2983–3000, 1991.
- [28] G. B. Cook. *Phys. Rev. D*, 50(8), pp. 5025–5032, 1994.
- [29] S. A. Orszag. *J. Comp. Phys*, 37, p. 70, 1980.
- [30] D. Funaro, A. Quarteroni and P. Zanolli. *SIAM J. Numer. Anal.*, 25(6), pp. 1213–1236, 1988.
- [31] M. G. Macaraeg and C. L. Streett. *Appl. Numer. Math*, 2, pp. 95–108, 1986.
- [32] J. B. Boyd. *Chebyshev and Fourier Spectral Methods, 2nd edition*. Dover, New York, 2001. For an online version, see <http://www-personal.engin.umich.edu/~jpbayd>.
- [33] P. Gervasio, E. Ovtchinnikov and A. Quarteroni. *SIAM J. Numer. Anal.*, 34(4), pp. 1616–1639, 1997.
- [34] M. Barrett, M. Berry, T. F. Chan, J. Van der Horst and H. Van der Horst. *Templates for the Solution of Linear Systems: Building Blocks for Iterative Methods*. SIAM, Philadelphia, PA, 1994.
- [35] P. Demaret and M. O. Deville. *J. Comp. Phys*, 95, pp. 359–386, 1991.
- [36] H.-C. Ku. *J. Comp. Phys*, 117, pp. 215–227, 1995.
- [37] A. Pinelli, A. Vacca and A. Quarteroni. *J. Comp. Phys*, 136, pp. 546–558, 1997.
- [38] P. Grandclément, S. Bonazzola, E. Gourgoulhon and J.-A. Marck. *J. Comp. Phys*, 170, pp. 231–260, 2001.
- [39] D. Gottlieb and S. A. Orszag. *Numerical Analysis of Spectral Methods: Theory and Applications*. Society of Industrial and Applied Mathematics, 1977.

- [40] C. Canuto, M. Y. Hussaini, A. Quarteroni and T. A. Zang. *Spectral Methods in Fluid Dynamics*. Springer, New York, 1987.
- [41] S. Orszag. *Monthly Weather Review*, 102(1), pp. 56–75, 1974.
- [42] L. E. Kidder and L. S. Finn. *Phys. Rev. D*, 62, p. 084026, 2000.
- [43] P. N. Swarztrauber. *SIAM J. Numer. Anal.*, 16(6), pp. 934–949, 1979.
- [44] P. N. Swarztrauber. *SIAM J. Numer. Anal.*, 18(2), pp. 191–210, 1981.
- [45] S. Balay, K. Buschelman, W. D. Gropp, D. Kaushik, L. C. McInnes and B. F. Smith. PETSc home page, 2001. <http://www.mcs.anl.gov/petsc>.
- [46] W. H. Press, S. A. Teukolsky, W. T. Vetterling and B. P. Flannery. *Numerical Recipes in C*. Cambridge University Press, Cambridge, UK, 1997.
- [47] O. Axelsson. *Iterative solution methods*. Cambridge University Press, 1994.
- [48] M. Deville and E. Mund. *J. Comp. Phys*, 60, pp. 517–533, 1985.
- [49] S. A. Baden and S. J. Fink. KeLP 1.3 home-page. <http://www-cse.ucsd.edu/groups/hpcl/scg/kelp.html>.
- [50] J. C. Adams and P. N. Swarztrauber. SPHEREPACK 3.0. <http://www.scd.ucar.edu/css/software/spherepack>.
- [51] P. N. Swarztrauber. DFFTPACK. <http://www.netlib.org/fftpack/index.html>.
- [52] G. B. Cook, M. W. Choptuik, M. R. Dubal, S. Klasky, R. A. Matzner and S. R. Oliveira. *Phys. Rev. D*, 47(4), pp. 1471–1490, 1993.
- [53] H. P. Pfeiffer, G. B. Cook and S. A. Teukolsky. *Phys. Rev. D*, 66, p. 024047, 2002.
- [54] B. F. Smith, P. Bjørstad and W. Gropp. *Domain Decomposition: Parallel Multilevel Methods for Elliptic Partial Differential Equations*. Cambridge University Press, 1996.
- [55] Y. Saad. *SIAM J. Sci. Comput*, 14(2), pp. 461–469, 1993.
- [56] P. Marronetti and R. A. Matzner. *Phys. Rev. Lett.*, 85(26), p. 5500, 2000.
- [57] R. M. Wald. *General Relativity*. University of Chicago Press, Chicago, IL, 1984.
- [58] J. B. Hartle and D. H. Sharp. *ApJ.*, 147, pp. 317–333, 1967.
- [59] T. W. Baumgarte. *Phys. Rev. D*, 62, p. 024018, 2000.

- [60] A. Garat and R. H. Price. *Phys. Rev. D*, 61, p. 124001, 2000.
- [61] J. M. Bardeen, W. H. Press and S. A. Teukolsky. *ApJ.*, 178, pp. 347–369, 1972.
- [62] G. B. Cook and A. M. Abrahams. *Phys. Rev. D*, 46(2), pp. 702–713, 1992.
- [63] R. A. Matzner, M. F. Huq and D. Shoemaker. *Phys. Rev. D*, 59(2), p. 024015, 1999.
- [64] T. W. Baumgarte, G. B. Cook, M. A. Scheel, S. L. Shapiro and S. A. Teukolsky. *Phys. Rev. D*, 54(8), pp. 4849–4857, 1996.
- [65] H. P. Pfeiffer, S. A. Teukolsky and G. B. Cook. *Phys. Rev. D*, 62, p. 104018, 2000.
- [66] E. Gourgoulhon, P. Grandclément, K. Taniguchi, J.-A. Marck and S. Bonazzola. *Phys. Rev. D*, 63, p. 064029, 2001.
- [67] E. Gourgoulhon, P. Grandclément and S. Bonazzola. *Phys. Rev. D*, 65, p. 044020, 2002.
- [68] P. Grandclément, E. Gourgoulhon and S. Bonazzola. *Phys. Rev. D*, 65, p. 044021, 2002.
- [69] A. Buonanno and T. Damour. *Phys. Rev. D*, 59, p. 084006, 1999.
- [70] T. Damour, P. Jaranowski and G. Schäfer. *Phys. Rev. D*, 62, p. 084011, 2000.
- [71] L. Blanchet. *Phys. Rev. D*, 65, p. 124009, 2002.
- [72] T. Damour, E. Gourgoulhon and P. Grandclément. *Phys. Rev. D*, 66, p. 024007, 2002.
- [73] J. Baker, B. Brügmann, M. Campanelli, C. O. Lousto and R. Takahashi. *Phys. Rev. Lett.*, 87(12), p. 121103, 2001.
- [74] M. Alcubierre, W. Bengert, B. Brügmann, G. Lanfermann, L. Nergel, E. Seidel and R. Takahashi. *Phys. Rev. Lett.*, 87(27), p. 271103, 2001.
- [75] J. Baker, M. Campanelli, C. O. Lousto and R. Takahashi. *Phys. Rev. D*, 65, p. 124012, 2002.
- [76] N. Ó. Murchadha and J. W. York. *Phys. Rev. D*, 10, pp. 437–446, 1974.
- [77] N. Ó. Murchadha and J. W. York, Jr. *Gen. Relativ. Gravit.*, 7(3), pp. 257–261, 1976.
- [78] J. Thornburg. *Class. Quantum Gravit.*, 4(5), pp. 1119–1131, 1987.

- [79] R. Rieth. In A. Królak, ed., *Mathematics of Gravitation. Part II. Gravitational Wave Detection*, pp. 71–74. Polish Academy of Sciences, Institute of Mathematics, Warsaw, 1997.
- [80] D. K. Monroe. *Spatial conformal curvature and gravitational radiation*. Ph.D. thesis, University of North Carolina, 1976.
- [81] C. O. Lousto and R. H. Price. *Phys. Rev. D*, 57(2), pp. 1073–1083, 1998.
- [82] S. Bonazzola, E. Gourgoulhon, M. Salgado and J.-A. Marck. *A & A*, 278, pp. 421–443, 1993.
- [83] S. Bonazzola, E. Gourgoulhon and J.-A. Marck. *Phys. Rev. D*, 58(104020), 1998.
- [84] L. E. Kidder, M. A. Scheel, S. A. Teukolsky, E. D. Carlson and G. B. Cook. *Phys. Rev. D*, 62, p. 084032, 2000.
- [85] M. Ansorg, A. Kleinwächter and R. Meinel. *A & A*, 381, pp. L49–L52, 2002.
- [86] H. P. Pfeiffer, L. E. Kidder, M. A. Scheel and S. A. Teukolsky. *Comput. Phys. Commun.*, 152, pp. 253–273, 2003.
- [87] S. Brandt, R. Correll, R. Gómez, M. Huq, P. Laguna, L. Lehner, P. Marronetti, R. A. Matzner, D. Neilsen, J. Pullin, E. Schnetter, D. Shoemaker and J. Winicour. *Phys. Rev. Lett.*, 85(26), pp. 5496–5499, 2000.
- [88] G. B. Cook. *Phys. Rev. D*, 65, p. 084003, 2002.
- [89] J. T. Whelan, C. Beetle, W. Landry and R. H. Price. *Class. Quantum Gravit.*, 19, pp. 1285–1290, 2002.
- [90] J. R. Wilson and G. J. Mathews. In C. R. Evans, L. S. Finn and D. W. Hobill, eds., *Frontiers in Numerical Relativity*, pp. 306–314. Cambridge University Press, Cambridge, England, 1989, 1989.
- [91] J. R. Wilson and G. J. Mathews. *Phys. Rev. Lett.*, 7(23), pp. 4161–4164, 1995.
- [92] A. Ashtekar, C. Beetle, O. Dreyer, S. Fairhurst, B. Krishnan, J. Lewandowski and J. Wisniewski. *Phys. Rev. Lett.*, 85(17), pp. 3564–3567, 2000.
- [93] O. Dreyer, B. Krishnan, D. Shoemaker and E. Schnetter. *Phys. Rev. D*, 67, p. 024018, 2003.
- [94] G. B. Cook. Private communication, 2003. .
- [95] E. Gourgoulhon and S. Bonazzola. *Class. Quantum Gravit.*, 11, pp. 443–452, 1994.

- [96] R. Beig. *Phys. Lett. A*, 69A(3), pp. 153–155, 1978.
- [97] F. Estabrook, H. Wahlquist, S. Christensen, B. DeWitt, L. Smarr and E. Tsiang. *Phys. Rev. D*, 7, pp. 2814–2817, 1973.
- [98] L. E. Kidder. Private communication. 2003.
- [99] R. H. Price. *Phys. Rev. D*, 5(10), pp. 2419–2438, 1972.
- [100] P. Papadopoulos. *Phys. Rev. D*, 65, p. 084016, 2002.
- [101] M. W. Choptuik. *Phys. Rev. Lett.*, 70(1), pp. 9–12, 1993.
- [102] A. M. Abrahams and C. R. Evans. *Phys. Rev. Lett.*, 70(20), pp. 2980–2983, 1993.
- [103] N. T. Bishop, R. Gómez, L. Lehner, M. Maharaj and J. Winicour. *Phys. Rev. D*, 56, pp. 6298–6309, 1997.
- [104] R. Gómez *et al.* (Binary Black Hole Grand Challenge Alliance). *Phys. Rev. Lett.*, 80(18), pp. 3915–3918, 1 1998.
- [105] K. Eppley. *Phys. Rev. D*, 16(9), pp. 1609–1614, 1977.
- [106] A. M. Abrahams, K. R. Heiderich, S. L. Shapiro and S. A. Teukolsky. *Phys. Rev. D*, 46(6), pp. 2452–2463, 1992.
- [107] D. Garfinkle and G. C. Duncan. *Phys. Rev. D*, 63(044011), 2001.
- [108] M. Alcubierre, G. Allen, B. Brügmann, G. Lanfermann, E. Seidel, W.-M. Suen and M. Tobias. *Phys. Rev. D*, 61, p. 041501, 2000.
- [109] M. Shibata. *Phys. Rev. D*, 55(12), pp. 7529–7537, 1997.
- [110] S. R. Brandt and E. Seidel. *Phys. Rev. D*, 54(2), pp. 1403–1416, 1996.
- [111] K. Camarda and E. Seidel. *Phys. Rev. D*, 59, p. 064019, 1999.
- [112] S. Brandt, K. Camarda, E. Seidel and R. Takahashi. *Class. Quantum Gravit.*, 20, pp. 1–20, 2003.
- [113] A. M. Abrahams and C. R. Evans. *Phys. Rev. D*, 46(10), pp. R4117–R4121, 1992.
- [114] S. A. Teukolsky. *Phys. Rev. D*, 26(4), pp. 745–750, 1982.
- [115] L. E. Kidder, H. P. Pfeiffer and D. Shoemaker. Private communication, 2003.